UTS UNIVERSITY OF TECHNOLOGY SYDNEY

Controllable synthesis of B,N co-doped C from metal-organic frameworks with tunable catalytic performance

by Xuefei Wang

Thesis submitted in fulfilment of the requirements for the degree of

Doctor of Philosophy

under the supervision of Prof Zhenguo Huang and Prof John Zhou

University of Technology Sydney
Faculty of Engineering and Information Technology

March 2023

CERTIFICATE OF ORIGINAL AUTHORSHIP

I, Xuefei Wang, declare that this thesis is submitted in fulfilment of the requirements for the award of Doctor of Philosophy, in the School of Civil and Environmental Engineering at the University of Technology Sydney.

This thesis is wholly my own work unless otherwise referenced or acknowledged. In addition, I certify that all information sources and literature used are indicated in the thesis.

This document has not been submitted for qualifications at any other academic institution.

This research is supported by the Australian Government Research Training Program.

Signature: Production Note:
Signature removed prior to publication.

Date: 24/03/2023

Acknowledgements

Firstly, I would like to express my deepest acknowledgment to my principal supervisor **Prof. Zhenguo Huang**, for his invaluable advice, continuous support, and patience during my PhD study. I am unable to accomplish my PhD study without his dedication and devotion to research.

Secondly, I deeply appreciate **Prof. Jian Liu** as the host during my visit at Dalian Institute of Chemical Physics, Chinese Academy of Sciences. Without his great support in the laboratory and equipment, I can hardly accomplish my PhD study during Covid. I also thank him for his invaluable advice.

Thirdly, I would like to thank **Dr. Tianyi Liu** for his help with the computational work of my project. His valuable advice greatly improves the quality of my PhD project.

I appreciate the kind support from my research collaborators: **Dr. Chao Han** and **A/Prof. Panpan Su**, for their help with data processing and analysis; **Prof. John Zhou**, for his input on research and candidacy assessment along the way.

Thanks to **Dr. Nirenkumar Pathak**, for his dedicated work as a Technical Support Assistant to assist in our daily research activities and **Dr. Mohammed Johir**, for his fulfilment of administrative duty.

Finally, I appreciate all the assistance and support from my lab colleagues and friends, **Yan Dai**, **Lei Ding**, **Guojin Zhang**, **Feng Liu**, **Zhimei Xu**, **Liwei Wang**, **Yutong Pi**,

Xinyao Wang, **Rongrong Han**, and **Haitao Li** (in no particular order). Their diligence, dedication, knowledge, and friendship motivate me to stay strong in research during the hard times.

Table of contents

List of Tables

List of Figures

List of Abbreviations and Notations

Symbol	Description
B	Boron
C	Carbon
N	Nitrogen
O	Oxygen
Zn	Zinc
Co	Cobalt
MOF	Metal-organic framework
ZIF	Zeolite imidazole framework
B,N@C	Boron- and nitrogen-doped carbon
ZnCo@NCO	Zinc, cobalt nanoparticles anchored in nitrogen-doped carbon
ZnCo@NCBO	Zinc, cobalt nanoparticles anchored in boron- and nitrogen-doped carbon
AB	Ammonia borane
PAB	Polyiminoborane
BA	Boric acid
HER	Hydrogen evolution reaction
OER	Oxygen evolution reaction
ORR	Oxygen reduction reaction
CO_2RR	Carbon dioxide electroreduction reaction
MAB	Metal-air batteries
LIB	Li-ion batteries
$Zn(NO_3)_2 \cdot 6H_2O$	Zinc nitrate hexahydrate
$Co(NO_3)_2 \cdot 6H_2O$	Cobalt nitrate hexahydrate
2-MIM	2-methylimidazole
MeOH	Methanol
DMF	Dimethylformamide
KOH	Potassium hydroxide
RHE	Reversible hydrogen electrode

List of publications

X. Wang, C. Han, H. Li, P. Su, N. Ta, Y. Ma, Z. Huang, J. Liu, Fabrication of monodispersed B, N co-doped hierarchical porous carbon nanocages through confined etching to boost electrocatalytic oxygen reduction, *Nano Research*, 16 (**2023**) 290-298.

X. Wang, T. Liu, H. Li, C. Han, P. Su, N. Ta, S. Jiang, B. Kong, J. Liu, Z. Huang, *et al.* Balancing mass transfer and active sites to improve electrocatalytic oxygen reduction by B,N co-doped C nanoreactors. *Nano Lett*, 23 (**2023**) 4699-4707.

R. Han, F. Liu, **X. Wang**, M. Huang, W. Li, Y. Yamauchi, X. Sun, Z. Huang, Functionalised hexagonal boron nitride for energy conversion and storage, *J. Mater. Chem. A*, 8 (**2020**) 14384-14399.

Abstract

Dual heteroatom-doped carbon materials have attracted widespread research attention as catalysts in the field of energy storage and conversion due to their unique electronic structures and chemical tunability. In particular, boron and nitrogen co-doped carbon (B,N@C) has shown great potential for electrocatalytic applications. However, more research is needed in designing and regulating the structure of these materials to improve their catalytic performance. Furthermore, mass transfer is critical in catalytic processes, more so when the reactions are facilitated by nanostructured catalysts. Strong efforts have been devoted to improving the efficacy and quantity of active sites, but often the mass transfer has not been well studied. This thesis aims to develop novel B,N@C nanoreactors with hierarchical porous structures as electrocatalysts that feature high catalytic activities and investigate the importance of mass transfer on the electrocatalyst performance based on these as-obtained nanoreactors.

Firstly, monodispersed hierarchical porous B,N@C nanocages are fabricated by pyrolyzing zeolite imidazole framework (ZIF) which is treated with ammonia borane (AB) or boric acid (BA) via an integrated double-solvent impregnation and nanoconfined etching. The treated ZIF-8 provides an essential structural template to achieve hierarchical B,N@C structures with micro/meso/macro multimodal pore size distributions. The resultant B,N@C nanocages display high catalytic activities for electrochemical oxygen reduction reaction (ORR) in alkaline media.

Then, mass transfer is regulated in electrocatalytic ORR by tailoring pore sizes. Using a confined-etching strategy, I fabricate B,N@C electrocatalysts featuring abundant active sites but different amounts of micro-, meso- and macropores. The ORR performance of these catalysts is found to correlate with the diffusion of the reactants. The optimized B,N@C with trimodal-porous structures feature enhanced O_2 diffusion and better catalytic activity per heteroatomic site toward the ORR process, with the performance being on par with commercial Pt/C.

Finally, preliminary results of the preparation of multilevel hollow ZnCo@NCO and ZnCo@NCBO nanoreactors by etching ZnCo-ZIF are reported. The nanoreactor is tested in electrocatalytic oxygen evolution reaction (OER) and electro-oxidation of benzyl alcohol.

Chapter 1 Introduction

Cells in nature are soft matter with microcompartments for particular functional groups. In materials science, the nanoreactors designed by simulating cells can serve as "artificial cells" to catalyse chemical reactions controllably. As illustrated in **Error! Reference s ource not found.**, nanoreactors provide a mesoscale-confined space where chemical reactions are limited and regulated [1]. In various designs of nanostructured materials, nanoreactors are most represented by hierarchical porous nanomaterials. They endow nanoreactors with the ability to simulate cells in nature, which allows cascade chemical conversions to take place due to precisely located functional groups. Based on such innovative nanostructures, there are key structural features as follows.

1) The porous structures and cavities provide a spatial environment for attaching functional groups on desired sites, [2].

2) Meso/microporous and hollow cavities provide confined space for concentrating the reactants through selective interactions, trapping reaction intermediates on active sites for further reactions, and enhancing mass transfer and selective sieving based on the specific pore structure. [3, 4].

3) Integrating spatially separated active sites into one particle makes cascade reactions

more efficient [5].

Therefore, nanoreactors with unique structural features and high catalytic efficacy bear a promising future. Up to now, nanoreactors have been applied in energy storage and conversion, catalytic reaction, pollutant adsorption and degradation, drug delivery, and so on [1, 6-9].

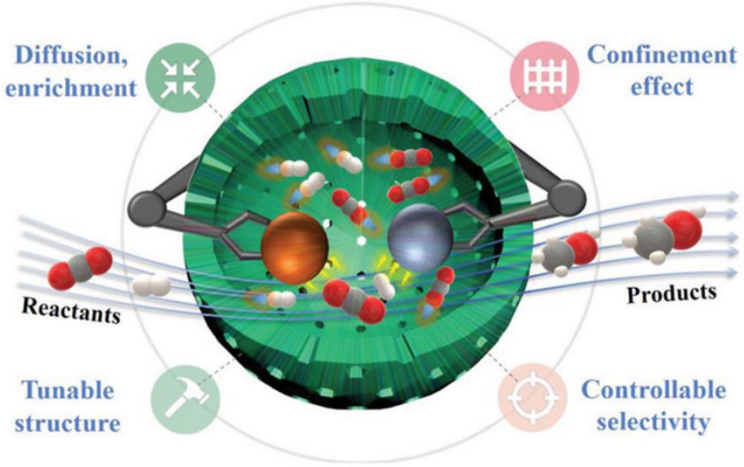

Figure 1.1. Schematic diagram of a nanoreactor. [1]

A typical nanoreactor design for the catalytic process should take both mass diffusion and surface reaction into account, which requires that the structure and composition of the nanoreactor is precisely controlled. Based on these considerations, metal−organic frameworks (MOFs), which are assembled from the coordination between metallic nodes and multitopic organic ligands, are often used for the fabrication of novel nanoreactors. MOFs typically have high porosity and modular assembly mode, so they can be customized for top-up synthesizing, or selectively etched by top-down processing to fabricate hierarchical porous and multilevel hollow nanomaterials, thus enriching the

construction of nanoreactors. Based on this intrinsic property, MOF-based and MOF-derived novel porous and hollow nanomaterials have been fabricated and used as nanoreactors for downstream catalytic applications over the past few decades [9-20].

In this project, efforts are focused on the controlled synthesis of B,N@C nanoreactors through novel strategies to boost electrocatalytic reactions. Firstly, the current status of research work on MOF-derived nanoreactors is reviewed. Secondly, based on the latest development, an integrated double-solvent impregnation and nanoconfined-etching method to prepare monodispersed hierarchical porous B,N@C nanoreactors from MOFs toward ORR was developed. The synthetic strategy and essential roles of B-containing etchants (ammonia borane and boric acid) as etchants were discussed in detail. Then their electrocatalytic ORR performances were investigated in alkaline media, using N@C as a control sample. Thirdly, based on the first work, B,N@C nanoreactors featuring abundant active sites but different amounts of micro-, meso- and macropores were prepared. The importance of mass transfer on the ORR performance was then investigated by discussing the structure-activity relationship systematically. Fourthly, multilevel hollow ZnCo@NCO and ZnCo@NCBO nanoreactors were fabricated by etching and pyrolyzing MOFs, and the nanoreactor effect in electrocatalytic ORR is expanded to electrocatalytic OER and selective electrooxidation of benzyl alcohol.

Finally, the achievements and inadequacies of this PhD project are pointed out. Future research work is suggested to solve the remaining questions of this project.

Chapter 2 Literature review

Herein, research progress of nanoreactors derived from MOFs in recent years is reviewed and MOF-derived B,N-doped carbon-based electrocatalysts for ORR and OER are highlighted. Firstly, the synthesis methods of hierarchical porous nanostructures are covered. Special emphasis is placed on the process of structural and compositional evolution achieved by etching MOFs. Afterward, nanoreactor engineering, including spatial-structure engineering of nanoreactors and location engineering of active sites, is discussed. Then, methods to improve efficacy of nanoreactor on chemical reactions are discussed, including adjusting the electronic state of the metal, enhancing the heat and mass transfer, improving the selectivity of the target product, and integrating multiple active sites to achieve a tandem reaction. Finally, recent developments in MOF-derived B,N-doped carbon-based electrocatalysts for ORR and OER are discussed.

2.1 Synthetic strategies for MOF-derived nanoreactors

Fabrication of hierarchical porous nanomaterial is the precondition in the construction of MOF-derived nanoreactors. The as-prepared porous and hollow MOF-derived nanoreactors can either be used directly or as templates and precursors to fabricate other complex nanoreactors. The synthetic methods of MOF-derived nanoreactors are mainly divided into "bottom-up" and "top-down" methods. The "bottom-up" method usually

relies on templates, including using hard templates and soft templates [21, 22]. By introducing templates in the crystal growth of MOFs, superior nano-architectures with secondarily generated pores can be obtained after removing the templates. The "top-down" method relies on chemical surgery or confined pyrolysis to engrave MOFs under specific reaction conditions, which can produce various porous products directly [11, 23]. For this part, detailed synthetic methods for fabricating MOF-derived nanoreactors will be presented.

2.1.1 Template-mediated assembly

The template methods utilize soft or hard templates with controllable shapes when preparing nanomaterials through physical, chemical, or biological methods. Mesopores, macropores, or even cavities with structural characteristics similar to that of the templates are generated after the templates are removed. The key to preparing hierarchical porous or multilevel hollow nanoreactors using templates is the selection of templating agents, which regulate the morphology and structure of the product by controlling the nucleation and growth.

2.1.1.1 Hard-templating strategy

Various materials have been developed as hard templates to control the growth of MOFs, including metal nanoparticles, metal oxide nanoparticles, polymers, and silica [22]. Metal and metal oxide nanoparticles usually serve as semi-sacrificial hard templates. During the

growth of external MOFs, the surface of metal and metal oxides interacts with the added ligands. As a result, metal ions from the semi-sacrificial hard template diffuse outward and are coordinated with ligands in solutions, resulting in the growth of the MOF shell over the templates [24]. Incompletely converted templates are finally etched away. By adjusting the sorts of solvents and the concentration of MOF precursors, the extent of template conversion can be controlled to obtain the target structure of MOF nanoreactors. For example, Li et al. prepared hollow ZIF-8 nanocages with PdAg nanoparticles inside by using Cu_2O layer as a semi-sacrificial template (Figure 2.1A) [25]. The Cu_2O layer was *in situ* etched by protons generated during the growth of the ZIF-8 shell, and further removed completely by ammonium hydroxide. As a result, PdAg@ZIF-8 nanoreactor with a yolk−shell structure was created (Figure 2.1B).

In addition, polymers with tunable morphology, which can be etched away by high-polarity solvents, are also commonly used as hard templates to fabricate MOF-derived nanoreactors [26]. Polymer templates are mostly spherical. After synthesizing periodically ordered polymer templates, the preparation of periodically ordered MOFs with macropores was developed [27, 28]. In this field, Shen et al. obtained a three-dimensional (3D) macro-microporous ZIF-8 for the first time [29]. Firstly, researchers used polystyrene (PS) nanosphere monolith as a template to obtain the "precursor@PS" structure by filling the interstices of the PS monolith with ZIF-8 precursor, 2-methylimidazole and $Zn(NO_3)_2$ (Figure 2.1C). Then, the "precursor@PS" structure was

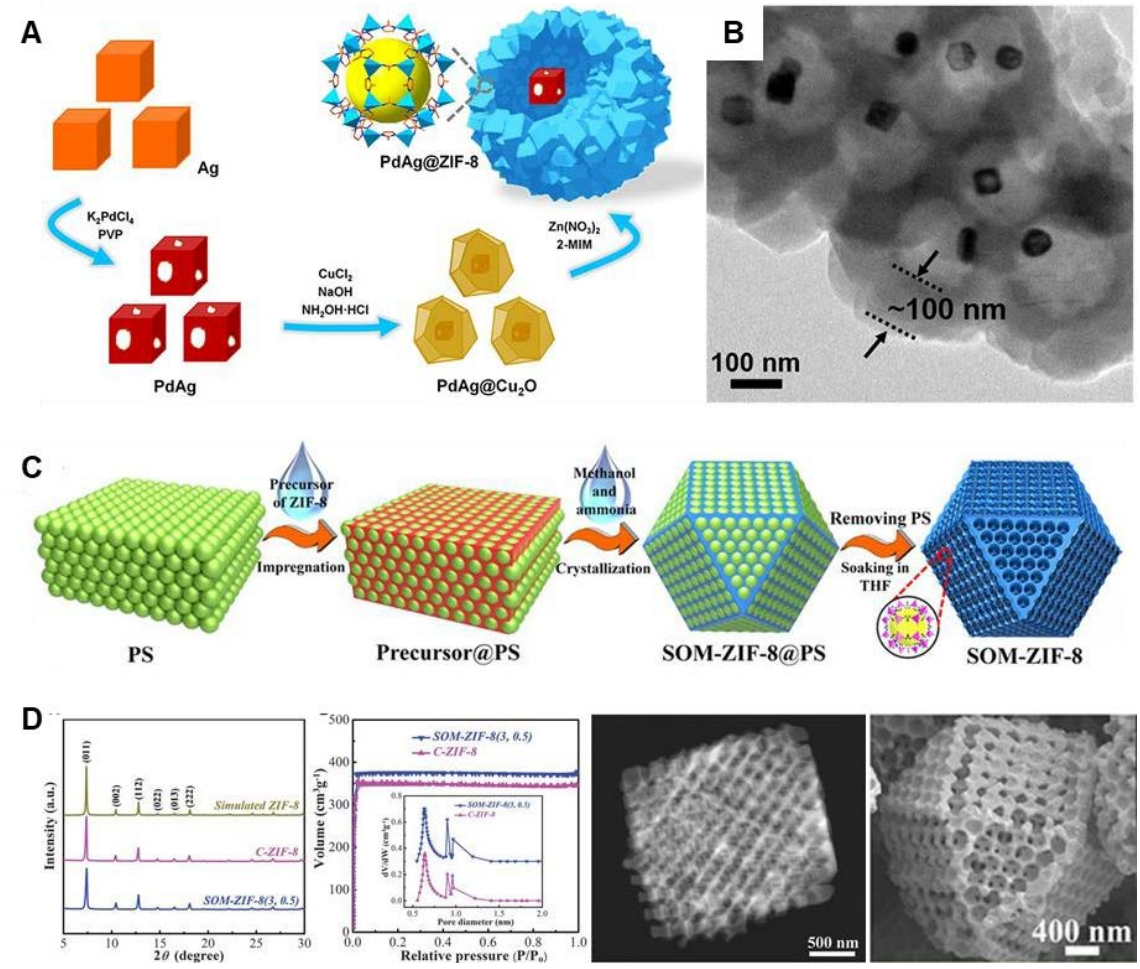

Figure 2.1. Fabrication of yolk-shell PdAg@ZIF-8 with PdAg@Cu_2O templates. A) Schematic illustration and B) TEM images of PdAg@ZIF-8. [25] Fabrication of periodic hollow SOM-ZIF-8 with PS nanosphere monolith templates. C) Schematic illustration and D) TEM images of SOM-ZIF-8. [29]

soaked in CH_3OH and $NH_3·H_2O$ solution, and ZIF-8 crystals grew in the interstitial space to form "SOM-ZIF-8@PS". Finally, SOM-ZIF-8 with periodically microporous topology featuring large cavities (11.6 Å) and small apertures (3.4 Å) was obtained (Figure 2.1D). Based on this method, Guo et al. further prepared ordered macro-mesoporous single-crystalline ZnCo-ZIFs (OMS-ZnCo-ZIFs) [30]. Subsequently, Co single atoms anchored

on nitrogen-doped ordered hierarchically porous carbon (Co-SAs@NHOPC) were prepared after pyrolysis. In addition to ordered PS spherical monolith, 3D-ordered colloidal SiO_2 spheres were also used as templates to prepare nitrogen-doped hierarchically ordered porous carbon polyhedrons with Zn single atoms (Zn-N-HOPCPs) [31].

Taken together, a hard template is useful to prepare hollow MOF-based materials, and their shape and size can be controlled by the sacrificial hard templates. The disadvantage of this method is that the hard templates cannot be removed in environmentally friendly ways.

2.1.1.2 Soft-templating strategy

Since the pioneering work of Mobil scientists and the subsequent revolutionary discovery of SBA-15 [32, 33], soft-template methods have been proven to be one of the most effective strategies for introducing mesopores into various materials including silicon, carbon, and metal oxides [34]. One obstacle to synthesize hierarchical porous or multilevel hollow MOFs via soft-template methods is the incompatibility of the self-assembly of surfactants with the crystallization process of MOF precursors in the organic phase.

To resolve this problem, Hofmeister effect was introduced into the self-assembly of the porous MOF through a solubilization-mediated mechanism (Figure 2.2A). Gu et al.

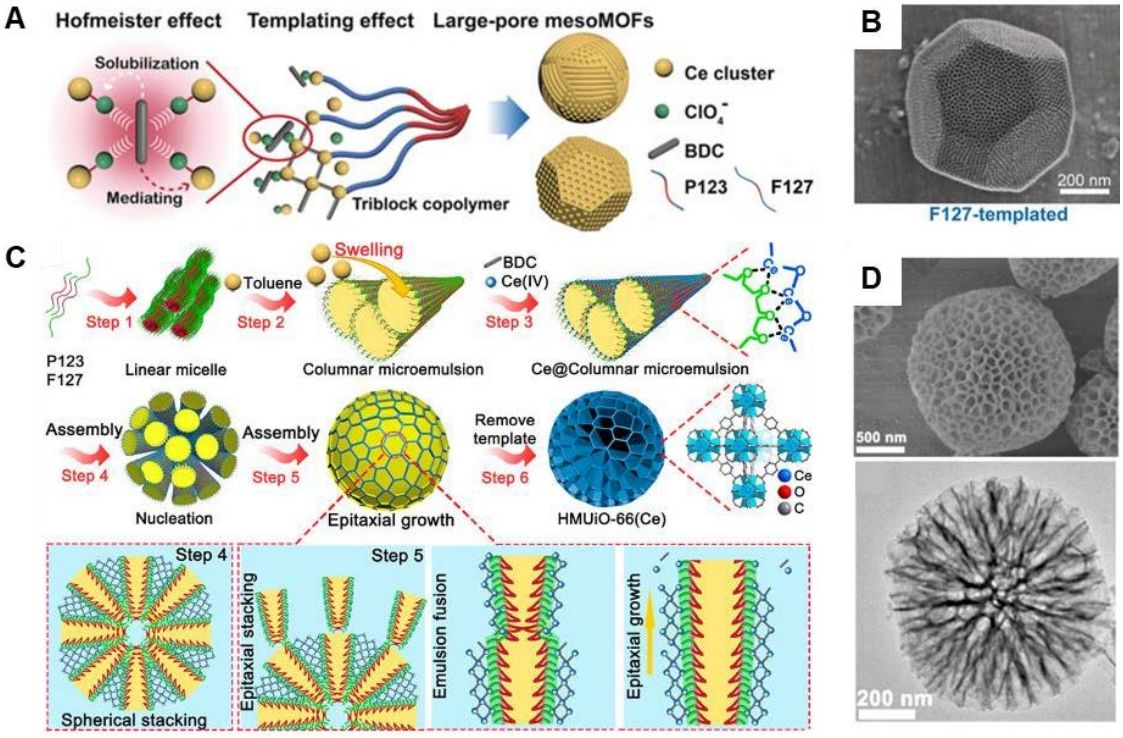

Figure 2.2. Fabrication of hierarchical mesoporous Ce-MOFs through solubilization-mediated self-assembly. A) Schematic illustration and B) TEM images of Ce-MOFs. [35] Fabrication of hierarchical porous HMUiO-66(Ce) through an emulsion-guided assembly. C) Schematic illustration and D) SEM and TEM images of HMUiO-66(Ce). [36]

synthesized secondary-level porous Ce-MOFs with mesopores (~10 nm) by combining the Hofmeister effect in the presence of a salting-in ion of ClO_4^- and the triblock copolymers (P123 and F127) as the structure-directing agent (Figure 2.2B) [35]. During the synthesis, Ce species were coordinated with the PEO corona of the micelles to form crown-ether-type complexes. ClO_4^- ions aggregated around the 1,4-dicarboxybenzene (BDC) ligands, increasing their solubility in water by weakening their hydrophobic

aggregation. Furthermore, ClO_4^- ions could facilitate the crystallization of MOFs around the micelles by bridging the BDC ligand with Ce-linked PEO coronas. Gu et al. further synthesized hierarchical micro/macroporous HMUiO-66(Ce) with macropore diameters as high as 100 nm through an emulsion-guided assembly (Figure 2.2C,D) [36]. Firstly, MOF seeds nucleated with the columnar microemulsions assembled as spheres. Then, ultra-thin MOF crystals grew with the seeds epitaxially, forming macroporous channels.

Synthesis of MOF-derived nanoreactors with specific pore sizes and structures via soft templates is still in its nascent stage. Block copolymers should be applied to lift the possibilities for developing novel MOF-derived nanoreactors with specific architectures. Also, self-assembly with general applicability still need to be developed in the future.

2.1.2 Competitive coordination etching

Limited by the instability of MOFs under harsh conditions, the selective removal of templates can be challenging. Therefore, simple methods without using templates are of great significance for the mass syntheses and practical applications of MOF-based nanoreactors.

Chemical etching has been an important method in obtaining hollow MOF-derived nanomaterials. Notably, MOFs usually serve as precursors and self-templates to be directly converted into hollow structural products in this process, without the need of template removal. According to the formation mechanism of internal voids, the MOF-

etching strategy is based on the scission of coordination bond. In detail, MOFs consist of a framework where deprotonated ligands are connected to metal nodes. Attacking ligands or metal nodes would cause depolymerization of MOFs. According to the processes, etching can be divided into competing for organic ligands and competing for metal nodes.

2.1.2.1 Competitive coordination etching: competing for organic ligands

Representative etchant that competes with metal nodes to bond with organic ligands is proton. Proton attacking the ligands could cause depolymerization of MOFs due to the protonation of ligands. Reported acids that are used to etch MOFs include hydrochloric acid [37, 38], acetic acid (AcOH) [39, 40], phosphoric acid (H_3PO_4) [41], citric acid [42], gallic acid [43], tannic acid [43], boric acid [44], phytic acid [45], cyanuric acid [46], and so on [12-14]. It should be emphasized that inorganic salts such as $Co(NO_3)_2$, $Ni(NO_3)_2$, $Fe(NO_3)_3$, and $Cu(NO_3)_2$ have also become common etchants to provide protons [19, 20].

The morphology of MOF tends to be completely changed when etched by inorganic acid, due to the random and non-protective etching process. The newly generated products finally self-assembled to the thermodynamically balanced structure under the etching condition. For example, ZIF-8 crystals can be etched by boric acid due to its acidity [44], as shown in Figure 2.3A. Solid ZIF-8 nanoparticles decomposed slowly during solvothermal conversion because of the protonation of 2-methylimidazole (2-MIM) ligands. Excess boric acid reacted progressively with released Zn^{2+} ions and 2-MIM to

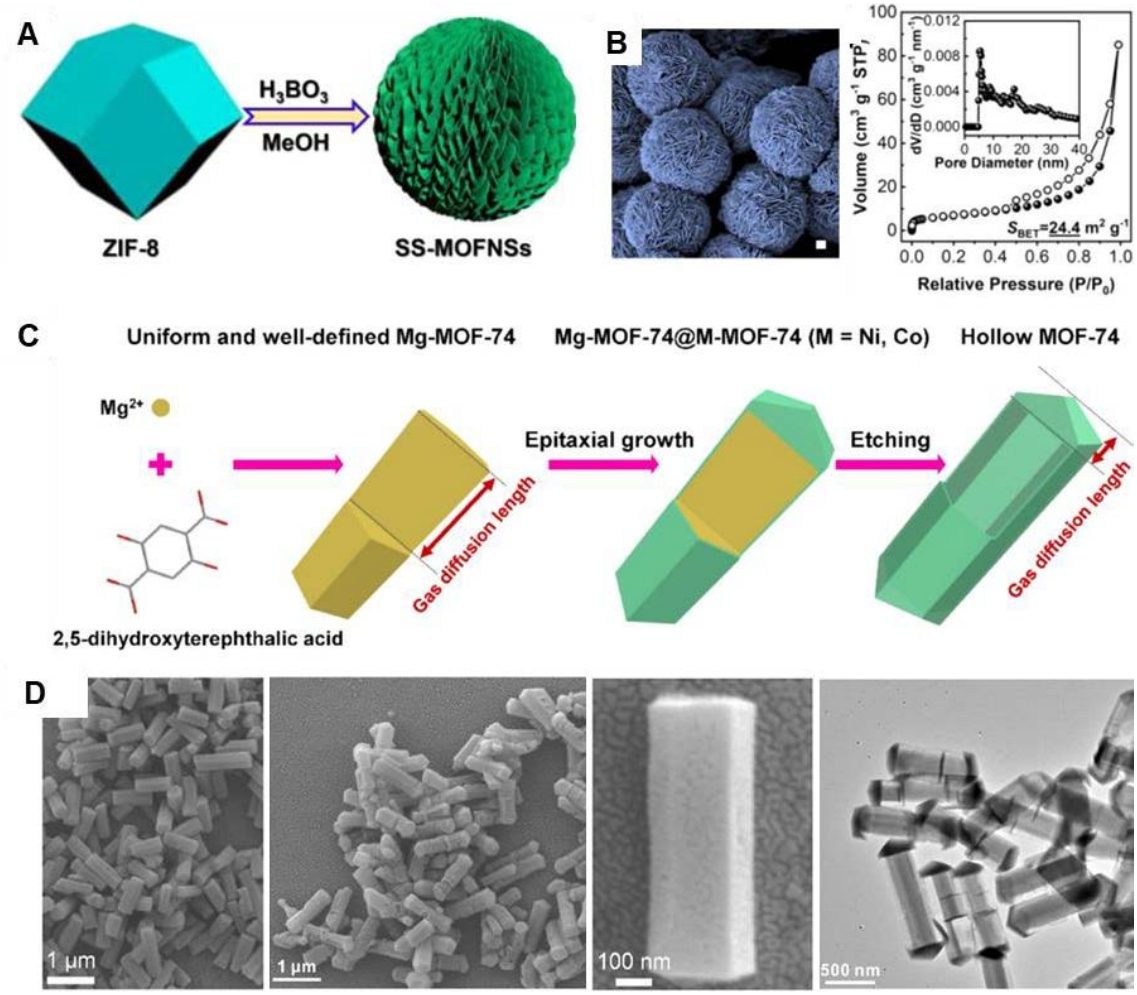

Figure 2.3. Conversion of solid ZIF-8 into spherical SS-MOFNS superstructure with competitive protons derived from $B(OH)_3$. A) Schematic illustration and B) Characterizations of SS-MOFNS. [44] Conversion of core-shell Mg-MOF-74@Co/Ni-MOF-74 into hollow Co/Ni-MOF-74 with competitive protons derived from HCl. C) Schematic illustration and D) characterizations of Mg-MOF-74 and Ni-MOF-74. [38]

form new MOF crystals, named as SS-MOFNSs ($Zn_2(BO_3)_1(C_4N_2H_5)_1$). Using ZIF-8 as a self-sacrificing template, three-dimensional well-organized superstructures composed of nanosheets were fabricated by controlling the temperature to balance the etching and polymerization process (Figure 2.3B). However, the direct etching of MOF materials by

inorganic acid without protection may cause the framework to collapse or even to be completely dissolved [47]. Therefore, to obtain a hollow structure by treating homogeneous MOF precursors with an inorganic acid, MOFs need to be well protected during the etching process [12]. In this regard, Wu et al. prepared a hollow MOF in hydrochloric acid (HCl) solution by etching a MOF@MOF composite (Figure 2.3C) [38]. The stability variance in MOF@MOF composite is important in preparing hollow MOFs by etching. The more stable MOF shell served as the protective agent to maintain the morphology during etching. As shown in Figure 2.3D, hollow Co/Ni-MOF-74 was obtained by removing the less stable Mg-MOF-74 core of the Mg-MOF-74@Co/Ni-MOF-74 composite using HCl as the etchant (MOF-74, known as M_2(dobdc) ($dobdc^{4-}$ = 2,5-dioxido-1,4-benzenedicarboxylate)) [38].

Organic acids such as phenolic acids can coordinate with metal ions, so they are prone to be adsorbed onto the outer surface of the MOF materials leading to metal-phenolic networks, preventing MOFs from collapsing during etching [43, 48, 49]. At the same time, protons released by the acids enter into the MOFs, protonating the ligands, thereby etching the internal components of the MOFs. As a result, protons diffuse into MOFs through the pores and etch the core of the crystal, and finally lead to a hollow nanomaterial. Gallic acid (GA) and tannic acid (TA) were also reported by Hu et al. as etchants to prepare hollow MOFs (Figure 2.4A) [43]. Such a method is suitable for etching a variety of MOFs, including ZIF-8 crystals, MIL-68 (In) microrods, and Tb-CP

spheres (Figure 2.4B-D). Notably, the size of molecules, pH value, and polymer structure (linear or network) are key factors in fabricating a hollow structure [43, 50], because the proper polymer can ensure a uniform coating on the MOF surface. Otherwise, random and non-uniform etching of MOFs may occur. Other organic acids such as phytic acid [45] and cyanuric acid [46] have also been reported as etchants to obtain hollow structures from MOFs.

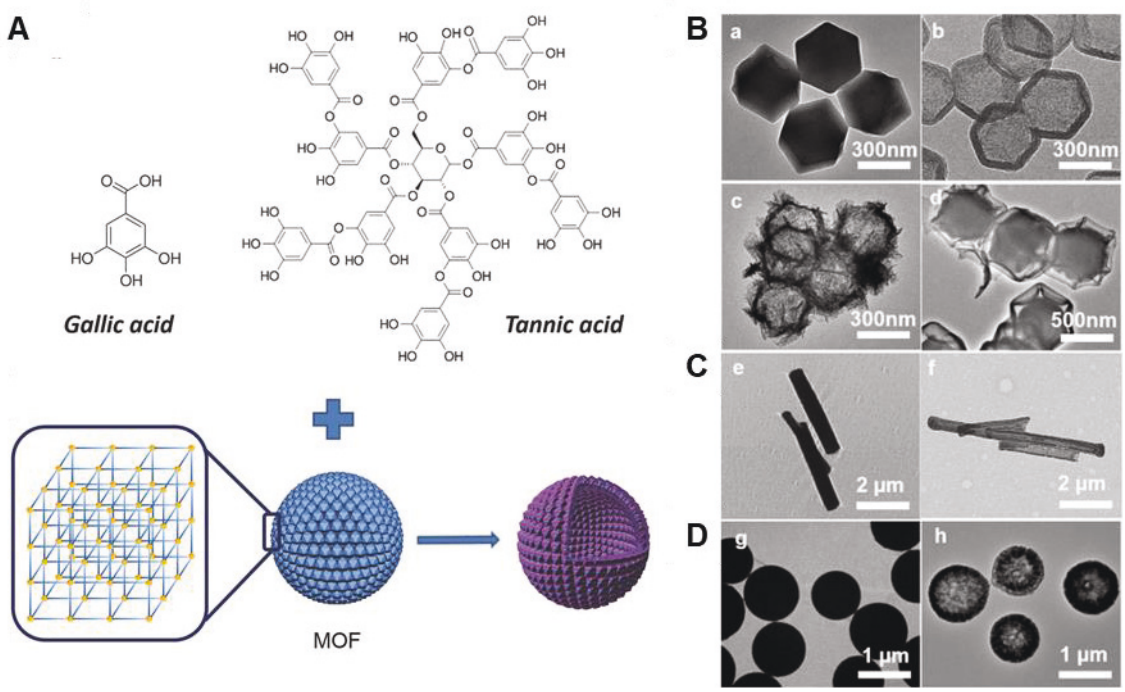

Figure 2.4. Conversion of solid MOFs into hollow MOFs by competitive protons derived from TA or GA. A) Schematic illustration and B-D) TEM images of the transformation of ZIF-8 crystals, MIL-68 crystals, and Tb-CP spheres. [43]

Besides acids, MOFs can also be etched by a variety of inorganic salts that act as Lewis acids [51], thus leading to the protonation of the original organic ligands and the transformation to various hollow derivatives. For example, MOFs can serve as self-

template and be etched into hollow layered double hydroxides (LDHs) by metal salts through two simultaneous processes: the etching of MOFs and the growth of LDH on the MOF surface [11]. Protons generated from the hydrolysis of $Me(I)^{2+}$ ions (from inorganic salt solution) attack 2-MIM in ZIFs, breaking the coordination bond in ZIF, which results in the release of $Me(II)^{2+}$ ions (from ZIF) into the solution. Then, $Me(II)^{2+}$ ions are partially oxidized to $Me(II)^{3+}$ ions by oxidizing agents (NO_3^- ions or O_2) dissolved in the solution. Finally, co-precipitation of two metal ions and hydroxide groups takes place on the surface of MOFs to form LDH nanosheet shells. Mirsaidov et al. observed the formation of ZnCo-LDH hollow nanocages from ZIF-8 by using liquid phase transmission electron microscopy (Figure 2.5A,B), which confirms the etching activation mechanism that protons and Co^{2+} compete for 2-MIM ligands [47]. Similarly, inorganic salts etching was used for producing other LDH and metal hydroxide nanocages, such as NiCoFe-HO@NiCo-LDH [52], $Co(OH)_2$/CoNi-LDH [53], and FeCoNi-LDH [54]. Furthermore, benefiting from the weak acidity (pKa = 9.85 in water) of hydroxyl groups, hydroquinone can also serve as an etchant to etch MOFs [55].

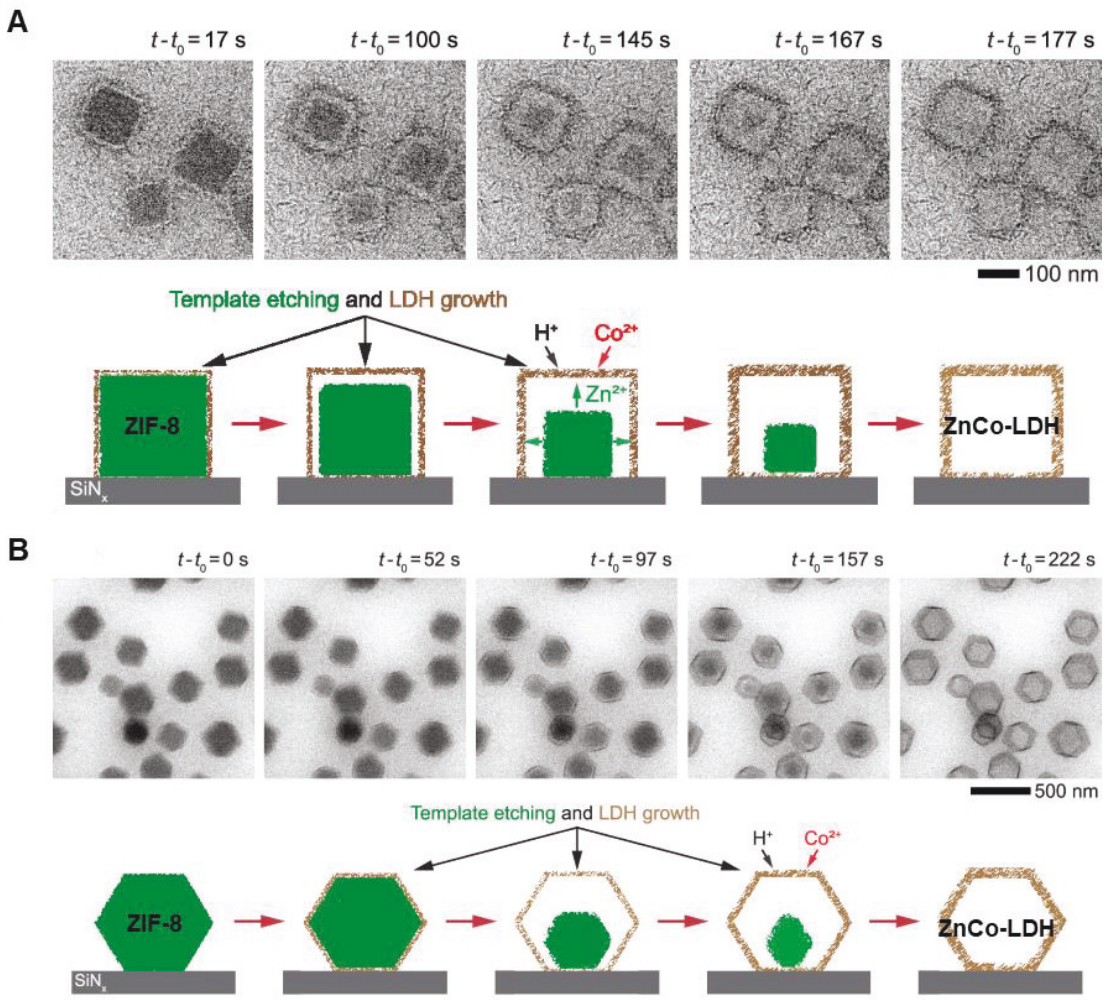

Figure 2.5. Conversion of A) ZIF-8 nanocubes and B) rhombic dodecahedrons into LDH nanocages in a $Co(NO_3)_2$ solution. [47]

The produced protons lead to the protonation of the original BTC ligands (Figure 2.5A). Macro-channels with the size of 3.9 μm were observed in the octahedral HKUST-1 in the SEM image and Hg intrusion porosimetry measurement indicated that the etching reaction went deep into the crystals (Figure 2.5B).

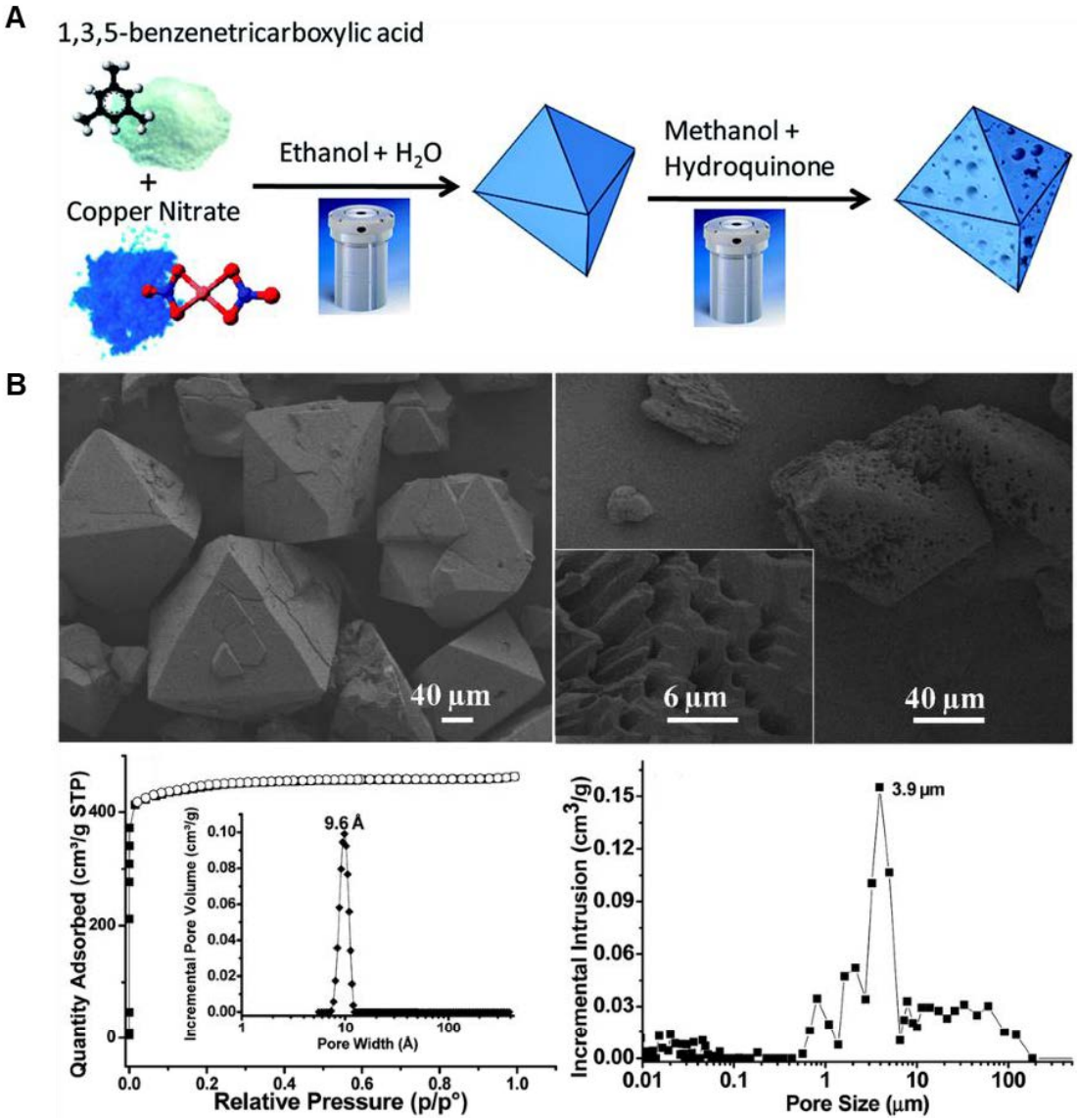

Figure 2.6. Conversion of microporous HKUST-1 into hierarchical porous MOFs with macro-channels by competitive protons derived from hydroquinone. A) Schematic illustration and B) characterizations of macro-channel HKUST-1. [55]

2.1.2.2 Competitive coordination etching: competing for metal ion/cluster nodes

Similarly, using molecules that contain groups similar to the original ligands in parent MOFs as competitive ligands, one can achieve co-coordination of different ligands and

metal ions, or the substitution of the original ligands in MOFs. As a result, MOFs can be converted to multilevel porous or hollow derivatives [56, 57]. For example, Wang et al. proposed a competitive coordination strategy to achieve a MOF nanostructure with both micropores and mesopores [56]. As shown in Figure 2.7A, lauric acid (LA) containing a carboxyl group can coordinate with the Zn_4O clusters and thus modulate their coordination with benzenedicarboxylic acid (H_2BDC), which is the origin linkers of MOF-5, as a competitive linker. In the initial stage of synthesis, deprotonated H_2BDC and LA are simultaneously coordinated with Zn_4O clusters, but the coordination with LA is weaker than that with H_2BDC because H_2BDC has one more carboxyl group than LA.

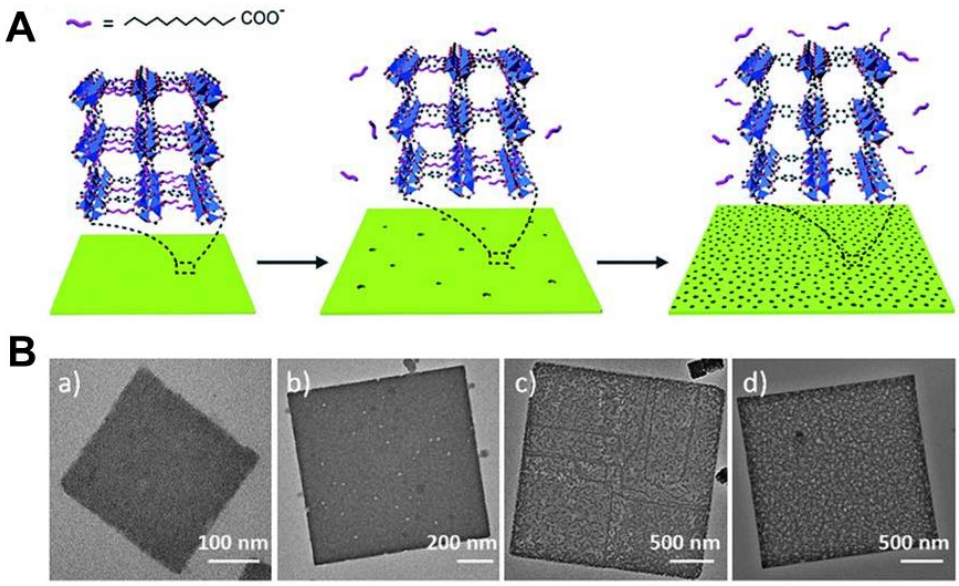

Figure 2.7. Conversion of MOF-5 microporous nanosheets into hierarchical porous nanosheets using lauric acid. A) Schematic illustration and B) TEM images of the competitive coordination etching process. [56]

So, as the reaction progresses, H_2BDC dominates the coordination, while weakly bonded

LA dissociates from MOF-5. The release and migration of LA linkers form mesopores in MOF nanosheets (Figure 2.7B).

In addition to controlling crystal growth in situ, competitive coordination strategies can also selectively etch MOF crystals by introducing gas molecules that can coordinate with metal nodes, such as water vapor (H_2O) [58], ammonia (NH_3) [57], phosphine (PH_3) [59, 60], and oxygen (O_2) [61, 62], to replace the original ligands. Specifically, many MOFs are unstable in water because water molecules can easily attack the coordination bond and remove metal ions through substitution or hydrolysis, thus causing the collapse of MOFs [63, 64]. Lee et al. utilize this property to fabricate hierarchical micro- and mesoporous POST-66(Y) MOF by using water as the etchant (Figure 2.8A) [63].

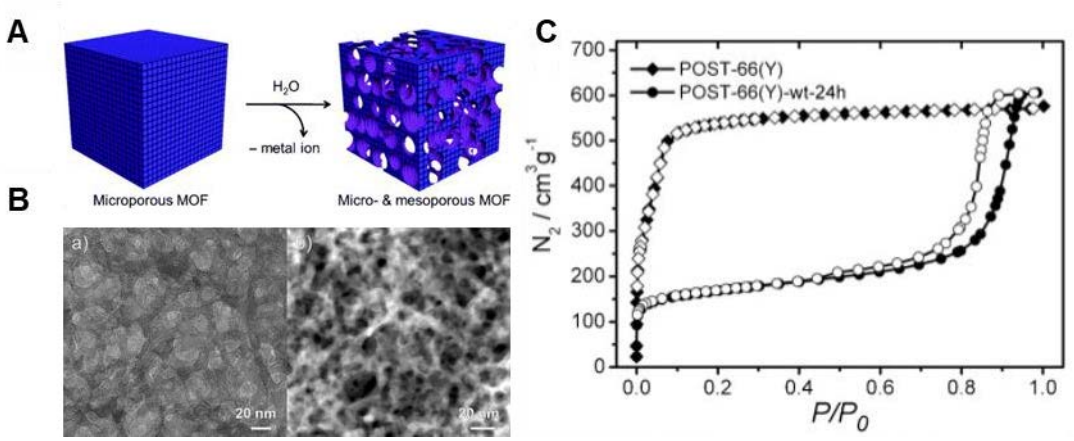

Figure 2.8. Conversion of microporous POST-66(Y) to hierarchical porous POST-66(Y) with water as the etchant. A) Schematic illustration, B) TEM images, and C) N_2 sorption isotherms of the as-prepared POST-66 and POST-66(Y)-wt-24h. [63]

The mesoporosity was verified by an extra hysteresis hoop in the N_2 sorption isotherm

after water treatment (Figure 2.8B). Mesopores with sizes ranging from 10 to 20 nm were also observed by transmission electron microscopy (TEM) and scanning transmission electron microscopy (STEM) studies of POST-66(Y)-wt-24h (Figure 2.8C). In addition, Huang et al. created mesopores and macropores in HKUST-1 (Cu_3BTC_2, BTC=1,3,5-Benzenetricarboxylate) crystals by replacing the ligands with H_2O due to their similar interaction energy with copper ions[58].

NH_3 can also serve as a competitive ligand to etch HKUST-1 due to the strong interaction between ammonia and metal ions [57]. After absorbing NH_3 inside the microporous HKUST-1, mesopores were created by cutting the original carboxyl-metal bond under heating, since NH_3 could replace the carboxylate linkers and coordinate with metal ligands (Figure 2.9A). Due to the differences in plane stability, coordinate bonds on {200} planes are preferentially broken during etching, thus resulting in triangular and rectangular mesopores on more-stable {222} planes (Figure 2.9B).

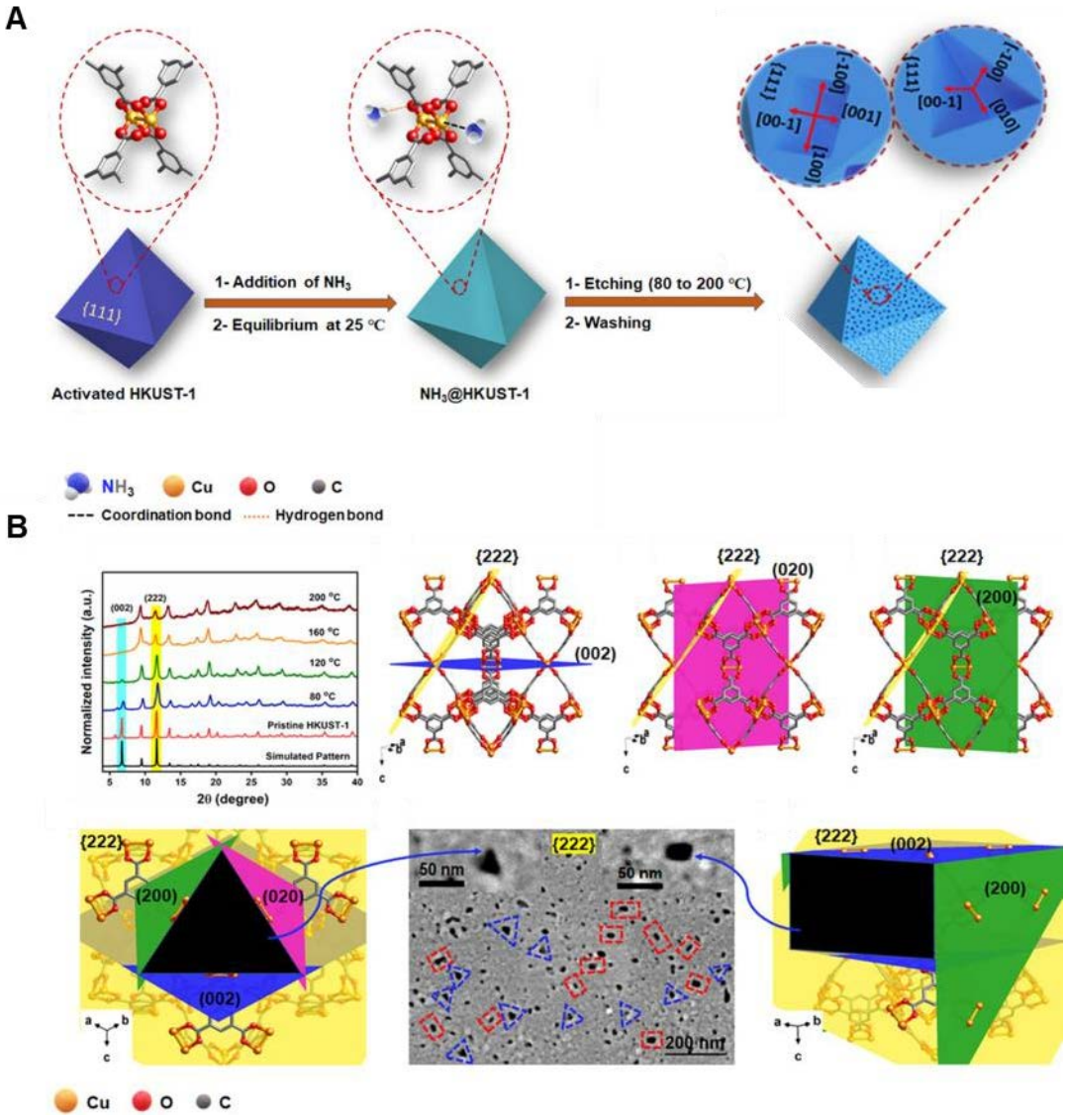

Figure 2.9. Conversion of microporous HKUST-1 into hierarchical porous octahedron with NH_3 as the etchant. A) Schematic illustration and B) etching mechanism. [57]

PH_3 is similar to NH_3 in terms of chemical properties. The lone pair electrons give it coordination ability. Hou et al. used PH_3 gas produced from the decomposition of sodium hypophosphite (NaH_2PO_2) to etch the ZIF-8 crystals [59]. After further carbonization at a high temperature, N/P-doped nanocages with hierarchical porosity were fabricated (Figure 2.10).

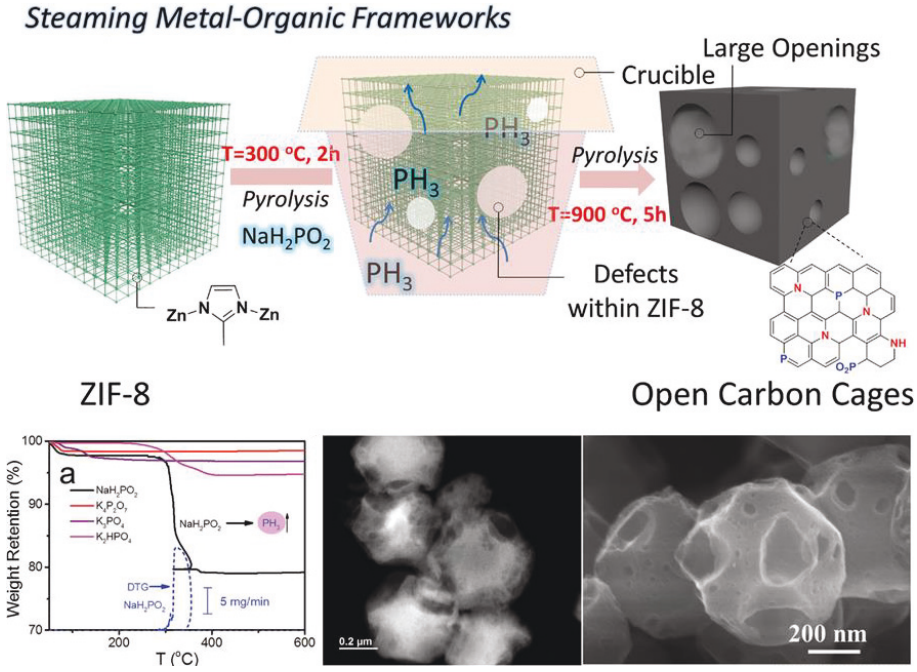

Figure 2.10. Conversion of ZIF-8 to N, P-doped carbon nanocages with PH_3 as the etchant. [59]

In addition, O_2 can also etch MOFs by oxidizing the metal nodes. Dou et al. used O_2 plasma as a powerful etching agent to prepare hierarchical porous CoO_x-ZIF from the parent ZIF-67 crystals where about 29.7% Co-N coordination bonds were oxidized to CoO_x species after O_2 plasma treatment (Figure 2.11) [65]. Therefore, atomic-scale CoO_x species were obtained while forming hierarchical porous ZIFs. Also, MOFs can be used as templates to fabricate hollow metal oxides through oxidation etching. Guo et al. prepared yolk-shell Fe_2O_3 nanostructures by calcining MIL-53(Fe)-2 in air at 500 °C [62]. During calcination, the adhesion force makes the shell outward, while the contraction force makes the core of the shell inward. Therefore, the solid MIL-53(Fe)-2 transformed into yolk−shell porous Fe_2O_3-2 after oxidation. Other hollow metal oxides, such as Co_3O_4

[61], Co_3O_4@Co-Fe oxide [66], and V_2O_5 [67] were also obtained from different MOF precursors.

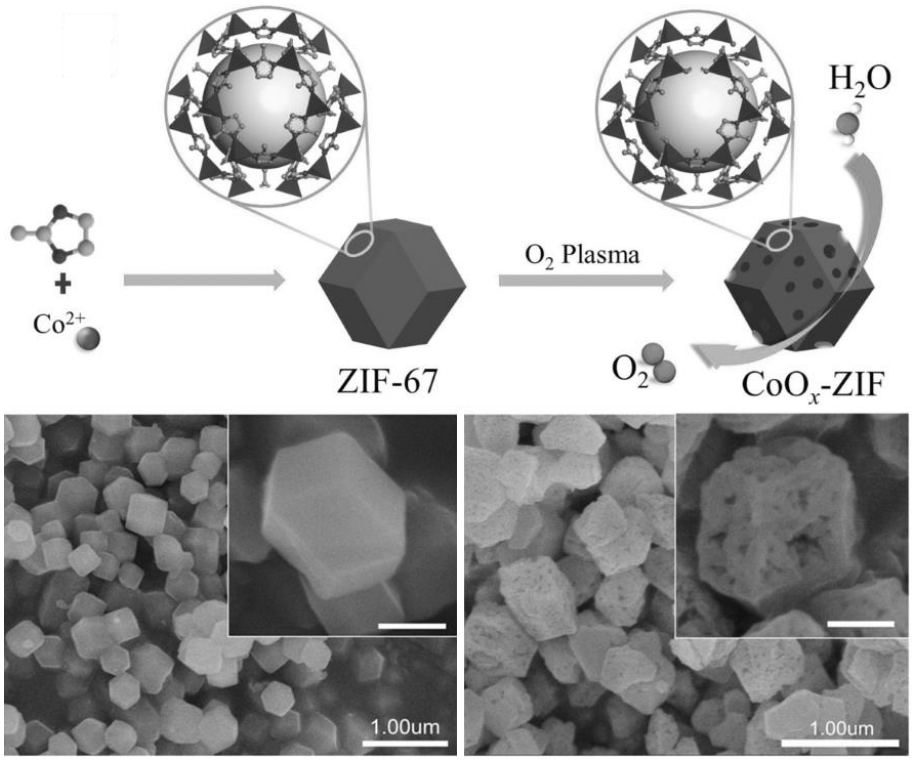

Figure 2.11. Conversion of ZIF-67 to CoOx-ZIF with O_2 plasma as the etchant. [65]

In addition, halogen ions can also break M-Nx bond by competitive coordination during pyrolysis [68]. Taking Br^-- mediated etching of ZIF-8 as an example, He et al. elaborated on the halide-mediated "bait and switch" mechanism during pyrolysis under Ar/H_2 (Figure 2.12A). Firstly, Br^- ions compete for Zn^{2+} ions with the 2MIM ligands of ZIF-8, leading to Zn-Br intermediates and N release from Zn-N_4 into the carbon matrix during the pyrolysis process. Then, Br^- in the Zn-Br intermediate is replaced by O^{2-}, forming ZnO in the carbon matrix near the N site. In this pyrolysis-etching process, the dodecahedral ZIF-8 nanoparticles were gradually transformed into porous nanosheets

with carbon vacancies due to ZnO etching (Figure 2.12B).

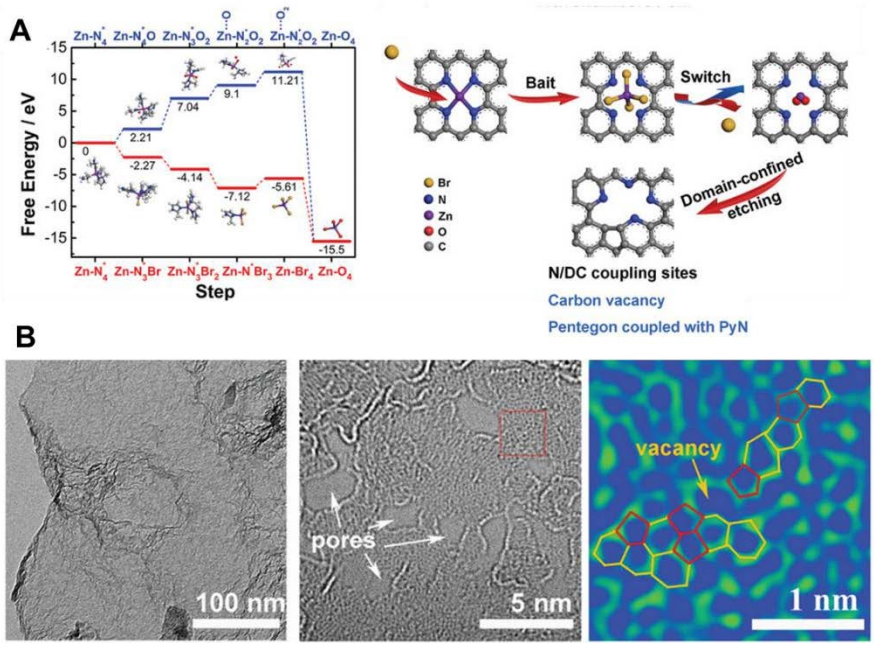

Figure 2.12. Conversion of ZIF-8 dodecahedron into porous N/C nanosheets with competitive Br^- ions. A) Free energy diagram of the intermediates and schematic illustration, B) TEM images and Fast Fourier transformation-filtered image of N/C-$Br_{0.3}$. [68]

Furthermore, wet chemical etching is also useful for shaping and modifying MOF nanocrystals by competitive coordination etching, thus fabricating various hierarchical porous and multilevel hollow MOFs and MOF derivatives. Chang et al. synthesized hierarchical porous mesoCu@Al-bpydc from microporous Al-bpydc crystals via a partial replacement of 2,2'-bipyridine-5,5'-dicarboxylic acid (bpydc) by tetrafluoroborate (BF_4^- anion) during competitive coordination etching (Figure 2.13A) [69]. In the meantime, Cu^{2+} from $Cu(BF_4)_2$ was also introduced to the mesoCu@Al-bpydc by coordination with

the pyridine nitrogen of the ligand. As shown in Figure 2.13B, the mesoCu@Al-bpydc contained pores in the range of 2 to 12 nm after etching.

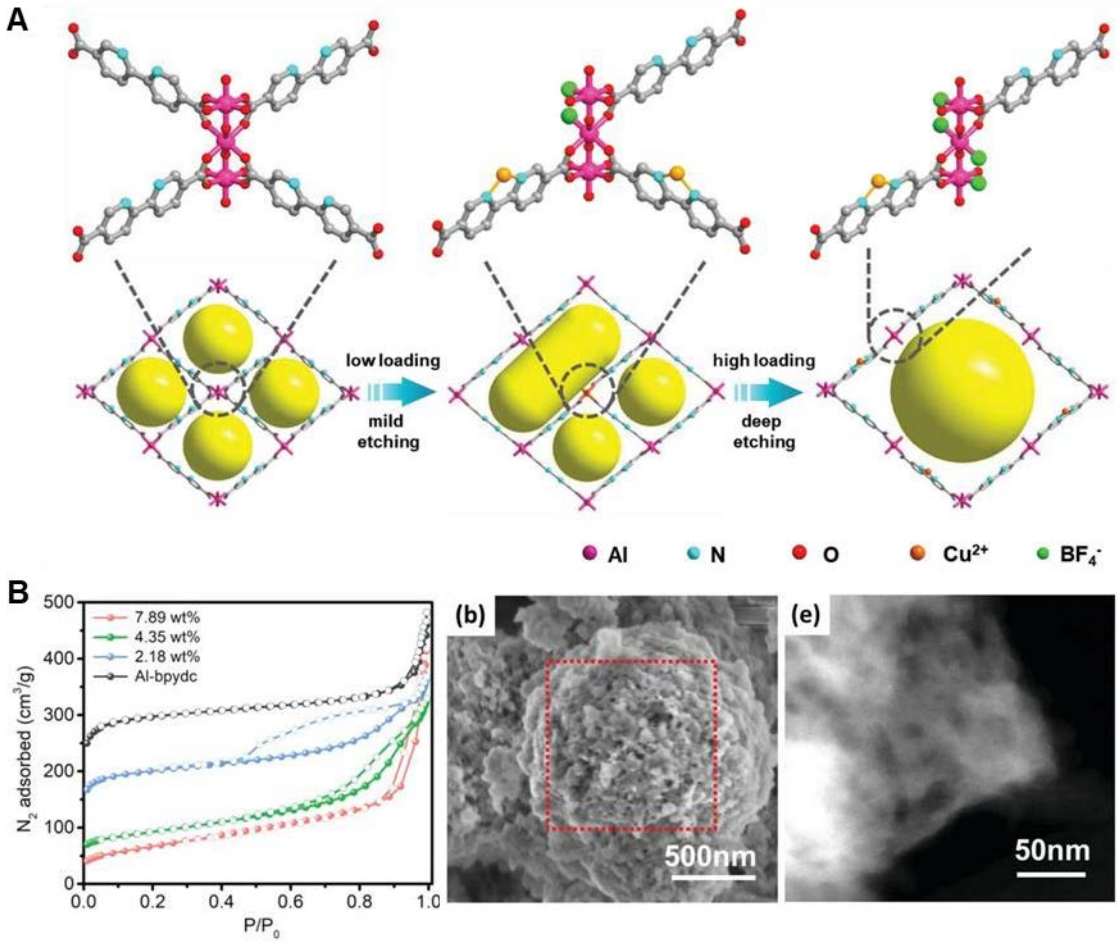

Figure 2.13. Conversion of Al-bpydc into mesoCu@Al-bpydc via competitive BF_4^- anions. A) Schematic illustration and B) N_2 adsorption–desorption isotherms and TEM images of mesoCu@Al-bpydc. [69]

MIL-74 and MIL-88A were used as self-sacrificial templates and precursors to prepare Fe-Ni-LDH nanocages, respectively [70, 71]. As shown in Figure 2.14A, hydroxide ions from KOH aqueous solution could combine with Ni and Fe ions from bimetallic FeNi-MOF-74, which cuts off the coordination bond in the parent MOF, resulting in the etching

of the MOF and co-precipitation to form Fe-Ni-LDH shell.

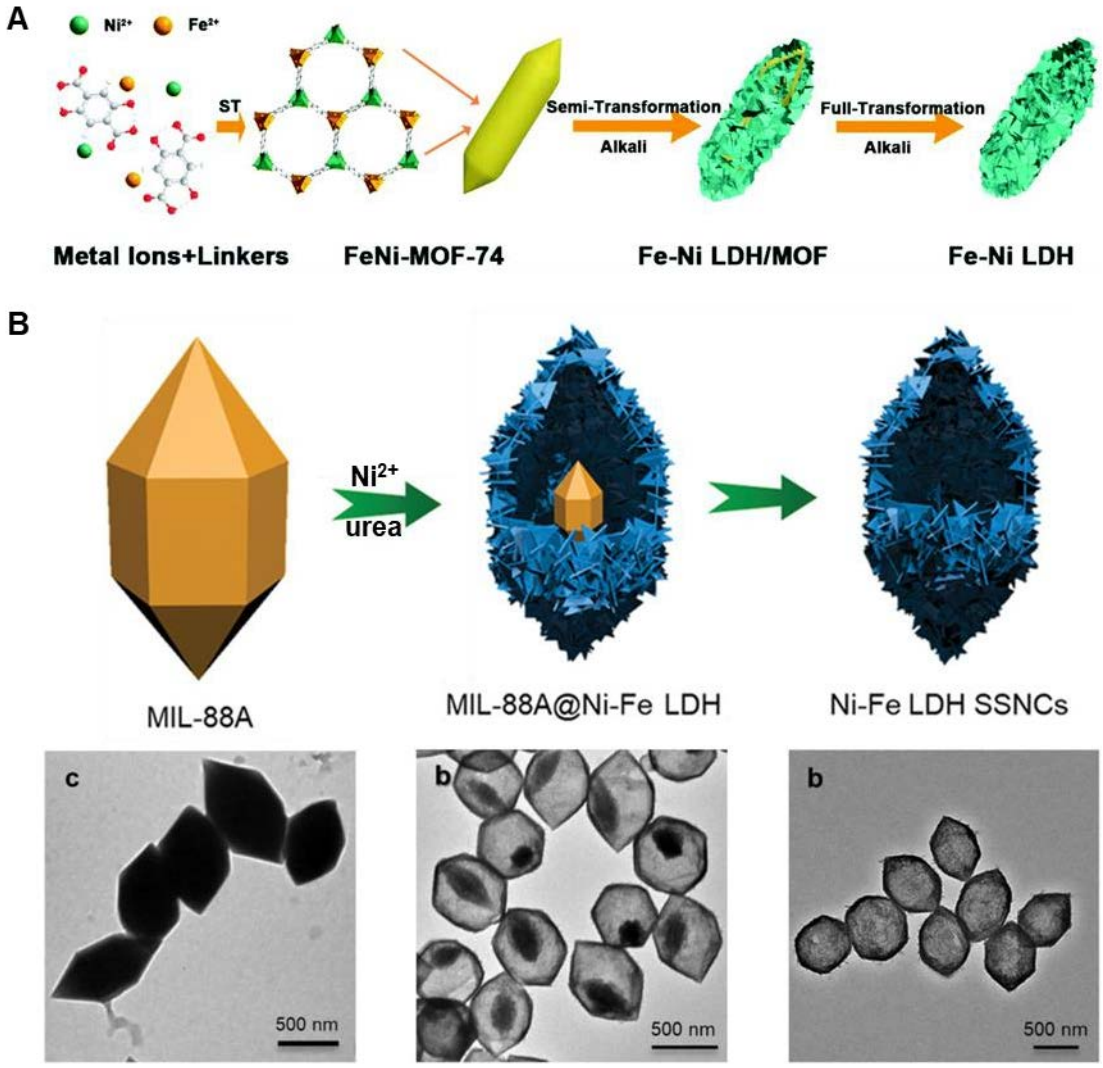

Figure 2.14. A) Conversion of solid FeNi-MOF-74 into hollow Fe-Ni-LDH by competitive coordination of hydroxyl ions. [71] B) Conversion of spindle-like MOF-88A into multilevel hollow Ni–Fe LDH in a solution with $Ni(NO_3)_2 \cdot 6H_2O$ and urea. [70]

Another way to prepare hollow LDH materials from MOFs is etching and precipitation by urea hydrolysis (Figure 2.14B). The hydrolyzation of urea gradually increases the pH

value of the solution, and as a result, MIL-88A templates are gradually etched by the competitive coordination of hydroxide ions with fumaric acid, the ligand of MIL-88A. The released Fe ions from MIL-88A coprecipitate with Ni ions and hydroxide ions to form Ni–Fe-LDH shells.

2.1.3 Confined nanospace pyrolysis

Carbon nanomaterials with high specific surface areas, high porosity, high electronic conductivity, and chemical stability have promising applications. In general, carbon nanomaterials are mostly prepared by the carbonization of organic substances. Although the resultant carbon nanomaterials have a high specific surface area, their porous structures cannot be customized, and their chemical compositions are difficult to control. In recent years, using various MOFs for customizing multilevel hollow carbon materials by a “confined nanospace pyrolysis” method [72], has attracted extensive attention. Thereafter, Liu et al. synthesized hollow mesoporous carbon nanocubes by pyrolyzing ZIF-8 coated by silica (Figure 2.15A) [73]. When the SiO_2 shell is thick, the rigidity of the SiO_2 shell which provides a force to pull the ZIF precursor "outward" during pyrolysis can offset the inward contraction of the ZIF-8 skeleton during pyrolysis, resulting in a hollow carbon foam. In contrast, when the SiO_2 shell is thin, the inward shrinkage cannot be counteracted during the carbonization of ZIF@mSiO_2 because the thin SiO_2 shell is not strong enough to provide a sufficient driving force. Thus, inward deformation results in a solid mesoporous carbon nanocube.

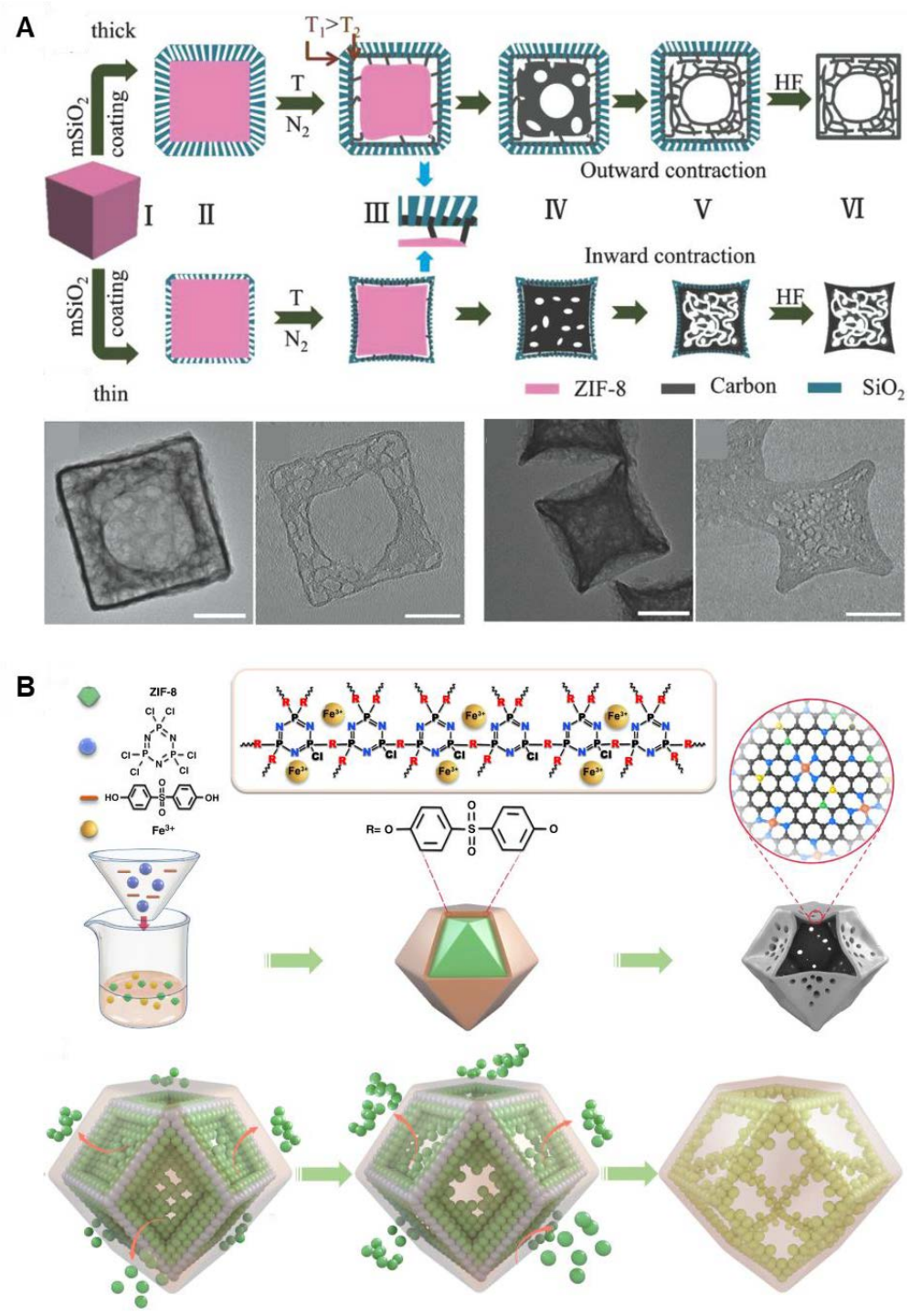

Figure 2.15. A) Fabrication of hollow mesoporous carbon nanocubes HMCNCs and SMCNCs. [73] B) Synthetic scheme of single Fe atomic sites supported on a N, P and S co-doped hollow carbon nanoreactor (Fe-SAs/NPS-HC). [74]

In addition to the SiO_2 shells, coating MOFs with polymers can also work in confined

nanospace pyrolysis. Song and Wang et al. reported that starting from both ZIF-67 and ZIF-8 with poly(cyclotriphospazene-co-4,4′-sulfonyldiphenol) (PZS) shell, hollow N, P, S co-doped carbon nanoreactors (NPS-HCs) was finally obtained after confined nanospace pyrolysis [74, 75]. Wang et.al proposed that confined nanospace pyrolysis may be caused by the Kokendal effect (Figure 2.15B) [74]. During the pyrolysis process, since the radius of Zn^{2+} ions is smaller than that of S^{2-} ions, the diffusion rate of Zn^{2+} ions outward is faster than that of S^{2-} ions inward. Thus, continuous uneven diffusion led to the emergence of Kirkendall cavities at the interface between the ZIF-8 core and the PZS shell. As ZIF-8 gradually decomposes inside, a thick hollow shell structure is formed at last.

2.2 Nanoreactor engineering based on MOF etching

Among the three fabrication methods of nanoreactors discussed above, the selective etching strategy based on a “top-down” chemical surgery is more effective for the precise construction of nanoreactors with tailored structures and components at the atomic level. Therefore, this chapter focuses on nanoreactor engineering based on the selective etching of MOFs and summarizes the regulation of the internal structure of nanoreactors.

2.2.1 Spatial-structure engineering of nanoreactors

In practical applications, the architecture of the MOF-derived nanoreactors needs to be customized accordingly. Spatial-structure engineering of nanoreactors is an efficient way

to precisely regulate the porosity and cavity of these materials. Structure engineering endows nanoreactors with an enhanced loading capacity of the guest molecules and a stable environment for catalytic reactions. Compared with MOFs with intrinsic micropores, hierarchical porous and multilevel hollow MOF-based nanoreactors intensify the diffusion-controlled and large-size species involved process. Therefore, it is necessary to prepare MOF-based nanoreactors with desired structures.

2.2.1.1 Structure engineering of hierarchical porous nanoreactors

MOF-based nanoreactors with precisely customized pore apertures, including pore shapes, sizes, and volumes, can be designed and synthesized by controlling etching conditions. By controlling the etching time, mesopore sizes in MOF within the range of 3 to 20 nm were introduced, which enables the control of micro- and mesoporosity (Figure 2.18) [63].

In addition, etching temperature is also an important parameter for controlling the pore size. In the process of NH_3 etching HKUST-1 (Figure 2.18A), mesopores with a wide range of sizes from 9.2 nm to 38 nm were introduced into microporous HKUST-1 by regulating the temperatures from 80 °C to 200 °C (Figure 2.18B) [57]. More importantly, the generated mesopores could be repaired after immersing into a solution of MOF precursors (Figure 2.18C). Such controllable etching and reparation serve as an example of controllable mesopore generation/closure, demonstrating a powerful protocol for precisely tailoring the pore structure of MOF materials at the molecular scale.

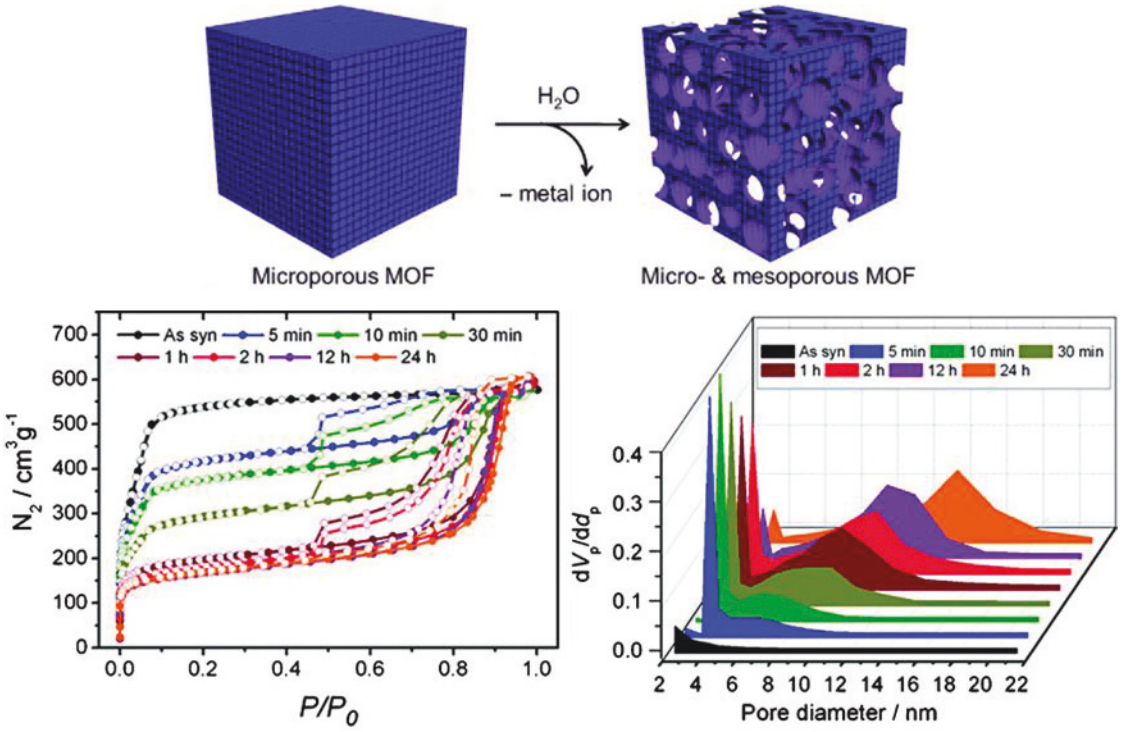

Figure 2.16. Precise control of the mesopore sizes by adjusting the etching time. [63]

Besides, precisely controlling the concentration of etchant can also regulate the mesopore size and mesopore volume. By increasing the concentration of H_3PO_4 (0 to 80 mM), the mesopore sizes gradually increased from 2.4 to 18.4 nm and the corresponding mesopore volume of MIL-100(Fe)-80 reached 750 cm^3/g from 1.15 cm^3/g of the parent MIL-100(Fe) [41].

In addition, for MOFs with complex coordination structures, hierarchically porous structures could be precisely controlled by adjusting weak coordination bond content in MOF crystals. Yuan et al. fabricated hierarchical porous PCN-160 with mesopores tuned from 1.5 to 18 nm through AcOH etching [76]. In this process, a stepwise ligand exchange was first carried out, so that CBAB (4-carboxybenzylidene-4-aminobenzate) partially

replaced the original AZDC (azobenzene-4,4′-dicarboxylate) ligands (Figure 2.18A). Then, CBAB linkers were selectively removed by AcOH etching to produce hierarchically porous PCN-160. The pore sizes of the obtained hierarchically porous PCN-160 are precisely controlled by both pro-labile-linker content and AcOH concentration (Figure 2.18B).

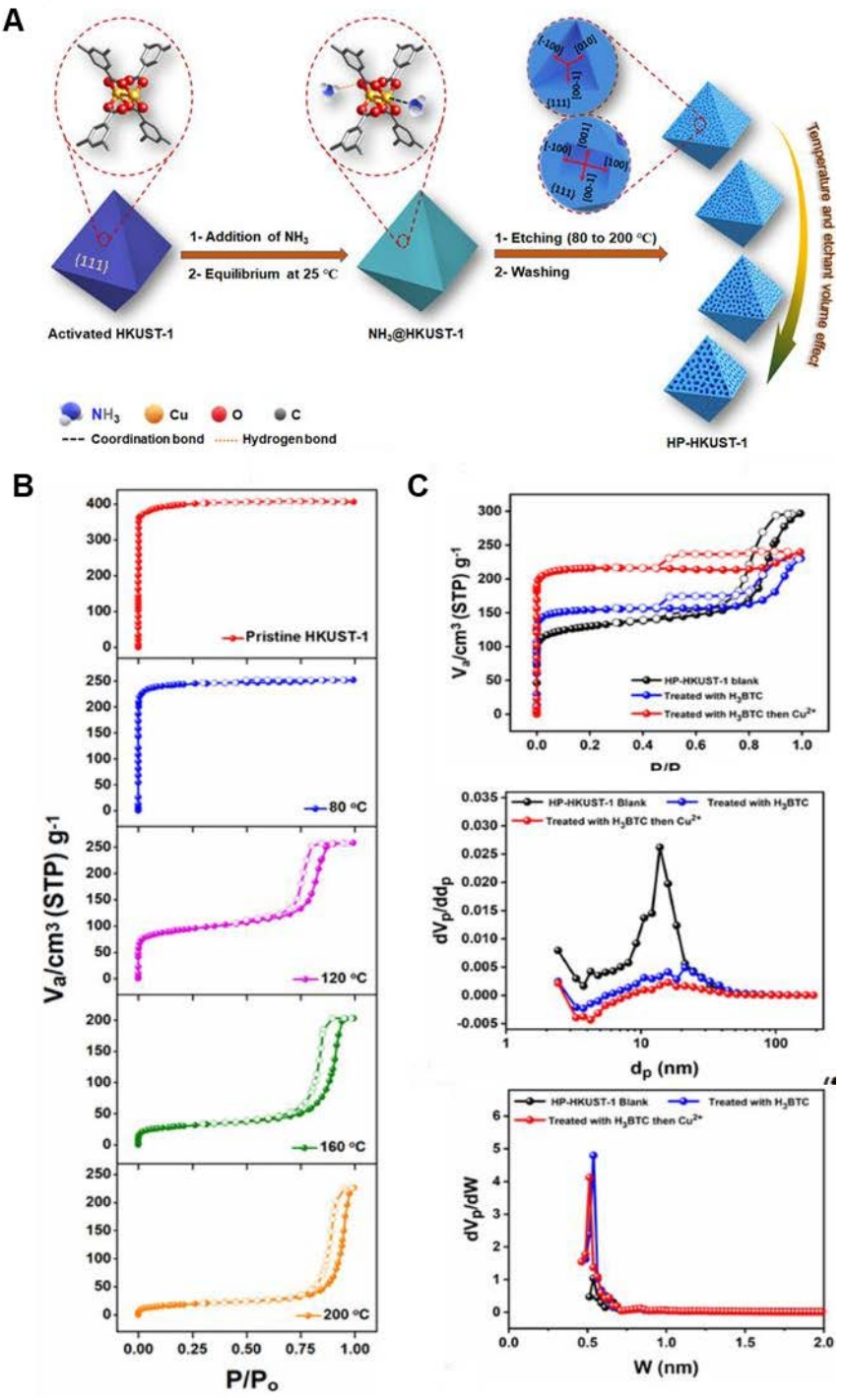

Figure 2.17. A) Schematic illustration of controllable mesopore generation/closure. B) Controllable conversion of microporous HKUST-1 into hierarchical porous nanoreactors by adjusting the etching temperature. C) Closure of mesopores in the etched HKUST-1 crystals. [57]

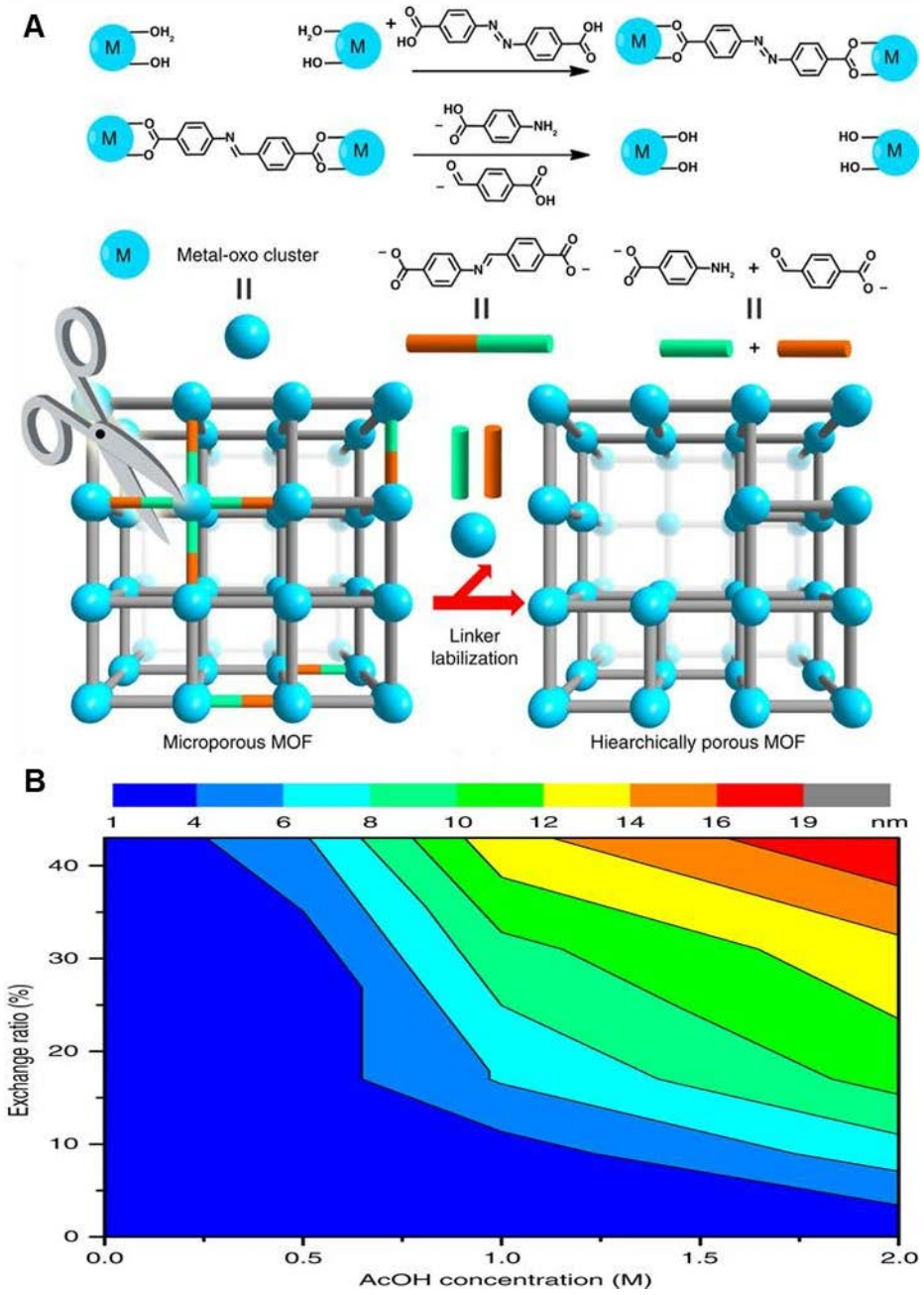

Figure 2.18. A) Schematic illustration of the introduction of mesopores in MOFs by the selective removal of chemically labile linkers, B) Pore size distribution of PCN-160-R%-C as a function of exchange ratio and AcOH concentration. [76]

2.2.1.2 Structure engineering of multilevel hollow nanoreactors

The etching method can be used not only to construct the hierarchical porous but also to prepare the multilevel hollow structure, though the preparation of complex hollow MOFs remains a considerable challenge. Drawing on the literature evidence that a large variety of hollow SiO_2 and phenol formaldehyde resin can be synthesized by chemical etching due to their chemically inhomogeneous nature underneath their uniform shape [77, 78], researchers tried to synthesize and etch MOF materials with complicated compositional chemistry and stability. The core-shell MOF precursor also includes a special type of less-stable core@more-stable shell MOF, prepared due to the inhomogeneous growth. To minimize the surface energy, MOFs rapidly nucleate to form the core at first. Subsequently, since the reactants are consumed gradually, the nucleation becomes difficult, and the outer layer with fewer defects is formed due to the slow growth. Multi-shelled hollow MOF nanoreactors can be prepared by etching their less stable parts [40, 79]. As shown in Figure 2.19A, Liu et al. prepared multi-shelled hollow MIL-101 (Cr) single crystals through a combination of crystal growth and etching [40]. By controlling the times of epitaxial growth, the number of shells of the nanoreactor after etching was precisely controlled. In addition, novel etching strategies to form multi-shelled derivates were developed continuously. In this effort, Wang et al. prepared cobalt divanadate multi-shelled nanoboxes by etching ZIF-67 using polyvanadate ions during a solvothermal treatment (Figure 2.19B) [80]. Importantly, the number of shells of the as-obtained

nanoboxes could be precisely controlled from 2 to 5 by differing the reaction temperature. After subsequent ion exchange with S^{2-} ions and annealing, cobalt sulfide nanoboxes with 2 to 5 shells were finally produced.

In addition, using MOF-based nanomaterials with different structures after etching as precursors, carbon-based nanoreactors with different structures can be obtained after subsequent heat treatment. Through a tannic acid-protected etching, Wei et al. prepared yolk–shelled (TA-YS) or hollow architecture (TA-Box) by precisely controlling the etching time (Figure 2.19C) [81]. After carbonization in N_2, solid ZIF-67 nanocubes and the corresponding derivatives were transformed into Co/C sub-microreactors in the architectures of solid cubes, double-shelled hollow boxes, and hollow boxes, accordingly.

By regulating the oxygen partial pressure and the heating rate, the degree of thermal oxidation etching can also be fine-tuned. Wang et al. prepared hollow multi-shelled Co_3O_4 dodecahedrons with different numbers of shells, including double, triple, and quadruple shells (Figure 2.19D) [61]. Especially, under the small oxygen partial pressure and slow heating rate, quadruple-shelled Co_3O_4 was obtained.

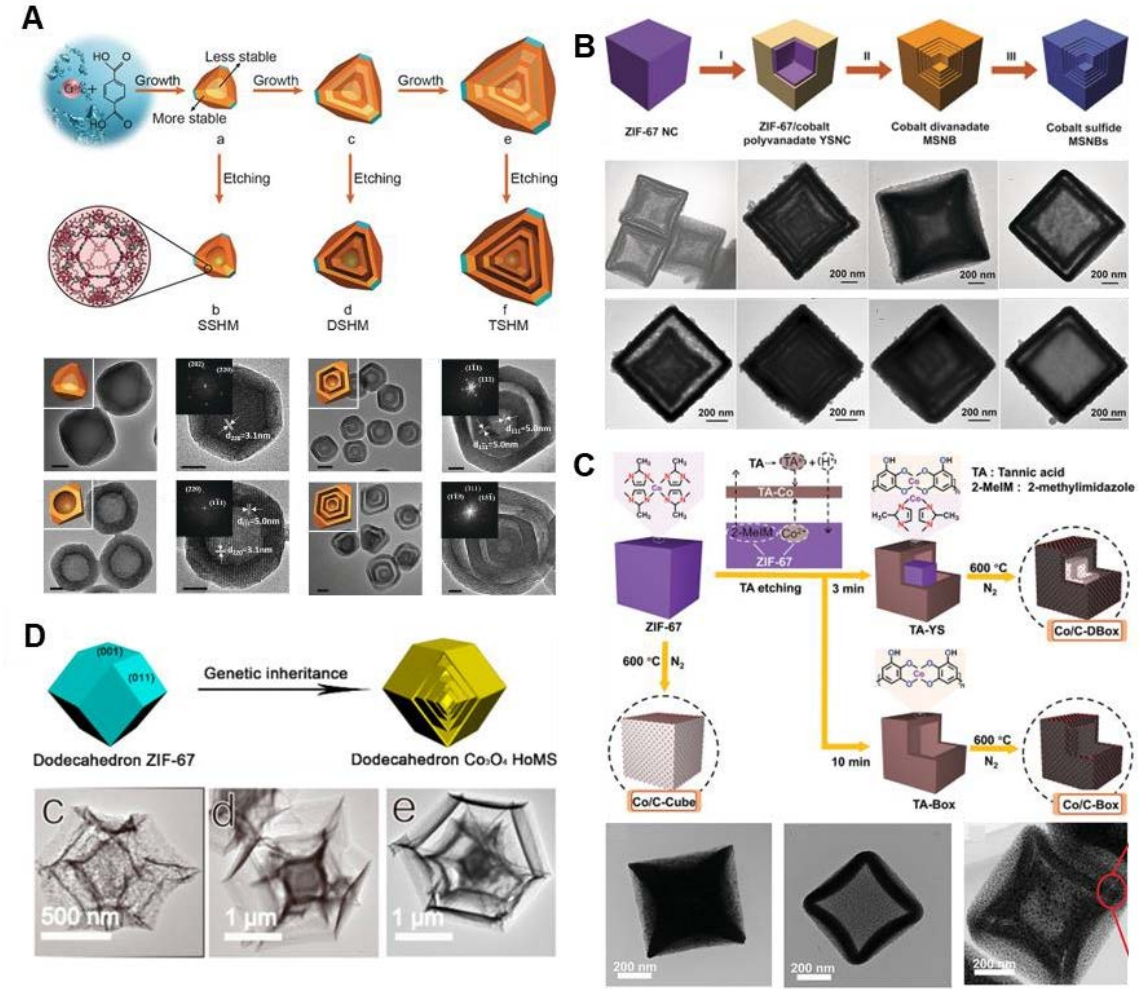

Figure 2.19. A) Conversion of MIL-101 into single-, double-, and triple-shelled hollow MIL-101. [40] B) Conversion of ZIF-67 into cobalt divanadate TSNBs, QuiSNBs, QuaSNBs, and DSNBs, and cobalt sulfide TSNBs, QuiSNBs, QuaSNBs, and DSNBs. [80] Conversion of ZIF-67 into Co/C-Cube, Co/C-DBox and Co/C-Box. [81] D) Conversion of ZIF-67 into DS-, TS-, and QS-Co_3O_4. [61]

Furthermore, matryoshka-type (ZIFs@)$_{n-1}$ZIFs could be obtained from multiple epitaxy growth of ZIF-8 and ZIF-67 that serve as the template and precursor for multilevel hollow MOF derivates. For example, using customizable (ZIFs@)$_{n-1}$ZIFs as precursors, multi-

shell metal oxide nanoreactors of up to eight layers were fabricated by thermal-oxidative etching, as shown in Figure 2.20A [82]. Remarkably, the multilevel composition of the multishell nanoreactors can be precisely controlled by regulating the growth order of $(ZIFs@)_{n-1}ZIFs$ precursors (Figure 2.20B).

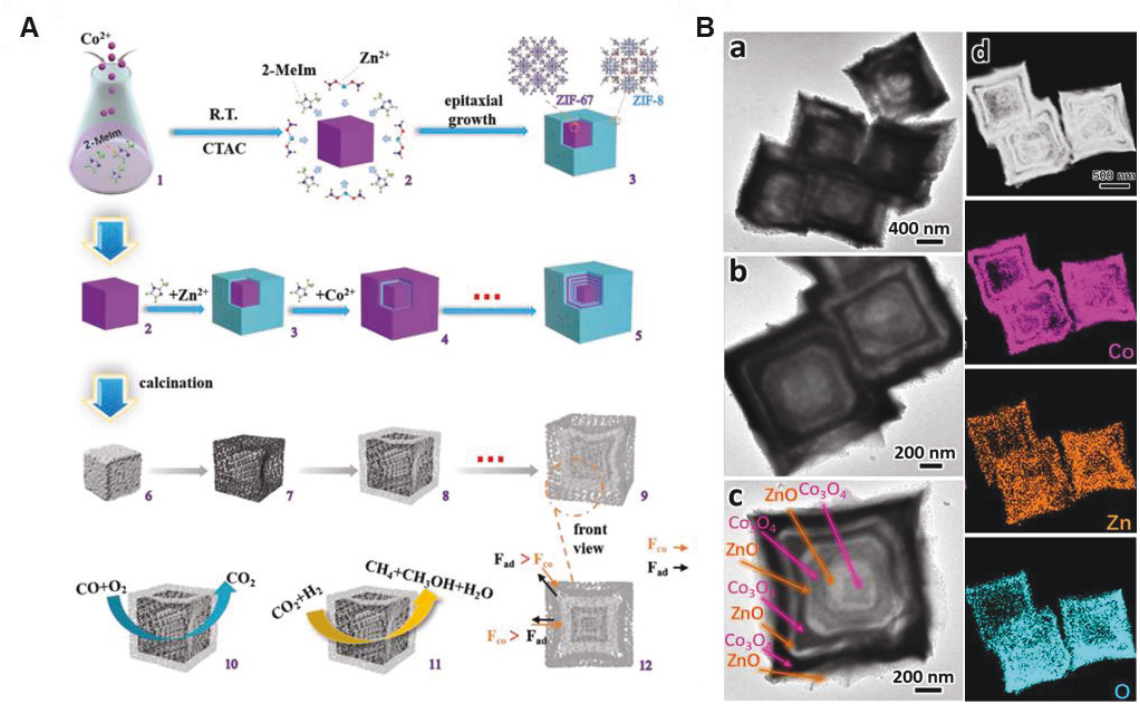

Figure 2.20. A) Conversion of $(ZIFs@)_{n-1}ZIF$ to multishell ZIF-derived metal oxides, B) TEM images and EDX mapping of eight-layer metal oxides. [82]

2.2.1.3 Structure engineering of other complex structures

At present, although complex MOF-derived structures have been realized, most of them are isotropic materials. Anisotropic etching of MOFs is still difficult because of the lack of systematic study on the etching position/rate of various etchants in MOFs. Spatial-selective etching allows controlled disassembly of the MOF's frame to form complex

nanostructures. Such spatial anisotropic etching is mainly caused by structural inhomogeneity. The spatial selectivity of etching is mainly caused by the different etching kinetics on corners, edges, and faces of MOFs. There are stability differences in MOF crystals, which can be used to prepare hollow or multi-shelled materials by selectively etching their less stable parts. Thus, if stability differences distribute unevenly in space, spatial-selective etching of MOF crystals can be possible.

For ZIF crystals with different morphologies, the exposed crystal phase faces exhibit different atomic compositions [83]. For example, the (100) and (211) planes have several numbers of coordination bonds, while no coordination bonds are contained in the (111) and (110) planes (Figure 2.21A). Based on the above differences, rhombic dodecahedral ZIF-67 crystals with 12 (110) planes and 12 <211> edges were etched to microboxes due to the preferential etching of less-stable <211> edges (Figure 2.21B).

For Prussian blue analogue (PBA) crystals, there are also differences in etching selectivity on different crystal faces. For example, Wang et al. reported a facet-selective etching process of NiCo-PBA nanocubes by S^{2-} anions combined with OH^-, BO_2^-, or PO_4^{3-} anions (Figure 2.21C) [84]. Firstly, anisotropic etching of S^{2-} anions is caused by the different densities of coordination bonds in different facets of PBA nanocubes. S^{2-} anions preferentially etched the edges and corners of the PBA to form PBA/NiS_2 cross@frame CHCs because the adsorption strength of S^{2-} anions to the (110) edges and (111) corners

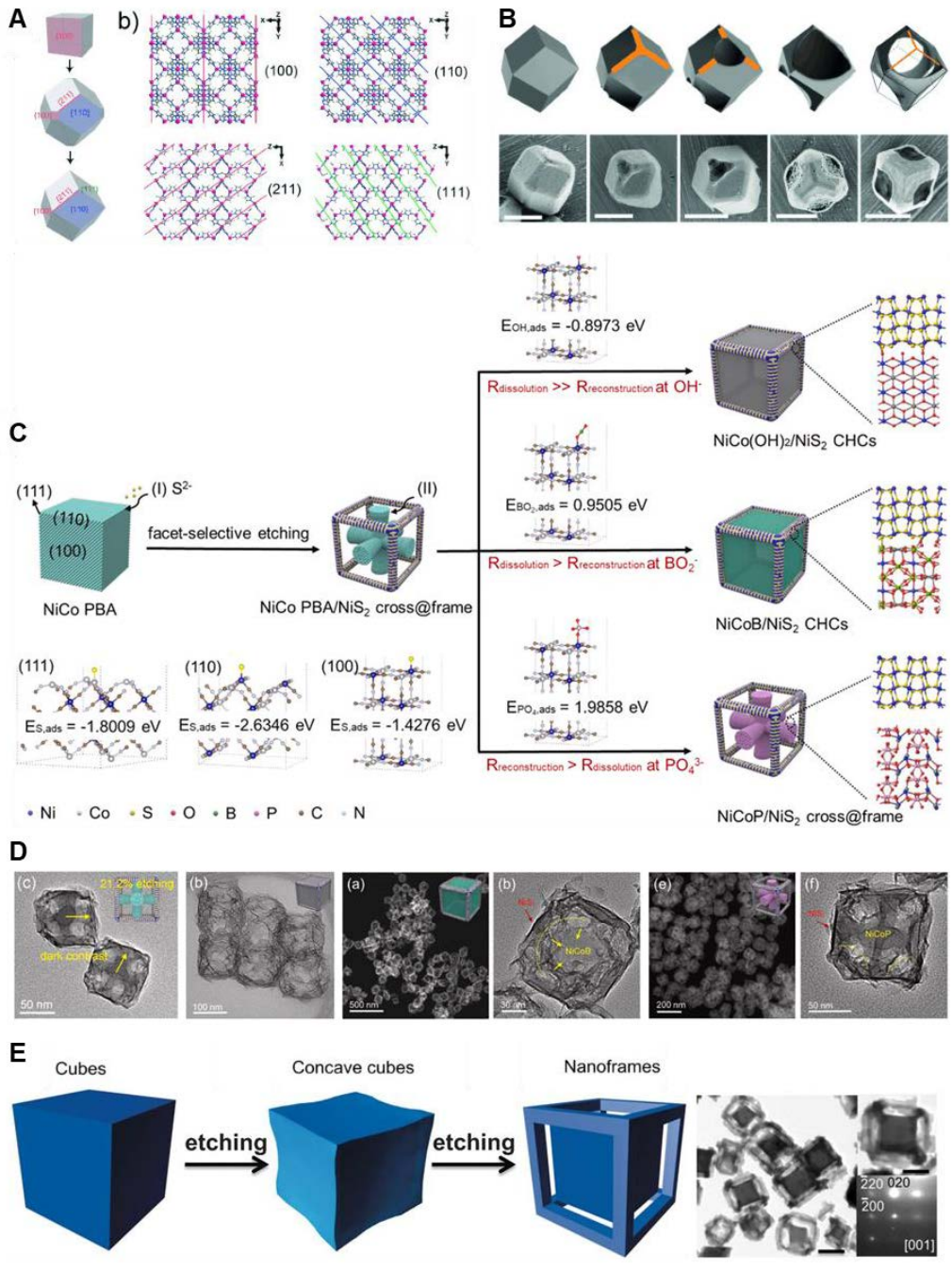

Figure 2.21. A) Crystallographic planes of various ZIF crystals and B) Schematic illustration and SEM images of ZIF-67 crystals during etching. [83] C) Schematic illustration and D) TEM images of $NiCo(OH)_2/NiS_2$, $NiCoB/NiS_2$, $NiCoP/NiS_2$ CHCs. [84] E) Schematic illustration and TEM images of the Ni-Fe PBA nanoframes. [85]

is higher than that to the (100) planes. Subsequently, the NiCo-PBA/NiS_2 cross@frame CHCs were etched by a second anion (OH^-, BO_2^-, or PO_4^{3-}) to obtain different heterojunctions. The structure of the final products is determined by the kinetics in the dissolution and reconstitution induced by different anions. Since OH^- and BO_2^- anions have stronger adsorption energy on the PBA surface than PO_4^{3-} anion, OH^- and BO_2^- anions show fast etching kinetics for PBA, resulting in a hollow $NiCo(OH)_2$ (Figure 2.21D). In contrast, PO_4^{3-} anion has slow etching kinetics for the PBA crossing, thus deducing an equilibrium of dissolution and reconstitution, allowing an *in situ* conversion of the PBA cross to NiCoP cross (Figure 2.21D). Furthermore, when OH^- anions are used as etchants, the etching of PBA nanocubes also preferentially starts from the center, thus forming nanocages with open frameworks [86-89].

In addition, cations and anions also show different preferences during the etching of crystals. When etching PBA crystals, cations (eg. H^+) prefer faces [85], while anions (eg. S^{2-}, OH^-) prefer corners and edges [84, 86-89]. For instance, Zhang et al. prepared NiFe(II) Prussian blue analogue (PBA) nanoframes by preferential etching of the freshly exposed surface in an HCl solution, rather than the corners or edges (Figure 2.21E) [85].

Besides different etchants, the composition of the parent MOFs also has a great influence on the etching process. With NaH_2PO_2, the gradually released PH_3 gas competes with the original ligands in MOF crystals and leads to different MOFs with different structures, because their thermal stability varies with compositions (Figure 2.22A) [60]. As shown

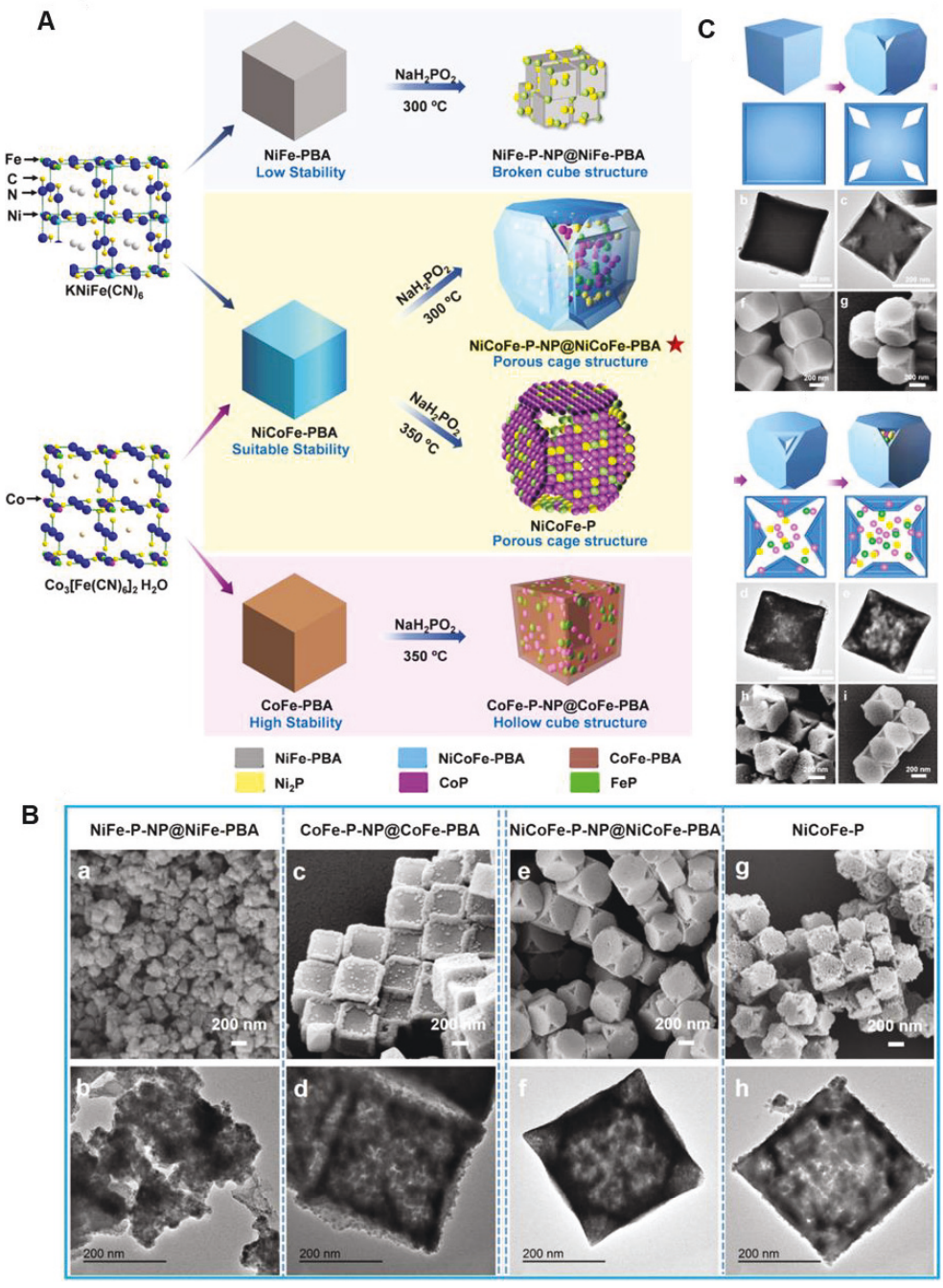

Figure 2.22. A) Schematic illustration of preparing NiCoFe-P nanocages from different PBA precursors, B) TEM images of the four phosphatization products, and C) Schematic illustration and corresponding TEM images of the metamorphic process of the NiCoFe-P-NP@NiCoFe-PBA. [60]

in Figure 2.22B, the framework of less-stable NiFe-PBA is inclined to be broken after

heating, while CoFe-PBA with high stability is too stable to be etched with spatial selectivity. In contrast, NiCoFe-PBA with moderate stability can be preferentially etched from its eight vertices (Figure 2.22C). Through this spatially selective-etching strategy, polymetallic phosphide nanoparticles (NiCoFe-P-NPs) were *in-situ* anchored into porous NiCoFe PBA cages.

2.2.2 Location engineering of active sites in nanoreactors

For nanoreactors, endowing the active sites with a controllable number and specific spatial location is also important. Firstly, the number of active sites has a great effect on the catalytic activity. Su at el. designed and synthesized a multilevel yolk-shell nanoreactor with an adjustable number of active sites by the sacrificial template method [90]. The number of catalytically active Au nanoparticles in each ZIF-8 nanoreactor could be controlled as a function of the amount of $Au@SiO_2$ precursor added before the growth of ZIF-8. The average number of active sites in the ZIF-8 nanoreactor was precisely controlled from 1 to 3, 5, 12, and 15 (Figure 2.23A). Furthermore, the matching of adsorptive sites and reactant substrates is significant when a reaction involves the activation of relatively large reactant molecules, especially for single-atom catalysts. Therefore, regulating the distance between atomic sites and controlling the synthesis of dual-atom catalysts bring new opportunities for heterogeneous catalysis. The catalytic behaviors could be optimized by regulating the spacing between two neighbouring atoms due to the electron transfer and synergistic effect. Therefore, precise control of the

distance between adjacent atoms through the selection of MOF assembly units is an attractive method. For example, Li at el. synthesized a hollow ZIF-8 nanoreactor with Pd and Ru single atom sites stabilized by mesoporous silica (MS Pd-Ru@ZIF-8) (Figure 2.23B) [91]. Pd and Ru atoms are firmly anchored in the framework of ZIF-8 by substituting Zn nodes via cation exchange. As a result, the distance between Pd and Ru atoms is 0.6 nm, which is consistent with the metal node spacing fixed by 2-MIM ligands in ZIF-8 crystals.

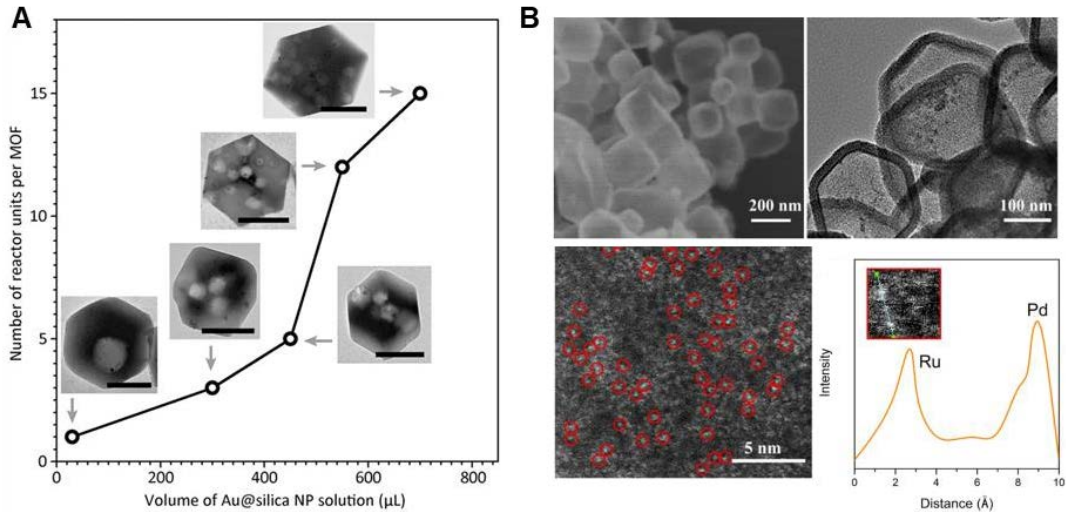

Figure 2.23. A) The control of unit number in each Au@ZIF-8 nanoreactor. [90] B) The control of the distance between active sites in MS Pd-Ru@ZIF-8 nanoreactor. [91]

In addition, the spatial relationship between the active sites and the nanoreactors is also crucial to the catalytic reaction. The introduction of metal sources that can coordinate with the etching agent can make metal active sites uniformly embedded in the wall of nanoreactors by simultaneous etching/polymerization. For example, phenolic acid, as an etching agent for ZIFs, can be coated on the surface of ZIF during etching to form yolk-

shell or single-shell products [92, 93]. At the same time, metal active sites can be introduced to the obtained shell via coordination [43, 94]. Therefore, hollow carbon-based materials embedded with metal active sites are obtained after confined pyrolysis. Telfer et.al first proposed the above synthetic route and pioneered the synthesis of hollow porous carbon (HPC) nanoreactors with bimetallic PtCo alloys uniformly distributed in the walls (Figure 2.24A) [94]. Furthermore, this method can be generalized for the preparation of hollow carbon nanoreactors decorated with atomically dispersed metal catalysts [95].

For some catalytic reactions, unique yolk–shell nanostructure with active sites inside MOF-based nanoreactors not only facilitates access to active sites but also benefits substrate enrichment and preferential adsorption [25]. To precisely locate active sites inside MOF-based nanoreactors, the sacrificial template method can be adopted. For example, in the work mentioned in Chapter 2.1.1.1, Li et al. used the Cu_2O as a sacrificial template to encapsulate PdAg nanoparticles into ZIF-8 nanoreactors, creating yolk-shell PdAg@ZIF-8 composite (Figure 2.24B) [25]. The diffuse reflectance infrared Fourier transform spectroscopy (DRIFTS) experiments revealed that the hollow space between yolk and shell is not only conducive to substrate enrichment but also to the preferential adsorption of $-NO_2$ groups under light irradiation, which leads to high selectivity and activity in the hydrogenation of nitrostyrene to vinylaniline.

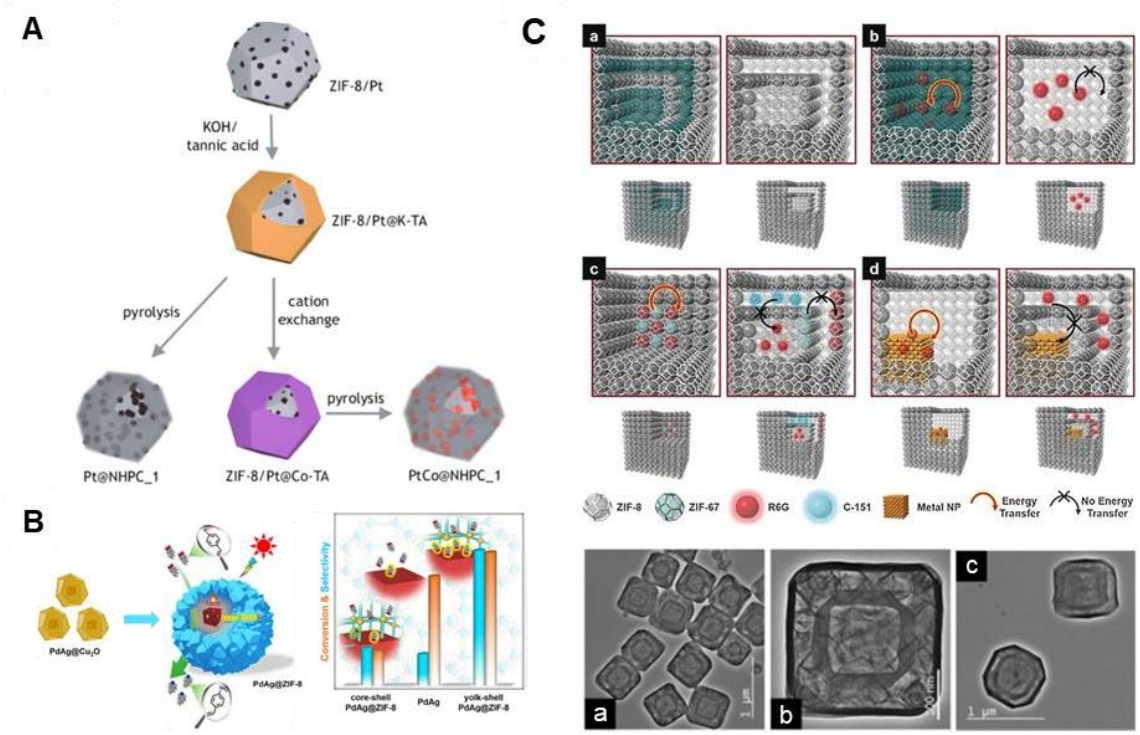

Figure 2.24. A) Synthesis of PtCo@NHPC nanoreactor. [94] B) Synthesis of yolk−shell PdAg@ZIF-8 nanoreactor and chemoselective hydrogenation of para-nitrostyrene over PbAg, yolk−shell, and core−shell PdAg@ZIF-8 catalysts. [25] C) Schematic of multi-shelled Pd@ZIF-8@R6G@ZIF-8 ZIF nanoreactors. [96]

Furthermore, nanoreactors also provide complex multifunctional platforms (e.g., pores, cavities, the interior surface, the exterior surface, etc.) to precisely separate multiple active sites to different compartments. Liu et al. selectively located guest molecules including rhodamine 6G (R6G), 7-amino-4-(trifluoromethyl)coumarin (C-151), and palladium nanoparticles (Pd NPs) into the multi-shelled hollow ZIF-8 host by the de novo method (Figure 2.24C) [96]. First, guest molecules were fixed into different layers of ZIF-67@ZIF-8 by the epitaxial layer-by-layer overgrowth. Then ZIF-67 layers were

selectively etched to form cavities between the ZIF-8 layers. Therefore, the guest molecules initially fixed in ZIF-8 layers remained in the ZIF-8 shells, while those initially fixed in ZIF-67 layers were released to the cavities between ZIF-8 shells.

2.3 Nanoreactor effects on catalytic performance

The narrow channel of MOFs limits their application as nanoreactors due to restricted mass transfer, heat transfer, and difficulty in molecule encapsulation. By structurally designing the MOF-derived nanoreactors, their application range can be well expanded. The main advantages of MOF-derived nanoreactors are (1) available hollow spaces and porous shells and (2) the precise location of active sites. Therefore, hierarchical porous and multilevel hollow MOF-derived nanoreactors are beneficial to exposing accessible active sites, concentrating reactants, regulating the retention time of intermediate products, enhancing mass diffusion, regulating the selectivity of the reaction, and even endowing size-selective and cascade catalysis.

2.3.1 Regulation of active site microenvironment

Nanoreactors not only provide a large number of accessible active sites but also rich metal-supported interfaces. The metal−supported interactions (MSIs) provide opportunities to regulate the electronic properties of active sites through charge transfer. The electronic properties can further affect the adsorption and desorption of reacting species. In addition, MSIs also provide nanoreactors with strong bounded active sites and

prevent them from migration and aggregation during reactions. Based on the above principles, Li et al. investigated the MSIs in Pt/Co_3O_4 nanoreactors on ammonia borane (AB) hydrolysis (Figure 2.25A) [97]. Pt clusters can effectively break B-H bonds to form electronegative H ($H^{\delta-}$) from AB, while Co_3O_4 with rich oxygen vacancies can proficiently adsorb and dissociate H_2O to provide electropositive H ($H^{\delta+}$). The synergetic effect of Pt clusters and Co_3O_4 substrates accelerates the spillover of $H^{\delta+}$ and $H^{\delta-}$ to Pt/Co_3O_4 interfaces and forms H_2.

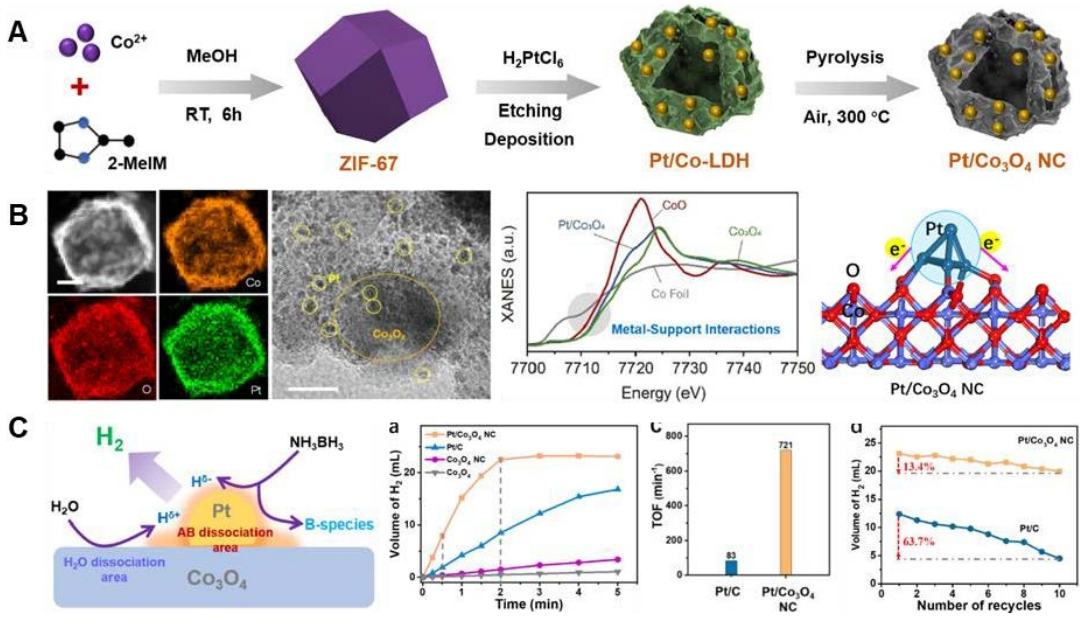

Figure 2.25. A) Synthetic scheme, B) TEM images and charge transfers, C) Catalytic performance of Pt/Co_3O_4 in ammonia borane hydrolysis. [97]

Furthermore, the strong MSIs cause the charge transfer from Pt to Co_3O_4, which is beneficial to the desorption of toxic B-containing byproducts from Pt active sites (Figure 2.25B). Therefore, compared with commercial Pt/C, the activity, and selectivity of Pt/CO_3O_4 in the catalytic hydrolysis of AB are significantly improved (Figure 2.25C).

2.3.2 Mass transfer enhancement

Microporous MOFs have the problem of diffusion blockage, so their catalytic efficiency is unsatisfactory. Therefore, the fabrication of MOF-based hierarchical porous nanoreactors plays a great role in the enhancement of mass diffusion. Qin et.al confirmed the enhanced diffusion of reactants in a hierarchical porous MOF with a hollow macroporous core and mesoporous shell [39]. Researchers compared the mass diffusion in hollow mesoporous MOF (HM-MIL) with that in solid MOF (S-MIL) and hollow microporous MOF (H-MIL) (Figure 2.26A).

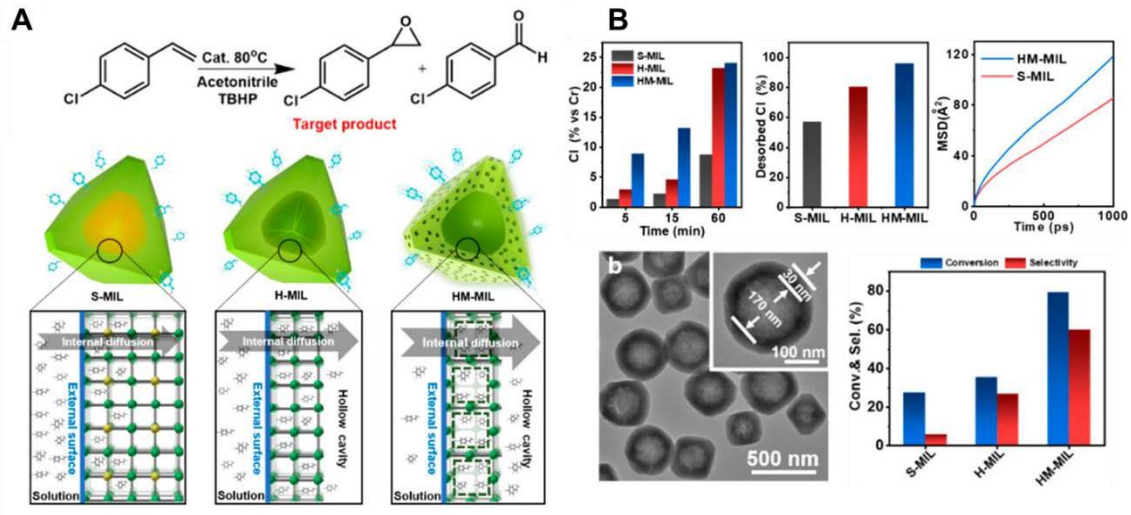

Figure 2.26. A) Molecular simulation, B) catalytic performance and diffusion within S-MIL, H-MIL, and HM-MIL for 4-chlorostyrene oxidation.

Catalytic reactions with 4-chlorostyrene as a probe confirmed enhanced mass diffusion in HM-MIL (Figure 2.26B). Diffusion experiments and molecular dynamics simulations also verified that HM-MIL significantly enhanced the reactant's diffusion rate within the

framework, relative to the S-MIL and H-MIL crystals.

Nanoreactors have also been used as anode materials for sodium-ion batteries, which are promising alternatives to lithium-ion batteries. Shortening the diffusion pathway and increasing accessible surfaces for Na^+/K^+ ions are necessary for ultra-fast intercalation in batteries. Compared with non-hollow carbon nanoparticles, Wang et al. found that hollow carbon nanobubbles with thin shells not only shortened the diffusion path of ions but also changed the behavior of ion intercalation from battery-type to pseudocapacitor-type (Figure 2.27) [92]. Therefore, the carbon nanobubbles improved the intercalation of Na^+/K^+ ions and enabled excellent battery performance.

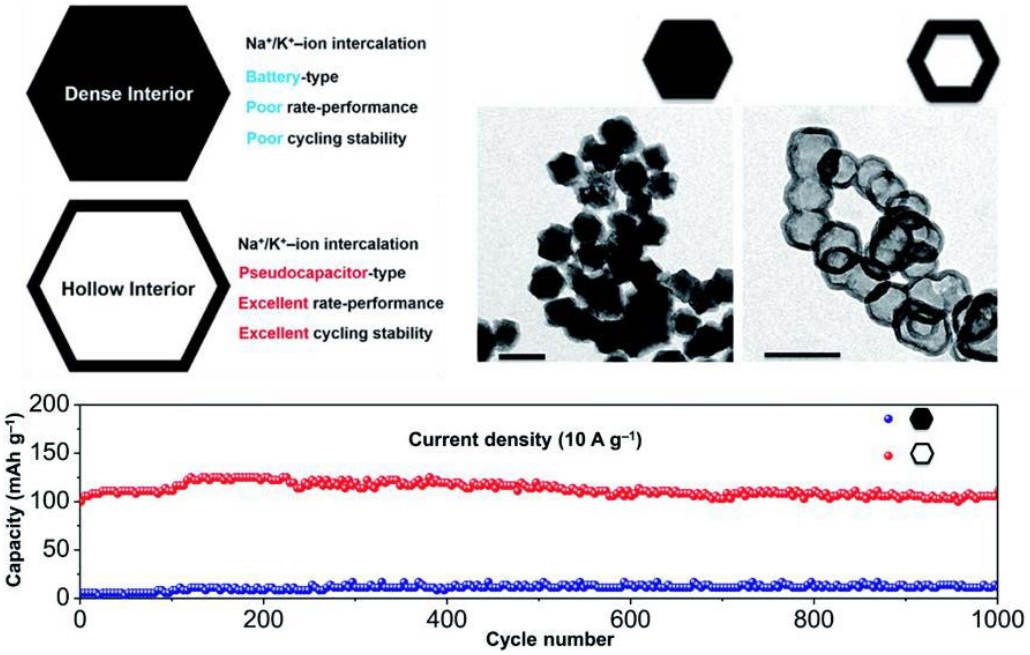

Figure 2.27. Na^+/K^+ ion intercalation performance and electrochemical performance of the dense and hollow carbons [92]

In addition to hollow structures, nanoframe-shaped nanoreactors also exhibited clear

shape effects when serving as a cathode for a sodium ion battery [85]. As shown in Figure 2.28, NiFe(II) Prussian blue analogue (PBA) nanoframes promoted the reversible insertion and extraction of Na^+ ions. As a result, these PBA nanoframes delivered improved rate performances and cycling stability at high current rates compared with the parent PBA cubes.

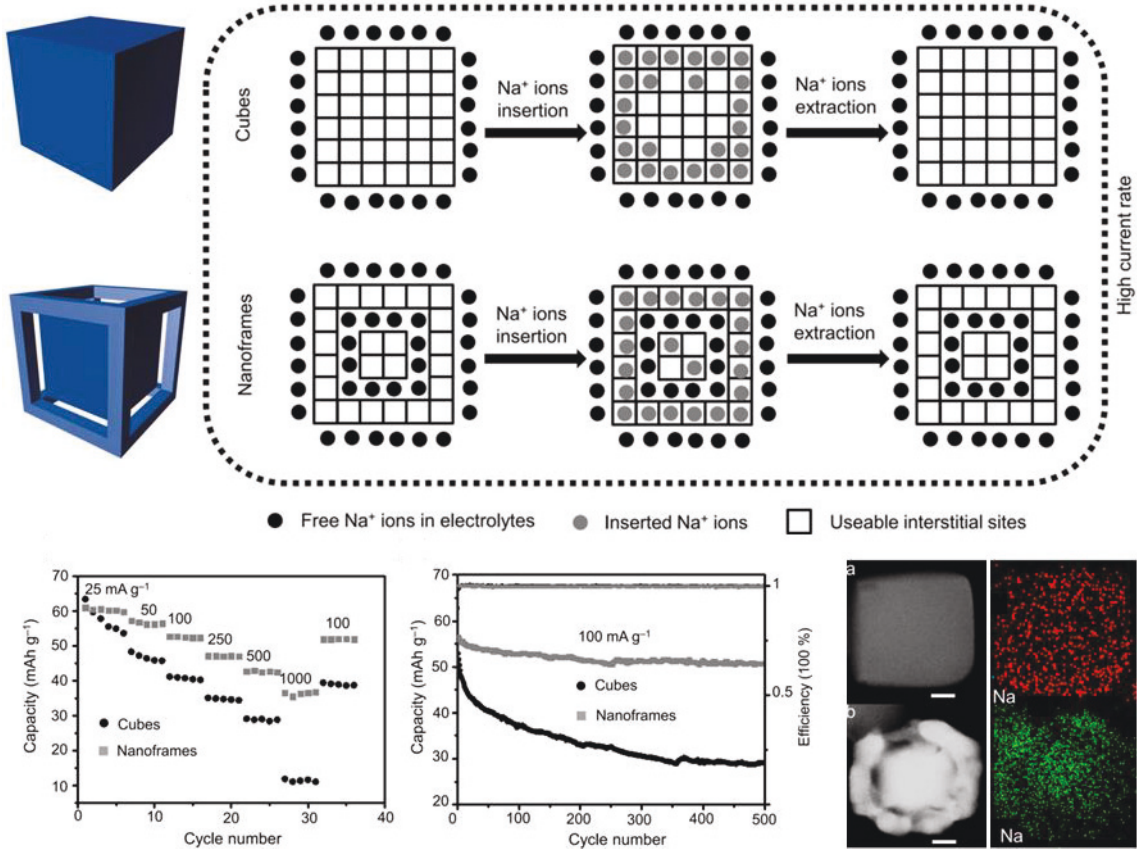

Figure 2.28. Iinsertion/extraction of Na^+ ion into PBA cubes and nanoframes at high current rates, and electrochemical performance and element mapping after insertion of Na^+ ions in Ni-Fe PBA cubes and nanoframes as cathode materials for SIBs. [85]

Research on gas-involving electrocatalytic reactions mostly focuses on improving the intrinsic activity of active sites. However, for catalytic reactions that occur at the solid-

liquid-gas three-phase interfaces such as oxygen reduction, reasonable nanoreactor engineering is conducive to enriching the three-phase interfaces and boosting the gas supply. For example, Ao et al. fabricated a FeNC-TA catalyst with a hierarchical porous structure with superior ORR performance compared with microporous FeNC (Figure 2.29A,B) [98]. The hierarchical porosity greatly promoted the diffusion of substances and the exposure of active sites.

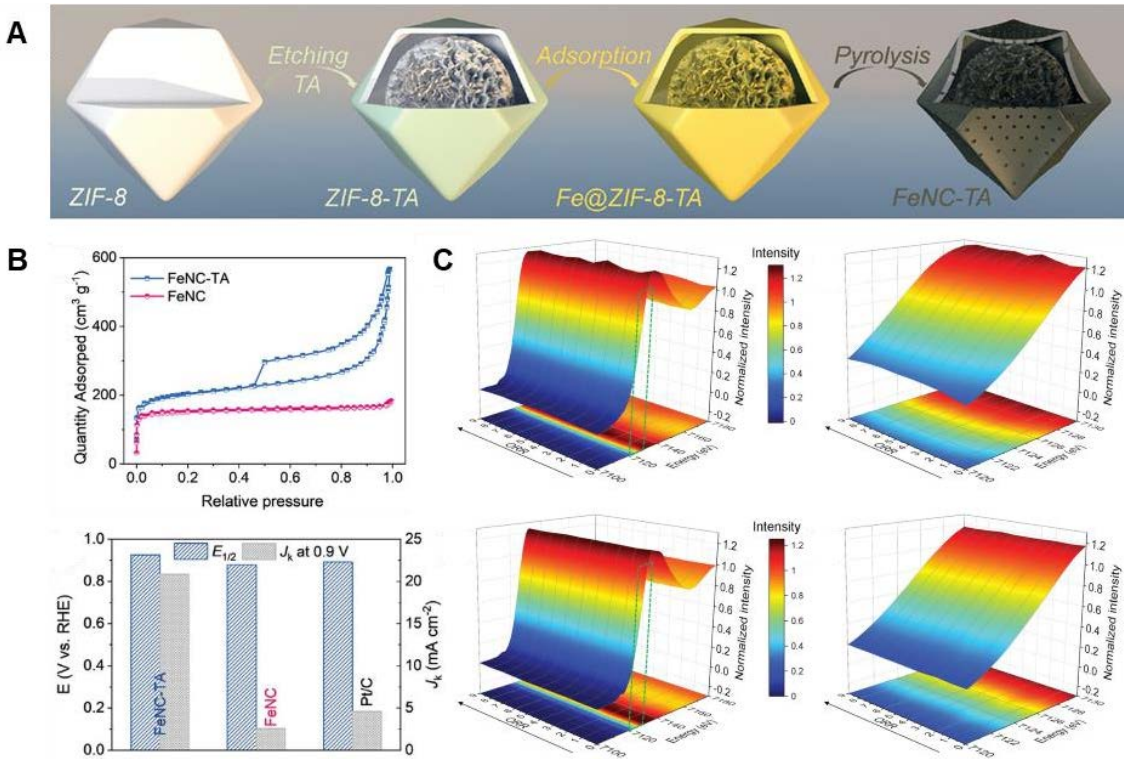

Figure 2.29. A) Schematic preparation of hierarchically porous FeNC-TA nanoreactor, B) catalytic performance, C) contour maps of operando Fe K-edge XANES of FeNC-TA and FeNC catalysts. [98]

Operando XAFS results further confirmed that the Fe-N_4 sites in the hierarchically porous FeNC-TA catalyst are more likely to participate in the ORR process than in the

microporous FeNC catalyst due to the enhanced exposure (Figure 2.29C). Thus, nanoreactors improve the utilization of active sites and enhance the mass transfer property, further optimizing the catalytic performance.

The mass diffusion enhancement can also be demonstrated by the improved accessibility of large molecules through enlarged channels. As for this aspect, the beneficial effect of hierarchical porous structure on the catalytic performances of the oxidation of o-phenylenediamine (o-PDA) and 2,20-azino-bis(3-ethylbenzothiazoline-6-sulphonic acid) (ABTS) was demonstrated by Yuan et al. [76]. Cytochrome c (Cyt c) enzyme was immobilized in the hexagonal channels of the original and defected MOF, named CYCU-3 and CYCU-3D, respectively. The catalytic performance of o-PDA oxidation is comparable because the o-PDA molecule is small enough to diffuse into the hexagonal channels of both CYCU-3 and CYCU-3D to reach the encapsulated enzymes（Figure 2.30A). However, the catalytic performance of ABTS oxidation dramatically decreased in CYCU-3, compared with that in CYCU-3D. Considering the relatively large size of ABTS, their access to the enzyme through the hexagonal channels is blocked by the encapsulated Cyt c. Meanwhile, the diffusion of ABTS in CYCU-3 is largely limited by its small size of triangular channels, while ABTS diffusion in CYCU-3D was enhanced by the larger windows on the triangular channels, allowing for efficient access to the active center of Cyt C. Therefore, the activity of Cyt c oxidation in CYCU-3D is almost five times compared with that in CYCU-3 due to diffusion enhancement. Meanwhile,

Chang et al. also found that mesoCu@Al-bpydc showed better catalytic activities than microCu@Al-bpydc in the cycloaddition reactions of epoxides and CO_2, especially for the epoxides with larger sizes (Figure 2.30B), which proves again that hierarchical porous nanoreactors could enhance the mass transfer to the catalytic active sites [69].

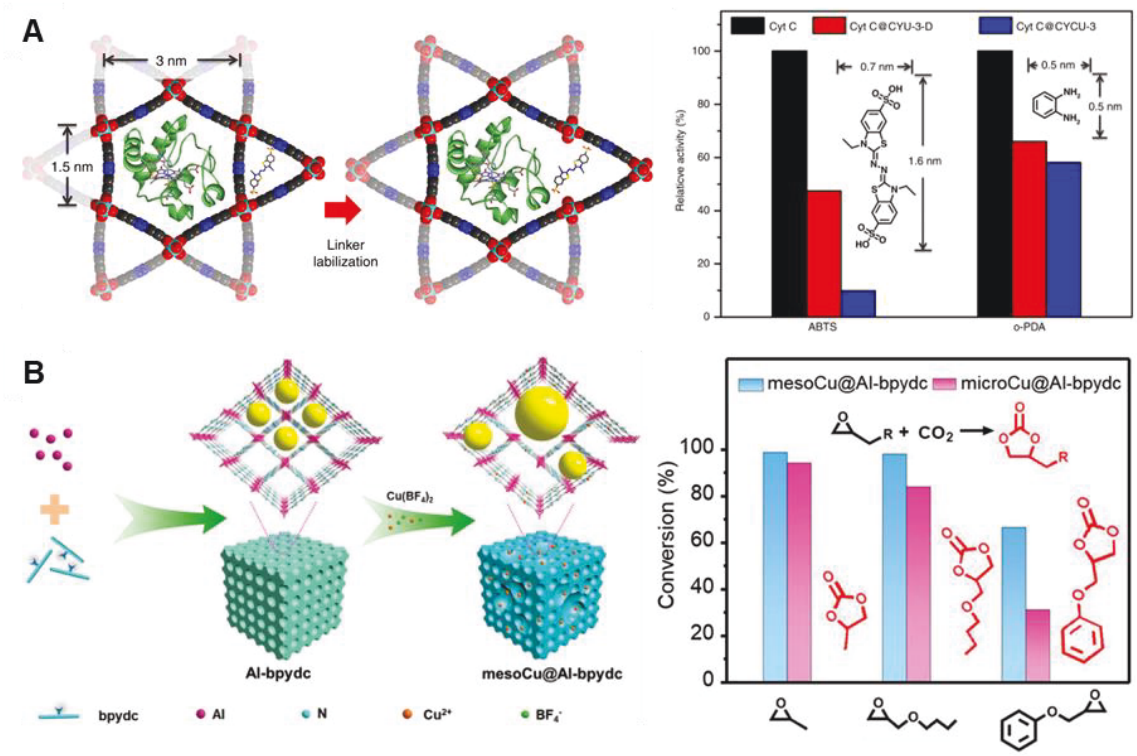

Figure 2.30. A) Schematic diagram of the accessibility of enzymes in CYCU-3 and CYCU-3D, and catalytic activity for the oxidation of ABTS and o-PDA by Cyt c, Cyt c@CYCU-3, and Cyt c@CYCU-3D. [76] B) Schematic preparation of hierarchically porous mesoCu@Al-bpydc, and catalytic activity for the cycloaddition reactions with different epoxides. [69]

2.3.3 Molecular sieving effect

MOF-derived nanoreactors can also allow for efficient molecule sieving and adsorption of large molecules by adjusting their pore sizes, which promises a wide range of potential applications in adsorption/separations and heterogeneous catalysis. For example, Li et al. prepared MOF-74-coated hollow Pt-Ni frameworks (Pt–Ni@Ni-MOF-74) by a competing-coordination etching strategy [99]. During the synthesis, 2,5-dioxidoterephthalate coordinates with Ni species from Pt-Ni polyhedral, so that etching Pt-Ni polyhedral and forming MOF-74 shells take place simultaneously (Figure 2.31A). For the hydrogenation of aryl olefins of different molecular sizes, Pt–Ni@Ni-MOF-74 showed size-sieving properties and only molecules smaller than the pore size of Ni-MOF-74 (0.86 nm) could be converted to the corresponding products (Figure 2.31B).

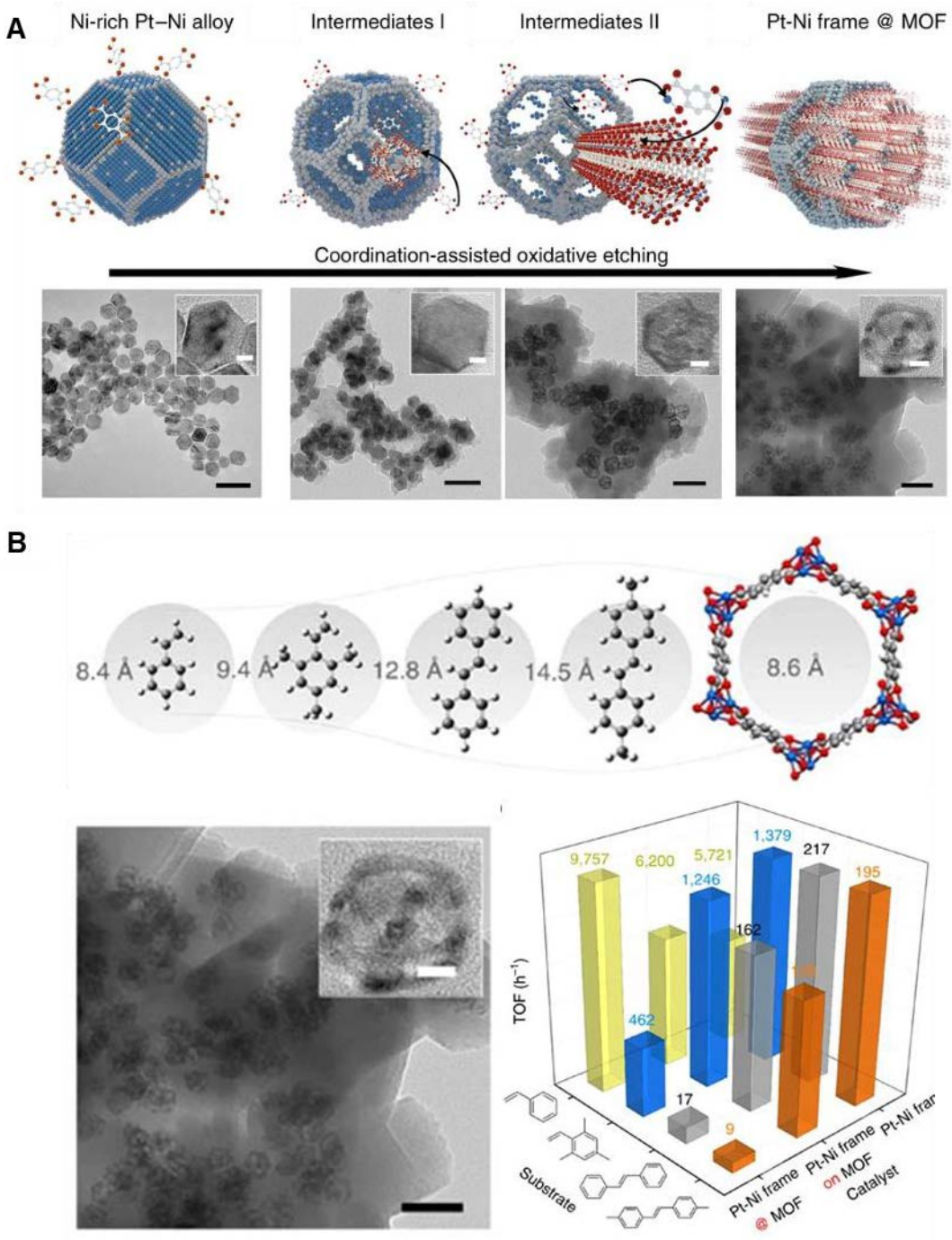

Figure 2.31. A) Synthetic scheme, TEM images, and B) the corresponding molecular sieving by Pt–Ni@Ni-MOF-74. [99]

2.3.4 Selectivity regulation

In a multi-step reaction, it is a challenge to precisely control the generation of a specific product. Li et al. achieved excellent selectivity of 4-nitrostyrene in the selective hydrogenation of phenylacetylene, taking advantage of the synergistic effect of Pd and Ru single sites due to their well-desired distance [91]. The specific distance of Pd and Ru active sites matched well with the size of the substrate, thus reducing the desorption energy of styrene and increasing the hydrogenation energy barrier of styrene. As a result, high selectivity (96%) was achieved in the semi-hydrogenation of phenylacetylene to styrene (Figure 2.32A). Besides, Yang et al. reported that the hollow interior also endowed catalysts with superior selectivity toward the semi-hydrogenation of acetylene (Figure 2.32B) [100]. It is worth noticing two structural advantages of the hollow Zn/Co-ZIF (H-Zn/Co-ZIF) nanoreactor with Pd nanoparticles confined in its hollow cavities. On one hand, the hollow nanoreactor shell showed the diffusion priority of smaller acetylene over larger ethylene molecules, which protected ethylene from over-hydrogenation to ethane, compared with bare Pd NPs/C. On the other hand, selective hydrogenation was facilitated in the hollow cavity of H-Zn/Co-ZIF by enhanced inward diffusion of substrate and accelerated desorption of product, compared with solid Zn/Co-ZIF nanoreactors with Pd nanoparticles inside (Pd@S-Zn/Co-ZIF).

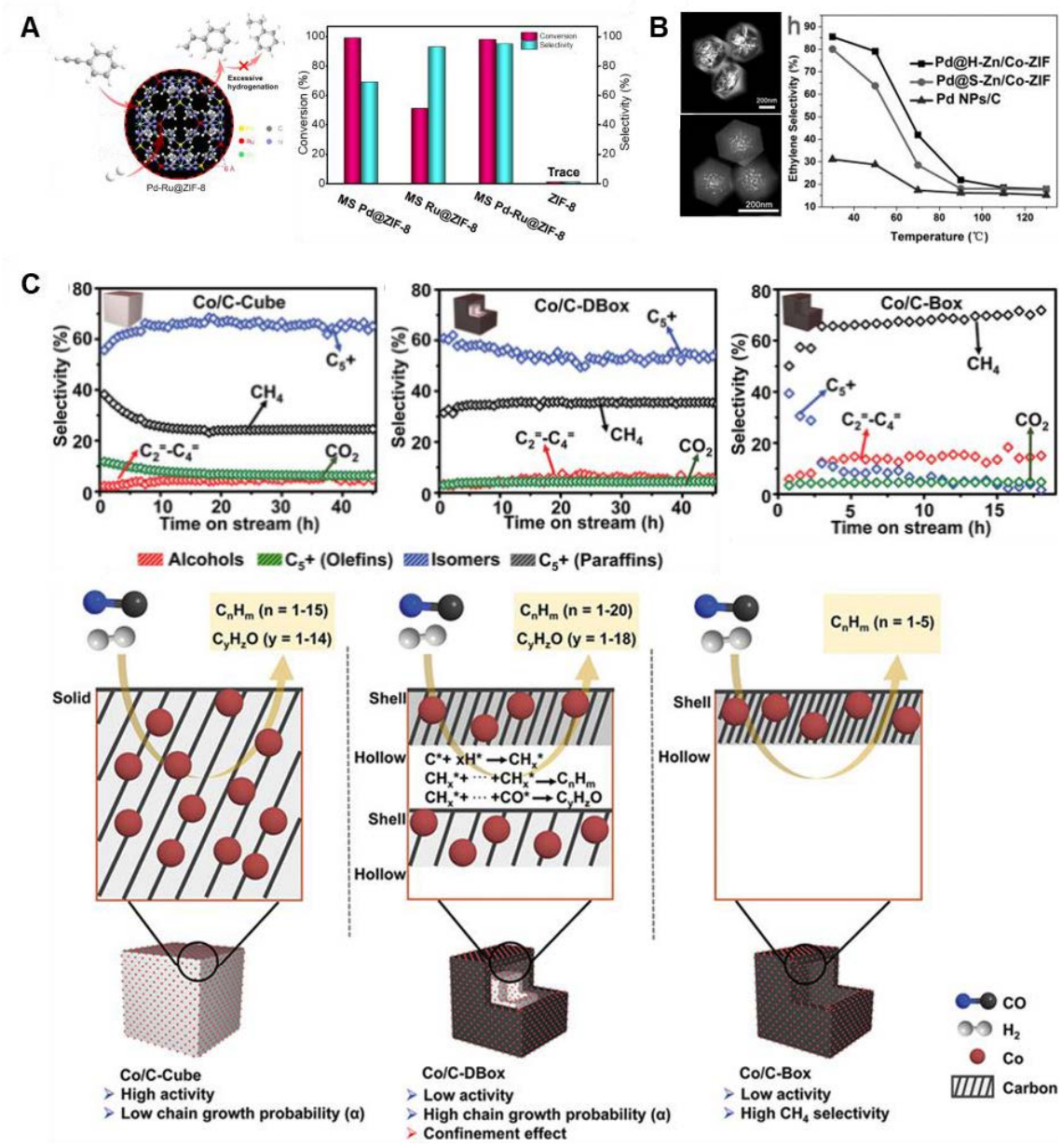

Figure 2.32. A) Schematic illustration of the selective hydrogenation of phenylacetylene by MS Pd-Ru@ZIF-8. B) Conversion of phenylacetylene, selectivity of styrene, and TOFs for hydrogenation of phenylacetylene over MS Ru@ZIF-8, MS Pd@ZIF-8, and MS Pd-Ru@ZIF-8. [91] C) Catalytic performance and schematic illustration of various Co/C sub/microreactors in the selective syngas conversion process. [81]

The complex structure of nanoreactors also has a great influence on the product

distribution in heterocatalysis because of the enrichment of substrate and the residence time of intermediates. For example, starting from ZIF-67 crystals, Wei et al. obtained a series of Co/C sub/microreactors: non-hollow Co/C-cube, double-shelled hollow Co/C-dbox, and single-shelled hollow Co/C-box by combining methods of TA-protected etching and carbonization [81]. In selective syngas conversion, the experimental results showed that compared with Co/C-Cube, Co/C-Box tended to generate methane, while Co/C-D Box tended to yield long-chain products (Figure 2.32C). This is because the single-shelled structure enabled the enrichment of hydrogen in the cavity. In contrast, the double-shelled structure showed a confinement effect between the two shells, which inhibits the diffusion and increases the residence time of the intermediates so that the intermediates can be further hydrogenated to products with longer chains. The above results show that the precise regulation of micro/nanoreactor structure benefits shape selection.

2.3.5 Tandem reaction

In nature, efficient intracellular metabolism and signal transduction depend on regionalization and cascade reaction. Therefore, it is of great significance to simulate such highly efficient and orderly catalysis in nanoreactors. The tandem catalytic reaction process does not require additional separation and purification steps, which can reduce the reaction steps, energy consumption, and by-product generation, maximize the consumption of reactants, and effectively improve the efficiency of catalytic reactions.

Therefore, an ideal nanoreactor is effective in organizing different functions to work together in different spaces. However, it is still a significant challenge to combine homogeneous catalytic sites and heterogeneous catalytic sites in a single nanoreactor. To this end, Cai et al. developed controllable multilevel hollow LDH@MOF nanoreactors with complementary strengths of homogeneous molecular catalysts and heterogeneous catalysts (Figure 2.33) [101]. First, metalloporphyrins were pre-adsorbed into the hollow LDHs with large open channels.

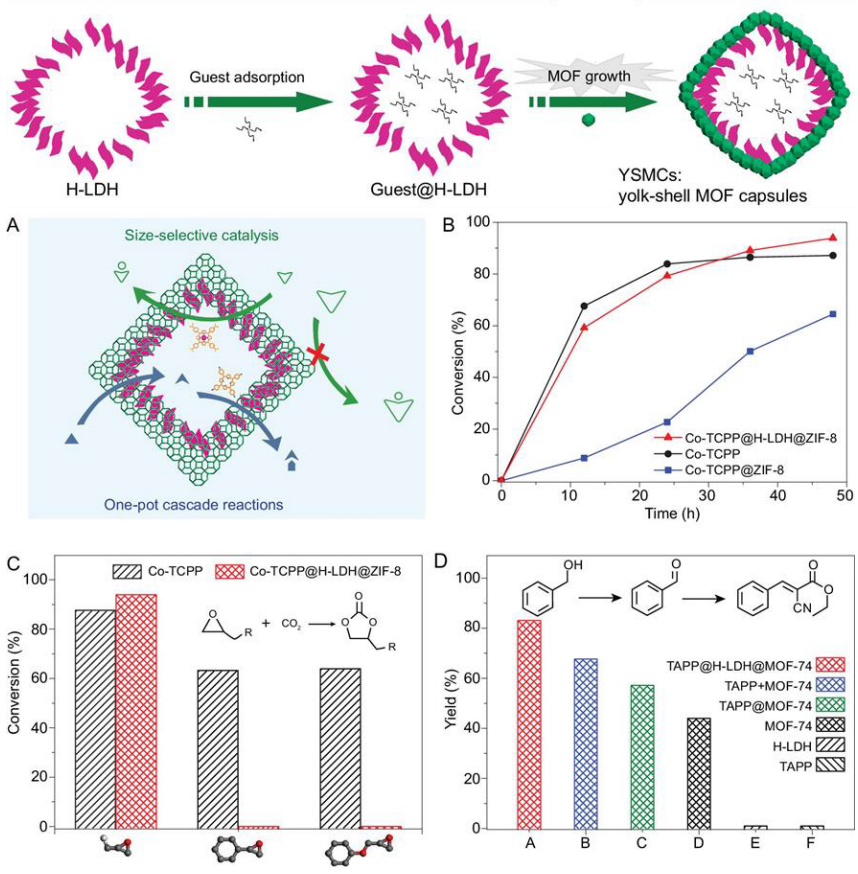

Figure 2.33. Schematic illustration, size-selective, and cascade catalysis of Co-TCPP@H-LDH@ZIF-8 and TAPP@H-LDH@MOF-74 nanoreactors. [101]

Then defect-free MOF shells were grown to form the external shell using LDHs as the

templates, thus closing the opening to prevent soluble catalysts from leaching. As a result, the LDH@MOF nanoreactor not only realized the homogeneous catalysis inside but also endowed the catalysts with an enriched substrate environment, enhanced mass transfer, and size-selective and cascade catalysis. As a typical model, H-LDH@MOF-74 encapsulated in with amino-functionalized porphyrin (TAPP) (denoted TAPP@H-LDH@MOF-74) outperformed its corresponding counterparts in the cascade oxidation/Knoevenagel condensation.

2.4 MOF-derived B,N-doped carbon-based electrocatalysts for ORR and OER

According to the International Energy Agency [102], global energy demand is expected to reach 24-26 petawatt hours (TWh) in 2040. Since the major energy supply comes from fossil sources, including coal, oil, natural gas, etc, the corresponding CO_2 emissions would be 37-44 Gt $year^{-1}$ in 2040. Therefore, along with the depletion of conventional fossil fuels and global warming caused by carbon dioxide emissions, clean and sustainable energy conversion, and storage via fossil-free pathways prompted major research efforts [103]. One of the promising ways to reduce reliance on fossil fuels is to develop cost-effective electrocatalysts for green electrochemical synthesis using electricity generated by renewable energy such as solar, wind, and tidal power [104]. Figure 2.34 shows (photo)electrochemical conversion can be coupled with renewable energy sources to effectively convert renewable raw materials (e.g., N_2, CO_2, H_2O, and biomass) into transportable fuels, commercial chemicals, and even specialty chemicals,

such as NH_3, hydrocarbons, oxygenates, and H_2 [104].

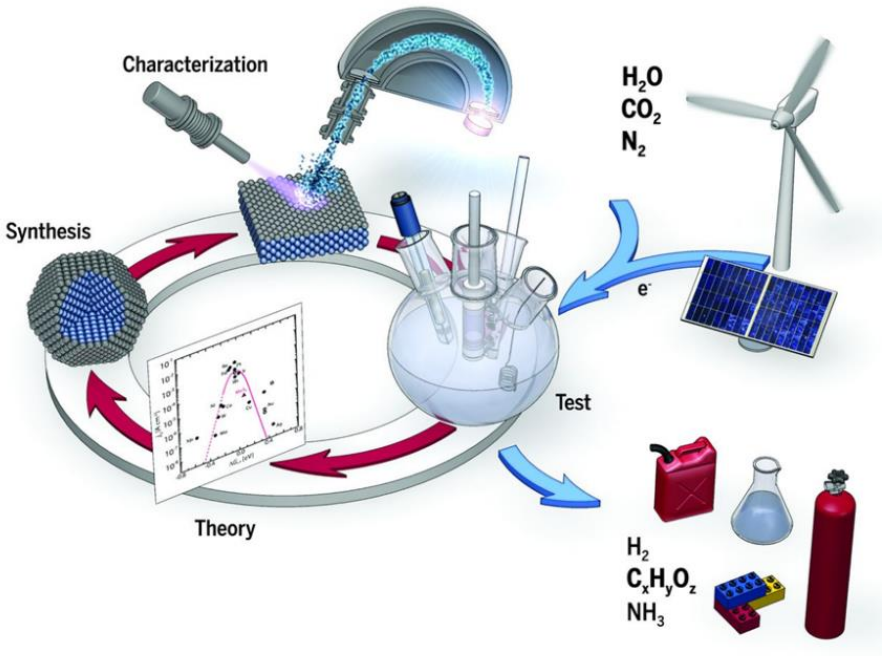

Figure 2.34. Schematic of a sustainable energy landscape based on electrocatalysis. [104]

H_2, for example, is considered to be an efficient and clean fuel to replace fossil energy because its combustion product is only H_2O. Electrocatalytic water splitting is an ideal way to produce H_2 (Figure 2.35A). However, due to the slow kinetics of hydrogen evolution reaction (HER) at the cathode and oxygen evolution reaction (OER) at the anode, especially that of OER, wide deployment of electrolysers is still not economical. Furthermore, proton exchange membrane fuel cells (PEMFCs) convert the chemical energy of H_2 into electric energy via hydrogen oxidation reaction (HOR) at the anode and oxygen reduction reaction (ORR) at the cathode (Figure 2.35B). In the whole process, only electricity, heat, and H_2O are generated, achieving zero carbon emission. The cost

of electrocatalysts, which account for half of the PEMFCs' total cost, remains the main obstacle to its commercialization. Since the kinetics of ORR is much slower than that of HOR, the cost of the electrocatalyst is mainly derived from the cathode material [105]. Meanwhile, enhancing the sluggish ORR process is also important for the application of metal-air batteries [106]. Meanwhile, OER is also essential in metal-air batteries (MABs) (*e.g.* zinc-air batteries), which are advocated as promising alternatives to Li-ion batteries (LIB) in applications such as electric vehicles due to their high theoretical energy densities, as shown in Figure 2.35C [107]. Therefore, the development of highly active, stable, and low-cost ORR and OER electrocatalysts plays a crucial role in the development of advanced energy conversion and storage systems, especially for rechargeable metal-air batteries.

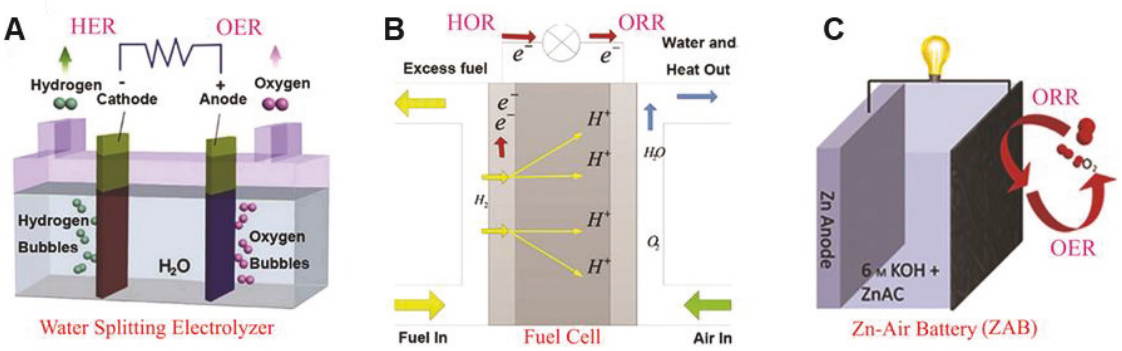

Figure 2.35. Schematic illustrations of electrocatalytic reactions in A) a water-splitting electrolyser, B) a proton exchange membrane fuel cell, and C) a zinc–air battery. [107]

2.4.1 Mechanism and configurations of MABs

The working mechanism of MABs can be summarized as a discharging process via an

oxidation reaction on the negative electrode (metals or alloys) and a charging process via reducing metal compounds to metals. During discharge, metals (eg. Li, Zn, Na, Mg, and Al) at the anode are oxidized, and the O_2 molecules at the air cathode (from the atmosphere) are reduced (Figure 2.36). Therefore, it is necessary to effectively catalyze ORR and OER processes at the air cathode, which are both sluggish reactions. The key to enhance the charge/discharge performance and realizing the large-scale application of MABs is to develop cost-effective electrocatalysts with high activity, good durability, and high selectivity.

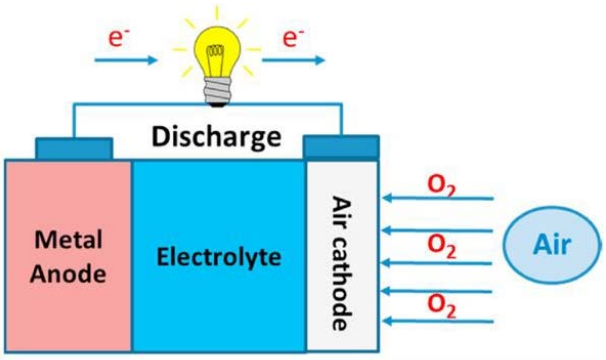

$$Anode: M \leftrightarrow M^{n+} + ne$$

$$Cathode: O_2 + ne + 2H_2O \leftrightarrow 4OH^-$$

Figure 2.36. Schematics of the mechanism and configurations of a metal-air battery (MAB). [108]

2.4.2 Mechanism of ORR and OER

Adsorption/desorption of O_2 molecules is the key step in ORR, which represents the diffusion/exchange of O_2. The oxygen can be effectively exchanged and reaction

resistance can be reduced by balancing the adsorption and desorption of oxygen, leading to high kinetic current and diffusion limiting current density. Furthermore, the way of oxygen species adsorption will change the overall reaction mechanism of ORR because of different potential barrier of subsequent reactions. In this term, ORR can be divided into a 4-electron pathway to H_2O or OH^- and a 2-electron pathway to H_2O_2 or HO_2^-, according to various pH values (Figure 2.37A). The 4-electron pathway has relatively high reaction kinetics and efficiency compared with the 2-electron pathway. Besides, the 4-electron pathway includes a direct 4-electron transfer process and a 2-plus-2 electron transfer process. Though the 2-plus-2 electron transfer process needs less energy, the intermediate product HO_2^- compromises the stability of MABs. Therefore, the direct 4-electron pathway is preferred for MABs. It is reported that bidentate adsorption and terminal adsorption of O_2 exist in ORR process, and bidentate adsorption leads to a direct 4-electron transfer pathway without H_2O_2 or HO_2^- formation [109].

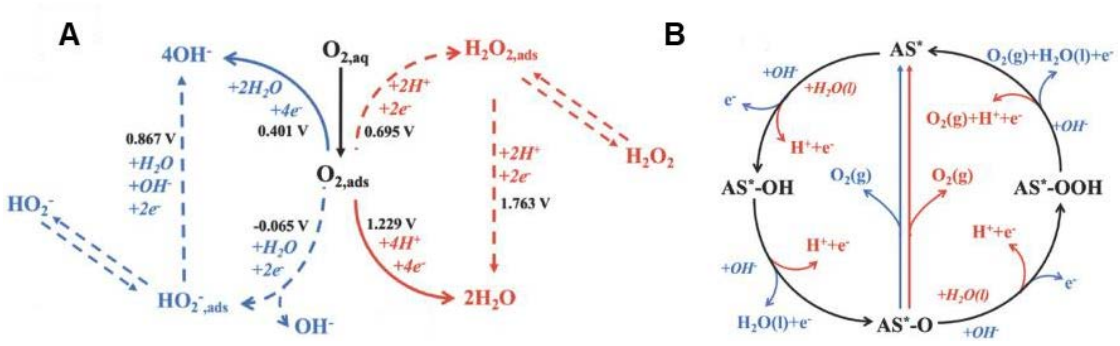

Figure 2.37. Schematics of chemical processes in A) ORR and B) OER in acidic (red) and alkaline (blue) electrolytes. [110]

As for OER, extremely high overpotentials are still required for the formation of O-O

bonds via the acid-base mechanism or the lattice oxygen oxidation mechanism (LOM) in practical applications (Figure 2.37B). In LOM, two adjacent -O atoms can be directly coupled to form O-O bond when rotating to a suitable angle [111]. Coupling occurs without being dictated by the change of metal–oxygen bond. In the acid-base mechanism, the AS*-O group on metal active sites transforms to AS*-OOH species after being attacked by H_2O or OH^- in an acidic or alkaline medium. Then AS*−OOH species are oxidized to lose protons, forming AS*−OO species. Finally, AS*−OO species break between active sites which produce O_2 [112].

2.4.3 The main principle of the electrocatalysts toward ORR and OER

In the past decades, numerous efforts have been devoted to optimizing the activity of electrocatalysts, including ORR and OER catalysts, via increasing the intrinsic activity of various active sites and increasing the number of active sites (Figure 2.38) [104]. Rational selection of the active sites determines the lower limit of the electrocatalytic activity. Increasing the intrinsic activity of catalysts by crystal plane control, electronic structure regulation, heteroatomic doping, etc., has become the most studied strategy to optimize catalytic activities. The design of the nanostructure of the catalysts is also an effective way to improve the catalytic performance by increasing the exposure of the active sites. At present, increasing the specific surface area of the catalyst is the main aim of nanostructure design. However, although the comparative area contributed by micropores increases the exposure of the active site, the improvement in catalytic activity in practical

applications is limited due to the limitation of gas-liquid-solid three-phase mass transport (eg. media, gas molecules, and products).

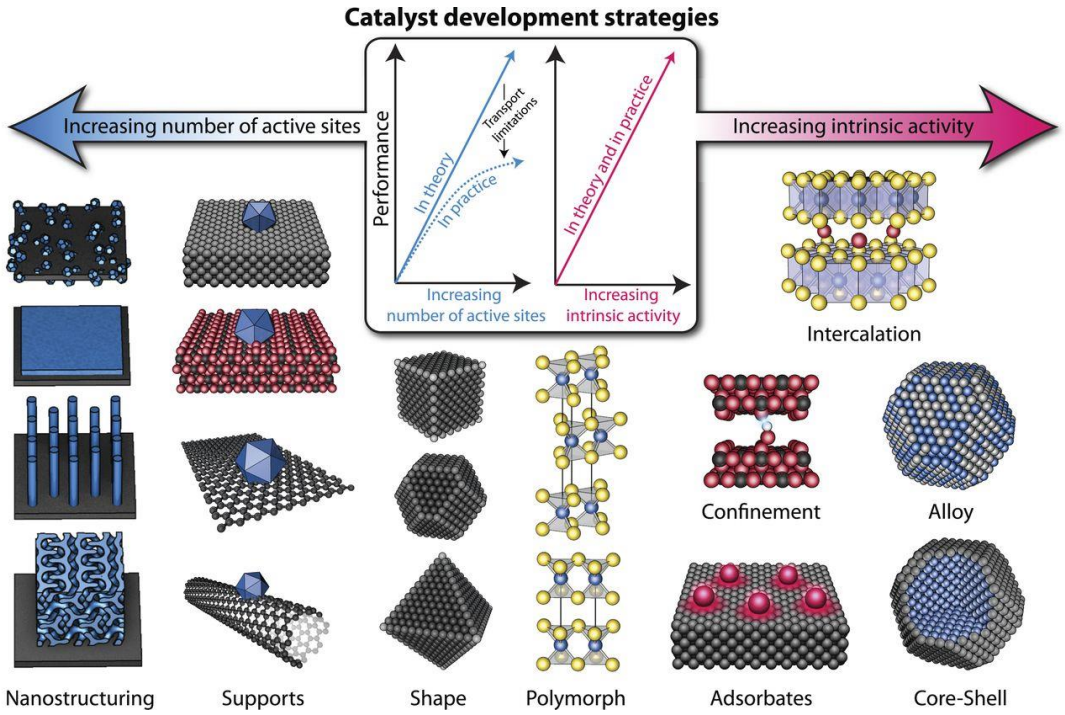

Figure 2.38. Strategies to improve the catalyst activity via increasing the intrinsic activity of active sites and the number of active sites. [104]

2.4.4 State-of-the-art carbon-based electrocatalysts for ORR and OER

Currently, noble metals and their compounds (Pt for ORR and RuO_2 for OER) are typical electrocatalysts. However, these noble metal-based electrocatalysts suffer from scarcity, prohibitive costs, and unsatisfactory stability. Therefore, non-noble-metal-based and metal-free electrocatalysts towards ORR and OER have received wide attention, but it remains challenging to find practical catalysts.

In the past decades, carbon-based catalysts with high electrical and thermal conductivities, and long-term stability has attracted strong attention [11, 113]. However, pure carbon materials are generally inert to the adsorption and activation of O_2 and its intermediates. In this regard, chemical doping and defect engineering have been deployed to improve the performance of carbon-based electrocatalysts via inducing lattice distortions and electron density redistributions (Figure 2.39) [114]. The optimized electronic structure of carbon enhances the structural matching with the adsorbents and promotes the formation of intermediates, thereby lowering the free energy barrier of the overall reaction.

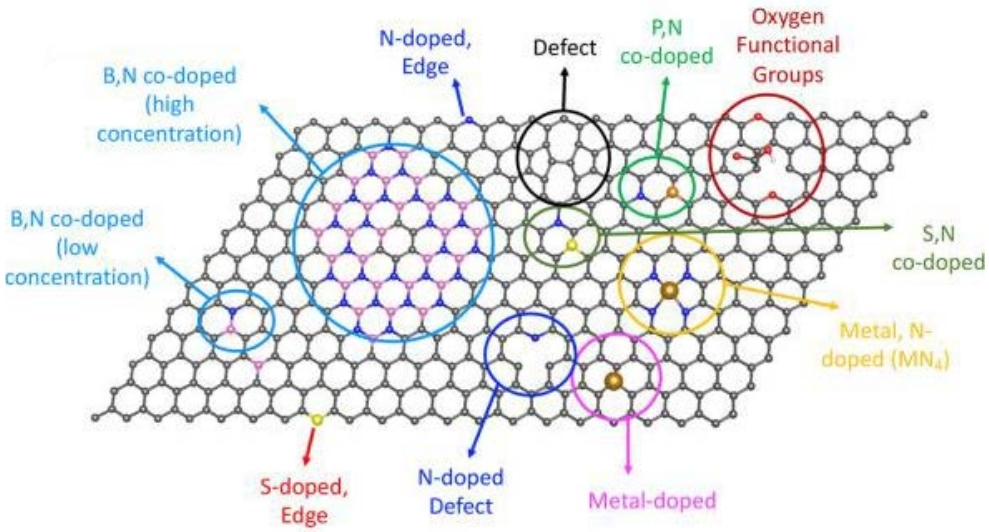

Figure 2.39. Chemical doping and defect engineering to improve the electrocatalytic performance of carbon-based materials. [114]

The well-designed carbon materials can also be used as substrates to prepare non-precious metal-carbon composite-based electrocatalysts. Due to the inherent characteristics of metals, the unique electronic structure of carbon substrates, as well as the synergistic

effect between metal and carbon substrates, these catalysts usually further improve the performances by lowering the reaction barrier and accelerating the charge transfer [109].

2.4.4.1 N-doped C electrocatalyst for ORR and OER

Different types of heteroatoms, such as boron (B), nitrogen (N), sulfur (S), phosphorus (P), fluorine (F), and oxygen (O), can be used for effectively changing the electronic structures of the carbons and providing active groups for high-performance ORR and OER electrocatalysis.

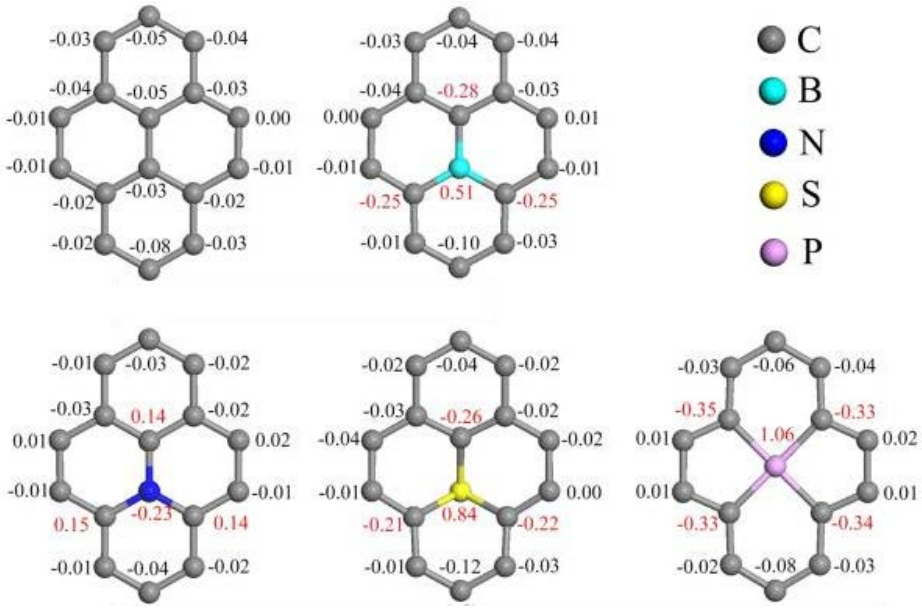

Figure 2.40. The Mulliken charges on the heteroatoms (B, N, S, and P) and the carbon atoms. [110]

Dopants with different atomic radiuses, electronegativities, and bond lengths with C atoms have different Mulliken charges. As shown in Figure 2.40, C atoms bonded to N atoms have positive Mulliken charges (+0.14, +0.15), whereas those bonded to B, S, and

P atoms have negative Mulliken charges.

Among various heteroatoms, N is widely used and extensively studied to dope C to achieve the optimal adsorption/coordination configuration [115]. N atoms are reported to form various configurations, such as pyridinic N (N6), pyrrolic N (N5), and graphitic N (NQ) (Figure 2.41A) [116].

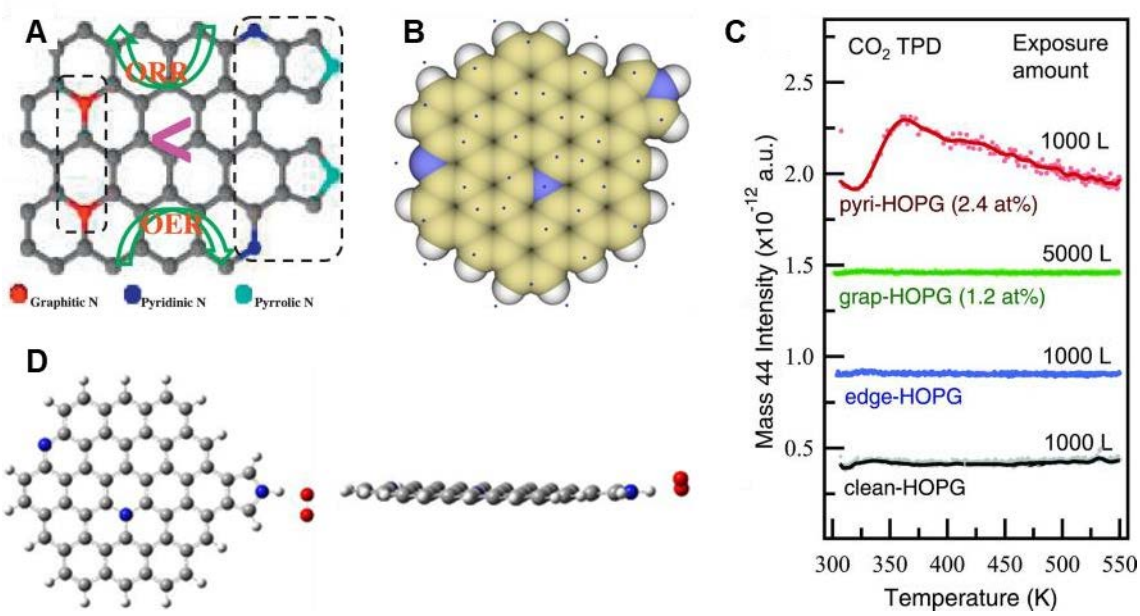

Figure 2.41. A) Scheme illustration of N configurations in N-doped C. [116] B) Average local ionization energy (ALIE) of N-doped C (blue dots are minimum points). [117] C) CO_2 temperature programmed desorption (TPD) results for the various highly oriented pyrrolic graphite (HOPG) catalysts [118], and D) the absorption of O_2 on pyrrolic N [116].

N6 and NQ have been shown to have good intrinsic catalytic activities among these forms [117, 119]. For example, Guo et al. reported that the minimum value of the average local

ionization energy (ALIE) associated with the highest reactivity, was located near the graphitic N (Figure 2.41B) [117]. Besides, the Lewis base sites created by pyridinic N are also reported to be active sites for ORR by promoting the adsorption of O_2, confirmed by CO_2 adsorption experiments (Figure 2.41C) [119]. Also, pyridinic N can promote the conversion of the 2-electron transfer of ORR into the 4-electron process [118]. Additionally, pyrrolic N is also an absorption site for O_2 (Figure 2.41D) and is active in ORR and OER [116] [117]. However, the mechanism is still controversial, and more research is needed.

2.4.4.2 B,N-doped C electrocatalyst for metal-air batteries

Compared to single-atom doping, heteroatom co-doping is expected to endow carbon-based materials with unique electronic structures, which can further increase the conductivity of carbon materials, lower activation barriers, and thus enhance the catalytic activity. Dual, ternary, and quaternary heteroatom-doping (N/B, N/P, N/S, N/O, N/B/P, N/S/P, N/B/S/P, etc.) can dramatically improve the performance of carbon in many applications [120-124]. Among these heteroatoms, N and B are of particular interest as co-dopant since they are next to carbon in the periodic table and are in similar atomic sizes. Like different types of N sites, B also has different configurations in the carbon matrix. For example, complex doping configurations featuring B-C bond and B-O bonds form when B doping graphene oxide (GO) took place at 900–1200 °C (Figure 2.42A), while substitutional doping dominated when B doping pure graphite occurred at above

2000 °C [125]. B can further substitute C in the N@C lattice and lead to the synergistic effect induced by the pairing and/or long-range coupling (Figure 2.42B) [126], which alters the electronic and charge density and consequently chemical properties [126-129].

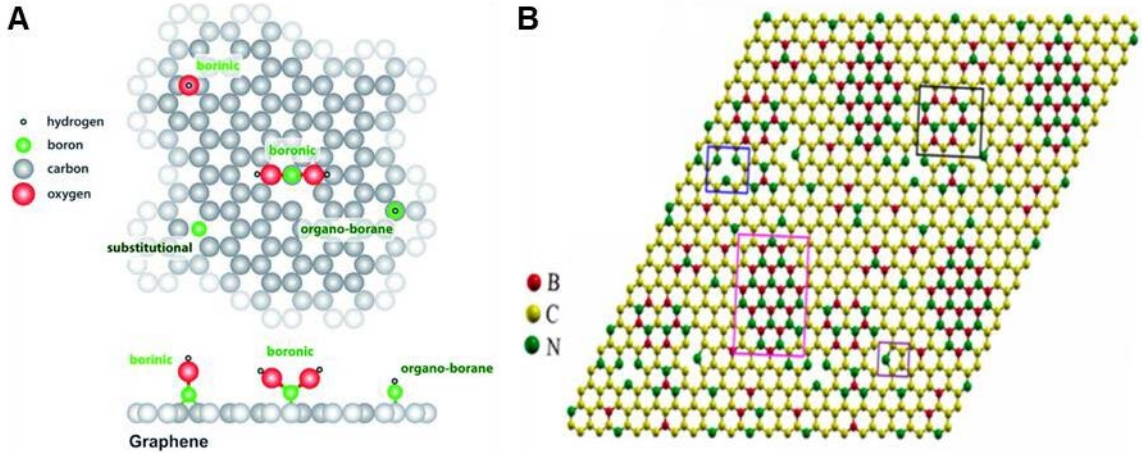

Figure 2.42. Schematic of A) N-doped C [125], and B) B,N co-doped C [126].

The electronegativity of B (2.04) and N (3.04) is lower and higher than that of C (2.55), respectively. Besides adsorption and reduction of O_2 on random N sites, positively charged B atoms adjacent to C atoms are also favorable for the adsorption of negatively charged O_2 molecules, thus benefiting the ORR kinetics [130]. Furthermore, the electron transfer from C to B can also facilitate ORR [130].The spatially separated B and N atoms in the carbon matrix can have a combined effect of improved electron mobility due to B serving as an electron acceptor while N serving as an electron donor [131]. In a recent report, the synergetic effect between BC_3 and pyridinic N significantly improved ORR (Figure 2.43A) [132]. The as-prepared 3D porous N and B dual-doped graphene aerogels (BN-GAs) also exhibited considerable OER activity (Figure 2.43B) and achieved

improved performance as an air cathode in zinc-air batteries (Figure 2.43C-F).

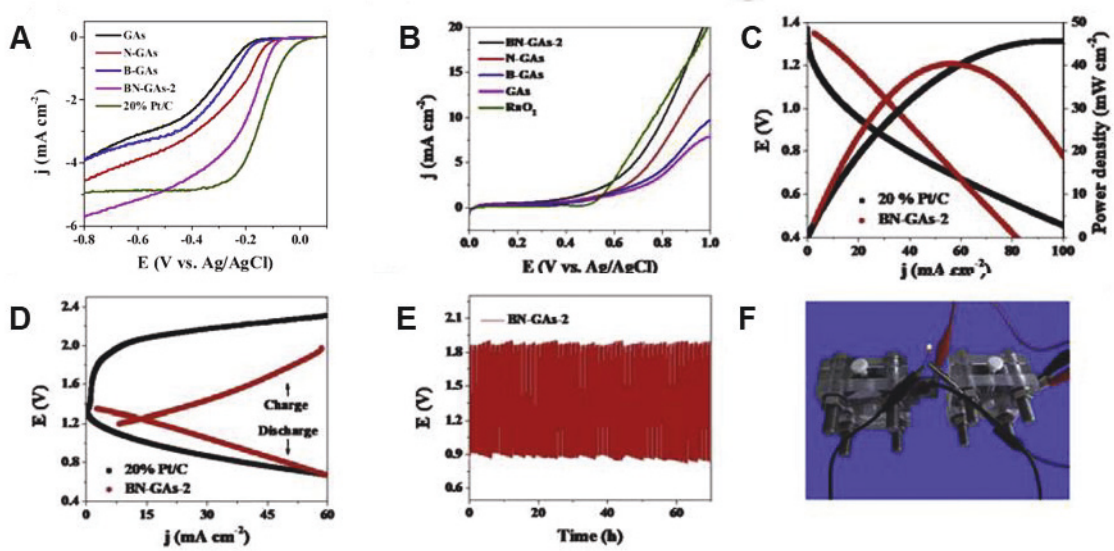

Figure 2.43. A) ORR and B) OER polarization curves in O_2-saturated 0.1 M KOH with a scan rate of 10 mV s^{-1}. C) Discharge polarization curves and power density of zinc-air batteries. D) Charge and discharge polarization curves of the zinc-air batteries. E) Cycling performance at a current density of 20 mA cm^{-2}. F) A LED (≈3.0 V) powered by two zinc-air batteries with BN-GAs-2 catalysts as air cathodes. [132]

Besides B-C species, B-N bonding is also reported to enhance the electrocatalytic activities of B,N co-doped C [133, 134]. Baik et al. reported that B-N bond combined with O-C bond in the carbon network enhanced 4-electron ORR [133]. By computing the Gibbs free energies using DFT for porous carbon with O-B-C and O-N-B-C bonds (PC-OBC and PC-ONBC), a preferred ORR with the 4-electron pathway was confirmed in BN doped PC-ONBC structure (Figure 2.44A). Li et al. also reported that B-N configurations in carbon are desirable for ORR catalysis, especially the B-

N_3 configurations [134]. DFT calculations revealed that B sites in the B-N_3 configurations served as favorable *OOH and *OH adsorption sites, thus accelerating the electrocatalyst reaction (Figure 2.44B).

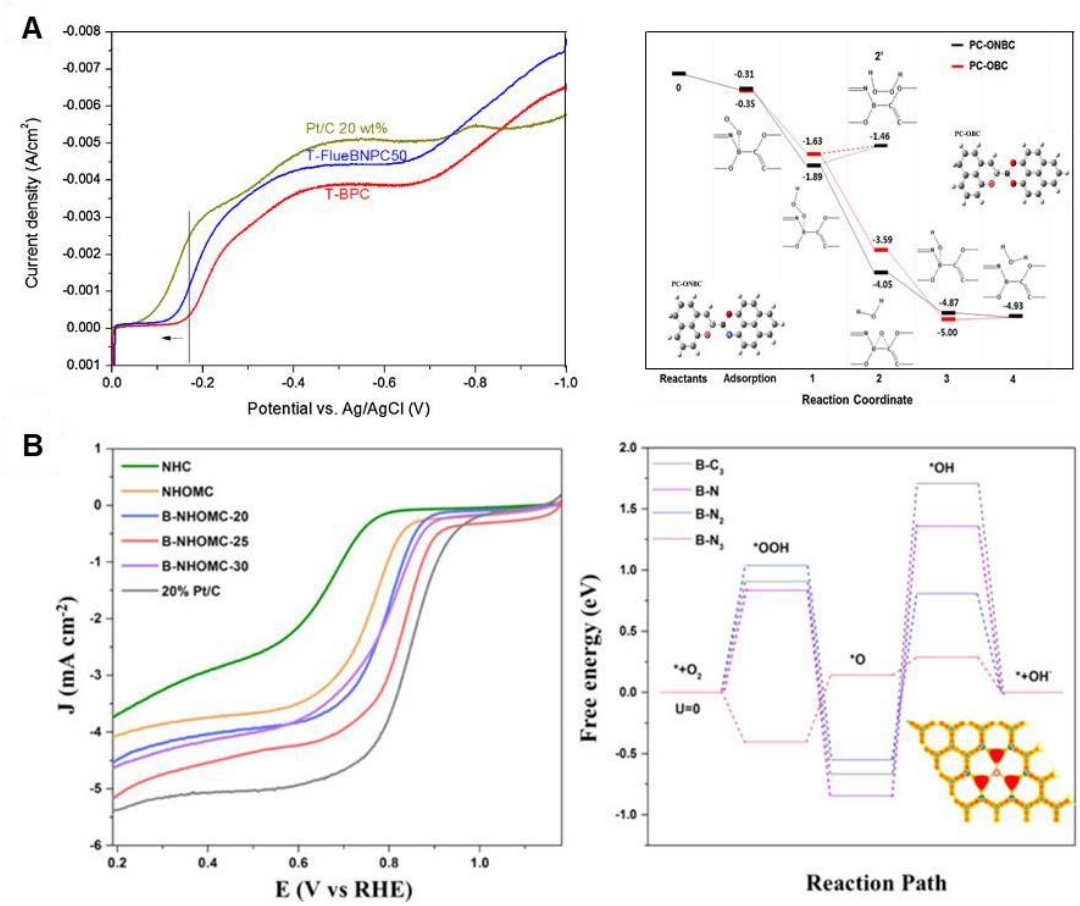

Figure 2.44. A) ORR polarization curves of T-BPC, T-FlueBNPC50, and Pt/C 20 wt% and Gibbs free energy diagram for PC-OBC and PC (units of energy: eV). [133] B) ORR polarization curves of NHC, NHOMC, B-NHOMC-20, B-NHOMC-25, B-NHOMC-30, and 20% Pt/C and free-energy diagrams for B-C and various B-N configurations. [134]

Therefore, B, N co-doped carbons (B,N@Cs), as metal-free ternary materials, have

shown great potential for ORR and OER [127, 129, 135-145].

2.4.5 MOF-derived B,N,metal-doped carbon nanostructures

There have been reports on synthesizing MOF-derived B,N-doped carbon nanostructures by directly pyrolyzing B,N-containing MOF (e.g., boron imidazolate framework (BIF)-82 [146] and BIF-1S [147]) and the mixture of MOFs with B-containing substances [124, 148-156]. For example, Liu et al. obtained Co contained N,B-co-doped interconnected graphitic carbon and carbon nanotube materials (Co/NBC) by direct pyrolysis of (BIF)-82-Co under N_2 (Figure 2.45A) [146]. Directly pyrolyzing B,N-containing MOF provides an easy and promising way toward the fabrication of B,N co-doped C nanomaterials. However, the as-obtained Co/NBC did not maintain the morphology of the (BIF)-82-Co precursor, so the selection of the precursor and the pyrolysis conditions need to be more finely controlled to obtain the desired morphology and structure. On the other hand, to get a reasonably homogeneous distribution of B, aqueous solutions were usually employed to mix MOFs with soluble B-containing precursors. However, most of these B,N co-doped C nanomaterials displayed collapsed structures, because MOFs are sensitive to water [150-156]. As such, B,N co-doped C nanomaterials obtained after pyrolysis exhibited irregular morphologies, as shown in Figure 2.45B [152]. Furthermore, the synthesis of B,N co-doped C by substitution of B atoms into ZIF-8-derived N-doped C can effectively avoid the destruction of morphology, but the doping efficiency of B is limited (Figure 2.45C) [149].

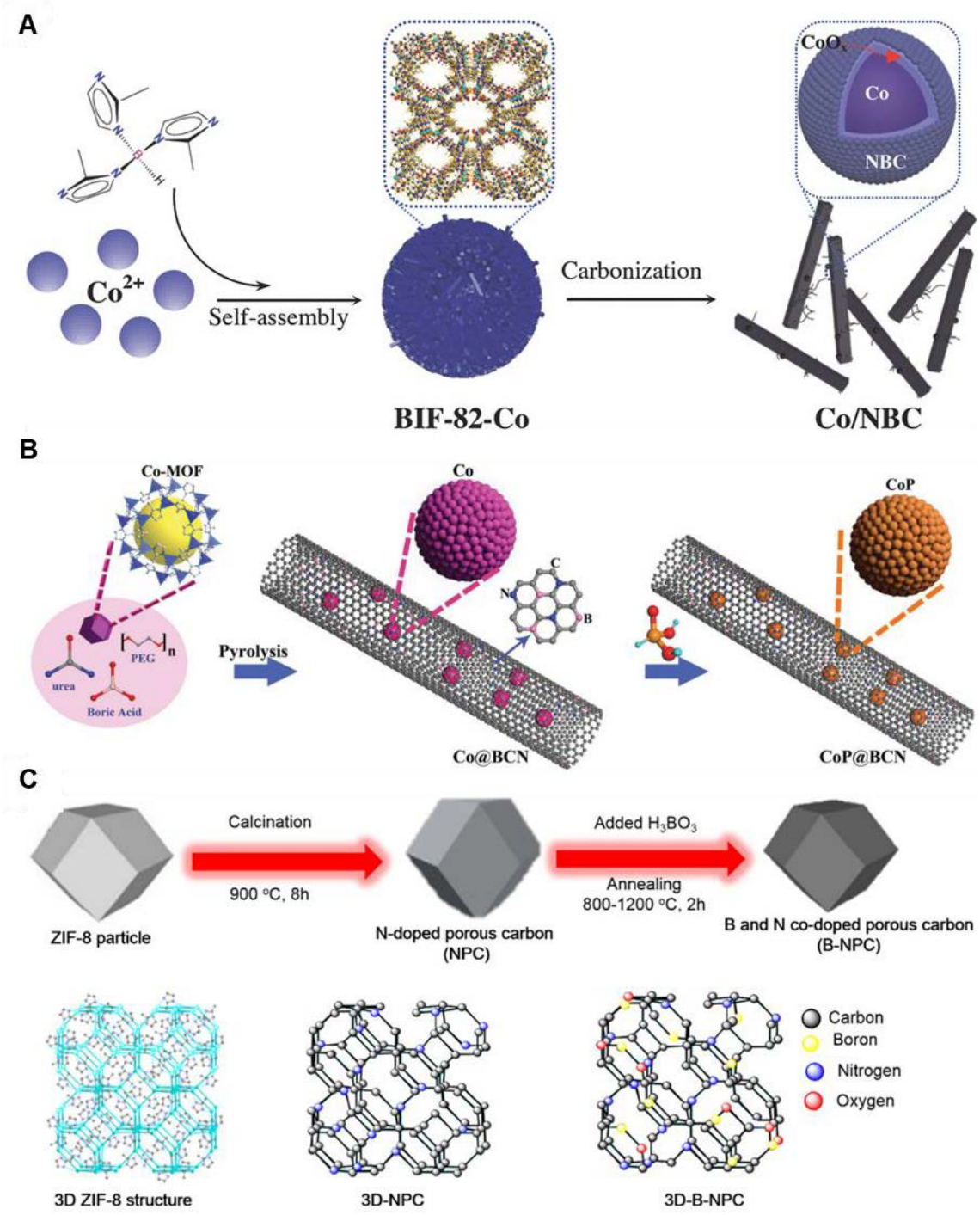

Figure 2.45. Synthetic schemes of MOF-derived B,N co-doped C. [146, 149, 152]

B,N co-doped C nanomaterials derived from MOFs have been used for ORR and OER. MOF-derived B,N co-doped C as ORR, and OER electrocatalysts can be divided further into two categories: metal-free B,N co-doped C materials and non-noble-metal-decorated

B,N co-doped C materials. Qian et al. reported B,N co-doped and metal-free porous carbon as ORR and OER electrocatalysts by pyrolysis of Zn-MOF (MC-BIF-1S) with B,N, and C in ligands under H_2/Ar (Figure 2.46A) [147]. The SEM image showed a cracked nanostructure with a porous texture (Figure 2.46B). N_2 sorption isotherms of Type I shape with small hysteresis revealed that these BNPCs were mainly microporous (Figure 2.46C). Electrochemical evaluations showed that BNPC-1100 with high surface area and high pyridinic N content exhibited high ORR and OER activities (Figure 2.46D,E).

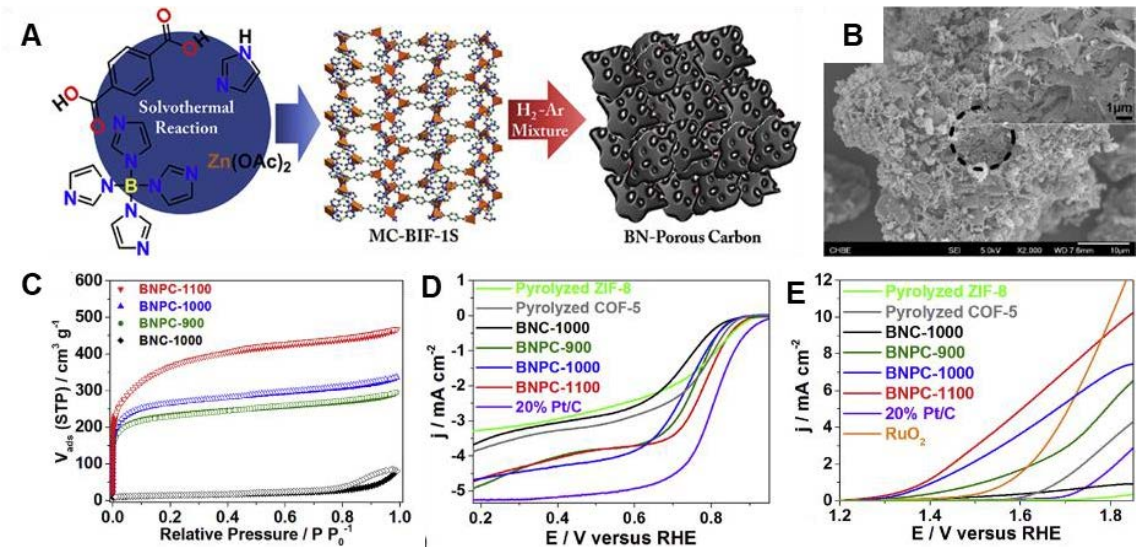

Figure 2.46. A) The synthetic scheme and B) SEM images of BNPC-1100, C) N_2 sorption isotherms, D) ORR, and E) OER polarization curves of BNPCs. [147]

Compared with the development of metal-free carbon materials for ORR and OER, metal or metallic compound/carbon hybrid materials have received more attention. Carbon, especially heteroatom-doped carbon, can regulate the electronic structure and prevent the

aggregation of metal nanoparticles as a support for metal particles through the strong interaction between them, thus enhancing the activity of catalysts [157, 158]. At the same time, metal nanoparticles can also increase the degree of graphitization, enhancing electrical conductivity and improving the protective effect of carbon on metal nanoparticles [159]. Enlightened by these results, Ahsan et al. developed low-dimensional nanohybrids formed by ZrO_2 nanoparticles and B,N co-doped carbon (BCN/ZrO_2) from UiO-66 (Figure 2.47A) [155]. After pyrolysis with boric acid and urea, ZrO_2 nanoparticles were embedded in the BCN nanoplatforms (Figure 2.47B,C). The overvoltage between OER and ORR ($\Delta E = \eta_{10} - E_{1/2}$) of 0.72 V in 0.1 M KOH reflected the excellent bifunctional OER/ORR activity (Figure 2.47D). As shown in Figure 2.47E, the doping of B and N played an important role in interfacial electronic polarization. As a result, the positively charged Zr would enhance the adsorption of OH^-, which is beneficial to OER, while the polarized electron cloud is beneficial to ORR.

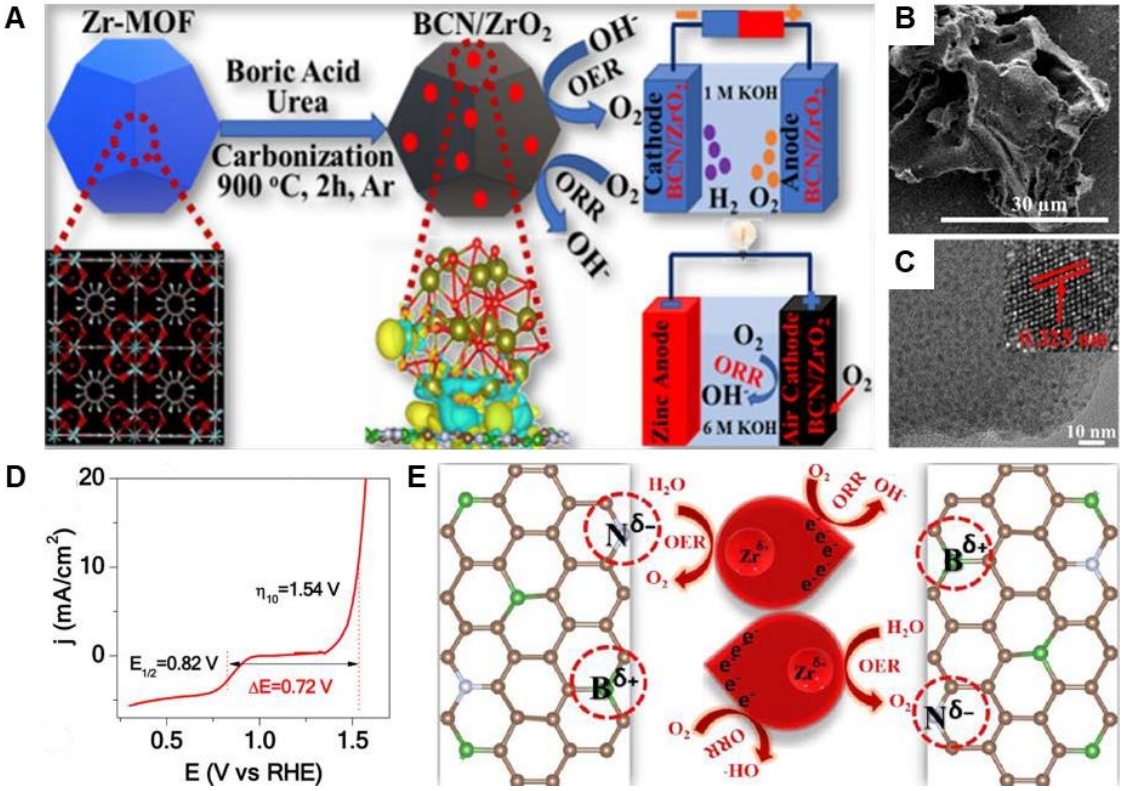

Figure 2.47. A) The synthetic scheme, B) SEM image, C) TEM image, D) bifunctional catalytic activity, and E) the scheme of the plausible OER and ORR reaction mechanism of BCN/ZrO_2 nanohybrids according to the electronic polarization at the interface. [155]

2.5 Summary and gap identification

As described above, various strategies to build nanoreactors as electrocatalysts from MOFs have been developed. Meanwhile, nanoreactor effects on catalytic performance have been investigated. Also, a plethora of B,N@C nanomaterials as ORR and OER electrocatalysts have been prepared, including metal-free B,N co-doped C materials and non-noble-metal-decorated B,N co-doped C materials. These efforts partially solved the problems facing metal-air batteries. There are still some key problems to be solved before

BCN-based electrocatalysts can be applied in practical cases. They are summarized as follows:

a) Poor control over morphology, particularly when involving boron-containing precursors, results in the crack of the B,N@C framework, thus hindering the exposure of the active sites and the mass transfer in reactions;

b) Most studies reported so far have focused on tuning chemical compositions and nanostructures to improve the efficacy and quantity of active sites. However, mass transfer, a significant factor affecting the catalytic process, has been less studied.

c) Synthetic strategies toward a series of nanoreactors with different porous structures but similar active sites in efficacy and quantity is far less developed, which results in a lack of systematic discussion on the relationship between mass transfer and catalytic activity.

2.6 Aims and objectives

This Ph.D. project aims to obtain desired B,N co-doped C nanoreactors for ORR and OER by molecular level design and to fabricate structure featuring abundant active sites and enhanced mass transfer.

The objectives of this research project include:

a) Custom build and characterize B,N co-doped C nanoreactors from MOFs with

different porous structures.

b) Investigate the structure-activity relationship of the nanoreactor on the electrocatalytic ORR.

c) Reveal the impact of pore sizes on the mass transfer, which will help with nano-engineering design and synthesis.

d) Study the structure-activity relationship of nanoreactor in electrocatalytic OER and selective electrooxidation of benzyl alcohol.

Chapter 3 General experimental details

3.1 Chemicals

Zinc nitrate hexahydrate ($Zn(NO_3)_2 \cdot 6H_2O$), cobalt nitrate hexahydrate ($Co(NO_3)_2 \cdot 6H_2O$), potassium hydroxide (KOH), boric acid ($B(OH)_3$), cyclohexane, methanol (MeOH), ethanol (EtOH), and dimethylformamide (DMF) were purchased from Sinopharm Chemical Reagent Co., Ltd. 2-methylimidazole (2-MIM) was purchased from Aladdin Reagent. Ammonia borane (AB, NH_3BH_3) was purchased from Macklin Co., Ltd. Commercial 20 wt% Pt/C was purchased from Alfa Aesar Chemical Reagent Co., Ltd. Nafion (5 wt %) was purchased from Sigma-Aldrich. All chemicals were of analytical grade and used without further purification. Deionized water was used for all experiments.

3.2 Instruments and techniques

3.2.1 Transmission electron microscope

Transmission electron microscopy (TEM) is a microscopy technique which is useful to determine the morphology of nanomaterials. Differences of materials in composition or thickness will provide different image contrast at lower magnifications. TEM observations were carried out on a Hitachi HT7700 TEM system operated at 100 kV. A high-resolution transmission electron microscopy (HRTEM) equipped with energy-dispersive X-ray spectra (EDS) provides major analytical results by imaging a sample at

nanoscale and determining chemical elements in a sample. The aberration-corrected high-angle annular dark-field scanning transmission electron microscopy (HAADF-STEM) measurements were performed on JEM-ARM200F (JOEL), which was also used to collect energy-dispersive X-ray spectra (EDS).

Figure 3.1. Hitachi HT 7700.

Figure 3.2. JEM-ARM200F

3.2.2 Scanning electron microscope

Field emission scanning electron microscope (SEM) can provide high-quality and low-voltage images of a minor area of a sample. The morphologies were observed using a

JSM-7900F field emission SEM at an accelerating voltage of 2 kV.

Figure 3.3. JSM-7900F

3.2.3 X-ray diffraction

Powder X-ray diffraction (PXRD) is a technique used for analysing average bulk phase of a crystalline sample. Wide-angle PXRD patterns were obtained on a Rigaku SmartLab diffractometer with Cu Kα radiation (λ = 1.5418 Å) at a scanning rate of 20°/min.

Figure 3.4. Rigaku SmartLab.

3.2.4 Nitrogen adsorption-desorption

Nitrogen adsorption‐desorption is a standard way of characterizing the porosity of carbon nanomaterials. Nitrogen adsorption-desorption isotherms were collected on Micromeritcs ASAP 2460. The Brunauer–Emmett–Teller (BET) method was used to analyze the specific surface areas. The pore size distributions were determined using the non-local density functional theory method.

Figure 3.5. Micromeritcs ASAP 2460.

3.2.5 X-ray photoelectron spectroscopy

X-ray photoelectron spectroscopy (XPS) is a technique for measuring a material's surface chemistry, including elemental composition and electronic state of the atoms. XPS analysis was conducted on Thermo Scientific K-Alpha apparatus with monochrome Al K_{α} as the excitation light source. All the binding energies were referenced to C 1s standard peak at 284.8 eV.

Figure 3.6. Thermo Scientific K-Alpha.

3.2.6 Electrochemical measurements for ORR

A PARSTAT 3000A-DX workstation was used to record the electrochemical response at applied potential. The rotation ring disk electrode (RRDE) measurements were carried out at room temperature in a typical three-electrode system. An Ag/AgCl electrode (saturated KCl) was used as the reference electrode. An RRDE assembly consisting of a glassy carbon rotation disk electrode (s = 0.2475 cm^2) and a Pt ring (s = 0.1866 cm^2) was used with a theoretical collection efficiency of 37%. To prepare a working electrode with a catalyst layer, 5 mg of the as-prepared nonmetal doped carbon catalyst was mixed with 175 µL of ethanol and 47.5 µL of Nafion 117 solution (5%, Sigma-Aldrich), and sonicated for 20 mins to get a homogeneous catalyst ink. 7 µL of the ink was pipetted onto a glassy carbon disk and dried in a vacuum environment.

The kinetic current density (J_K) was calculated from the Koutecky-Le1vich equation:

$$\frac{1}{J}=\frac{1}{J_L}+\frac{1}{J_K} \qquad 1$$

where J is the measured current density, J_K and J_L are the kinetic and limiting current

densities, respectively.

The transferred electron number (n) and H_2O_2 (H_2O_2%) selectivity were calculated based on the disk current (I_d) for O_2 reduction and ring current (I_r) for H_2O_2 oxidation at the Pt ring from RRDE using the following equation.

$$n=\frac{4I_d}{I_d+I_r/N} \quad (2)$$

$$H_2O_2\%=200\frac{I_r/N}{I_d+I_r/N} \quad (3)$$

Figure 3.7. PARSTAT 3000A-DX.

3.2.7 Electrochemical measurements for OER and benzyl alcohol electrooxidation

An electrochemical work station (CHI 760E) was used to record the electrochemical response at applied potential. The measurements were carried out at room temperature in an H-type electrolytic cell with a typical three-electrode system. The as-prepared electrocatalysts were used as the working electrodes, a Pt foil as the counter electrode, and An Ag/AgCl electrode (saturated KCl) as reference electrode. To prepare a working electrode, the catalyst (3 mg) and Ketjen Black (0.6 mg) was dispersed in an ethanol/Nafion solution (115 μL, V/V = 20:3) by sonication. The resulting suspension

was loaded onto carbon paper (1 cm × 1 cm) and dried under an infrared lamp. The OER measurements were conducted in 1.0 M KOH solution, while the measurements of benzyl alcohol electrooxidation were conducted in 1.0 M KOH solution in the presence of 0.02 M benzyl alcohol. Linear sweep voltammetry (LSV) corrected by iR-compensation was performed.

3.2.8 Finite-element simulation methods

The finite element analysis (FEA) simulation was conducted using COMSOL Multiphysics. The simulation was implemented in a 2D mode. According to the experimental data, the model of the micropore-dominated materials was constructed as a hexagon with 80 nm on a side with microchannels of 0.9 nm; the model of trimodal-porous materials was plotted with microchannels of 0.9 nm, mesochannels of 7 nm, and cavities of 30 nm inside the hexagon; the model of the macropore-dominated hollow materials was constructed with mesochannels of 7 nm in the hexagonal shell about 10 nm thick and 80 nm on an external side. These models could effectively simplify the structures of B,N@Cs while maintaining their structural properties. A rectangular region with a width of 6000 nm and a height of 6000 nm was filled with water, which served as the calculated domain. The water was poured from the left boundary, and outflowed from right boundary. The inflow velocity was set to 0.25 m s^{-1} at the entrance. The flow field was done on the “Laminar Flow” module. The flow field was solved by the Navier–Stokes equations:

$$\nabla \cdot u=0 \quad (4)$$

$$\rho(u\cdot\nabla)u=\nabla\cdot[-pI+\mu(\nabla u+(\nabla u)^{T})]+F \quad (5)$$

Where u, ρ, p, and F represent the flow velocity, fluid density, pressure, and volume force vector, respectively.

Chapter 4 Fabrication of hierarchical porous B,N@C nanocages through confined etching to boost ORR

4.1 Background

Metal-organic frameworks (MOFs), which consist of metal nodes and organic ligands, are desirable precursors and templates for metal/carbon-based nanostructures used in diverse applications including energy storage and conversion [160-162]. Zeolite imidazole frameworks (ZIFs) are a subclass of MOFs, featuring high N content, large surface areas, and ordered porous textures [163]. Because of these special features, ZIFs can act as ideal sacrificial templates and precursors to generate porous nitrogen-doped carbons (N@Cs) used in electrochemical energy storage and conversion [16, 164, 165]. However, the direct pyrolysis of ZIFs at high temperatures often leads to micropore-dominated structures with poor conductivity, which limits their performance [166-168]. The structures and functions of ZIFs-derived N@Cs could be tuned by controlling the precursor compositions via introducing templates, pore-forming agents, and dopants [46, 169].

Dual, ternary, and quaternary heteroatom-doping (N/B, N/P, N/S, N/O, N/B/P, N/S/P, N/B/S/P, etc.) can dramatically improve the performance of carbon in many applications

[120-124]. Among these heteroatoms, N and B are of particular interest as co-dopant since they are next to carbon in the periodic table and are of similar atomic sizes. The electronegativity of B (2.04) and N (3.04) is lower and higher than that of C (2.55), respectively. B can further substitute C in N@C lattice and lead to a synergistic effect induced by the pairing and/or long-range coupling, which alters the charge density and consequently chemical properties [126-129]. B, N co-doped carbons (B,N@Cs), as metal-free ternary materials, have shown great potential for energy storage and conversion devices [127, 129, 135-145].

There have been reports on synthesizing MOF-derived B-containing carbon nanostructures by directly pyrolyzing B-containing MOF (e.g., boron imidazolate framework (BIF)-82 [146] and BIF-1S [147]) or the mixture of MOFs with B-containing substances [124, 148-156]. However, most of these B-containing carbon nanomaterials displayed collapsed structures of MOFs, which is because to get the reasonably homogeneous distribution of B elements, aqueous solutions were employed to mix MOFs with B-containing precursors, and MOFs are sensitive to water. As such, B-containing carbon nanomaterials obtained via pyrolysis exhibited irregular morphologies [150-156]. Furthermore, most of these resultant B-containing carbon nanomaterials possessed predominantly microporous structures [124, 149-154]. The efficiency of mass transport and reactant diffusion are quite restricted by the micropores. Typically, micropores (< 2 nm) lead to high surface areas and large numbers of active sites; mesopores (2–50 nm)

contribute to local accessibility through a shortened diffusion length; macropores (> 50 nm) provide an interconnected and stable framework with superior mass long-range transfer [169, 170]. Therefore, it is desired to have structures with micro-, meso-, and macro-pores. To maximize the availability of interior active sites and facilitate the diffusion of substrates and products, hollow MOFs such as nanocages, yolk-shells, and double shells will be quite attractive and yet challenging [100, 171]. Moreover, the doping amounts of B in the reported ZIF-8 derived B,N@C are rather low (usually < 6 at.%) [124, 146-150, 152, 153, 155].

Herein, I employed a host-guest chemical strategy to immobilize boron species inside the cavities of a ZIF and achieved a high doping content of B (15 at.%). It is known that small organic and inorganic compounds (e.g., CH_4 [172], N_2 [172], $FeCl_3$ [173], $PdCl_2$ [174], $CuCl_2$ [174], and thiourea [175, 176]) can be introduced into ZIF-8s through their channels. Occasionally, guest molecules (Rhodamine 6G) larger than the pore sizes of ZIF-8 were successfully incorporated into ZIF-8 when ligand dissociation occurred during the incorporating process [177]. In this study, during the integrated process of double-solvent impregnation (DSI) and nanoconfined-etching (Error! Reference source n ot found.), guest molecules such as ammonia borane (AB) and boric acid (BA) dispersed into the pores of the ZIF-8 act as B source and also as an etching agent to *in-situ* enlarge the pores of ZIF-8 hosts. The trapped AB or BA was then thermally decomposed, leading to B,N@C containing micro/meso/macro multimodal porosities. The combination of the

unique hierarchical structure and the synergetic effect between the heteroatoms renders the resulting B,N@C an ideal catalyst for electrochemical oxygen reduction reaction in alkaline electrolytes (half-wave potentials as high as 895 mV). This work reveals a novel strategy to achieve hierarchical porous B,N@C catalysts, i.e., impregnating small guest molecules whose aqueous solutions are acidic and etching MOFs which are unstable under acidic conditions.

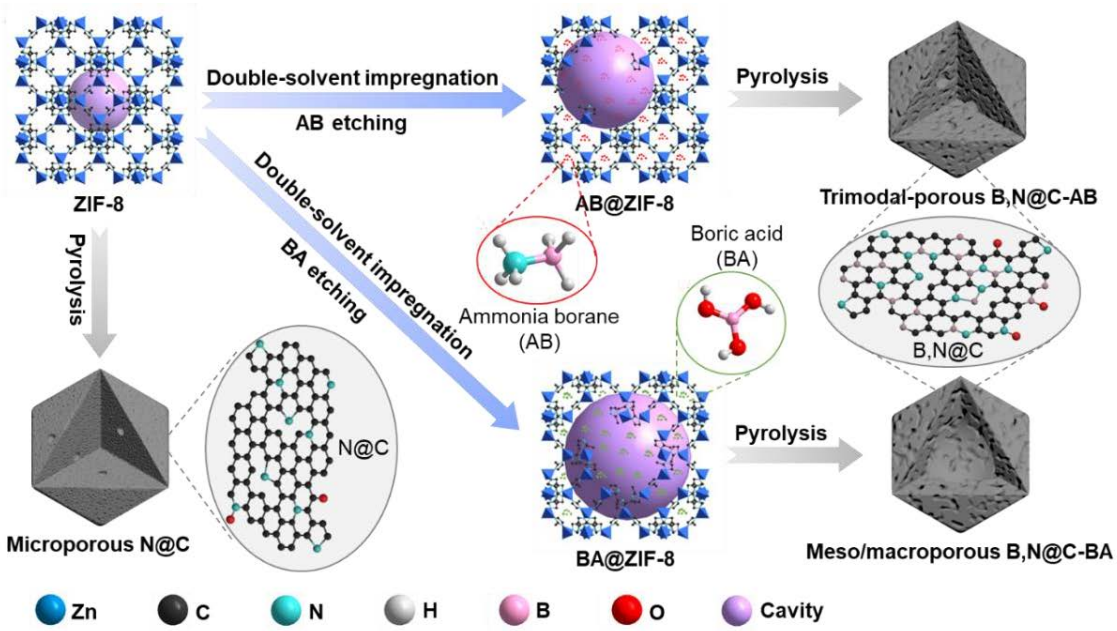

Figure 4.1. Schematic illustration of the fabrication of B,N@C nanocages.

4.2 Experimental

4.2.1 Synthesis of ZIF-8

$Zn(NO_3)_2 \cdot 6H_2O$ (0.89 g) and 2-MIM (1.970 g) were first dissolved in 30 mL and 20 mL methanol, respectively. Then 2-MIM methanol solution was added to $Zn(NO_3)_2 \cdot 6H_2O$

methanol solution, followed up with stirring for 24 h. The resultant white precipitate was obtained, washed, and dried for further use.

4.2.2 Synthesis of AB@ZIF-8 and BA@ZIF-8 composites

100 mg of the as-prepared ZIF-8 powders were dispersed in 20 mL of cyclohexane assisted by ultrasonication. Then 100 μL of ammonia borane aqueous solution (100 mg/mL) was added into ZIF-8 dispersion dropwise. The AB@ZIF-8 composite was collected by centrifugation after impregnation for 3 h. Similarly, 100 μL of boric acid aqueous solution (51 mg/mL) was used to prepare BA@ZIF-8. To introduce the same amount of B into ZIF-8 hosts, the impregnation of AB was repeated 4 times.

4.2.3 Synthesis of N@C, B,N@C-AB, and B,N@C-BA

To obtain N@C and B,N@C, 300 mg of the ZIF-8, BA@ZIF-8, and AB@ZIF-8 were heated at 1,000 °C for 2 h with a ramping rate of 5 °C/min under N_2 atmosphere, respectively.

4.3 Results and discussion

4.3.1 Synthesis and characterization of B@ZIF-8 composites via an integrated double-solvent impregnation and nanocofined-etching method

Figure 4.2a and Figure 4.2b present TEM and SEM images of the ZIF-8 host, respectively. The rhombic dodecahedral host has an average particle size of 150 nm, with a PXRD

pattern matching the simulated pattern of ZIF-8 single-crystal (Figure 4.2c). To prepare B@ZIF-8 hybrids, AB or BA was applied as guest molecules to embed boron species into ZIFs by a DSI method. Given the relatively large spherical pore size of the ZIF-8 host (cavity diameter ~ 11.6 Å and window (channel) diameter ~ 3.4 Å) [178, 179], both AB (size ≤ 3.2 Å) and BA (size ≤ 3.3 Å) can be confined within the pores of ZIF-8 (Figure 4.3). BA ($B(OH)_3$) is one of the most used molecules for B doping [180-184]. However, it has limited solubility in water (0.9 mol/L), which results in limited loading efficiency [185, 186]. In comparison, AB (NH_3BH_3), the simplest B-N compound has a high solubility in many solvents [187]. The solubility of AB in water is 11.4 mol/L [188], nearly 13 times that of BA. Therefore, to introduce 0.32 mmol of B into ZIF-8 hosts in this study, the impregnation process using BA aqueous solution (0.8 mol/L) was repeated four times, while one impregnation was sufficient using AB aqueous solution (3.2 mol/L).

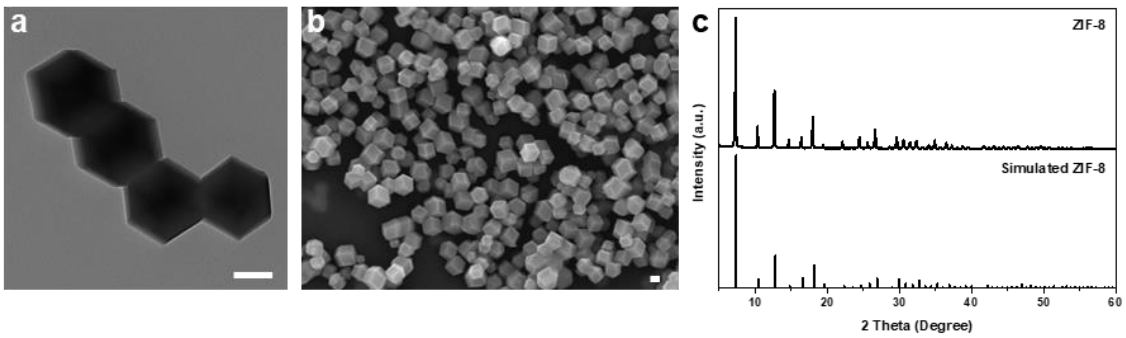

Figure 4.2. (a) TEM image, (b) SEM image of ZIF-8, (c) XRD patterns of ZIF-8 and simulated ZIF-8. Scale bars are 100 nm.

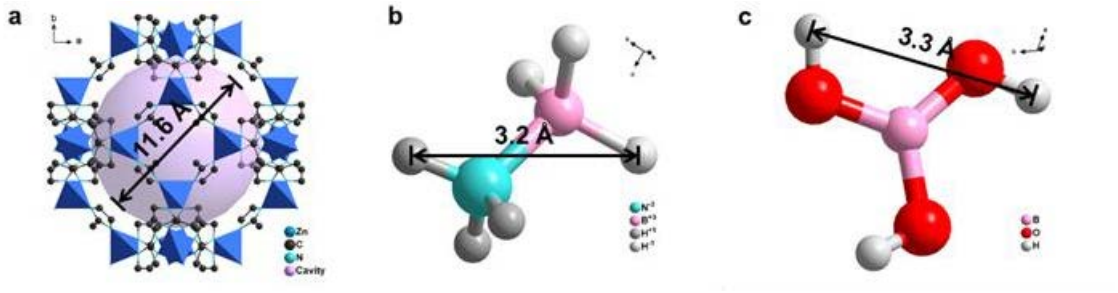

Figure 4.3. Structure and sizes of (a) ZIF-8, (b) AB, and (c) BA.

When AB or BA aqueous solution was added dropwise into cyclohexane suspension of ZIF-8, the dispersed aqueous droplets containing the guest molecules could completely diffuse into the hydrophilic pores in ZIF, rather than deposit on the outer surface of ZIF-8 hosts, which is based on the immiscibility between water and cyclohexane. As a result, the morphologies of B@ZIF-8 composites stay like that of ZIF-8, as shown by SEM images (Figure 4.4a,b). AB@ZIF-8 and BA@ZIF-8 composites also display PXRD patterns similar to that of the parent ZIF-8 (Figure 4.4c). This indicates that there are no appreciable structural changes in ZIF-8 upon the encapsulation of guest molecules in the pores of the host. No diffractions were detected for AB and BA in the B@ZIF-8 composite, indicating that B species are distributed in a disordered way. Nevertheless, because of its sensitivity to the aqueous solution, especially acidic solution, the host ZIF-8, which is predominantly microporous, was etched and formed structures with larger pores after impregnation, confirmed by TEM images of AB@ZIF-8 and BA@ZIF-8 composites (Figure 4.5).

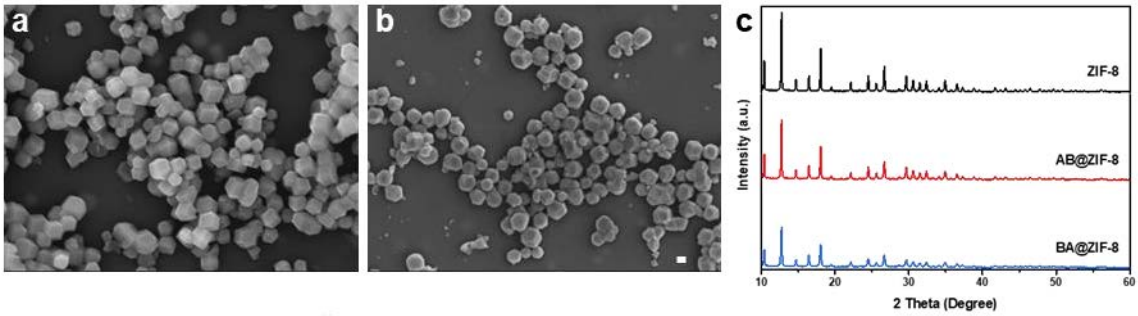

Figure 4.4. SEM images of (a) AB@ZIF-8 and (b) BA@ZIF-8 composites. (c) XRD patterns of ZIF-8, AB@ZIF-8, and BA@ZIF-8. Scale bars are 100 nm.

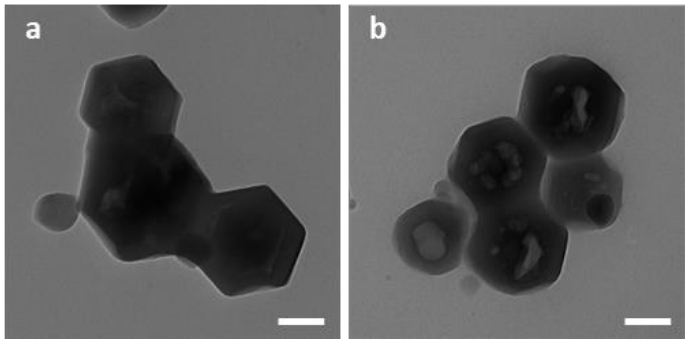

Figure 4.5. TEM images of (a) AB@ZIF-8 and (b) BA@ZIF-8. All scale bars are 100 nm.

AB hydrolyzes slowly in a water-based solution following the equation $NH_3BH_3 + 4H_2O \rightarrow NH_4^+ + B(OH)_4^- + 3H_2$. After three hours in the water, AB remained quite stable without obvious hydrolysis when checked using solution ^{11}B nuclear magnetic resonance (NMR) (Figure 4.6a). Fourier transform infrared (FTIR) spectra (Figure 4.6b,c) also show that AB and BA were successfully loaded into ZIF-8 because the FTIR spectra of AB@ZIF-8 and BA@ZF-8 exhibit multiple IR bands which are combinations of those observed in the ZIF-8 and the AB or BA spectra. Some new bands of AB@ZIF-8 at

around 3,307 and 2,323 cm^{-1} could be attributed to the N–H stretching and B–H stretching modes, respectively [189]. Other characteristic IR bands of AB, including N–H deformation at 1,602 and 1,377 cm^{-1}, B–H deformation at 1,159 and 1,062 cm^{-1}, B–N stretching at 785 cm^{-1}, and a combination of B–H and N–H deformation at 728 cm^{-1} [189], overlap with the characteristic peaks of ZIF-8. The new broad peak of BA@ZIF-8 at around 3,254 cm^{-1} could be attributed to the stretching vibration of O–H bond [190]. Other characteristic IR bands of BA, including B–O stretching at 1,472 cm^{-1}, B–O–H bending at 1,196 cm^{-1}, O–H stretching at 721 cm^{-1} [190], overlap with the characteristic peaks of ZIF-8. So, it is believed that AB and BA have diffused into the pores of ZIF-8.

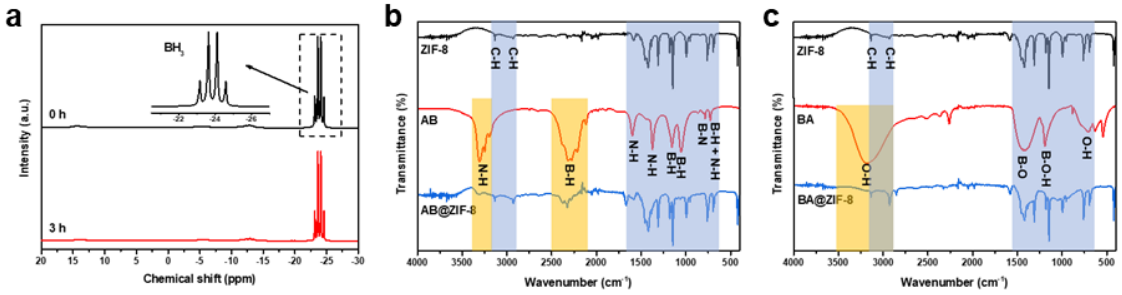

Figure 4.6. (a) ^{11}B NMR spectra of AB in D_2O solution, (b) FTIR spectra of ZIF-8, AB and AB@ZIF-8, (c) FTIR spectra of ZIF-8, BA and BA@ZIF-8.

EDS mapping analysis (Figure 4.7) of the AB@ZIF-8 sample shows a concentration of B and O inside the pores of ZIF-8, most likely associated with the B–O species produced in the process of AB hydrolysis. Solid-state ^{11}B NMR spectra were collected (Figure 4.8) to identify the B species presented in the AB@ZIF-8 and BA@ZIF-8 composites. The signal at 15.7 ppm for BA@ZIF-8 composite can be ascribed to BO_3 group [191, 192],

while the one at 1.8 ppm is related to BO_4 [191, 193], produced by the equilibrium $B(OH)_3 + H_2O \rightleftharpoons B(OH)_4^- + H^+$. The spectrum of the AB@ZIF-8 composite is similar to that of BA@ZIF-8 but features a much weaker peak at −20 ppm, suggesting that AB hydrolyzes predominately to $B(OH)_4^-$. The overall reaction can be written as $NH_3BH_3 + 4H_2O \rightarrow NH_4^+ + B(OH)_4^- + 3H_2$, instead of $NH_3BH_3 + 3H_2O \rightarrow NH_3 + B(OH)_3 + 3H_2$ [188]. Therefore, the fewer protons in the case of AB@ZIF-8 resulted in a milder etching of ZIF-8. This is corroborated by the change in surface area as can be seen in the N_2 adsorption–desorption isotherms (Figure 4.9a), and the specific surface area and pore volume parameters calcutated based on the isotherms are shown in Error! Reference s ource not found.. Compared with the ZIF-8 hosts, both AB@ZIF-8 and BA@ZIF-8 exhibit a decreased surface area. BA@ZIF-8 has the smallest one, which is due to the enlargement of the pores and channels within the ZIF-8 host by BA etching. All three samples show a steep increase in nitrogen uptake at lower p/p_0, indicating a high ratio of micropores. AB@ZIF-8 and BA@ZIF-8 composites show a slight increase in N_2 uptake at a higher p/p_0 ratio ($p/p_0 > 0.95$) with a hysteresis loop, indicating the presence of more mesopores and macropores than in ZIF-8. The corresponding decrease in the nitrogen uptake ($p/p_0 < 0.1$) for AB@ZIF-8 and BA@ZIF-8 indicates that the adsorption occurs mainly into the micropores [194, 195]. Pore size distribution was analyzed based upon non-local density functional theory (NL-DFT) calculations (Figure 4.9b). Consistent with the decreased nitrogen uptake ($p/p_0 < 0.1$), the micropore size decreases from 1.17 nm for ZIF-8 to 1.09 nm for AB@ZIF-8 and 1.00 nm for BA@ZIF-8. The microporous volume

(Figure 4.9c) decreases from 0.69 cm^3/g for ZIF-8 to 0.55 cm^3/g for AB@ZIF-8 and 0.33 cm^3/g for BA@ZIF-8. The decrease in the pore volume of micropores is due to a combined effect of impregnation and etching. Furthermore, AB@ZIF-8 and BA@ZIF-8 have larger meso- and macroporous volumes (0.13 cm^3/g and 0.14 cm^3/g, respectively) than ZIF-8 (0.12 cm^3/g) due to the etching of ZIF-8. Therefore, a decrease in microporous volume, an increase in mesoporous volume, and the corresponding increase in the ratios of meso/macroporous volume to microporous volume (0.18 for ZIF-8, 0.25 for AB@ZIF-8, and 0.43 for BA@ZIF-8) occur after the impregnation and etching process. The microporous surface area (Figure 4.9d) decreases from 2,008.4 cm^2/g for ZIF-8, to 1,466.7 cm^2/g for AB@ZIF-8, and to 849.2 cm^2/g for BA@ZIF-8, while the meso/macroporous surface area increases from 6.9 cm^2/g for ZIF-8, to 11.1 cm^2/g for AB@ZIF-8, and to 22.2 cm^2/g for BA@ZIF-8. Accordingly, the ratio of meso/macroporous to microporous specific surface area (0.003 for ZIF-8, 0.008 for AB@ZIF-8, and 0.026 for BA@ZIF-8) also increases after the impregnation and etching process.

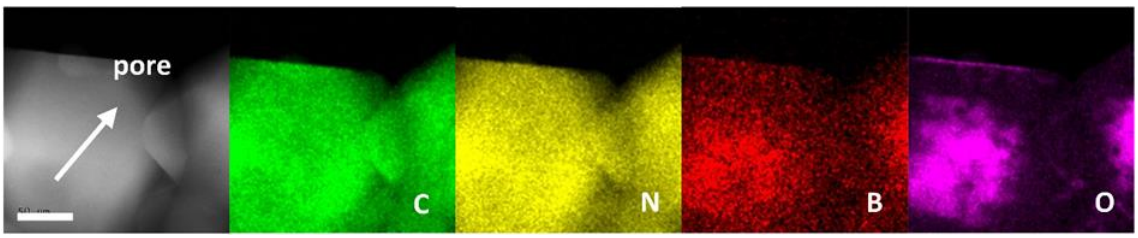

Figure 4.7. EDS mapping of AB@ZIF-8, with a scale bar of 50 nm.

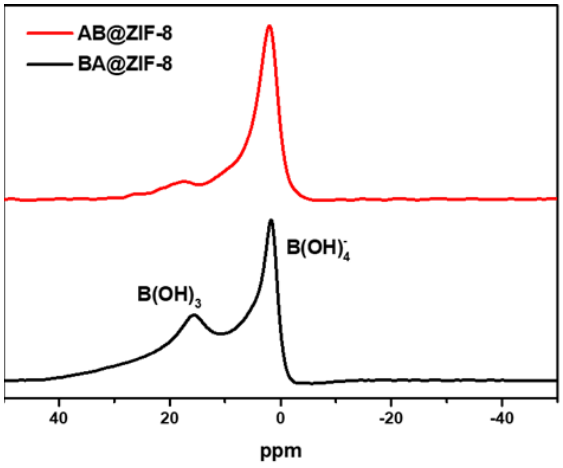

Figure 4.8. ^{11}B solid-state NMR spectra of AB@ZIF-8 and BA@ZIF-8 composites.

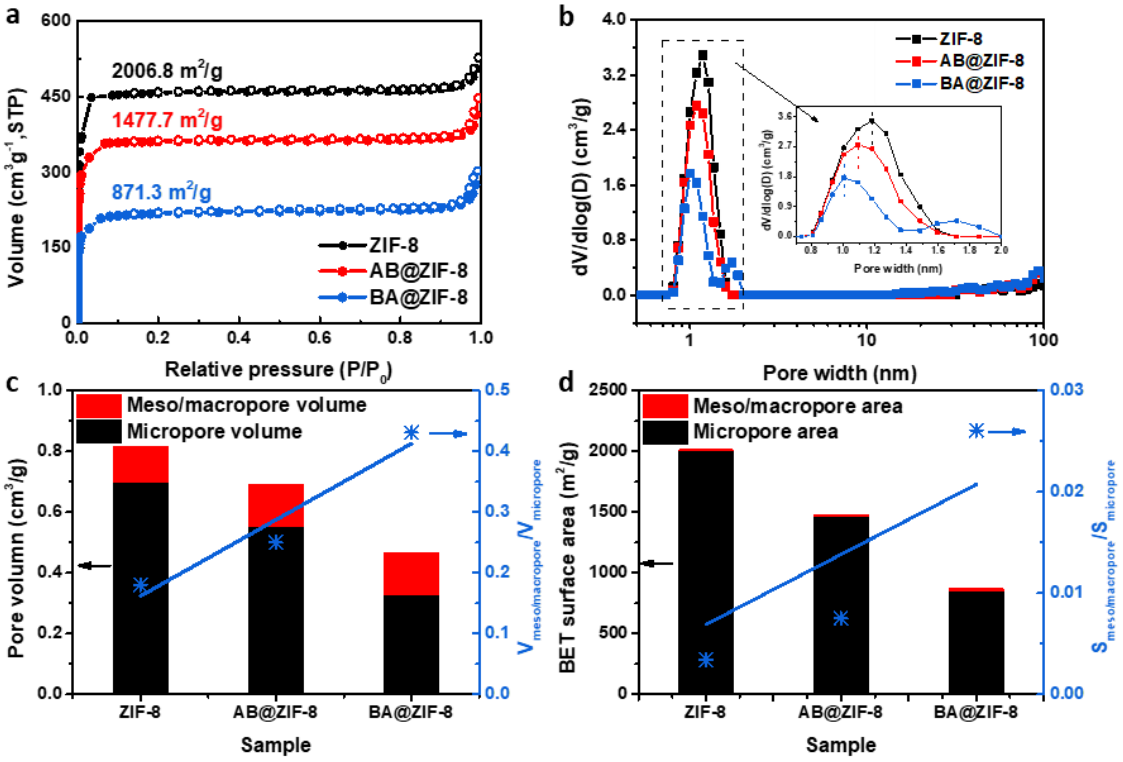

Figure 4.9. (a) N_2 sorption isotherms, (b) pore size distributions, (c) pore volumes and pore volume ratio, (d) BET surface area and the ratios of meso/macroporous to microporous specific surface area of ZIF-8, AB@ZIF-8, and BA@ZIF-8.

Table 4.1. Nitrogen adsorption and desorption parameters of ZIF-8, AB@ZIF-8, and BA@ZIF-8.

Parameters	Catalysts		
	ZIF-8	AB@ZIF-8	BA@ZIF-8
Surface area (m^2/g)	2015.3	1477.7	871.3
Micropore area (m^2/g)	2008.4	1466.7	849.2
Meso/macropore area (m^2/g)	6.9	11.1	22.2
Pore volume (m^3/g)	0.81	0.68	0.47
Micropore volume (m^3/g)	0.69	0.55	0.33
Meso/macropore volume (m^3/g)	0.12	0.13	0.14

4.3.2 Synthesis and characterization of B,N@C-AB and B,N@C-BA

Following the schematics in Figure 4.1, B,N@C catalysts were obtained from the boron species@ZIF-8 (B@ZIF-8) composites. Similar to N@C, B,N@C-AB and B,N@C-BA display only two XRD (Figure 4.10a) peaks but with much higher intensity at 25.1° and 43.3°, which can be assigned to (002) and (100) of the graphitic carbon. The higher intensity demonstrates that B doping significantly improves crystallinity. Raman spectra (Figure 4.10b) can be deconvoluted into four types of carbon configurations at 1,336 (D_1), 1,186 (D_2), 1,501 (D_3), and 1,592 (G) cm^{-1}, respectively. The D_1 band is ascribed to the defects and disorders in the carbon while the G band corresponds to the ordered sp^2 bonded graphite carbon. The lower I_{D1}/I_G value (1.97 and 1.91) of B,N@C than N@C

(2.12), as shown in Figure 4.10c, indicates a higher degree of structural graphitization, which is in agreement with the XRD results.

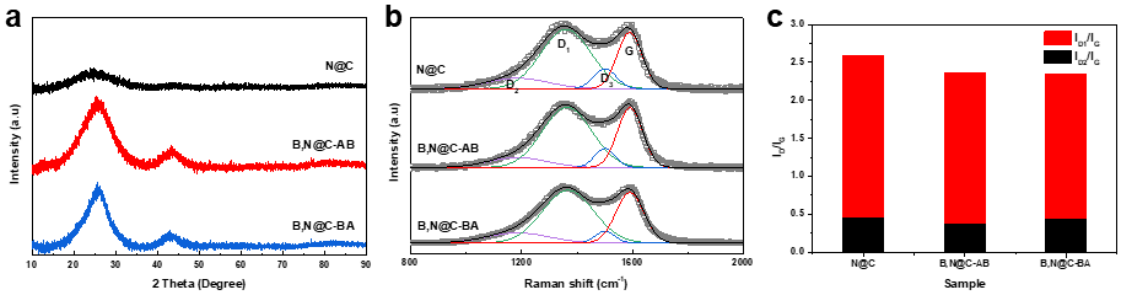

Figure 4.10. (a) XRD patterns, (b) Raman spectra, (c) I_D/I_G values of N@C and B,N@C samples.

The change in microstructure after impregnation has a direct impact on the microstructure of B,N@C obtained by pyrolyzing these ZIF-8 precursors. After pyrolysis in N_2, AB@ZIF-8 and BA@ZIF-8 composite are converted into hierarchical porous carbon nanocages with uniform B and N co-doping, denoted as B,N@C-AB and B,N@C-BA, respectively. SEM characterizations reveal that the resultant materials inherit the morphology of N@C precursors with a mean diameter of 80 nm (Figure 4.11a-c). TEM and aberration corrected HAADF-STEM images reveal that compared with N@C (Figure 4.11d), B,N@C-AB features larger pores in its hierarchical porous structures (Figure 4.11e,g) while B,N@C-BA displays a hollow space inside (Figure 4.11f). These observations clearly indicate a correlation in structure between the B doped ZIF-8 and the resultant B,N@C. The elemental mapping analysis of B,N@C-AB demonstrates that B and N are uniformly distributed in the entire carbon matrix (Figure 4.11h). XPS analyses

were carried out to study the bonding contributions. B contents in B,N@C-AB and B,N@C-BA are 15.0 at.% and 16.9 at.%, respectively (Figure 4.12). The contents of N in B,N@C (14.4 at.% for B,N@C-AB and 13.2 at.% for B,N@C-BA) are much higher than 9.4 at.% in N@C (Figure 4.12). These results demonstrate that B is beneficial in preventing N loss during the heat treatment due to the formation of B–N (Figure 4.13a,b) [196]. High-resolution XPS spectra reveal the existence of multiple types of B dopants in the materials. The B 1s peaks can be deconvoluted into three peaks at 190.6, 191.9, and 192.5 eV, which can be assigned to B–C, B–N, and B–O, respectively (Figure 4.13a). B–B peaks (at 187.8 and 189.1 eV [197]) are invisible for all the B,N@C samples, indicating B atoms are embedded in the carbon skeleton as single atoms. Similarly, the N 1s peak can be deconvoluted into peaks at 397.8, 398.4, 399.5, 400.7, and 402.4 eV, which are associated with N–B, pyridinic (N6), pyrrolic (N5), quaternary N (NQ), and oxidic N atoms, respectively (Figure 4.13b) [152, 153]. Notably, no B–B peak at 187.8 and 189.1 eV [197] and N–N peak at 395.9 eV [198] were observed for both B,N@C and N@C samples, which indicates that B and N atoms are embedded in the carbon skeleton are monodispersed. C 1s spectra display four peaks centered at ca. 284.4, 284.8, 285.9, and 288.5 eV after deconvolution, which can be assigned to C–B, C–C, C–N, and C=O, respectively (Figure 4.13c) [140, 183]. Peak fitting was performed to determine the composition of each type of dopant (Figure 4.13d). For B,N@C-AB, approximately 4.7 at.% B is in the form of B–C, and 4.9 at.% B is in the form of B–N. In comparison, there are slightly more B–C (5.3 at.%) and less B–N (4.1 at.%) in B,N@C-BA. Consistently,

about 2.2 at.% and 1.8 at.% N in B,N@C-AB and B,N@C-BA are in the form of N–B, respectively. These results indicate that there is about twice as many B as N in the B–N motif, meaning a B:N ratio of 2:1. The introduction of B helps with the retainment of N by forming B–N during pyrolysis. The co-existence of B and N breaks the electroneutrality of the carbon matrix due to the electronegativity difference between B, N and C, producing not only C^+ but also B^+ for O_2 adsorption that improves the ORR activity [134, 138, 199].

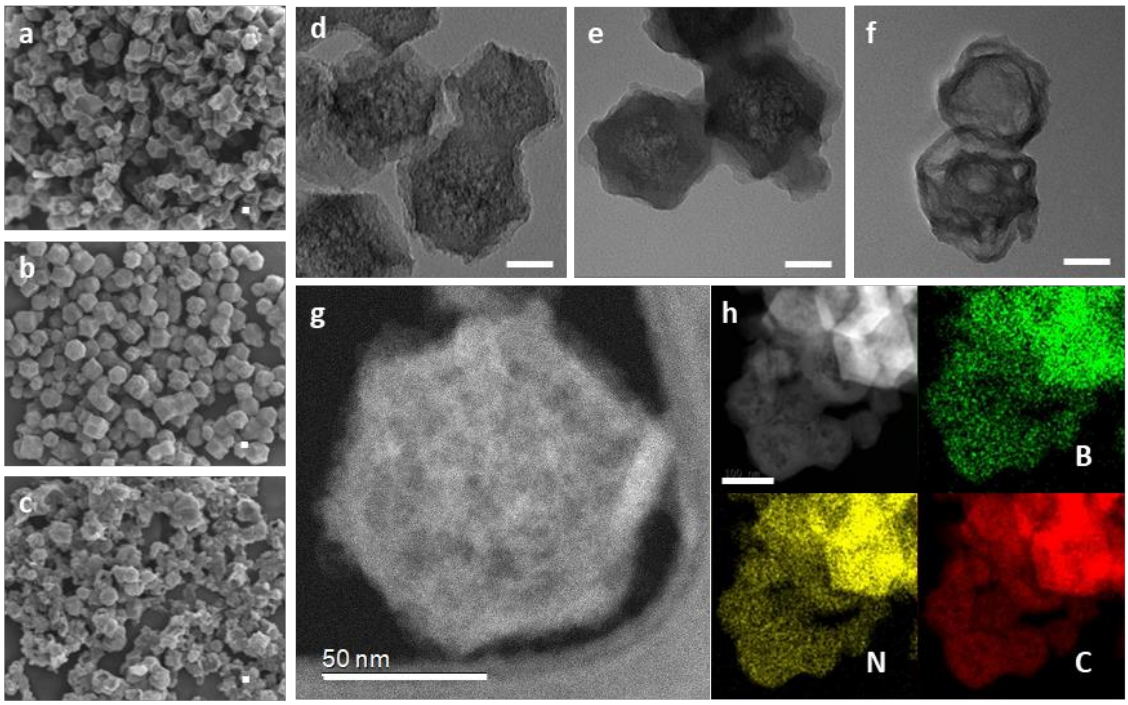

Figure 4.11. SEM and TEM images of (a,d) N@C, (b,e) B,N@C-AB, and (c,f) B,N@C-BA. All scale bars are 50 nm. (g) Aberration corrected HAADF-STEM, and (h) EDS mapping of B,N@C-AB, with the scale bar being 100 nm.

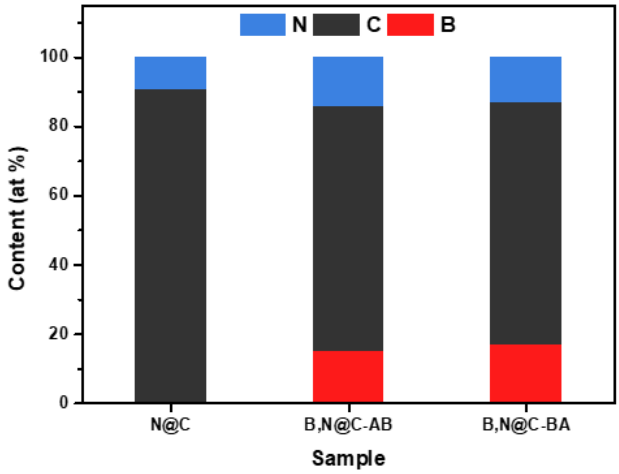

Figure 4.12. B, C, and N contents of N@C and B,N@C samples.

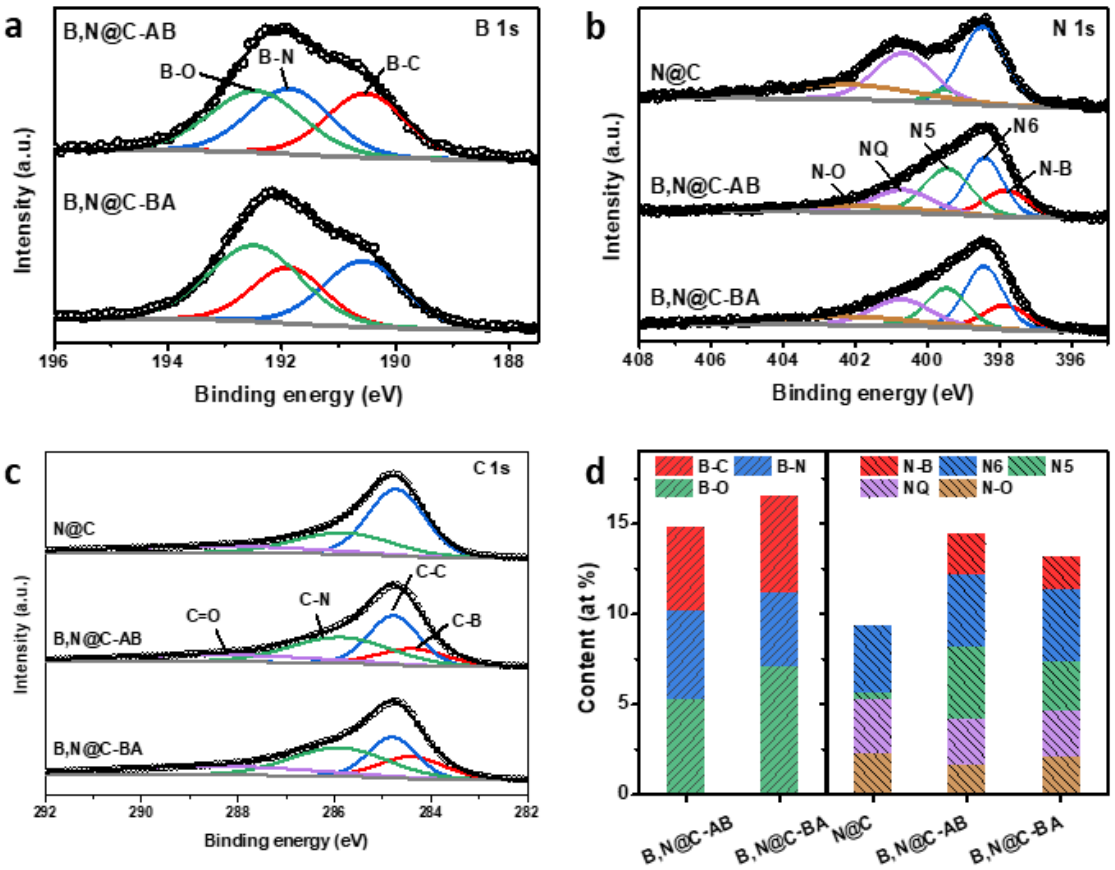

Figure 4.13. The high-resolution XPS spectra of (a) B 1 s, (b) N 1 s, and (c) C 1 s of N@C and B,N@Cs. (d) The contents of B and N determined by fitting the XPS spectra.

Samples derived from ZIF-8 and B@ZIF-8s exhibit different N_2 sorption isotherms (Figure 4.14a), indicating different porous structures (Figure 4.14b). N@C shows a reversible type I isotherm which is typical for microporous samples. B,N@C-BA shows a type IV isotherm featuring a broad hysteresis loop and a steep increase of the N_2 uptake at p/p_0 close to 1, suggesting meso/macropores-dominated structure. B,N@C-AB exhibits combined characteristics of type I and IV isotherms, which is due to the existence of pore sizes spanning from micro- to macropores (Figure 4.14b). As a result, B,N@C-AB has a larger Brunauer–Emmett–Teller (BET) surface area of 523.0 m^2/g but a smaller pore volume of 0.69 m^3/g than B,N@C-BA (295.3 m^2/g and 1.29 m^3/g). Furthermore, the proportion of meso/macroporous surface areas and volumes of B,N@C-AB and B,N@C-BA are all higher than those of N@C (Figure 4.14c). The relatively high surface of B,N@Cs and their hierarchical porous structure with considerable amounts of meso/macropores would be favorable for the accessibility of electrolytes and exposing more active sites for oxygen reduction.

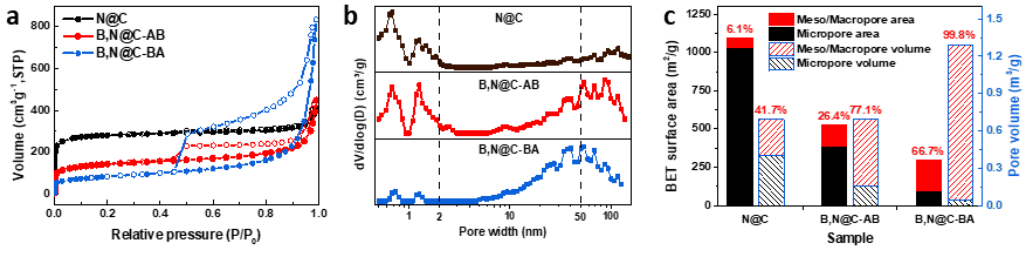

Figure 4.14. (a) N_2 sorption isotherms, (b) pore size distributions, and (c) BET surface areas and pore volumes of N@C and B,N@Cs.

4.3.3 ORR performance of B,N@C-AB and B,N@C-BA

To examine the influence of doping on catalytic performance, the ORR activities of the N@C and B,N@C catalysts were first evaluated by cyclic voltammogram (CV) tests in N_2- and O_2-saturated electrolyte (0.1 M KOH) at a scan rate of 10 mV/s (Figure 4.15a). All the samples show no redox peaks in the N_2-saturated medium, but distinct cathodic peaks appear in all the cases with the O_2-saturated electrolyte, which can be ascribed to oxygen reduction. The B,N@C-AB shows a peak at 900 mV, which is higher than N@C (786 mV) and B,N@C-BA (841 mV) and closest to that of the benchmark Pt/C catalyst, demonstrating the best oxygen reduction activity. As shown in Figure 4.13d, all the samples have similar amounts of N6 (3.7 at.% for N@C, 4.0 at.% for B,N@C-AB, and 4.0 at.% for B,N@C-BA), which are known to lower the overpotential in ORR [200, 201]. Therefore, other factors such as boron doping and structures cause the difference in ORR performance. Rotating ring-disc electrode (RRDE) measurements were carried out to compare the electrocatalytic ORR activities and determine the electron transfer numbers over different catalysts in alkaline (0.1 M KOH) solution. The ORR linear sweep voltammogram (LSV) polarization curves of different catalysts in RRDE were recorded in O_2-saturated 0.1 M KOH solution at a rotation rate of 1,600 rpm, with commercial Pt/C catalyst as a comparison (Figure 4.15b) and with the H_2O_2 currents detected by the Pt ring (Figure 4.15c).

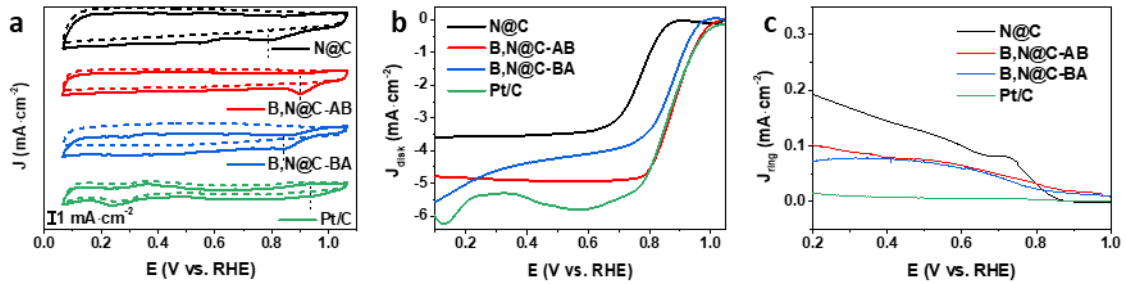

Figure 4.15. (a) CV curves in N_2-saturated (dotted lines) and O_2-saturated (solid lines) 0.1 M KOH electrolytes. (b) LSV curves and (c) The detected ring currents on the Pt ring electrode with a fixed rotation rate of 1,600 rpm at 10 mV/s.

In agreement with the CV observations, B,N@C-AB shows an exceedingly high ORR activity with the most positive half-wave potential ($E_{1/2}$) of 887 mV, which is much better than that of the N@C ($E_{1/2}$ = 767 mV) and also comparable to that of commercial Pt/C ($E_{1/2}$ = 859 mV). B,N@C-BA also exhibits a relatively high $E_{1/2}$ of 840 mV. Both B,N@C samples show larger diffusion-limited current density (DLCD = 4.79 mA/cm^2 for B,N@C-AB, 5.55 mA/cm^2 for B,N@C-BA) than N@C (3.61 mA/cm^2), which indicates that meso- and macropores are beneficial for mass transfer [169, 202]. The performance of B,N@C nanocages is on par or even better than the reported metal-free BCN catalysts (Error! Reference source not found.). In comparison with the catalysts prepared using t raditional methods mentioned in Table S1, B,N@C-AB and B,N@C-BA are of high B doping content with a feasible structure control, which benefits the ORR activity.

Table 4.2. Comparison of the ORR performance of B,N@C in 0.1M KOH.

Catalysts	$E_{1/2}$ (mV vs RHE)	Content of B (at %)	Pore structures	Preparation methods of precursors
B,N@C-AB nanocage (this work)	887	15.0	Micro/meso/macropores	Confined etching
B,N@C-BA nanocage (this work)	840	16.9	Meso/macropores	Confined etching
B,N@C nanotubes [1]	820	~ 2.0	Mesopores	Mechanical mixing
B,N@ordered macroporous C [2]	810	0.5 wt%	Micro/meso/macropores	Chemical vapor deposition
B,N@ordered mesoporous C [3]	748	1.1	Mesopores	Soft template method
B,N@graphene aerogels [4]	785	-	Meso/macropores	Hydrothermal reaction
Porous BCN nanosheets [5]	820	11.5	Micro/mesopores	Polymer sol−gel method
B,N@hollow C tubes [6]	810	1.23	-	Physical mixing
B,N@graphene [7]	820	7.3	Micro/mesopores	Physical mixing
B,N@graphite layers [8]	811	4.4	Micro/mesopores	Physical mixing

Furthermore, the improvement in graphitization degree can enhance the conductivity of carbon materials and decrease the electron transfer resistance in the ORR process, thus giving rise to a better ORR performance [203, 204]. Therefore, according to Refs. [203, 204], ZIF-8 was carbonized at 1,100 °C for 2 h under N_2 (labelled as N@C-1100) to obtain a higher graphitization than N@C and studied the effect of graphitization degree on the ORR performance. N@C-1100 shows a half-wave potential of 717 mV (Figure 4.16a), more negative than that of N@C prepared at 1,000 °C, indicating that higher graphitization is not the reason for the better ORR activity in this study. It should be noted

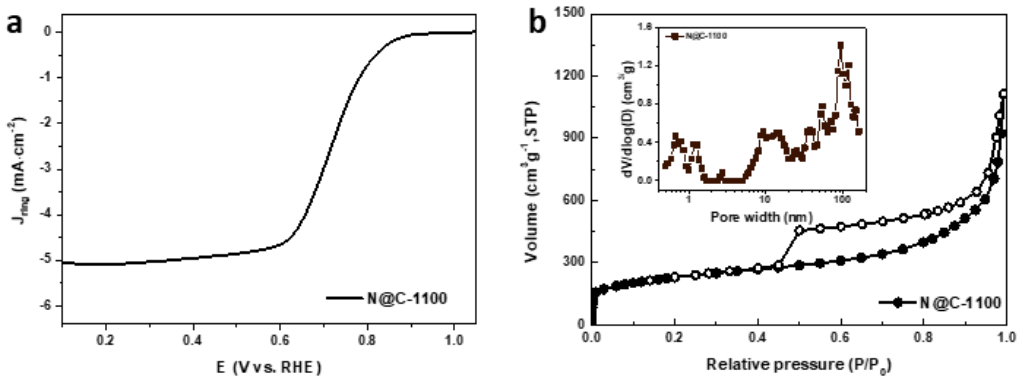

Figure 4.16. (a) Electrocatalytic performance of N@C-1100 for ORR in 0.1 M KOH electrolyte and (b) N_2 sorption isotherms of N@C-1100, and pore size distributions.

that the diffusion-limited current density of N@C-1100 (5.05 mA/cm^2, Figure 4.16a) is much larger than that of N@C (3.61 mA/cm^2) and comparable to that of B,N@C-AB (4.79 mA/cm^2) and B,N@C-BA (5.55 mA/cm^2). This is because that N@C-1100 possesses meso/macroporous surface areas and volumes (52.6% and 90.6%), comparable to those of B,N@C-AB (26.4% and 77.1%) and B,N@C-BA (66.7% and 96.8%), but larger than those of N@C (6.1% and 41.7%), as shown in Figure 4.16b. It proves again that meso- and macropores are advantageous for mass transfer, thus enhancing diffusion-limited current density for oxygen reduction. In addition, an increased degree of graphitization and loss of nitrogen can occur when raising the pyrolysis temperature to 1,100 °C [205]. Therefore, the more negative half-wave potential of N@C-1100 compared with N@C demonstrates that expelling N dopant leads to lower ORR activity. Therefore, the excellent ORR activity of B,N@C benefits from the co-doping of B and N and the unique hierarchical porous structure.

Besides the catalytic activity, immunity to contamination is another factor affecting the application of catalysts. Using B,N@C-AB and Pt/C as examples, alkaline stabilities were evaluated by the chronoamperometric tests (Figure 4.17). As shown in Figure 4.17, the current of B,N@C-AB did not change much after the addition of methanol into O_2 saturated 0.1 M KOH solution, whereas the current for the Pt/C dropped to almost zero. Taken together, B,N@C-AB is an effective ORR catalyst with high catalytic activity and methanol tolerance in the alkaline media.

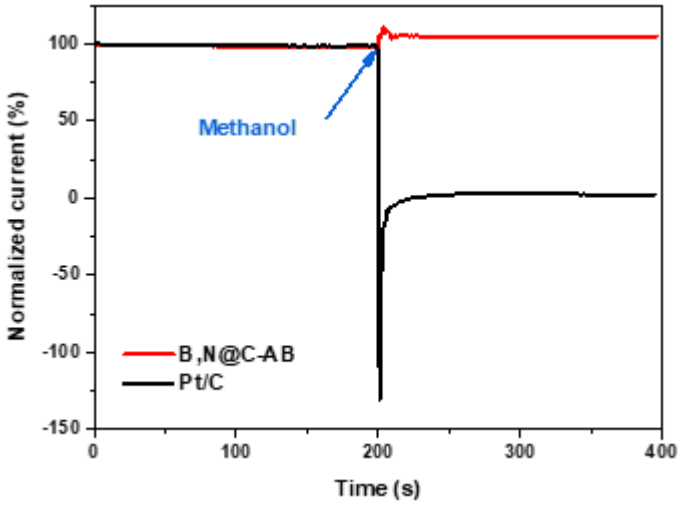

Figure 4.17. Methanol-crossover from ORR chronoamperometric response of the B,N@C-AB and Pt/C electrodes in O_2-saturated 0.1 M KOH. The arrows indicate the addition of 5 mL methanol into 90 mL electrolyte.

Tafel plots of N@C, B,N@C-AB, B,N@C-BA, and commercial Pt/C are displayed in Figure 4.18a. The B,N@C-AB displays a lower Tafel slope than those of N@C and B,N@C-BA, further manifesting that the B,N@C-AB catalyst exhibits the fastest kinetics toward ORR. The H_2O_2 molar yields and electron transfer numbers calculated based on

the corresponding disk and ring currents are both plotted in Figure 4.18b. The H_2O_2 yields of B,N@C-AB and B,N@C-BA are below 12% from 0.2 to 0.7 V with electron transfer numbers larger than 3.75, indicating a strong catalytic effect in converting O_2 to O^{2-} via a four-electron pathway. Much higher H_2O_2 yield and smaller electron transfer number are observed on N@C, indicating its lower-efficiency $4e^-$ pathway in ORR. The high ORR activities of B,N@C are likely due to two key factors. First, the electronic structure of the catalysts is optimized by high boron doping, which promotes the adsorption of the *OH and *OOH intermediates at the B sites [134]. Second, the etching caused by boron species in ZIF-8 generates meso- and macroporous structure which exposes more active sites and contributes to better mass transfer.

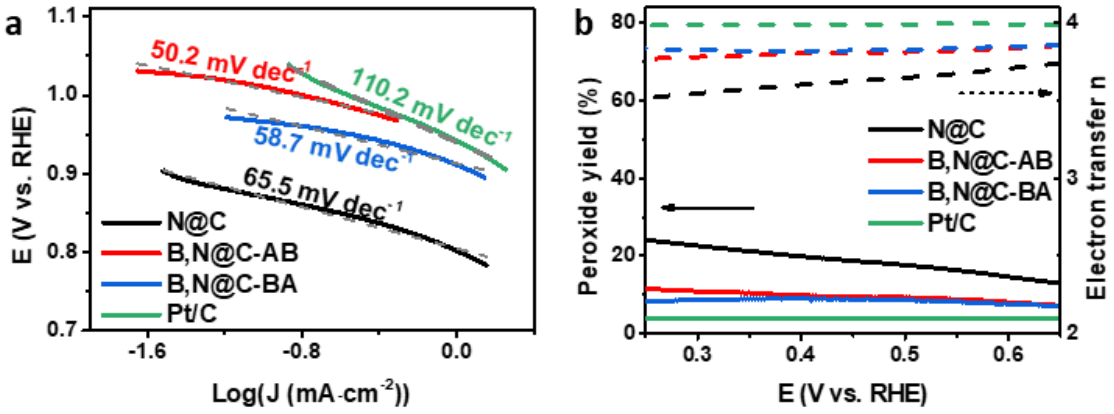

Figure 4.18. (a) Tafel plots and (b) electron transfer number and H_2O_2 selectivity derived from LSV curves.

4.4 Conclusions

In summary, I have developed an effective method for the fabrication of B and N co-

doped hierarchical porous carbon nanocages. The key step in the fabrication is the introduction of boron species into ZIF precursors via an integrated double-solvent impregnation and nanoconfined-etching. The encapsulation of boron-containing guests in the ZIF-8 pores plays an important role in achieving a uniform and dense doping of B atoms in the N@C nanocages and inducing the hierarchical micro/meso/macro multimodal porosities. The excellent electrochemical ORR performance of B,N@Cs could be associated with their hierarchical porous structures that contribute to mass transfer and exposure of active sites, as well as abundant reactive sites due to the high level of boron doping. This integrated method of impregnation and confined etching is applicable to fabricate complex nanoarchitectures with desired pore sizes and pore volume, which will be beneficial for various catalytic reactions.

4.5 Related publications

Wang, X., Han, C., Li, H. *et al.* Fabrication of monodispersed B, N co-doped hierarchical porous carbon nanocages through confined etching to boost electrocatalytic oxygen reduction. *Nano Res.* **16**, 290–298 (2023). https://doi.org/10.1007/s12274-022-4786-4

Chapter 5 Balancing mass transfer and active sites to improve electrocatalytic ORR

5.1 Background

Carbon-based metal-free catalysts with stable structures, rich defects, and tunable electronic structures, have attracted much attention for various chemical reactions, including thermocatalytic, electrocatalytic, and photocatalytic reactions. [11, 113] In the past decades, numerous efforts have been devoted to optimizing the electronic structure of active centers at the nanoscale by heteroatom doping, especially with multiple heteroatoms. [51] Among these, boron and nitrogen co-doped carbon (B,N@C) has displayed interesting catalytic performance. [120, 121, 124] Most of the studies reported so far have focused on tuning chemical compositions and nanostructures to improve the efficacy and quantity of active sites.

An often less studied but significant factor affecting the catalytic process is mass transfer, which determines the efficiency of supply of reactants and removal of products to and from the active sites, and consequently the catalytic performance. For various gas-involving electrocatalysis, including HER, OER, ORR, electrochemical reduction of carbon dioxide (CO_2RR), and electrochemical reduction of nitrogen (N_2RR), the diffusion behavior of reactants and products plays a practical role in these

heterogeneous catalysis processes. So far, electrode fabrication and device configuration design have been the common approach to enhance mass transfer, [206-209] rather than tailoring the pore sizes and volumes of the nanocatalysts. [210, 211]

Nanoreactors are effective platform materials with a wide range of structures where confined environments can modulate chemical reactions. [6, 9] Trimodal porous nanoreactors with micropores (< 2 nm), mesopores (2−50 nm), and macropores (> 50 nm) are desirable to simultaneously achieve large numbers of active sites and improve mass diffusion. [7, 212-214] MOFs are ideal precursors to obtain nanoreactors due to their customizable modular assembly and controllable morphologic and structural evolution. [15, 56, 106, 113, 215] Key pore parameters including pore shape, size, and volume, can be regulated by controlling etching conditions such as the etching time, etching temperature, and etchant concentration. So far, mesopore sizes were normally confined within a range of 2-38 nm, [41, 57, 63] and the range is not wide enough. Pyrolyzing zinc-based MOFs (Zn-MOFs) has been often used to obtain porous metal-free carbon materials with heteroatomic active sites. [16] However, most of these active sites are deeply hidden in the micropores of MOFs-derived nanocarbon and are unreachable for the catalytic reactions. [216] Selective etching of MOFs followed by pyrolysis proves effective in obtaining tunable nanostructures where active sites are exposed to reactants. [92, 217] However, synthesizing a series of platform materials with different porous structures but similar active sites in efficacy and quantity is far

less developed. Therefore, the relationship between mass transfer and catalytic activity is not well understood. B,N@C nanostructures have been derived by directly pyrolyzing B,N-containing MOF (e.g., boron imidazolate framework (BIF)-82 [146] and BIF-1S [147]) or MOFs mixed with B-containing substances [124, 148-156]. Most of these MOF-derived B,N@C nanomaterials exhibit collapsed structures and narrow pore size distributions. [150-156] To obtain a great variety of pores with good controllability, more research is needed to select the right precursors and optimize the pyrolysis conditions.

Herein, I developed an effective method to fabricate porous three-dimensional (3D) B,N@C catalysts by sequentially etching and pyrolyzing a series of ZIF-8 precursors. It is known that most of the reported etching processes are too fast to precisely regulate the porosity of the MOF precursors. [92, 161] For example, tannic acid transformed solid ZIF-8 and NH_2-MIL-125(Ti) into hollow MOFs in a very short time (< 30 min). [161] To solve this problem, ammonia borane (AB) which features mild hydrolysis was used to make the etching process controllable. Consequently, the structure of the B,N@C nanocages was effectively tailored. These 3D B,N@Cs feature similar catalytic active sites for ORR, in terms of chemical composition and quantity. But their performance correlates with the porous structure, especially at the meso- and macroscale, which affects the mass transfer during the heterogeneous process. The performance of optimized B,N@C-24 catalyst is on par with commercial Pt/C, and the

outstanding catalysis is associated with the trimodal-porosity enabling the best combination of active site exposure and mass transfer.

5.2 Experimental

5.2.1 Synthesis of AB@ZIF-8-xh

In a typical synthesis, 0.1 g of ZIF-8 was added to 20 mL of cyclohexane and ultrasonically treated to form a uniform suspension. Then 0.1 mL of AB aqueous solution (0.1 g/mL) was added into the ZIF-8 dispersion dropwise and stirred for different times (2, 6, 12, 24, and 48 hours). The resultant solids were collected by centrifugation and vacuum dried and were labeled as AB@ZIF-xh, where x is the treatment time.

5.2.2 Synthesis of B,N@C-xh

For carbonization, the obtained AB@ZIF-xh were heated from room temperature to 1000 °C at a heating rate of 5 °C min^{-1} and held at 1000 °C for 2 h under N_2. The obtained samples were denoted as B,N@C-xh.

5.3 Results and discussion

5.3.1 Synthesis of hierarchical porous B,N@C nanoreactors from modified ZIF-8 nanoparticles

The synthesis of B,N@C nanoreactors is illustrated in Figure 5.1. A double-solvent method was first used to immobilize ammonia borane (AB) as guest molecules in the

ZIF-8 hosts on account of the immiscibility between water and cyclohexane. AB provides B and N as dopants and also acts as a mild etching agent by releasing protons during its slow hydrolysis, i.e., $NH_3BH_3 + 4H_2O \rightarrow NH_4^+ + B(OH)_4^- + 3H_2$. [188, 217] Therefore, compositional and structural modifications of ZIF-8 hosts were achieved at the same time, producing AB@ZIF-*x*h particles, where *x* represents the etching time. In the subsequent pyrolysis step, AB@ZIF-*x*h were transformed to corresponding B,N@C-*x*h nanocages with hierarchical porosities. [176]

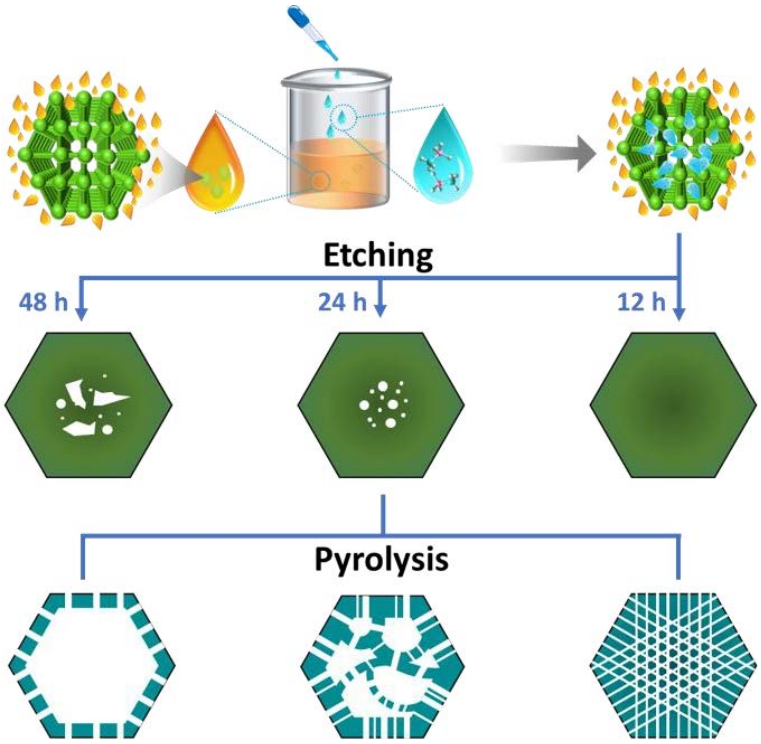

Figure 5.1. Schematics of the preparation of the B,N@C nanoreactors.

The XRD patterns of the resulting AB@ZIF-8 match the simulated powder XRD patterns based upon ZIF-8 single crystal XRD data (Figure 5.2). The SEM images show negligible changes in morphologies and sizes after etching (Figure 5.3). TEM images reveal the

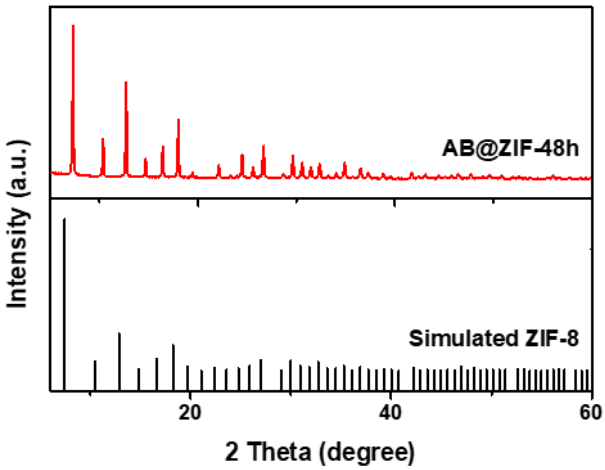

Figure 5.2. Powder XRD patterns of the as-synthesized AB@ZIF-8 precursors in comparison with simulated XRD patterns of ZIF-8 based upon single crystal XRD data.

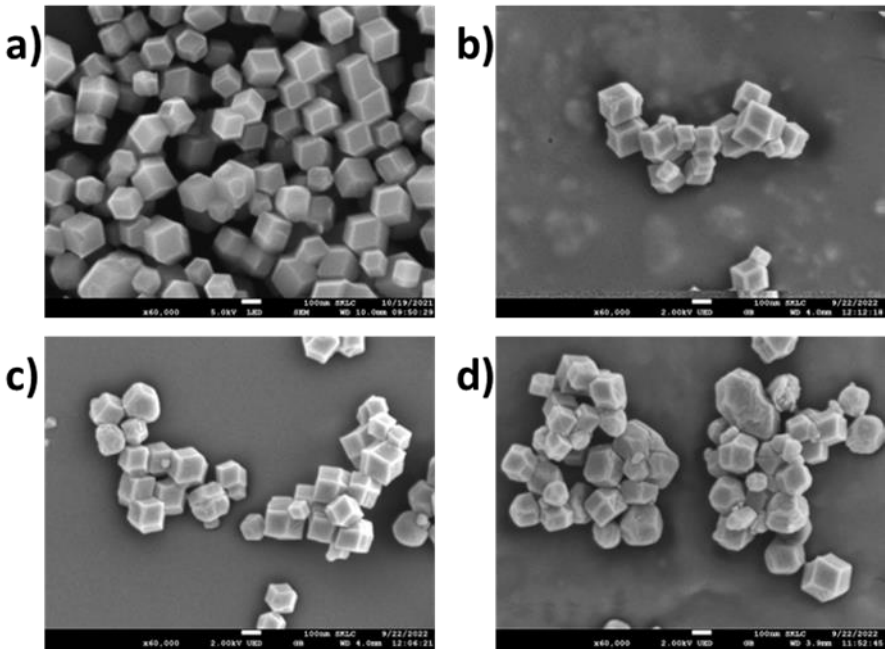

Figure 5.3. SEM images of a) ZIF-8, b) AB@ZIF-12h, c) AB@ZIF-24h, and d) AB@ZIF-48h. Scale bar: 100 nm.

structural evolution of the AB@ZIF-8 nanoparticles through etching (Figure 5.4a-f). AB@ZIF-2/6/12h nanoparticles retain the solid rhombic dodecahedron structure without

obvious pores as the parent ZIF-8 (Figure 5.4a-d). Extended etching gradually led to the formation of larger pores inside the host (Figure 5.4e,f). EDS mapping of AB@ZIF-24h in Figure 5.4g reveals that N and C are uniformly dispersed in the whole nanoparticle, while B and O are concentrated onto the center of the particles, indicating that AB molecules were diffused inward through capillary action and hydrolyzed inside the host. These results prove that confined etching is effective in structurally modifying the MOF hosts.

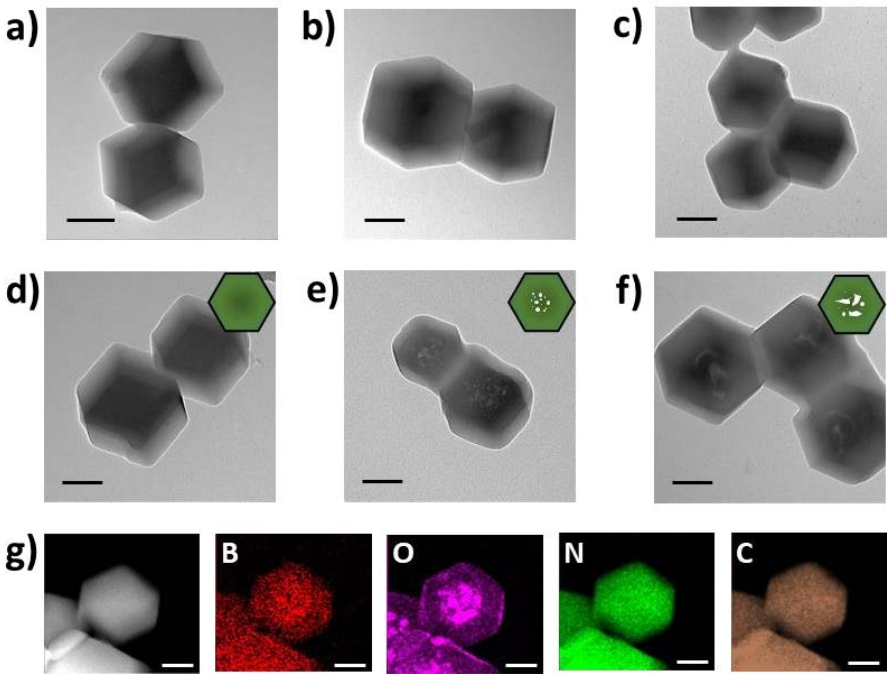

Figure 5.4. Controllable etching of ZIF-8 precursors. TEM images of (a) ZIF-8, (b) AB@ZIF-2h, (c) AB@ZIF-6h, (d) AB@ZIF-12h, (e) AB@ZIF-24h, (f) AB@ZIF-48h. EDS mapping of (d) AB@ZIF-24h. Black and white scale bars are 100 and 50 nm, respectively.

Subsequently, B,N@C nanoreactors with different architectures were prepared by pyrolyzing the AB@ZIF-8 precursors at 1000 °C under N_2. As illustrated by SEM images in Figure 5.5a, B,N@C-12h retains polyhedral morphology similar to AB@ZIF-12h precursor after pyrolysis. With the extension in etching, B,N@C became hollow and porous with rough surfaces collapsing inward (Figure 5.5b,c). TEM images further verify

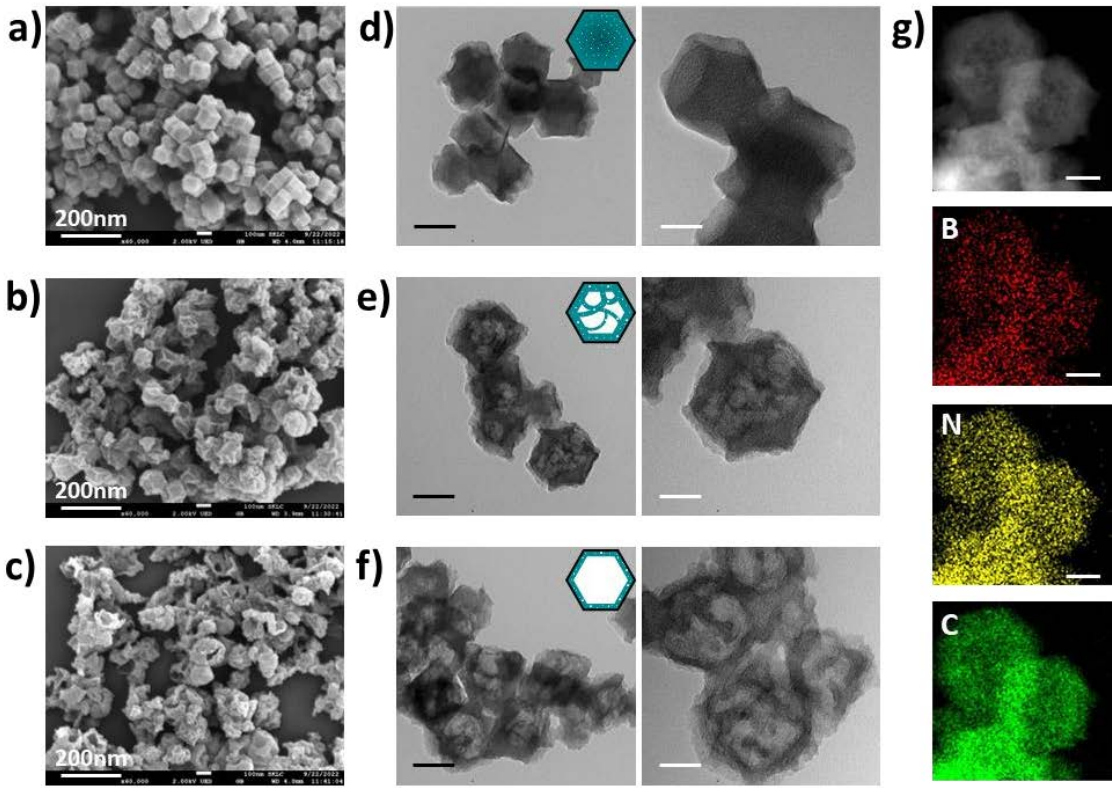

Figure 5.5. AB@ZIFs-derived hierarchical porous B,N@Cs. SEM images of (a) B,N@C-12h, (b) B,N@C-24h, and (c) B,N@C-48h. TEM images of (d) B,N@C-12h, (e) B,N@C-24h, and (f) B,N@C-48h. EDS mapping of (g) B,N@C-24h. Black and white scale bars are 100 and 50 nm, respectively.

the correlation between the nanoarchitecture of B,N@C (Figure 5.5d-f), and AB@ZIF-8 precursors (Figure 5.4d-f). Specifically, the greater degree the precursor was etched to, the larger cavities the derived materials have. As a result, B,N@C-12h possesses small voids inside; B,N@C-24h transforms into nanocages with multiple compartments; B,N@C-48h becomes hollow cages. Elemental mapping images reveal that B and N heteroatoms are homogenously distributed together with C in all these structures (Figure 5.5g), indicating the formation of uniform co-doping of C by B and N.

5.3.2 Structural relevance between AB@ZIF-8 precursors and B,N@C

To further explore the structural dependency of B,N@C on AB@ZIF-8, their structures were evaluated using N_2 adsorption−desorption analysis (Figure 5.6a,b). The sorption isotherms of AB@ZIF-8 precursors (Figure 5.6a) display typical type I isotherms, indicating the dominance of micropores in these materials. The specific surface area decreased with longer etching, meaning that etching transformed some micropores into mesopores or macropores. [218] The pore size distribution profiles calculated based on non-local density functional theory (NLDFT) in Figure 5.6a confirm the decrease in micropore (< 2 nm) proportions and the increase in mesopore (2−50 nm) and macropore (> 50 nm) proportions during etching. N_2 adsorption−desorption isotherms were also collected to characterize the porosities of B,N@C nanocages (Figure 5.6b). Different from AB@ZIF-8, B,N@C exhibited a combination of type I and IV isotherms with clear hysteresis loops, indicating the existence of micro-, meso- and macropores. [182, 214]

There are several possible mechanisms for the formation of porous B,N@C nanocages, which include the generation of gases, [219] the evaporation of Zn atoms, [220] and the generation of graphitic structure. [92] All the samples have undergone the same pyrolytic conditions, so the differences in porous structures of B,N@C nanocages are mainly derived from the difference among the AB@ZIF-8 precursors.

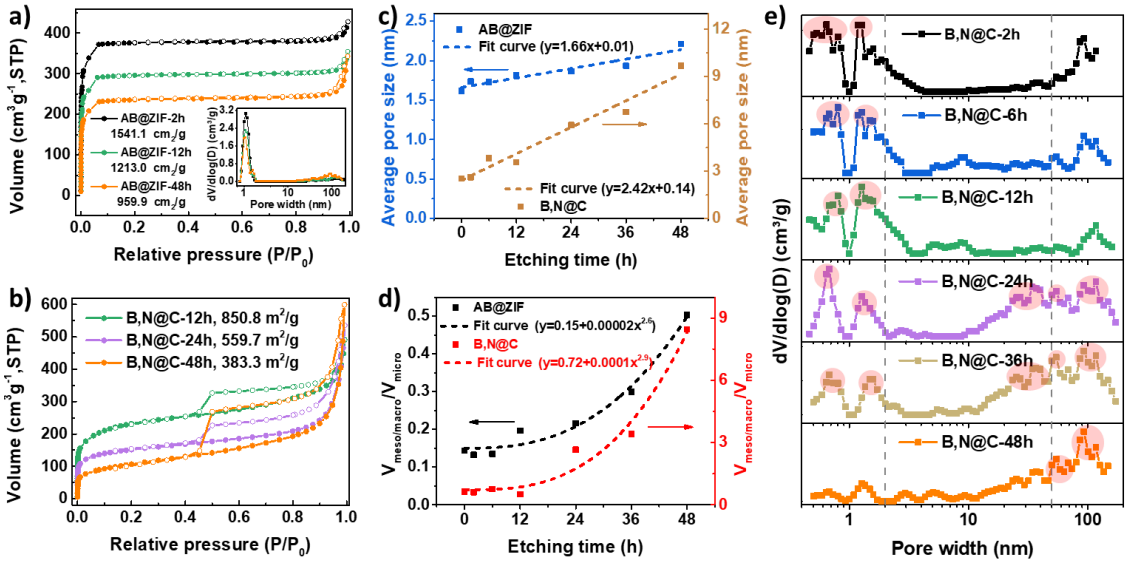

Figure 5.6. Structural characterization of AB@ZIF-8 nanoparticles and B,N@C nanocages. N_2 adsorption-desorption isotherms of a) AB@ZIF-8 (inset: the pore size distribution curves of AB@ZIF-8 precursors.) and b) B,N@C, c) average pore size and d) pore volume ratios of meso/macro to micropore in AB@ZIF-8 and B,N@C, and e) pore size distributions of B,N@C.

To study the correlation of the porosity between AB@ZIF-8 nanoparticles and B,N@C nanocages, the relationship between pore sizes and etching time was studied based on the N_2 adsorption−desorption curves. Figure 5.6c presents plots of average pore size versus

etching time for AB@ZIF-8 and B,N@C, and the relationship between these two based upon curve fitting. For both AB@ZIF-8 and B,N@C, there is a linear correlation between the average pore size and etching time. The ratios of meso/macroporous to microporous volumes of AB@ZIF-8 precursors with etching time were also analyzed (Figure 5.6d). The difference in the first 6 hours is minimal, while the ratio increases faster after 12 hours, approximating to a power function relationship. This agrees well with the TEM images and confirms the essential role of AB in the host-guest assisted etching to structurally modify the host so that B,N@C with tunable structures can be obtained. The ratio of meso/macroporous to microporous volumes of B,N@C nanocages shows a similar trend to that of AB@ZIF-8 and can be fitted to the power function with a similar power. These results bring out the feature of MOF-derived carbon, i.e., its architectures depending on the MOF precursors. However, most of the reported etching processes are too fast to precisely regulate the porosity of the parent MOFs. For example, tannic acid changed solid ZIF-8 and NH_2-MIL-125(Ti) into hollow MOFs in a very short time (< 30 min). [92, 161] In contrast, AB features mild hydrolysis which makes the etching process moderate and controllable. Consequently, the structure of the B,N@C nanocages can be effectively tailored.

The NLDFT pore size distribution analysis (Figure 5.6e) shows that B,N@C-2/6/12h samples possess mainly micropores with sizes around 0.7 and 1.3 nm. B,N@C-24/36h samples have mesopores at about 25.3 and 37.1 nm, macropores at 93.1 and 117.2 nm,

together with micropores at 0.7 and 1.3 nm, respectively, confirming them to be trimodal-porous. Macropores with the sizes of 54.4, 93.1, and 117.2 nm dominate in B,N@C-48h. These results indicate that B,N@C-12/24/48h possess different nanoarchitectures, rendering them ideal material platforms to test the impact of porosity on mass transfer, and consequent ORR performance.

5.3.3 Characterization of B,N@C nanoreactors

B,N@C-12/24/48h were further investigated using XRD, Raman spectroscopy, and XPS techniques. XRD patterns in Figure 5.7a show broad diffraction peaks at 25°, which could be indexed as the (002) crystal plane of amorphous carbon. [221] Raman spectra (Figure 5.7b) can be deconvoluted into four types of carbon configurations at 1,348 (D_1), 1,196 (D_2), 1,471 (D_3), and 1,577 (G) cm^{-1}. D_1, D_2, and D_3 bands are corresponding to the disordered carbon structure, amorphous carbon, and carbon atoms outside of a perfectly planar graphene network, respectively, while G band is attributed to the ordered graphite carbon. [222, 223] The I_{D1}/I_G values for all the B,N@C nanoreactors are similar, within the range of 1.44 to 1.54, indicating their similar degree of graphitization and defects. Note that D_2 and D_3 bands contribute little to the ORR performance. [222] Chemical compositions and chemical states were analyzed with XPS. Survey scans show that all these catalysts contain B, C, N, and O (Figure 5.8 and Table 5.1).

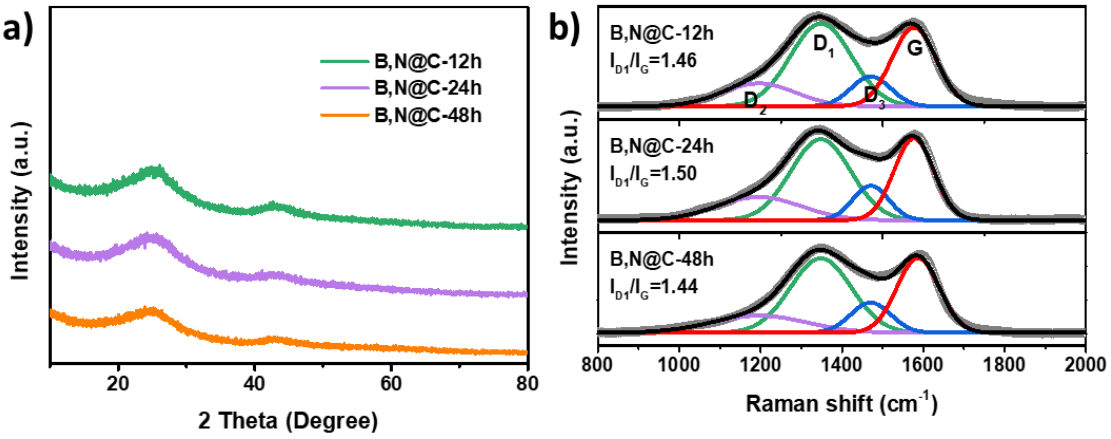

Figure 5.7. (a) PXRD patterns and (b) Raman spectra of the B,N@C nanoreactors.

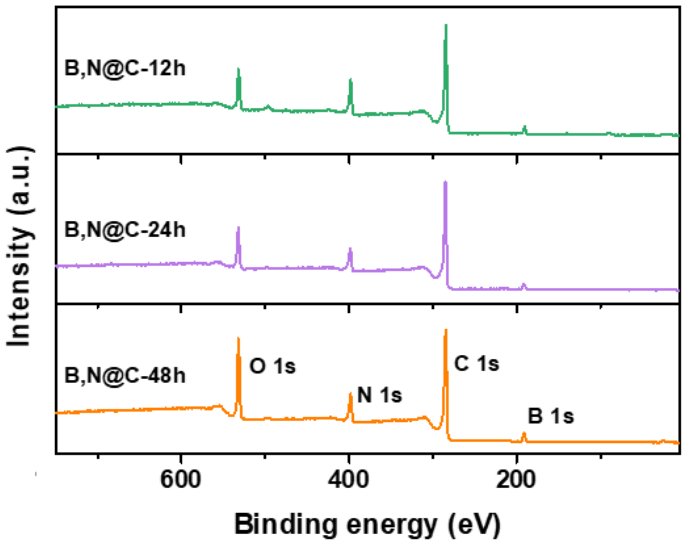

Figure 5.8. XPS survey spectra of B,N@C nanoreactors.

Table 5.1. Elemental contents of B, N, and C according to XPS spectra.

Sample	Elemental content (at.%)			Heteroatomic B and N content (at.%)
	B	C	N	
B,N@C-12h	12.0	72.7	15.3	27.3
B,N@C-24h	9.9	77.6	12.5	22.4
B,N@C-48h	14.2	73.8	12.1	26.3

High-resolution XPS spectra of B 1s can be deconvolved into three peaks, which are assigned to B−C (190.6 eV), B−N (191.9 eV), and B−O (192.5 eV) (Figure 5.9a and Table 5.2). It is notable that, by prolonging the etching time, the proportion of B−O increased significantly from 0% in B,N@C-12h to 23% in B,N@C-48h, indicating the gradual accumulation of B−O during etching. This result matches well with the proposed etching mechanism that the mild hydrolysis of AB gradually releases protons, which then attack 2-MIM ligands in ZIF-8. For ORR, B−O bonds are reported to have a rather limited contribution to the performance, [134] where B−C and B−N benefit the ORR. [196, 224] The N 1s XPS spectra are well fitted by five peaks, corresponding to N−B (397.9 eV), pyridinic N6 (398.5 eV), pyrrolic N5 (399.5 eV), graphitic N (400.8 eV), and N−O (402.4 eV). Pyridinic N6, pyrrolic N5 and graphitic N are also known to contribute to ORR. [200, 201] The ratios of B (in B–N) to N species (in N–B) are similar in these catalysts (2.4 for B,N@C-12h, 2.5 for B,N@C-24h, and 2.5 for B,N@C-48h), but the total amounts of B and N in B,N@C-24h are slightly lower compared with the other two samples (Table 5.2). As shown in Figure 5.9b and Table 5.2, all these catalysts have similar chemical features of N and all these known active sites involving B and N are similar in ratio. Therefore, these three catalysts with similar heteroatomic $B_{2.5}$–N_1 motifs can serve as an ideal material platform to investigate the structure–performance relation of nanoreactors toward catalytic reactions.

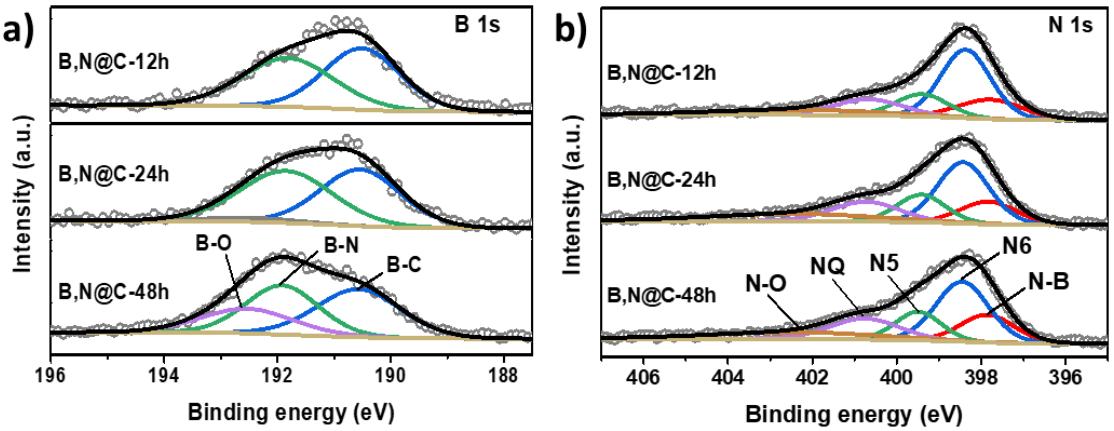

Figure 5.9. High-resolution XPS spectra of the B,N@C nanoreactors. (a) XPS spectra of B 1s, and (b) XPS spectra of N 1s.

Table 5.2. B and N configurations according to XPS spectra.

Sample	Content of B (at.%)			Content of N (at.%)				
	B–C	B–N	B–O	N–B	N6	N5	NQ	N–O
B,N@C-12h	6.0	5.8	0	2.4	6.7	2.3	2.2	1.8
B,N@C-24h	4.7	4.9	0.4	2.0	4.9	2.1	2.1	2.0
B,N@C-48h	5.8	5.2	3.3	2.1	4.6	2.0	2.1	1.4

5.3.4 Impact of mass transfer on electrocatalytic ORR performance

Electrochemical ORR was used as a model reaction to test the effect of porous structural engineering on the catalytic performance and to understand the importance of mass transfer during the reaction. The performance was assessed using RRDE in a typical three-electrode system. The LSV disk curves collected at 1600 rpm in an O_2-saturated 0.01 M (pH = 12) and 0.1 M (pH = 13) KOH solution are shown in Figure 5.10a and Figure 5.10b, respectively. Generally, dilute electrolytes exhibit low viscosity, therefore

having negligible effects on mass diffusion. As a result, the active site determines the electrocatalytic performance. As can be seen from Figure 5.10a, the difference in diffusion-limited current density (DLCD) among the three samples is negligible in the 0.01 M KOH solution. As expected, B,N@C-12h with the largest surface area shows the most positive half-wave potential ($E_{1/2}$) of 0.557 V vs. RHE (Figure 5.10c), while B,N@C-48h with the lowest surface area shows the most negative $E_{1/2}$ of 0.524 V vs. RHE. These results confirm that the electrocatalytic performance is determined by the exposure of active sites in dilute electrolytes, which is typically related to surface areas. In contrast, the ORR performance of the three samples in 0.1 M KOH varies greatly (Figure 5.10b,d). It is known that when the electrolyte concentration increases, the viscosity of the electrolyte increases correspondingly [225] and the effect of mass transfer on catalytic performance becomes more significant. Therefore, the catalytic activity was determined by both the exposure of the active sites and the mass transfer efficiency. As shown in Figure 5.10d, B,N@C-24h with the most balanced trimodal-porous structure among the three catalysts (Figure 5.11), achieved the largest diffusion-limited current density (DLCD) of −5.9 mA cm^{-2} at 0.2 V vs. RHE. In addition, B,N@C-24h catalyst featured the most positive onset potential (E_{on}) of 0.979 V and $E_{1/2}$ of 0.861 V vs. RHE, as summarized in Figure 5.10d. The better ORR performance of B,N@C-24h than B,N@C-12h in 0.1 M KOH is mainly due to the enhancement of mass transfer in meso/macropores compared with micropores, demonstrating that mass transfer is vital for ORR in concentrated electrolyte solutions. Meanwhile, B,N@C-48h shows the low

activity among these three catalysts, which indicates that mass transfer is not the only important factor in determining performance.

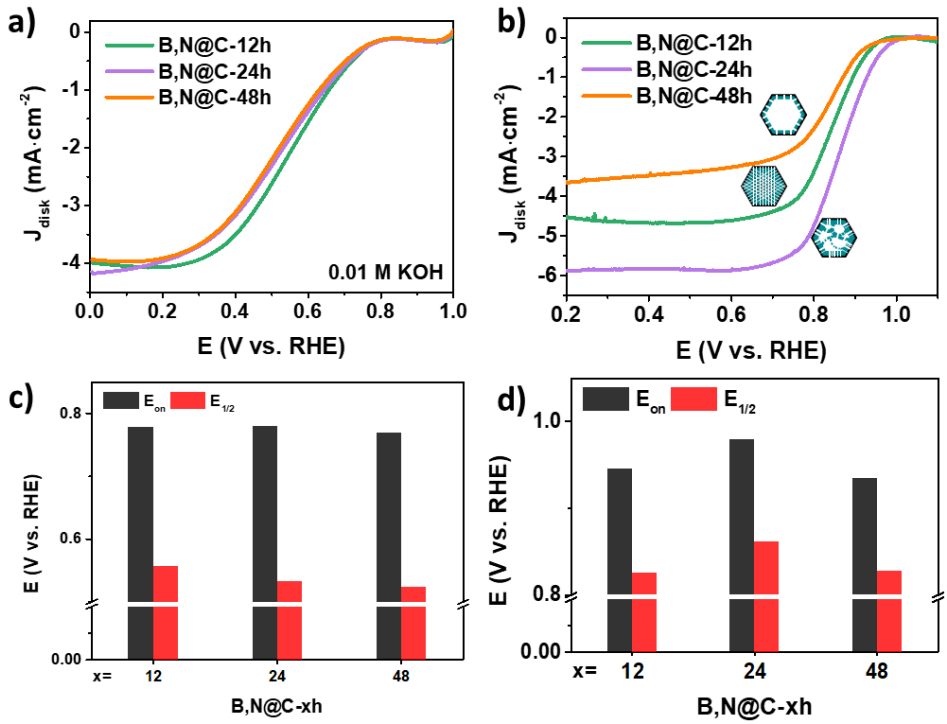

Figure 5.10. Electrocatalytic ORR performance of the B,N@C nanoreactors. (a) LSV curves and (c) corresponding onset and half-wave potentials in 0.01 M KOH; (b) LSV curves and (d) corresponding onset and half-wave potentials in 0.1 M KOH.

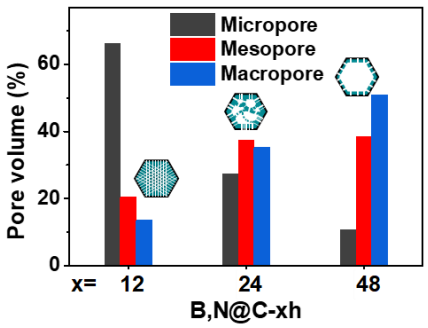

Figure 5.11. Relative pore portions in the B,N@C nanoreactors.

Finite element analysis (FEA) simulations were carried out to further understand the influence of mass transfer on electrocatalytic performance. According to the structural characterizations (Figure 5.5 and Figure 5.12), the main difference between the three samples is the pore sizes and volumes in the nanoreactor. Models were constructed to reflect the cavity size and porous channels. As shown in Figure 5.12a-c, the models exhibit micropore-dominated, balanced trimodal-porous, and macropore-dominated structures, corresponding to the experimentally synthesized B,N@C-12h, B,N@C-24h, and B,N@C-48h, respectively. The different colour in Figure 5.12a-c is associated with the velocity of simulated flow fields. The flow velocity, which is significantly influenced by the geometric architectures of the materials, is an important index to evaluate mass diffusion. As expected, the flow rate in the macropore-dominated hollow cage is overall larger than that in the micropore-dominated and balanced trimodal-porous structures (Figure 5.12d), with only a few positions having rates similar to those of the trimodal-porous structures (Figure 5.12b,c). The electrochemical ORR process is mainly determined by the accessibility of active sites, which is affected not only by the mass transfer efficiency but also by the exposure of active sites. Therefore, the flux passing the entire internal surface was introduced (denoted as flux density hereafter), which takes into account both the active site exposure affected by the specific surface areas and the mass transfer determined by the porous structure. The flux density helps to investigate the process intensification by porous structural engineering of nanoreactors. The micro/meso/macropore-balanced model has a clear advantage over the other two models

(Figure 5.12d). The flux density decreases significantly in the macropore-dominated hollow cage because of the limited surface area. Meanwhile, the flux density of the micropore-dominated sample is also smaller than that of the trimodal-porous structure because of the limited mass transfer. On all these counts, trimodal-porous architecture is considered to be the desired nanoreactor to boost the process intensification.

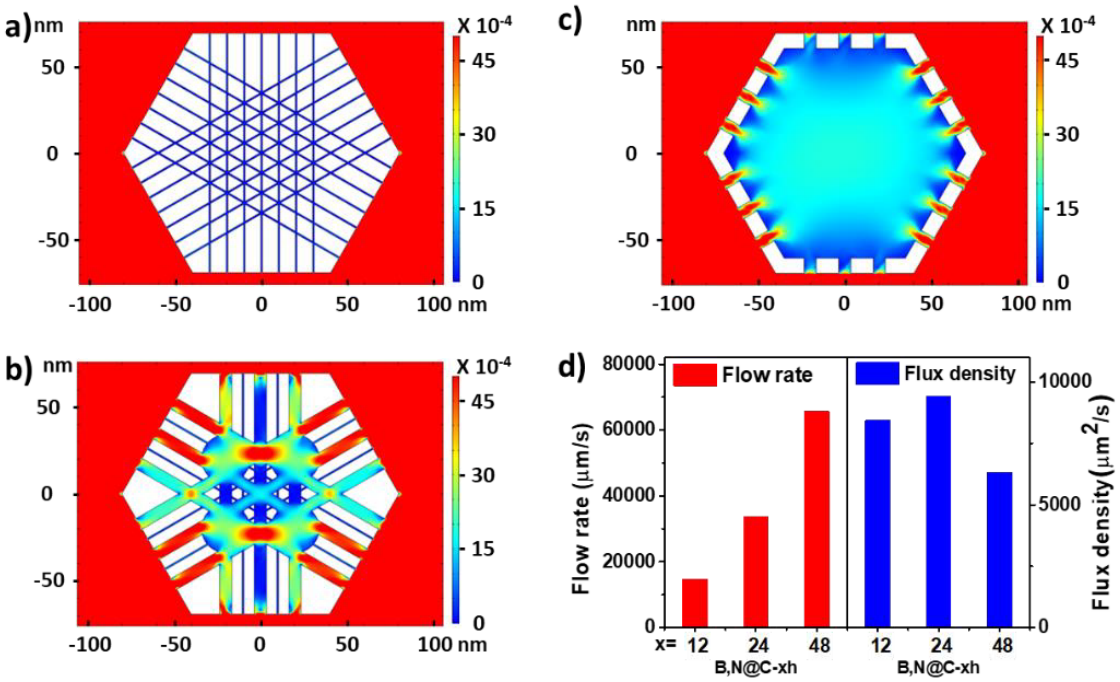

Figure 5.12. Velocity fields of nanoarchitecture models: a) B,N@C-12h, b) B,N@C-24h, and c) B,N@C-48h; d) the simulated flow rate and flux density for B,N@C-12/24/48h.

As discussed above, B,N@C-24h with trimodal-porous structure delivered the largest E_{on}, $E_{1/2}$, and the largest DLCD among these three catalysts, and its performance is comparable to commercial Pt/C (Figure 5.13), which shows an E_{on} of 1.01 V, an $E_{1/2}$ of 0.867 V, and a DLCD of −5.6 mA cm^{-2} at 0.2 mV vs. RHE. Besides, the performance of B,N@C-24

nanoreactors is on par or even better than the reported metal-free carbon-based catalysts (Table 5.3). In contrast, micropore-dominated B,N@C-12h demonstrated lower E_{on}, $E_{1/2,}$ and DLCD than B,N@C-24h though it has the highest heteroatom content (

Table 5.1).

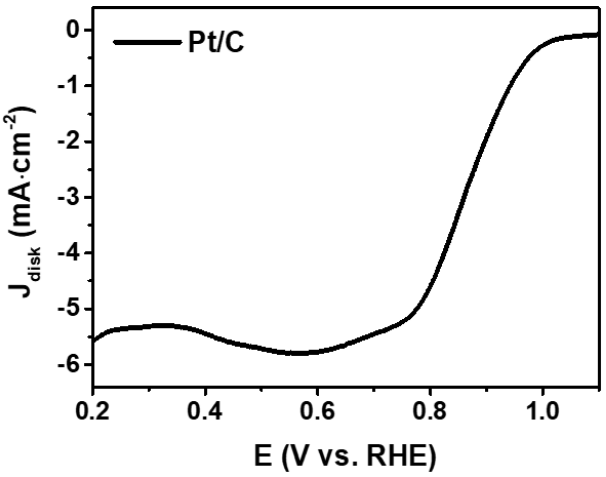

Figure 5.13. LSV curve of commercial Pt/C in an O_2-saturated 0.1 M KOH.

Table 5.3. Comparison of the ORR performance for carbon-based metal-free electrocatalysts in 0.1M KOH.

Catalysts	$E_{1/2}$ (V vs RHE)	DLCD (mA/cm^2)	Pore structures
B,N@C-24h (this work)	0.979	-5.9	Micro/meso/macropores
B,N@C nanotubes [196]	0.820	-5.5	Mesopores
B,N@ordered macroporous C [134]	0.810	-5.2	Micro/meso/macropores
B,N@ordered mesoporous C [226]	0.748	-5.6	Mesopores
B,N@graphene aerogels [132]	0.785	-5.7	Meso/macropores
hollow N@C [159]	0.818	-5.3	Meso/macropores

N, S@C nanosphere [227]	0.870	-6.0	Micro/mesopores

This suggests that certain active sites in the micropores have no contact with the reactants so the ORR rate is limited. [228] In addition, B,N@C-48h with a larger portion of macropores also shows decreased ORR activities compared with B,N@C-24h (Figure 5.10b,d), which is mainly due to reduced surface active sites.

To further test the effect of porous structural engineering on process intensification during ORR, heteroatomic mass activity and kinetic current density (J_K) were calculated. B,N@C-24h with trimodal-porous distributions delivers the highest mass-specific activity and J_k among the three catalysts (Figure 5.14a). In addition, B,N@C-24h possesses the lowest Tafel slope (Figure 5.14b), further manifesting that the trimodal-porous nanoreactor exhibits the fastest kinetics toward ORR. All these results prove that a trimodal-porous nanoreactor is desired for improving both mass transfer and exposure of active sites. Based on RRDE measurement (Figure 5.14c and Figure 5.10b), the average electron transfer number (n) of B,N@C-24h was calculated to be about 3.83 (Figure 5.14d), indicating an efficient $4e^-$ pathway toward ORR, which is desirable for Zinc-air batteries. Similarly, electron transfer numbers were found for B,N@C-12h and B,N@C-48h.

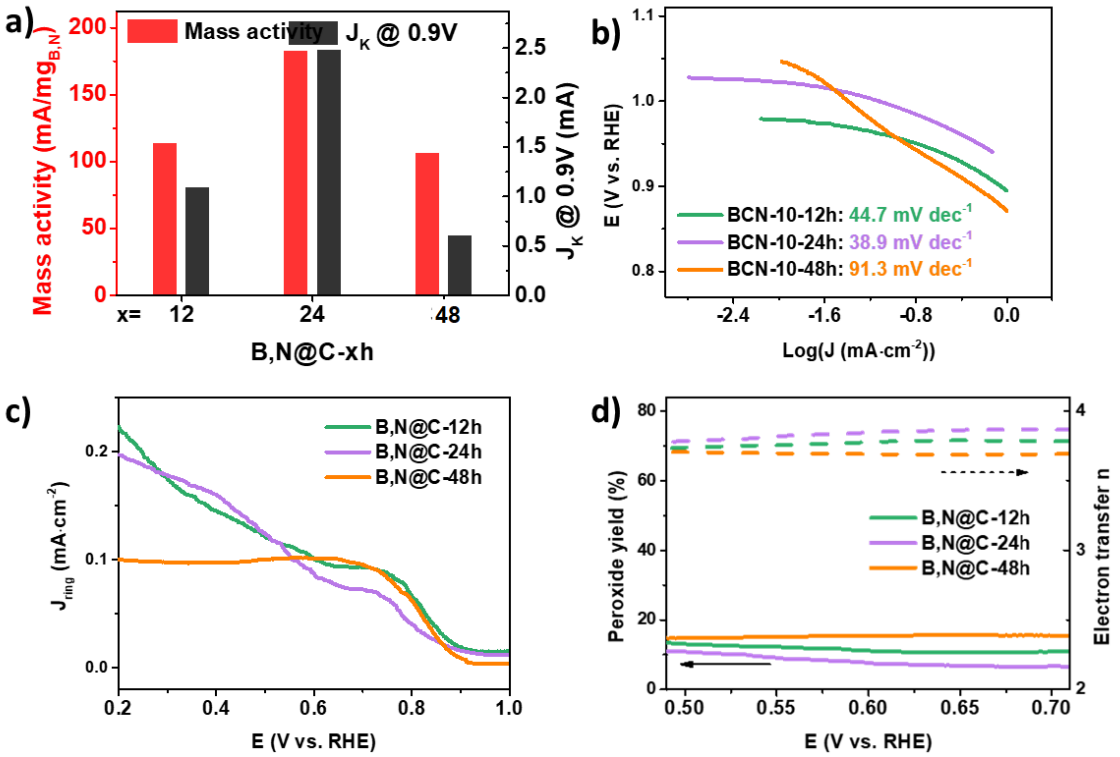

Figure 5.14. a) Mass-specific activities and kinetic current densities, b) Tafel plots, c) The detected ring currents on the Pt ring electrode, and d) electron transfer numbers of B,N@C catalysts in O_2-saturated electrolytes (0.1 M KOH).

5.4 Conclusions

A series of hierarchical porous carbon nanoreactors doped with B and N were obtained via the efficient confined-etching and pyrolysis of ZIFs. The B,N@C nanocages have similar catalytic active sites in terms of intrinsic activity and quantity but have different pores in terms of size and volume. When tested for ORR, the B,N@C nanoreactor with abundant micro-, meso-, and macropores shows the highest catalytic activity. Experimental results and FEA calculations confirm that such trimodal-porous architecture enhances process intensification during ORR because of enhanced mass

transfer and effective active site exposure, in comparison with microporous and macroporous architectures. This work demonstrates the importance of mass transfer during heterogenous catalysis, which should be considered when designing novel catalysts. It also proves the efficacy of host-guest assisted etching strategy, especially with mild etchants, for the synthesis of heteroatom-doped carbon nanoreactor systems.

5.5 Related publications

Wang, X., Liu T., Li, H. *et al.* Balancing mass transfer and active sites to improve electrocatalytic oxygen reduction by B,N co-doped C nanoreactors. *Nano Lett.* **23** 4699-4707 (2023).

Chapter 6 Hollow ZnCo@NC and ZnCo@BNC nanoreactors

6.1 Background

OER is essential in both water-splitting and MABs development. On one hand, electrochemical water splitting technology can enable the environmentally friendly conversion of electric energy to chemical energy [229]. On the other hand, the high theoretical energy density of MABs has made them promising alternatives to LIBs in applications such as electric vehicles [107].

However, OER is a slow process involving 4-electron transfer, which restricts the energy conversion efficiency in water splitting and MABs. Meanwhile, O_2, the product of OER, has low added value. Therefore, electrochemical oxidation of small molecules, such as organic alcohols, which has a relatively low oxidation potential (Figure 6.1) and can be converted into high value-added chemical products under appropriate conditions (Figure 6.2), is a promising alternative to improve the energy conversion efficiency of the overall reaction [230]. To this end, replacement of OER by benzyl alcohol electrochemical oxidation can be an effective way to reduce the potential barrier between anode and cathode and obtain beneficial anodic products at the same time.

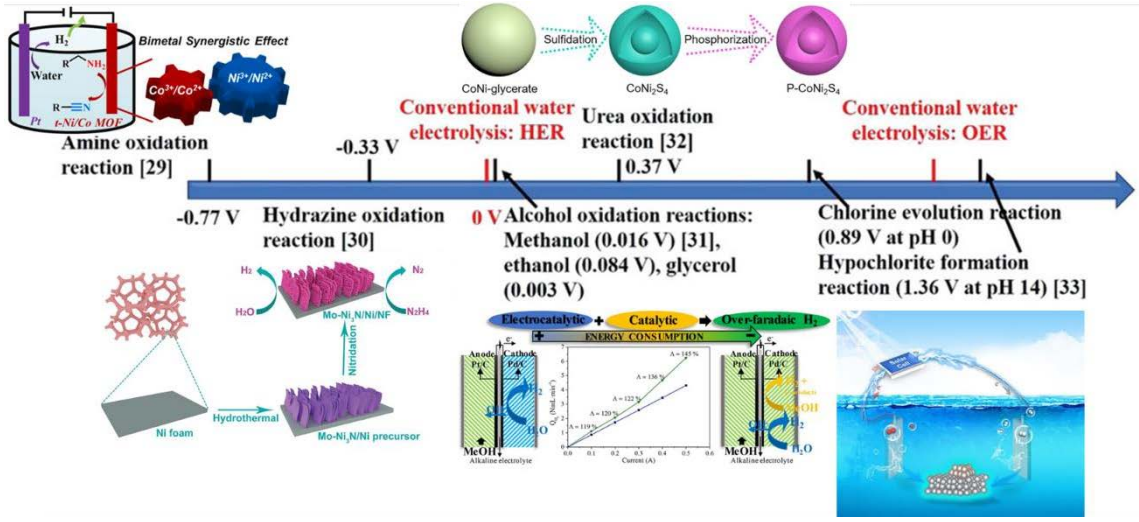

Figure 6.1. Thermodynamic equilibrium potential of hybrid water electrolysis. [230]

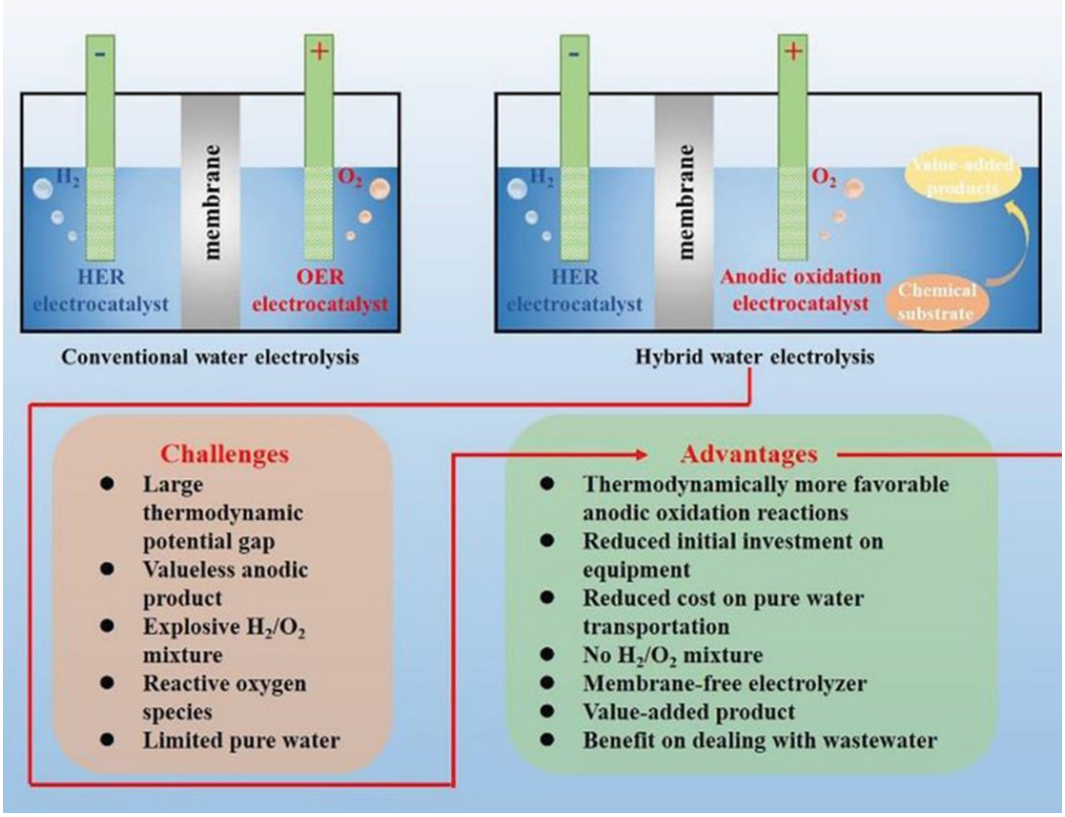

Figure 6.2. Challenges of OER in conventional water electrolysis and advantages of hybrid water electrolysis with electrochemical oxidation of small molecules. [230]

The electrooxidation of benzyl alcohol mainly involves the dehydrogenation with the

cleavage of the C-H bonds [231]. There are two main products of benzyl alcohol electrooxidation. One is benzaldehyde generated by two consecutive oxidation and deprotonation of benzyl alcohol; the other is benzoic acid produced by further oxidation of benzaldehyde (Figure 6.3).

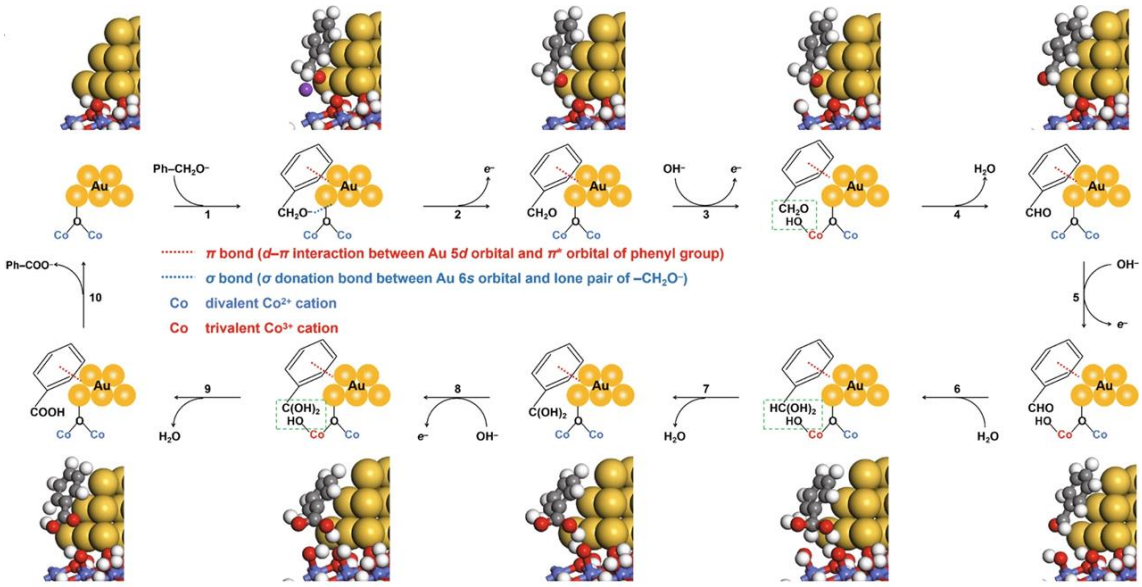

Figure 6.3. Schematic illustration of the proposed mechanism for benzyl alcohol electrooxidation. [231]

At present, there are still some challenges in benzyl alcohol electrooxidation. One challenge is low selectivity. Too strong adsorption and slow mass transfer restrict the desorption of benzaldehyde. If benzaldehyde cannot be desorbed in time, it will lead to excessive oxidation to benzoic acid, thus lowing the formation of benzaldehyde. Another challenge is the slow reaction rate. If substrates and products cannot diffuse in/out in time, the reaction rate will be low, which will cause a low current density and make benzyl alcohol electrooxidation difficult to meet industrial production requirements. Therefore,

research has been focused on 1) improving the substrate/product transfer and 2) accelerating the reaction rate of electrooxidation.

Herein, the research objectives of this chapter are:

a) Build ZnCo@NCO and ZnCo@NCBO nanoreactors for benzyl alcohol electrooxidation.

b) Study the structure-activity relationship of the nanoreactor in benzyl alcohol electrooxidation.

c) Understand the effects of nanoreactors via *in-situ* technologies and theoretical calculations.

6.2 Experimental

6.2.1 Synthesis of ZnCo-ZIF

$Zn(NO_3)_2 \cdot 6H_2O$ (1.787 g) and $Co(NO_3)_2 \cdot 6H_2O$ (1.745 g) were dissolved in 100 mL methanol to form solution A. Solution B contains 7.88 g 2-MIM dissolved in 100 mL methanol. Then, solution B was added to solution A. The mixture was stirred for 10 min at first and then aged under a static condition at room temperature for 24 h. The resultant purple precipitate was collected by centrifugation, washed with methanol three times, and finally dried overnight.

6.2.2 Synthesis of ZnCo-ZIF-O-x

In a typical synthesis, 300 mg of ZnCo-ZIF was added to 120 mL of DMF and ultrasonically treated for 10 min to form a uniform suspension. O_2 was then bubbled into the ZnCo-ZIF dispersion at 20 sccm with stirring for different times at 140 °C. The resultant solids were collected by centrifugation and freeze-drying and labelled as ZnCo-ZIF-O-xh, where x is the treatment time. For the reference sample, ZnCo-ZIF was treated in DMF without O_2 feeding for 4 h, named ZnCo-ZIF-DMF.

6.2.3 Synthesis of ZnCo-ZIF-AB-x

In a typical synthesis, 300 mg of ZnCo-ZIF was added to 60 mL of DMF and ultrasonically treated for 10 min to form a uniform suspension A. Solution B contains 300 mg AB dissolved in 60 mL DMF. Solution B was added to solution A under stirring at a rate of 2 mL/min. Then the mixture was stirred for different time at 140 °C. The resultant solids were collected by centrifugation and freeze drying and labelled as ZnCo-ZIF-AB-xh, where x is the treatment time.

6.2.4 Synthesis of ZnCo-ZIF-ABO-r-x

In a typical synthesis, 300 mg of ZnCo-ZIF was added to 60 mL of DMF and ultrasonically treated for 10 min to form a uniform suspension A. Solution B contains 300 mg AB dissolved in 60 mL DMF. Solution B was added to solution A under stirring at a rate of 2 mL/min, together with O_2 feeding at 20 sccm. Then the mixture was stirred for

different time at different temperatures with O_2 feeding at 20 sccm. The resultant solids were collected by centrifugation and freeze drying and labelled as ZnCo-ZIF-ABO-r-xh, where r is the weight ratio of AB to ZnCo-ZIF and x is the treatment time.

6.2.5 Synthesis of ZnCo@NCO-x

In a typical synthesis, the obtained ZnCo-ZIF-O-x were heated from room temperature to 500 °C at a heating rate of 2 °C min^{-1} and held at 500 °C for 1 h under N_2. The obtained samples were denoted as ZnCo@NCO-x. For the reference sample, pure ZnCo-ZIF was pyrolyzed under the same condition, named ZnCo@NC.

6.2.6 Synthesis of ZnCo@NCBO-T

In a typical synthesis, the obtained ZnCo-ZIF-ABO-1-6 was heated from room temperature to 600 °C and 700 °C at a heating rate of 2 °C min^{-1} and held for 1 h under N_2, respectively. The obtained samples were denoted as ZnCo@NCBO-T, where T is temperature of pyrolysis.

6.3 Results and discussion

6.3.1 Multilevel hollow ZnCo-ZIF-O-x

As illustrated in Figure 6.4, O_2 was applied to etch ZnCo-ZIF in DMF forming ZnCo-ZIF-O-x. In this way, pores are formed through efficient etching and partial oxidation by O_2. In the subsequent pyrolysis step, ZnCo-ZIF-O-x was transformed to corresponding

ZnCo@NCO-x nanoreactors with various structures.

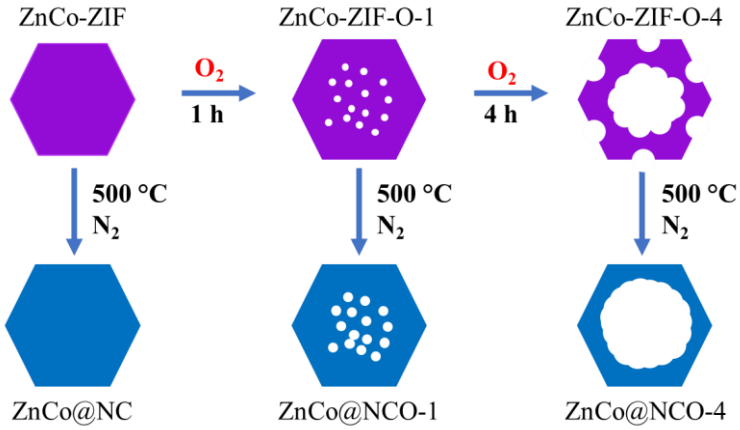

Figure 6.4. Schematics of the preparation of the ZnCo@NCO-x nanoreactors.

The morphologies were first examined with SEM and TEM. It can be seen from Figure 6.5a,b ZnCo-ZIF shows a rhombic dodecahedral structure with a smooth surface and without cavities inside. After treatment by O_2 for 4 h, visible pores are on the surface (Figure 6.5c) and random cavities with irregular distribution appeared inside (Figure 6.5d). From the optical observation of ZnCo-ZIF and ZnCo-ZIF-O-4 (Figure 6.5a and Figure 6.5c), the color of ZnCo-ZIF changes from purple to purple-red due to the change of absorbance. To exclude the effect of solvent, ZnCo-ZIF was treated directly in DMF without feeding O_2. As seen from Figure 6.5e,f, there is no significant change in the color and morphology of the sample, indicating that etching is caused by O_2 rather than solvent.

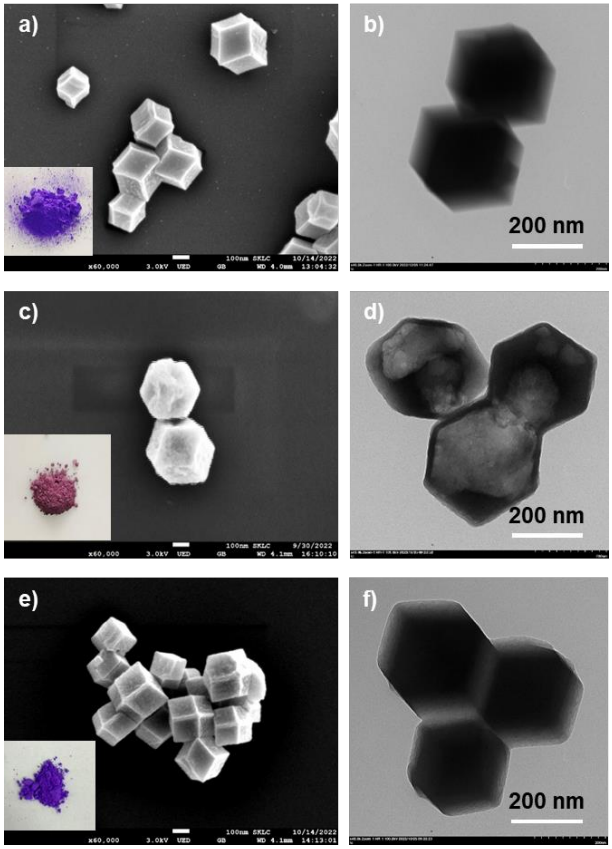

Figure 6.5. (a), (c), (e) SEM images (inset: the optical images) and (b), (d), (f) TEM images of ZnCo-ZIF, ZnCo-ZIF-O-4, and ZnCo-ZIF-DMF.

To investigate the structural change, XRD measurement and N_2 adsorption−desorption analysis were carried out (Figure 6.6). The XRD pattern of ZnCo-ZIF-O-4 agrees well with the original ZnCo-ZIF, but with reduced diffraction intensity (Figure 6.6a). Furthermore, a slight shift in the XRD peaks of ZnCo-ZIF-O-4 compared with those of the original ZnCo-ZIF is shown in Figure 6.6b. These results demonstrate that the crystalline structure of ZnCo-ZIF does not vary much, but defects are generated during etching [65, 232].

Based upon N_2 adsorption−desorption analysis, surface area decreases with the

prolonging of the etching time (Figure 6.6c and

Table 6.1), demonstrating that the microporous structure of ZnCo-ZIF was partially destroyed by the etching process. Besides, ZnCo-ZIF-O-1 shows a high percent of micropores, while ZnCo-ZIF-O-6 shows a larger portion of meso- to macropores (Figure 6.6d and

Table 6.1). The mesopores and interior cavities generated by etching would facilitate the mass diffusion of substrates and products.

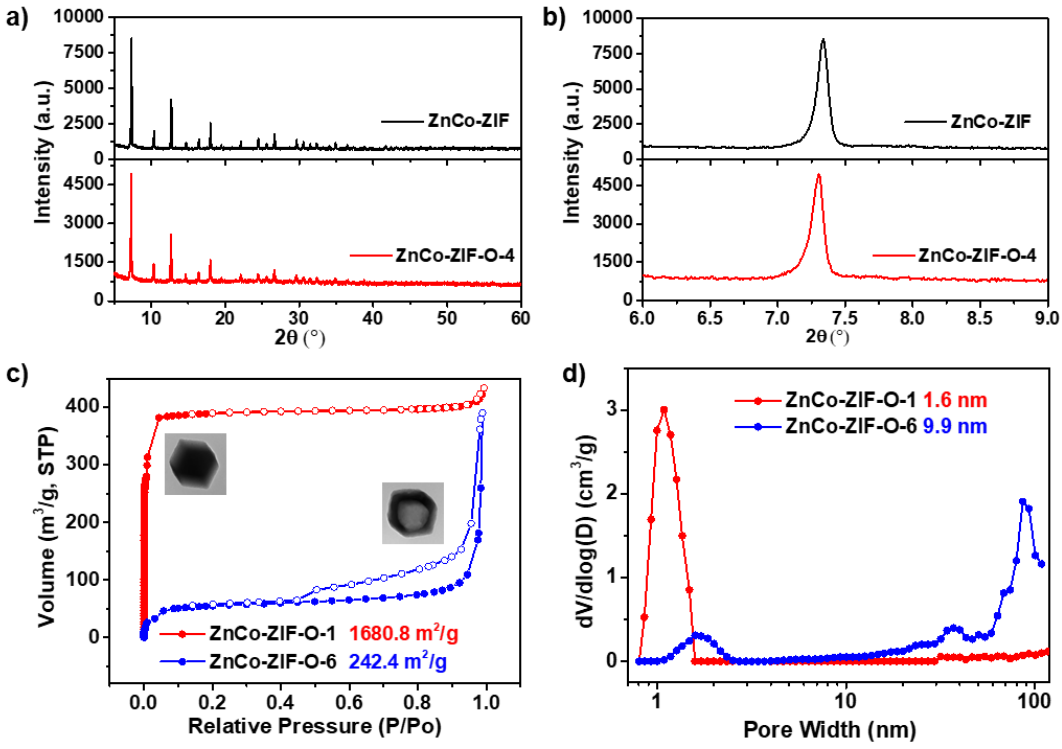

Figure 6.6. (a) Full-range PXRD and (b) selected XRD patterns of ZnCo-ZIF and ZnCo-

ZIF-O-x. (c) N_2 adsorption-desorption isotherms of ZnCo-ZIF-O-1 and ZnCo-ZIF-O-6 at −196 °C, and (d) their corresponding pore size distributions calculated using NL-DFT method.

Table 6.1. N_2 adsorption−desorption results of ZnCo-ZIF-O-1 and ZnCo-ZIF-O-6.

Sample	Surface area (m^2/g)	Micropore area (m^2/g)	Pore volume (cm^3/g)	Micropore volume (cm^3/g)	Average pore diameter (nm)
ZnCo-ZIF-O-1	1680.79	1660.72	0.67	0.59	1.59
ZnCo-ZIF-O-6	242.44	189.17	0.60	0.06	9.95

FTIR and XPS measurements were carried out to study the etching mechanisms. As shown in Figure 6.7a, bands associated with the 2-MIM ring stretching at 1420 cm^{-1}, in-plane bending at 800–1350 cm^{-1}, and out-of-plane bending below 800 cm^{-1} demonstrate that ZnCo-ZIF-O-x still has the basic chemical characters of ZnCo-ZIF after etching. In addition, the presence of C−O, N−O, Zn/Co−O IR bands in ZnCo-ZIF-O-x framework confirms that O_2 causes the etching. XPS survey scans show a significant increase in O amount (Figure 6.7b), further indicating the incorporation of O in the product. Chemical states were further analyzed with high-resolution XPS. From the high-resolution XPS spectra of N 1s of ZnCo-ZIF and ZnCo-ZIF-O-6 (Figure 6.7c), the ratio of N-Zn/Co to N-C is decreased, indicating that N-Zn/Co coordination bonds were partially destroyed during O_2 etching. Besides, high-resolution XPS spectra of O 1s after O_2 etching can be

deconvolved into three peaks (Figure 6.7d). Except the peak of H_2O (532.8 eV), another two peaks can be assigned to Zn/Co−OH (531.4 eV) and C−OH (530.7 eV), demonstrating that O atoms are mainly bonded with metal atoms and C atoms after etching. High-resolution XPS spectra of Co 2p and C 1s also prove this point as evidenced by the emerging Co−O species (780.2 eV) and the increasing tensity of C−O/O=C−O (287.7 eV) in ZnCo-ZIF-O-6, compared with the parent ZnCo-ZIF (Figure 6.7e,f). These results confirm that O_2 etching converts Zn/Co−N coordination bonds in ZnCo-ZIF to Zn/Co-O, accompanied by oxidation of C species.

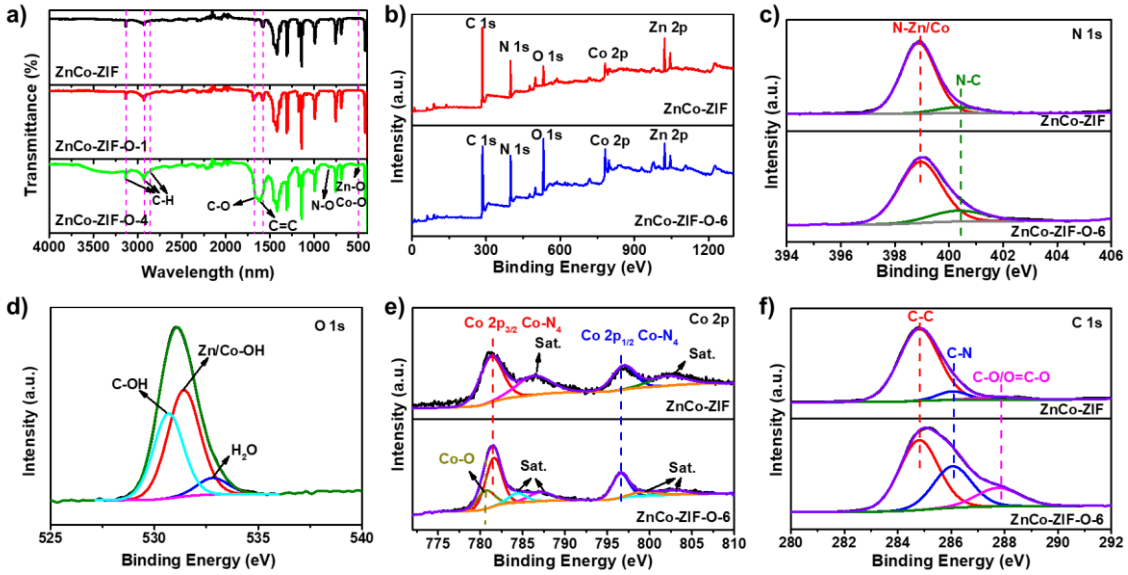

Figure 6.7. (a) FTIR spectra of ZnCo-ZIF, ZnCo-ZIF-O-1 and ZnCo-ZIF-O-4. (b) XPS survey spectra of ZnCo-ZIF and ZnCo-ZIF-O-6. (c-f) High-resolution XPS spectra of N

1s, O 1s, Co 2p, and C 1s.

6.3.2 ZnCo@NCO-x nanoreactors for OER and benzyl alcohol electrooxidation

To prepare various ZnCo@NC-based nanoreactors, ZnCo-ZIF and ZnCo-ZIF-O-x were carbonized at 500 °C under N_2. TEM images reveal the structural evolution caused by heating (Figure 6.8). Hollow ZnCo@NCO structures were obtained after heating for 2 h, and the shell became thinner with the prolongation of the heating (Figure 6.8c,d). The conjectured structure models are inserted into the top right-hand corners of the TEM figures (Figure 6.8).

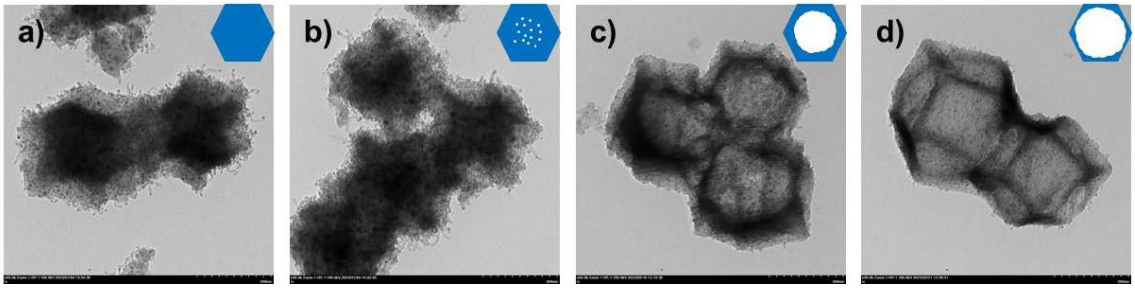

Figure 6.8. TEM images of (a) ZnCo@NC, (b) ZnCo@NCO-1, (c) ZnCo@NCO-2, and (d) ZnCo@NCO-4.

To examine the influence of structure on catalytic performance, the OER activities of ZnCo@NC, ZnCo@NCO-1, and ZnCo@NCO-4 catalysts were first evaluated by LSV polarization tests in 1 M KOH at a scan rate of 10 mV/s (Figure 6.9a). LSV profile shows that the overpotential decreases gradually with etching time, and the hollow ZnCo@NCO-4 requires 1.52 V vs. RHE to reach a current density of 10.0 $mA \cdot cm^{-2}$.

Furthermore, the overpotentials of ZnCo@NC, ZnCo@NCO-1, and ZnCo@NCO-4 were significantly reduced for the electrooxidation of benzyl alcohol (Figure 6.9b). Similar to OER, the performance of benzyl alcohol electrooxidation increases with etching time. In particular, the potential of ZnCo@NCO-4 was reduced to 1.38 V at 10.0 $mA \cdot cm^{-2}$, which is less than those of ZnCo@NCO-1 (1.44 V) and ZnCo@NC (1.53 V). Therefore, the hollow nanoreactor is more conducive to electrocatalytic reaction.

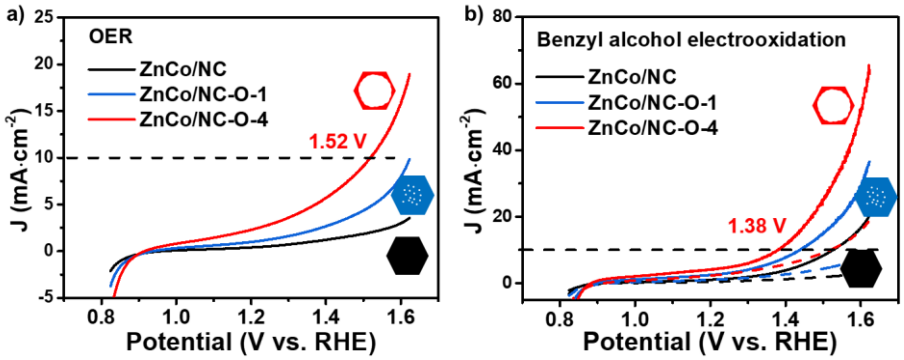

Figure 6.9. (a) LSV curves for OER on ZnCo@NC, ZnCo@NCO-1, and ZnCo@NCO-4 in 1.0 M KOH. (b) LSV curves of ZnCo@NC, ZnCo@NCO-1, and ZnCo@NCO-4 in 1.0 M KOH with (solid line) and without (dotted line) 0.02 mmol benzyl alcohol.

6.3.3 Synthesis of yolk-shelled ZnCo-ZIF-ABO-r-x structures via AB and O_2 co-assisted etching

To introduce heteroatomic boron into catalysts, ZnCo-ZIF-ABO-x was fabricated by treating ZnCo-ZIF in DMF at 140 °C with AB and O_2 as the etchants. TEM images reveal the impact of AB amount on the structure of ZnCo-ZIF-ABO-r-1 nanoparticles (Figure 6.10a-c). ZnCo-ZIF-ABO-0-1 retains the solid rhombic dodecahedral structure of the

parent ZnCo-ZIF (Figure 6.10a). Increasing the AB amount leads to the formation of yolk−shell structures after treatment for 1 h (Figure 6.10b,c). Besides, a hollow structure was obtained after 6 h etching (Figure 6.10d). Unlike ZnCo-ZIF-O-4 with pores on the surface, the shell of nanoparticles forms for ZnCo-ZIF-ABO-1-6 (Figure 6.10e). Meanwhile, shells consisting of stacked nanoparticles also appeared on the surface of ZnCo-ZIF-AB-6 (Figure 6.10f,g) which was obtained with AB etchant only, indicating a specific role of AB in etching.

To explore the formation mechanism of the shell, $Zn(NO_3)_2 \cdot 6H_2O$, $Co(NO_3)_2 \cdot 6H_2O$), and AB are first mixed in DMF to obtain a transparent solution. After heating to 140 ℃, and purple precipitate appeared (Figure 6.10h). Polyiminoborane (PAB, $[-H_2N\text{-}BH_2\text{-}]_n$) can be produced by the thermal decomposition of AB in the range of 95-132 °C [189], which maycoordinate with metal ions to form precipitates, named PAB-ZnCo. Both the optical color and the nanoparticle-like morphology of the precipitate are consistent with the characteristics of ZnCo-ZIF-AB-6 shell (Figure 6.10h,i). Subsequently, O_2 was bubbled into PAB-ZnCo dispersion at 140 °C, and the precipitate changed from purple to brown (Figure 6.10j). Given the competitive coordination ability of O to metal discussed in Chapter 6.3.1, the brown nanoparticle-like precipitate (Figure 6.10j.k) is assumed to be PAB-ZnCo-O coordination polymer. Both the optical color and the nanoparticle-like morphology of the PAB-ZnCo-O precipitate are consistent with the characteristics of ZnCo-ZIF-ABO-1-6. In addition, after co-etching by AB and O_2 for 6 h, XRD

characteristic peaks of ZnCo-ZIF and stretching vibration of Zn/Co-N in FTIR spectrum disappear (Figure 6.10l,m), while IR bands associated with PAB dominate the FTIR spectrum of ZnCo-ZIF-ABO-1-6 sample. These results are also consistent with the hypothesis that the original coordination bonds in ZnCo-ZIF completely break under the treatment by AB and O_2.

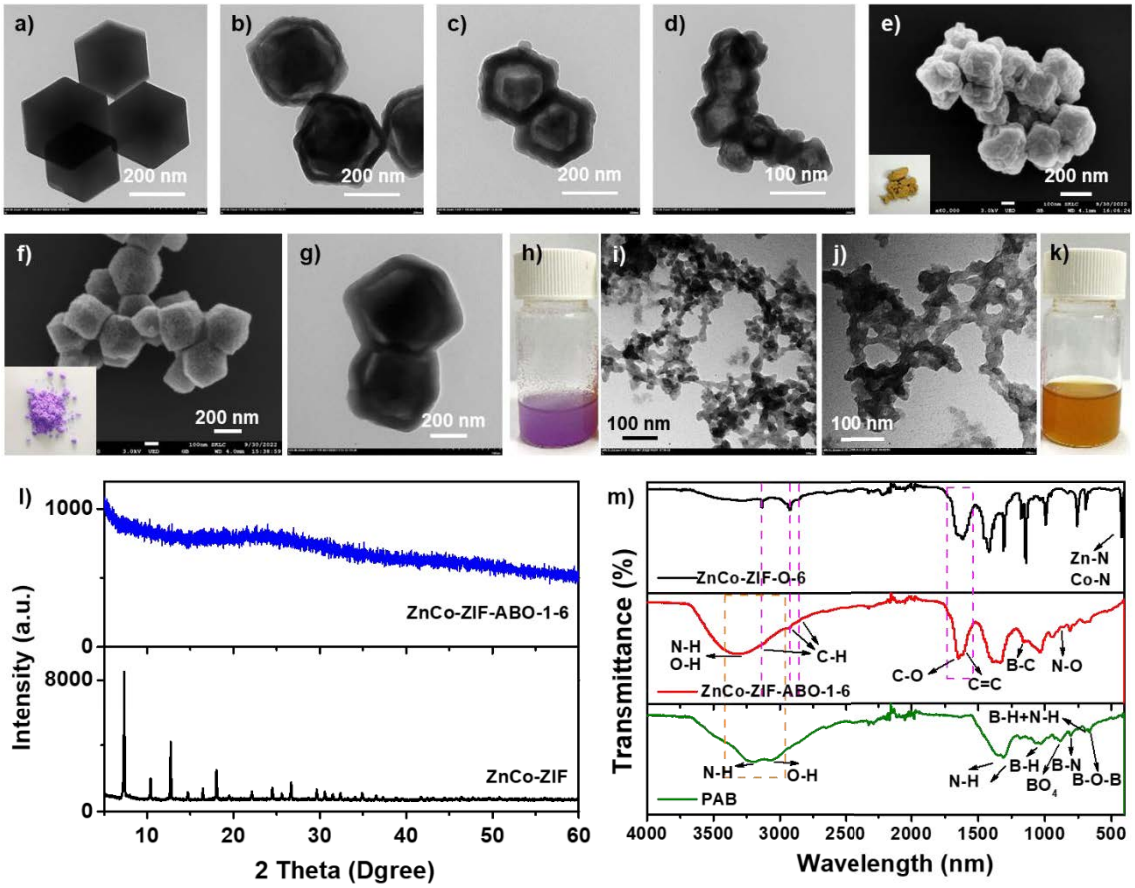

Figure 6.10. TEM images of (a) ZnCo-ZIF-O-1, (b) ZnCo-ZIF-ABO-0.5-1, (c) ZnCo-ZIF-ABO-1-1, (d) ZnCo-ZIF-ABO-1-6, (g) ZnCo-ZIF-AB-6, (i) PAB-ZnCo, and (j) PAB-ZnCo-O. SEM images (inset: the optical images) of (e) ZnCo-ZIF-ABO-1-6 and (f) ZnCo-ZIF-AB-6. Optical images of (h) PAB-ZnCo and (k) PAB-ZnCo-O. (l) PXRD patterns of ZnCo-ZIF and ZnCo-ZIF-ABO-1-6. (m) FTIR spectra of ZnCo-ZIF-O-6,

ZnCo-ZIF-ABO-1-6, and PAB.

XPS measurement was also carried out to study the chemical composition of ZnCo-ZIF-AB-1-6. XPS survey scan and the elemental contents of ZnCo-ZIF-ABO-1-6 calculated according to the high-resolution XPS spectra show a significant amount of C (Figure 6.11a and Table 6.2). The co-existence of Co-O, Co-Nx, and Co-Nx-B in the high-resolution XPS spectrum of Co 2p indicates the complexity of the coordination environment around the metal ions (Figure 6.11b). Also, the co-existence of B-C (Figure 6.11c,d), B-N (Figure 6.11c,e), B-O (Figure 6.11c), C-N (Figure 6.11d,e), and, C-O/O=C-O (Figure 6.11d,f) in high-resolution XPS spectrum also indicates the interconnected ligands in ZnCo-ZIF-ABO-1-6.

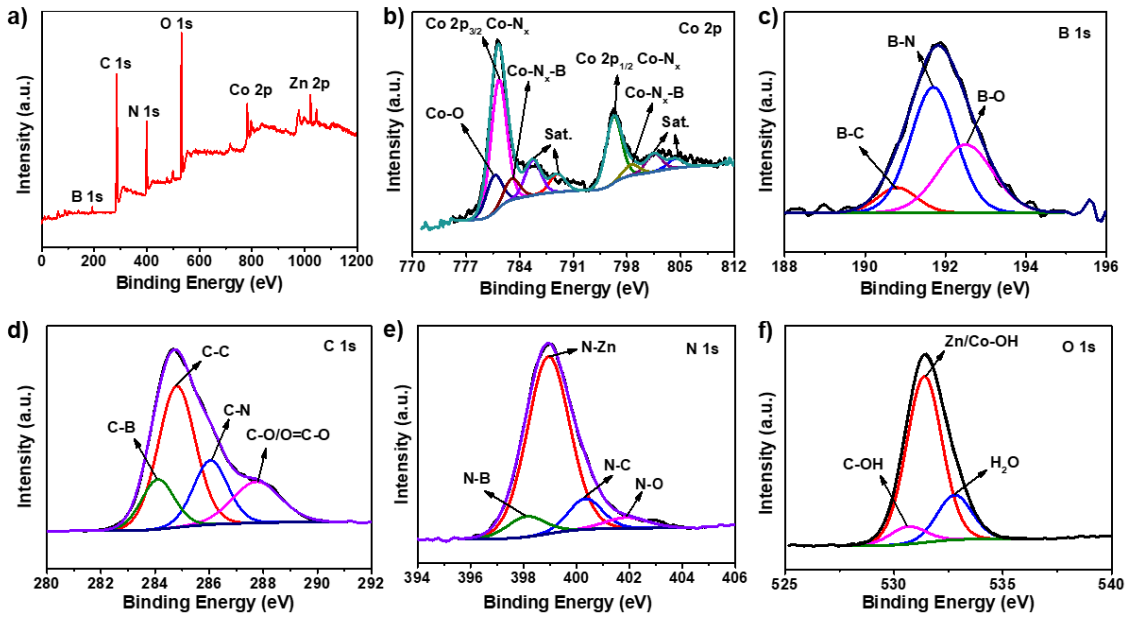

Figure 6.11. (a) XPS survey spectrum and (b-f) high-resolution XPS spectra of Co 2p, B

1s, C 1s, N 1s, and O 1s for ZnCo-ZIF-ABO-1-6.

Table 6.2. Elemental contents calculated according to the high-resolution XPS spectra of ZnCo-ZIF-ABO-1-6.

Sample	Elemental content (at.%)					
	B	C	N	O	Co	Zn
ZnCo-ZIF-ABO-1-6	4.55	54.99	16.13	20.73	2.43	1.19

According to ICP results, the contents of Zn, Co, and B are similar between the samples etched for 0.5 h and 6 h (Table 6.3). Therefore, AB likely rapidly decomposes at 140 °C and polymerizes on the Zn-Co-ZIF surface, and the ZIF core is gradually consumed with continuous etching. Finally, a hollow structure that consists of Zn, Co, 2-MIM, PAB, and O is obtained. Through similar etching process, a series of nanomaterials with different structures have been obtained, which can be very beneficial to be used as the precursors to B,N@C catalysts anchored with Zn, Co nanoparticles.

Table 6.3. Elemental contents derived from ICP analysis.

Sample	Elemental content (wt.%)		
	Zn	Co	B
ZnCo-ZIF	9.15	14.17	16.13
ZnCo-ZIF-ABO-1-0.5	5.91	8.94	10.05
ZnCo-ZIF-ABO-1-6	5.42	8.22	8.22

6.3.4 Synthesis of hollow ZnCo@NCBO-T nanoreactors

To prepare various ZnCo@NCBO-based nanoreactors, ZnCo-ZIF-ABO-6 was carbonized at 600 °C and 700 °C under N_2, respectively. TEM images reveal that hollow ZnCo@NCBO-600 and ZnCo@NCBO-700 were formed after carbonization (Figure 6.12a-d). After immersing in hydrochloric acid, big nanoparticles in ZnCo@NCBO-700 was removed and hollow ZnCo@NCBO-700-HCl was obtained (Figure 6.12e,f). For comparison, Pt nanoparticles were introduced inside the ZnCo@NCBO-700-HCl via impregnation at low pressures (Figure 6.12g,h).

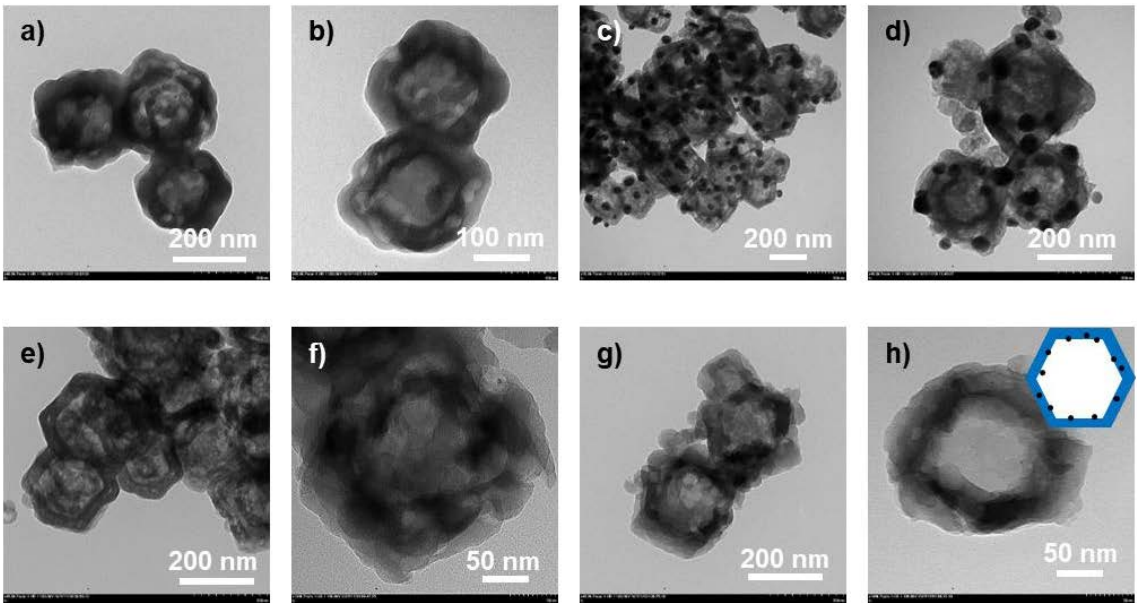

Figure 6.12. TEM images of (a,b) ZnCo@NCBO-600, (c,d) ZnCo@NCBO-700, (e,f) ZnCo@NCBO-700-HCl, and (g,h) Pt@ZnCo@NCBO-700-HCl.

6.4 Conclusions

In summary, I have developed an effective method for the fabrication of hollow B-doped

C and B,N co-doped C nanoreactors incorporated with Zn, Co nanoparticles. O_2 and AB play important roles in the fabrication processes. The hollow structure of ZnCo@NCO can be beneficial for the electrocatalytic processes including OER and benzyl alcohol electrooxidation. Unfortunately, due to various constraints, the electrocatalytic reactions have not been carried out on ZnCo@NCBO samples.

Chapter 7 Conclusions and outlook

7.1 Conclusions

In this PhD work, effective fabrication of monodispersed porous B,N@C nanocages was first developed via an integrated double-solvent impregnation and nanoconfined-etching method. The encapsulation of boron-containing etchants including AB and BA in the ZIF-8 pores plays an important role in achieving a uniform and dense doping of B atoms in the N@C nanocages and inducing the hierarchical structures with micro/meso/macro multimodal pore size distribution. The resultant B,N@C-AB and B,N@C-BA nanocages displayed high catalytic activities for electrochemical ORR in alkaline media, outperforming most carbon-based catalysts, particularly from the perspective of the half-wave potentials. Such high catalytic performance is due to the enhanced activity by the coexistence of B and N and the mass transfer promoted by the unique hierarchical porous structure. This work reveals a novel strategy to achieve hierarchical porous B,N@C catalysts, i.e., confining small B-containing guests as etchants into MOF precursors, which can be used in various energy conversion and storage applications.

The importance of mass transfer in electrocatalytic ORR was further investigated by tailoring the pore sizes of B,N@C nanoreactors. A series of B,N@C electrocatalysts featuring abundant active sites but different porous structures were prepared by AB

confined-etching. The ORR performance of these catalysts was found to correlate with the diffusion of the reactant. The optimized B,N@C with trimodal-porous structures feature enhanced O_2 diffusion and better activity per heteroatomic site toward the ORR process. FEA calculations confirm that such trimodal-porous architecture enhances process intensification during ORR because of improved mass transfer and effective active site exposure, in comparison with microporous and macroporous architectures. This work demonstrates the significance of the nanoarchitecture-engineering of catalysts and also sheds light on how to optimize structure featuring abundant active sites and enhanced mass transfer.

In addition, ZnCo@NCO and ZnCo@NCBO nanoreactors were also fabricated via novel etching strategies. Pore sizes, surface areas, pore volumes, chemical composition of the derived structures can be largely tuned and controlled. By incorporating different metal nanoparticles, these structures can be effective catalysts for electrooxidation of small organic molecules.

7.2 Outlook

7.2.1 Deep understanding of the nanoreactor effect of ZnCo@NCO in OER and selective electrooxidation of benzyl alcohol

In this thesis, a series of ZnCo@NCO nanoreactors with different cavity sizes were prepared via an O_2 assisted etching method. The structure-activity relationship of

ZnCo@NCO nanoreactors on OER and benzyl alcohol electrooxidation in alkaline media is yet to be carried out. An in-depth understanding of mass transfer and electrochemical conversion of benzyl alcohol is desired. Specifically, the impacts of spatial confinement, substrate enrichment, preferential adsorption, mass transfer enhancement, and microenvironment control on OER and benzyl alcohol electrooxidation need to be investigated.

7.2.2 Further investigation of synthetic mechanism and electrocatalytic performance of ZnCo@NCBO nanoreactors

In this thesis, yolk-shelled and hollow ZnCo-ZIF-ABO precursors were prepared via an AB and O_2 co-assisted etching method. However, more characterization needs to be carried out to understand the principles of materials synthesis from the molecular and atomic level. The relationships between mass transfer, active sites, and electrocatalytic performance of ZnCo@NCBO need to be investigated.

7.2.3 Assemble of electrochemical energy storage device

Electrocatalysts for ORR, OER, and benzyl alcohol electrooxidation have been prepared in this thesis. They can be a key part of an electrochemical device such as metal air batteries and water electrolyzers. To assess their full potentials in practical applications, devices should be assembled to test efficiency, selectivity, cycling performance, etc.

References

[1] R.-P. Ye, X. Wang, C.-A.H. Price, X. Liu, Q. Yang, M. Jaroniec, J. Liu; Engineering of yolk/core–shell structured nanoreactors for thermal hydrogenations. Small. 2021, 17, 1906250.

[2] Z. Xiong, B. Sun, H. Zou, R. Wang, Q. Fang, Z. Zhang, S. Qiu; Amorphous-to-crystalline transformation: General synthesis of hollow structured covalent organic frameworks with high crystallinity. J. Am. Chem. Soc. 2022, 144, 6583-6593.

[3] Z. Yu, X. Lu, L. Sun, J. Xiong, L. Ye, X. Li, R. Zhang, N. Ji; Metal-loaded hollow carbon nanostructures as nanoreactors: Microenvironment effects and prospects for biomass hydrogenation applications. ACS Sustainable Chemistry & Engineering. 2021, 9, 2990-3010.

[4] Z. Yu, N. Ji, X. Li, R. Zhang, Y. Qiao, J. Xiong, J. Liu, X. Lu; Kinetics driven by hollow nanoreactors: An opportunity for controllable catalysis. Angew. Chem. Int. Ed. 2023, 62, e202213612.

[5] X. Zhang, G. Li, G. Chen, D. Wu, Y. Wu, T.D. James; Enzyme mimics for engineered biomimetic cascade nanoreactors: Mechanism, applications, and prospects. Adv. Funct. Mater. 2021, 31, 2106139.

[6] X. Wang, P. Su, M.S. Duyar, J. Liu; Microenvironment and nanoreactor engineering of single-site metal catalysts for electrochemical CO_2 reduction. Energy Fuels. 2021, 35, 9795-9808.

[7] Y. Boyjoo, H. Shi, Q. Tian, S. Liu, J. Liang, Z.-S. Wu, M. Jaroniec, J. Liu; Engineering nanoreactors for metal–chalcogen batteries. Energy Environ. Sci. 2021, 14, 540-575.

[8] M. Viciano-Chumillas, M. Mon, J. Ferrando-Soria, A. Corma, A. Leyva-Pérez, D. Armentano, E. Pardo; Metal–organic frameworks as chemical nanoreactors: Synthesis and stabilization of catalytically active metal species in confined spaces. Acc. Chem. Res. 2020, 53, 520-531.

[9] W. Zhu, Z. Chen, Y. Pan, R. Dai, Y. Wu, Z. Zhuang, D. Wang, Q. Peng, C. Chen, Y. Li; Functionalization of hollow nanomaterials for catalytic applications: Nanoreactor construction. Adv. Mater. 2019, 31, 1800426.

[10] M. Yang, C.H. Zhang, N.W. Li, D. Luan, L. Yu, X.W. Lou; Design and synthesis of hollow nanostructures for electrochemical water splitting. Advanced Science. 2022, 9, 2105135.

[11] X. Liu, G. Verma, Z. Chen, B. Hu, Q. Huang, H. Yang, S. Ma, X. Wang; Metal-organic framework nanocrystal-derived hollow porous materials: Synthetic strategies and emerging applications. The Innovation. 2022, 3, 100281.

[12] Y. Feng, J. Yao; Tailoring the structure and function of metal organic framework by chemical etching for diverse applications. Coord. Chem. Rev. 2022, 470, 214699.

[13] S.-Q. Zhu, J.-C. Shu, M.-S. Cao; Tailorable MOF architectures for high-efficiency electromagnetic functions. Mater. Chem. Front. 2021, 5, 6444-6460.

[14] X. Zhou, H. Jin, B.Y. Xia, K. Davey, Y. Zheng, S.-Z. Qiao; Molecular cleavage of

metal-organic frameworks and application to energy storage and conversion. Adv. Mater. 2021, 33, 2104341.
[15] Q. Dang, Y. Li, W. Zhang, Y.V. Kaneti, M. Hu, Y. Yamauchi; Spatial-controlled etching of coordination polymers. Chin. Chem. Lett. 2021, 32, 635-641.
[16] X. Song, Y. Jiang, F. Cheng, J. Earnshaw, J. Na, X. Li, Y. Yamauchi; Hollow carbon-based nanoarchitectures based on ZIF: Inward/outward contraction mechanism and beyond. Small. 2020, 17, 2004142.
[17] H. Yang, X. Wang; Secondary-component incorporated hollow MOFs and derivatives for catalytic and energy-related applications. Adv. Mater. 2019, 31, 1800743.
[18] J. Nai, X.W. Lou; Hollow structures based on prussian blue and its analogs for electrochemical energy storage and conversion. Adv. Mater. 2019, 31, 1706825.
[19] D. Liu, J. Wan, G. Pang, Z. Tang; Hollow metal–organic-framework micro/nanostructures and their derivatives: Emerging multifunctional materials. Adv. Mater. 2019, 31, 1803291.
[20] Z.-X. Cai, Z.-L. Wang, J. Kim, Y. Yamauchi; Hollow functional materials derived from metal–organic frameworks: Synthetic strategies, conversion mechanisms, and electrochemical applications. Adv. Mater. 2019, 31, 1804903.
[21] K. Li, J. Yang, J. Gu; Hierarchically porous MOFs synthesized by soft-template strategies. Acc. Chem. Res. 2022, 55, 2235-2247.
[22] E. Doustkhah, R. Hassandoost, A. Khataee, R. Luque, M.H.N. Assadi; Hard-templated metal–organic frameworks for advanced applications. Chem. Soc. Rev. 2021, 50, 2927-2953.
[23] R.-P. Zhang, W.-C. Li, G.-P. Hao, A.-H. Lu; Confined nanospace pyrolysis: A versatile strategy to create hollow structured porous carbons. Nano Research. 2021, 14, 3159-3173.
[24] X. Liu, G. Verma, Z. Chen, B. Hu, Q. Huang, H. Yang, S. Ma, X. Wang; Metal-organic framework nanocrystal-derived hollow porous materials: Synthetic strategies and emerging applications. Innovation (Camb). 2022, 3, 100281.
[25] L. Li, Y. Li, L. Jiao, X. Liu, Z. Ma, Y.-J. Zeng, X. Zheng, H.-L. Jiang; Light-induced selective hydrogenation over pdag nanocages in hollow MOF microenvironment. J. Am. Chem. Soc. 2022, 144, 17075-17085.
[26] K. Shen, L. Zhang, X. Chen, L. Liu, D. Zhang, Y. Han, J. Chen, J. Long, R. Luque, Y. Li, et al.; Ordered macro-microporous metal-organic framework single crystals. Science. 2018, 359, 206-210.
[27] F. Zhang, Y. Wei, X. Wu, H. Jiang, W. Wang, H. Li; Hollow zeolitic imidazolate framework nanospheres as highly efficient cooperative catalysts for [3+3] cycloaddition reactions. J. Am. Chem. Soc. 2014, 136, 13963-13966.
[28] Y.-n. Wu, F. Li, W. Zhu, J. Cui, C.-a. Tao, C. Lin, P.M. Hannam, G. Li; Metal–organic frameworks with a three-dimensional ordered macroporous structure: Dynamic photonic materials. Angew. Chem. Int. Ed. 2011, 50, 12518-12522.
[29] H. Hong, J. Liu, H. Huang, C. Atangana Etogo, X. Yang, B. Guan, L. Zhang; Ordered macro–microporous metal–organic framework single crystals and their derivatives for

rechargeable aluminum-ion batteries. J. Am. Chem. Soc. 2019, 141, 14764-14771.
[30] Y. Guo, F. Liu, L. Feng, X. Wang, X. Zhang, J. Liang; Single Co atoms anchored on nitrogen-doped hierarchically ordered porous carbon for selective hydrogenation of quinolines and efficient oxygen reduction. Chem. Eng. J. 2022, 429, 132150.
[31] Y. Guo, L. Feng, C. Wu, X. Wang, X. Zhang; Confined pyrolysis transformation of ZIF-8 to hierarchically ordered porous Zn-N-C nanoreactor for efficient co2 photoconversion under mild conditions. J. Catal. 2020, 390, 213-223.
[32] D. Zhao, J. Feng, Q. Huo, N. Melosh, G.H. Fredrickson, B.F. Chmelka, G.D. Stucky; Triblock copolymer syntheses of mesoporous silica with periodic 50 to 300 angstrom pores. Science. 1998, 279, 548-552.
[33] C.T. Kresge, M.E. Leonowicz, W.J. Roth, J.C. Vartuli, J.S. Beck; Ordered mesoporous molecular sieves synthesized by a liquid-crystal template mechanism. Nature. 1992, 359, 710-712.
[34] C. Li, Q. Li, Y.V. Kaneti, D. Hou, Y. Yamauchi, Y. Mai; Self-assembly of block copolymers towards mesoporous materials for energy storage and conversion systems. Chem. Soc. Rev. 2020, 49, 4681-4736.
[35] K. Li, J. Yang, R. Huang, S. Lin, J. Gu; Ordered large-pore mesoMOFs based on synergistic effects of triblock polymer and hofmeister ion. Angew. Chem. Int. Ed. 2020, 59, 14124-14128.
[36] J. Yang, K. Li, J. Gu; Hierarchically macro-microporous Ce-based MOFs for the cleavage of DNA. ACS Materials Letters. 2022, 4, 385-391.
[37] X. Cai, X. Deng, Z. Xie, S. Bao, Y. Shi, J. Lin, M. Pang, M. Eddaoudi; Synthesis of highly monodispersed Ga-soc-MOF hollow cubes, colloidosomes and nanocomposites. Chem. Commun. 2016, 52, 9901-9904.
[38] C. Wu, L.-Y. Chou, L. Long, X. Si, W.-S. Lo, C.-K. Tsung, T. Li; Structural control of uniform MOF-74 microcrystals for the study of adsorption kinetics. ACS Appl. Mater. Interfaces. 2019, 11, 35820-35826.
[39] Y. Qin, X. Han, Y. Li, A. Han, W. Liu, H. Xu, J. Liu; Hollow mesoporous metal–organic frameworks with enhanced diffusion for highly efficient catalysis. ACS Catal. 2020, 10, 5973-5978.
[40] W. Liu, J. Huang, Q. Yang, S. Wang, X. Sun, W. Zhang, J. Liu, F. Huo; Multi-shelled hollow metal–organic frameworks. Angew. Chem. Int. Ed. 2017, 56, 5512-5516.
[41] J. Koo, I.-C. Hwang, X. Yu, S. Saha, Y. Kim, K. Kim; Hollowing out MOFs: Hierarchical micro- and mesoporous MOFs with tailorable porosity via selective acid etching. Chemical Science. 2017, 8, 6799-6803.
[42] T. Liu, Y. Liu, L. Yao, W. Yang, L. Tian, H. Liu, D. Liu, C. Wang; Controllable formation of meso- and macropores within metal–organic framework crystals via a citric acid modulator. Nanoscale. 2018, 10, 13194-13201.
[43] M. Hu, Y. Ju, K. Liang, T. Suma, J. Cui, F. Caruso; Void engineering in metal–organic frameworks via synergistic etching and surface functionalization. Adv. Funct. Mater. 2016, 26, 5827-5834.
[44] L. Cao, P. Dai, J. Tang, D. Li, R. Chen, D. Liu, X. Gu, L. Li, Y. Bando, Y.S. Ok, et

al.; Spherical superstructure of boron nitride nanosheets derived from boron-containing metal–organic frameworks. J. Am. Chem. Soc. 2020, 142, 8755-8762.
[45] X. Wang, Z. Na, D. Yin, C. Wang, Y. Wu, G. Huang, L. Wang; Phytic acid-assisted formation of hierarchical porous CoP/C nanoboxes for enhanced lithium storage and hydrogen generation. ACS Nano. 2018, 12, 12238-12246.
[46] Z.-X. Cai, Z.-L. Wang, Y.-J. Xia, H. Lim, W. Zhou, A. Taniguchi, M. Ohtani, K. Kobiro, T. Fujita, Y. Yamauchi; Tailored catalytic nanoframes from metal–organic frameworks by anisotropic surface modification and etching for the hydrogen evolution reaction. Angew. Chem. Int. Ed. 2021, 60, 4747-4755.
[47] W. Wang, H. Yan, U. Anand, U. Mirsaidov; Visualizing the conversion of metal–organic framework nanoparticles into hollow layered double hydroxide nanocages. J. Am. Chem. Soc. 2021, 143, 1854-1862.
[48] H. Sun, B. Tang, P. Wu; Hydrophilic hollow zeolitic imidazolate framework-8 modified ultrafiltration membranes with significantly enhanced water separation properties. J. Membr. Sci. 2018, 551, 283-293.
[49] M. Wu, C. Li, J. Zhao, Y. Ling, R. Liu; Tannic acid-mediated synthesis of dual-heteroatom-doped hollow carbon from a metal–organic framework for efficient oxygen reduction reaction. Dalton Trans. 2018, 47, 7812-7818.
[50] Y. Sun, J. Shi, S. Zhang, Y. Wu, S. Mei, W. Qian, Z. Jiang; Hierarchically porous and water-tolerant metal–organic frameworks for enzyme encapsulation. Ind. Eng. Chem. Res. 2019, 58, 12835-12844.
[51] S.L. Zhang, B.Y. Guan, X.F. Lu, S. Xi, Y. Du, X.W. Lou; Metal atom-doped co3o4 hierarchical nanoplates for electrocatalytic oxygen evolution. Adv. Mater. 2020, 32, 2002235.
[52] Q. Niu, M. Yang, D. Luan, N.W. Li, L. Yu, X.-W. Lou; Construction of Ni-Co-Fe hydr(oxy)oxide@Ni-Co layered double hydroxide yolk-shelled microrods for enhanced oxygen evolution. Angew. Chem. Int. Ed. 2022, 61, e202213049.
[53] J. Zhang, H. Hu, Z. Li, X.W. Lou; Double-shelled nanocages with cobalt hydroxide inner shell and layered double hydroxides outer shell as high-efficiency polysulfide mediator for lithium–sulfur batteries. Angew. Chem. Int. Ed. 2016, 55, 3982-3986.
[54] X. Zhang, F. Yan, X. Ma, C. Zhu, Y. Wang, Y. Xie, S.-L. Chou, Y. Huang, Y. Chen; Regulation of morphology and electronic structure of feconi layered double hydroxides for highly active and stable water oxidization catalysts. Adv. Energy Mater. 2021, 11, 2102141.
[55] A. Ahmed, N. Hodgson, M. Barrow, R. Clowes, C.M. Robertson, A. Steiner, P. McKeown, D. Bradshaw, P. Myers, H. Zhang; Macroporous metal–organic framework microparticles with improved liquid phase separation. J. Mater. Chem. A. 2014, 2, 9085-9090.
[56] S. He, Y. Chen, Z. Zhang, B. Ni, W. He, X. Wang; Competitive coordination strategy for the synthesis of hierarchical-pore metal–organic framework nanostructures. Chemical Science. 2016, 7, 7101-7105.
[57] M.K. Albolkany, C. Liu, Y. Wang, C.-H. Chen, C. Zhu, X. Chen, B. Liu; Molecular

surgery at microporous MOF for mesopore generation and renovation. Angew. Chem. Int. Ed. 2021, 60, 14601-14608.

[58] C. Huang, J. Dong, W. Sun, Z. Xue, J. Ma, L. Zheng, C. Liu, X. Li, K. Zhou, X. Qiao, et al.; Coordination mode engineering in stacked-nanosheet metal–organic frameworks to enhance catalytic reactivity and structural robustness. Nat. Commun. 2019, 10, 2779.

[59] C.-C. Hou, Y. Wang, L. Zou, M. Wang, H. Liu, Z. Liu, H.-F. Wang, C. Li, Q. Xu; A gas-steamed MOF route to P-doped open carbon cages with enhanced Zn-ion energy storage capability and ultrastability. Adv. Mater. 2021, 33, 2101698.

[60] G. Zhang, Y. Li, X. Xiao, Y. Shan, Y. Bai, H.-G. Xue, H. Pang, Z. Tian, Q. Xu; In situ anchoring polymetallic phosphide nanoparticles within porous prussian blue analogue nanocages for boosting oxygen evolution catalysis. Nano Lett. 2021, 21, 3016-3025.

[61] L. Wang, J. Wan, Y. Zhao, N. Yang, D. Wang; Hollow multi-shelled structures of Co_3O_4 dodecahedron with unique crystal orientation for enhanced photocatalytic co2 reduction. J. Am. Chem. Soc. 2019, 141, 2238-2241.

[62] W. Guo, W. Sun, L.-P. Lv, S. Kong, Y. Wang; Microwave-assisted morphology evolution of Fe-based metal–organic frameworks and their derived Fe_2O_3 nanostructures for li-ion storage. ACS Nano. 2017, 11, 4198-4205.

[63] Y. Kim, T. Yang, G. Yun, M.B. Ghasemian, J. Koo, E. Lee, S.J. Cho, K. Kim; Hydrolytic transformation of microporous metal–organic frameworks to hierarchical micro- and mesoporous MOFs. Angew. Chem. Int. Ed. 2015, 54, 13273-13278.

[64] S. El-Hankari, J. Huo, A. Ahmed, H. Zhang, D. Bradshaw; Surface etching of hkust-1 promoted via supramolecular interactions for chromatography. J. Mater. Chem. A. 2014, 2, 13479-13485.

[65] S. Dou, C.-L. Dong, Z. Hu, Y.-C. Huang, J.-l. Chen, L. Tao, D. Yan, D. Chen, S. Shen, S. Chou, et al.; Atomic-scale coox species in metal–organic frameworks for oxygen evolution reaction. Adv. Funct. Mater. 2017, 27, 1702546.

[66] Q. Chen, X. Zhang, S. Li, J. Tan, C. Xu, Y. Huang; MOF-derived Co_3O_4@Co-Fe oxide double-shelled nanocages as multi-functional specific peroxidase-like nanozyme catalysts for chemo/biosensing and dye degradation. Chem. Eng. J. 2020, 395, 125130.

[67] Y. Cai, G. Fang, J. Zhou, S. Liu, Z. Luo, A. Pan, G. Cao, S. Liang; Metal-organic framework-derived porous shuttle-like vanadium oxides for sodium-ion battery application. Nano Research. 2018, 11, 449-463.

[68] G. Ye, S. Liu, K. Huang, S. Wang, K. Zhao, W. Zhu, Y. Su, J. Wang, Z. He; Domain-confined etching strategy to regulate defective sites in carbon for high-efficiency electrocatalytic oxygen reduction. Adv. Funct. Mater. 2022, 32, 2111396.

[69] G.-G. Chang, X.-C. Ma, Y.-X. Zhang, L.-Y. Wang, G. Tian, J.-W. Liu, J. Wu, Z.-Y. Hu, X.-Y. Yang, B. Chen; Construction of hierarchical metal–organic frameworks by competitive coordination strategy for highly efficient CO_2 conversion. Adv. Mater. 2019, 31, 1904969.

[70] J. Huo, Y. Wang, L. Yan, Y. Xue, S. Li, M. Hu, Y. Jiang, Q.-G. Zhai; In situ semi-

transformation from heterometallic MOFs to Fe–Ni ldh/MOF hierarchical architectures for boosted oxygen evolution reaction. Nanoscale. 2020, 12, 14514-14523.

[71] J. Zhang, L. Yu, Y. Chen, X.F. Lu, S. Gao, X.W. Lou; Designed formation of double-shelled Ni–Fe layered-double-hydroxide nanocages for efficient oxygen evolution reaction. Adv. Mater. 2020, 32, 1906432.

[72] A.-H. Lu, T. Sun, W.-C. Li, Q. Sun, F. Han, D.-H. Liu, Y. Guo; Synthesis of discrete and dispersible hollow carbon nanospheres with high uniformity by using confined nanospace pyrolysis. Angew. Chem. Int. Ed. 2011, 50, 11765-11768.

[73] C. Liu, X. Huang, J. Wang, H. Song, Y. Yang, Y. Liu, J. Li, L. Wang, C. Yu; Hollow mesoporous carbon nanocubes: Rigid-interface-induced outward contraction of metal-organic frameworks. Adv. Funct. Mater. 2018, 28, 1705253.

[74] Y. Chen, S. Ji, S. Zhao, W. Chen, J. Dong, W.-C. Cheong, R. Shen, X. Wen, L. Zheng, A.I. Rykov, et al.; Enhanced oxygen reduction with single-atomic-site iron catalysts for a zinc-air battery and hydrogen-air fuel cell. Nat. Commun. 2018, 9, 5422.

[75] S. Yang, L. Peng, P. Huang, X. Wang, Y. Sun, C. Cao, W. Song; Nitrogen, phosphorus, and sulfur co-doped hollow carbon shell as superior metal-free catalyst for selective oxidation of aromatic alkanes. Angew. Chem. Int. Ed. Engl. 2016, 55, 4016-4020.

[76] S. Yuan, L. Zou, J.-S. Qin, J. Li, L. Huang, L. Feng, X. Wang, M. Bosch, A. Alsalme, T. Cagin, et al.; Construction of hierarchically porous metal–organic frameworks through linker labilization. Nat. Commun. 2017, 8, 15356.

[77] Y.J. Wong, L. Zhu, W.S. Teo, Y.W. Tan, Y. Yang, C. Wang, H. Chen; Revisiting the stöber method: Inhomogeneity in silica shells. J. Am. Chem. Soc. 2011, 133, 11422-11425.

[78] D.S. Bin, Z.X. Chi, Y. Li, K. Zhang, X. Yang, Y.G. Sun, J.Y. Piao, A.M. Cao, L.J. Wan; Controlling the compositional chemistry in single nanoparticles for functional hollow carbon nanospheres. J. Am. Chem. Soc. 2017, 139, 13492-13498.

[79] M. Hu, A.A. Belik, M. Imura, Y. Yamauchi; Tailored design of multiple nanoarchitectures in metal-cyanide hybrid coordination polymers. J. Am. Chem. Soc. 2013, 135, 384-391.

[80] X. Wang, Y. Chen, Y. Fang, J. Zhang, S. Gao, X.W. Lou; Synthesis of cobalt sulfide multi-shelled nanoboxes with precisely controlled two to five shells for sodium-ion batteries. Angew. Chem. Int. Ed. 2019, 58, 2675-2679.

[81] J. Wei, Y. Chen, Y. Ma, X. Shi, X. Zhang, C. Shi, M. Hu, J. Liu; Precisely engineering architectures of Co/C sub-microreactors for selective syngas conversion. Small. 2021, 17, 2100082.

[82] Z. Huang, L. Fan, F. Zhao, B. Chen, K. Xu, S.-F. Zhou, J. Zhang, Q. Li, D. Hua, G. Zhan; Rational engineering of multilayered CO_3O_4/ZnO nanocatalysts through chemical transformations from matryoshka-type ZIFs. Adv. Funct. Mater. 2019, 29, 1903774.

[83] C. Avci, J. Ariñez-Soriano, A. Carné-Sánchez, V. Guillerm, C. Carbonell, I. Imaz, D. Maspoch; Post-synthetic anisotropic wet-chemical etching of colloidal sodalite ZIF crystals. Angew. Chem. Int. Ed. 2015, 54, 14417-14421.

[84] J. Wang, A. Yang, J. Li, K. Su, Y. Tang, X. Qiu; Top-down and facet-selective phase-segregation to construct concave nanocages with strongly coupled hetero-interface for oxygen evolution reaction. Appl. Catal., B. 2022, 300, 120727.
[85] W. Zhang, Y. Zhao, V. Malgras, Q. Ji, D. Jiang, R. Qi, K. Ariga, Y. Yamauchi, J. Liu, J.-S. Jiang, et al.; Synthesis of monocrystalline nanoframes of prussian blue analogues by controlled preferential etching. Angew. Chem. Int. Ed. 2016, 55, 8228-8234.
[86] V. Ganesan, J. Kim; Prussian blue analogue metal organic framework-derived $CoSe_2$ nanoboxes for highly efficient oxygen evolution reaction. Mater. Lett. 2018, 223, 49-52.
[87] Y. Feng, X.-Y. Yu, U. Paik; Formation of CO_3O_4 microframes from MOFs with enhanced electrochemical performance for lithium storage and water oxidation. Chem. Commun. 2016, 52, 6269-6272.
[88] L. Han, X.-Y. Yu, X.W. Lou; Formation of prussian-blue-analog nanocages via a direct etching method and their conversion into Ni–Co-mixed oxide for enhanced oxygen evolution. Adv. Mater. 2016, 28, 4601-4605.
[89] J. Nai, Y. Lu, L. Yu, X. Wang, X.W. Lou; Formation of Ni–Fe mixed diselenide nanocages as a superior oxygen evolution electrocatalyst. Adv. Mater. 2017, 29, 1703870.
[90] S. Wang, Y. Fan, J. Teng, Y.-Z. Fan, J.-J. Jiang, H.-P. Wang, H. Grützmacher, D. Wang, C.-Y. Su; Nanoreactor based on macroporous single crystals of metal-organic framework. Small. 2016, 12, 5702-5709.
[91] Z. Li, M. Hu, J. Liu, W. Wang, Y. Li, W. Fan, Y. Gong, J. Yao, P. Wang, M. He, et al.; Mesoporous silica stabilized MOF nanoreactor for highly selective semi-hydrogenation of phenylacetylene via synergistic effect of Pd and Ru single site. Nano Research. 2022, 15, 1983-1992.
[92] W. Zhang, X. Jiang, Y. Zhao, A. Carné-Sánchez, V. Malgras, J. Kim, J.H. Kim, S. Wang, J. Liu, J.-S. Jiang, et al.; Hollow carbon nanobubbles: Monocrystalline MOF nanobubbles and their pyrolysis. Chemical Science. 2017, 8, 3538-3546.
[93] Y. Huang, Y. Fang, X.F. Lu, D. Luan, X.W. Lou; CO_3O_4 hollow nanoparticles embedded in mesoporous walls of carbon nanoboxes for efficient lithium storage. Angew. Chem. 2020, 132, 20086-20090.
[94] H. Yang, S.J. Bradley, A. Chan, G.I.N. Waterhouse, T. Nann, P.E. Kruger, S.G. Telfer; Catalytically active bimetallic nanoparticles supported on porous carbon capsules derived from metal–organic framework composites. J. Am. Chem. Soc. 2016, 138, 11872-11881.
[95] H. Yang, X. Chen, W.-T. Chen, Q. Wang, N.C. Cuello, A. Nafady, A.M. Al-Enizi, G.I.N. Waterhouse, G.A. Goenaga, T.A. Zawodzinski, et al.; Tunable synthesis of hollow metal–nitrogen–carbon capsules for efficient oxygen reduction catalysis in proton exchange membrane fuel cells. ACS Nano. 2019, 13, 8087-8098.
[96] X.Y. Liu, F. Zhang, T.W. Goh, Y. Li, Y.C. Shao, L. Luo, W. Huang, Y.T. Long, L.Y. Chou, C.K. Tsung; Using a multi-shelled hollow metal–organic framework as a host to switch the guest-to-host and guest-to-guest interactions. Angew. Chem. 2018, 130,

2132-2136.
[97] M. Li, S. Zhang, J. Zhao, H. Wang; Maximizing metal–support interactions in Pt/CO_3O_4 nanocages to simultaneously boost hydrogen production activity and durability. ACS Appl. Mater. Interfaces. 2021, 13, 57362-57371.
[98] X. Ao, Y. Ding, G. Nam, L. Soule, P. Jing, B. Zhao, J.Y. Hwang, J.-H. Jang, C. Wang, M. Liu; A single-atom Fe-N-C catalyst with ultrahigh utilization of active sites for efficient oxygen reduction. Small. 2022, 18, 2203326.
[99] Z. Li, R. Yu, J. Huang, Y. Shi, D. Zhang, X. Zhong, D. Wang, Y. Wu, Y. Li; Platinum–nickel frame within metal-organic framework fabricated in situ for hydrogen enrichment and molecular sieving. Nat. Commun. 2015, 6, 8248.
[100] J. Yang, F. Zhang, H. Lu, X. Hong, H. Jiang, Y. Wu, Y. Li; Hollow Zn/Co ZIF particles derived from core–shell ZIF-67@ZIF-8 as selective catalyst for the semi-hydrogenation of acetylene. Angew. Chem. Int. Ed. 2015, 54, 10889-10893.
[101] G. Cai, M. Ding, Q. Wu, H.-L. Jiang; Encapsulating soluble active species into hollow crystalline porous capsules beyond integration of homogeneous and heterogeneous catalysis. National Science Review. 2020, 7, 37-45.
[102] O. IEA, World energy outlook 2015, international energy agency, IEA Paris, France, 2015.
[103] S. Chu, A. Majumdar; Opportunities and challenges for a sustainable energy future. Nature. 2012, 488, 294-303.
[104] Z.W. Seh, J. Kibsgaard, C.F. Dickens, I. Chorkendorff, J.K. Nørskov, T.F. Jaramillo; Combining theory and experiment in electrocatalysis: Insights into materials design. Science. 2017, 355, eaad4998.
[105] L. Zhao, J. Zhu, Y. Zheng, M. Xiao, R. Gao, Z. Zhang, G. Wen, H. Dou, Y.-P. Deng, A. Yu, et al.; Materials engineering toward durable electrocatalysts for proton exchange membrane fuel cells. Adv. Energy Mater. 2022, 12, 2102665.
[106] X.F. Lu, B.Y. Xia, S.-Q. Zang, X.W. Lou; Metal–organic frameworks based electrocatalysts for the oxygen reduction reaction. Angew. Chem. Int. Ed. 2020, 59, 4634-4650.
[107] H. Zhang, R. Lv; Defect engineering of two-dimensional materials for efficient electrocatalysis. Journal of Materiomics. 2018, 4, 95-107.
[108] L. Zhang, Q. Shao, J. Zhang; An overview of non-noble metal electrocatalysts and their associated air cathodes for Mg-air batteries. Materials Reports: Energy. 2021, 1, 100002.
[109] K. Gao, B. Wang, L. Tao, B.V. Cunning, Z. Zhang, S. Wang, R.S. Ruoff, L. Qu; Efficient metal-free electrocatalysts from N-doped carbon nanomaterials: Mono-doping and co-doping. Adv. Mater. 2019, 31, 1805121.
[110] Z.-F. Huang, J. Song, Y. Du, S. Xi, S. Dou, J.M.V. Nsanzimana, C. Wang, Z.J. Xu, X. Wang; Chemical and structural origin of lattice oxygen oxidation in Co–Zn oxyhydroxide oxygen evolution electrocatalysts. Nature Energy. 2019, 4, 329-338.
[111] T. Reier, H.N. Nong, D. Teschner, R. Schlögl, P. Strasser; Electrocatalytic oxygen evolution reaction in acidic environments – reaction mechanisms and catalysts. Adv.

Energy Mater. 2017, 7, 1601275.
[112] Z. Wu, Y. Li, C. Zhang, X. Huang, B. Peng, G. Wang; Recent advances in metal-organic-framework-based catalysts for thermocatalytic selective oxidation of organic substances. Chem Catalysis. 2022, 2, 1009-1045.
[113] S. Siahrostami, S.J. Villegas, A.H. Bagherzadeh Mostaghimi, S. Back, A.B. Farimani, H. Wang, K.A. Persson, J. Montoya; A review on challenges and successes in atomic-scale design of catalysts for electrochemical synthesis of hydrogen peroxide. ACS Catal. 2020, 10, 7495-7511.
[114] H. Xu, J. Yang, R. Ge, J. Zhang, Y. Li, M. Zhu, L. Dai, S. Li, W. Li; Carbon-based bifunctional electrocatalysts for oxygen reduction and oxygen evolution reactions: Optimization strategies and mechanistic analysis. Journal of Energy Chemistry. 2022, 71, 234-265.
[115] Z. Lin, Y. Yang, M. Li, H. Huang, W. Hu, L. Cheng, W. Yan, Z. Yu, K. Mao, G. Xia, et al.; Dual graphitic-N doping in a six-membered C-ring of graphene-analogous particles enables an efficient electrocatalyst for the hydrogen evolution reaction. Angew. Chem. Int. Ed. 2019, 58, 16973-16980.
[116] M. Li, Z. Liu, F. Wang, J. Xuan; The influence of the type of N dopping on the performance of bifunctional N-doped ordered mesoporous carbon electrocatalysts in oxygen reduction and evolution reaction. Journal of Energy Chemistry. 2017, 26, 422-427.
[117] D. Guo, R. Shibuya, C. Akiba, S. Saji, T. Kondo, J. Nakamura; Active sites of nitrogen-doped carbon materials for oxygen reduction reaction clarified using model catalysts. Science. 2016, 351, 361-365.
[118] J. Guo, S. Zhang, M. Zheng, J. Tang, L. Liu, J. Chen, X. Wang; Graphitic-N-rich N-doped graphene as a high performance catalyst for oxygen reduction reaction in alkaline solution. Int. J. Hydrogen Energy. 2020, 45, 32402-32412.
[119] H. Han, Y. Noh, Y. Kim, W.S. Jung, S. Park, W.B. Kim; An N-doped porous carbon network with a multidirectional structure as a highly efficient metal-free catalyst for the oxygen reduction reaction. Nanoscale. 2019, 11, 2423-2433.
[120] Y. Fang, X. Wang; Metal-free boron-containing heterogeneous catalysts. Angew. Chem. Int. Ed. 2017, 56, 15506-15518.
[121] Z. Li, Y. Chen, T. Ma, Y. Jiang, J. Chen, H. Pan, W. Sun; 2D metal-free nanomaterials beyond graphene and its analogues toward electrocatalysis applications. Adv. Energy Mater. 2021, 11, 2101202.
[122] J. Wu, X. Zheng, C. Jin, J. Tian, R. Yang; Ternary doping of phosphorus, nitrogen, and sulfur into porous carbon for enhancing electrocatalytic oxygen reduction. Carbon. 2015, 92, 327-338.
[123] S. Zhao, J. Liu, C. Li, W. Ji, M. Yang, H. Huang, Y. Liu, Z. Kang; Tunable ternary (N, P, B)-doped porous nanocarbons and their catalytic properties for oxygen reduction reaction. ACS Appl. Mater. Interfaces. 2014, 6, 22297-22304.
[124] P. Huang, H. Li, X. Huang, D. Chen; Multiheteroatom-doped porous carbon catalyst for oxygen reduction reaction prepared using 3D network of ZIF-8/polymeric

nanofiber as a facile-doping template. ACS Appl. Mater. Interfaces. 2017, 9, 21083-21088.

[125] S. Agnoli, M. Favaro; Doping graphene with boron: A review of synthesis methods, physicochemical characterization, and emerging applications. J. Mater. Chem. A. 2016, 4, 5002-5025.

[126] C.N.R. Rao, K. Gopalakrishnan; Borocarbonitrides, bxcynz: Synthesis, characterization, and properties with potential applications. ACS Appl. Mater. Interfaces. 2017, 9, 19478-19494.

[127] C.N.R. Rao, M. Chhetri; Borocarbonitrides as metal-free catalysts for the hydrogen evolution reaction. Adv. Mater. 2019, 31, 1803668.

[128] M. Zheng, J. Shi, T. Yuan, X. Wang; Metal-free dehydrogenation of N-heterocycles by ternary h -BCN nanosheets with visible light. Angewandte Chemie. 2018, 130, 5585-5589.

[129] S. Wang , E. Iyyamperumal , A. Roy, Y. Xue, D. Yu, L. Dai; Vertically aligned bcn nanotubes as efficient metal-free electrocatalysts for the oxygen reduction reaction: A synergetic effect by co-doping with boron and nitrogen. Angew. Chem. Int. Ed. 2011, 50, 11756-11760.

[130] W. Wang, P. Wang, Y. Kang, J. Zhao, P. Tao, Z. Lei; Flame synthesis of nitrogen, boron co-doped carbon as efficient electrocatalyst for oxygen reduction reaction. Int. J. Hydrogen Energy. 2019, 44, 4771-4779.

[131] C. Li, Z. Yu, H. Liu, M. Xiong; Synergetic contribution of Fe/Co and N/B dopants in mesoporous carbon nanosheets as remarkable electrocatalysts for zinc-air batteries. Chem. Eng. J. 2019, 371, 433-442.

[132] W. Chen, L. Xu, Y. Tian, H. Li, K. Wang; Boron and nitrogen co-doped graphene aerogels: Facile preparation, tunable doping contents and bifunctional oxygen electrocatalysis. Carbon. 2018, 137, 458-466.

[133] S. Baik, B.L. Suh, A. Byeon, J. Kim, J.W. Lee; In-situ boron and nitrogen doping in flue gas derived carbon materials for enhanced oxygen reduction reaction. Journal of CO_2 Utilization. 2017, 20, 73-80.

[134] X. Li, L. Fan, B. Xu, Y. Shang, M. Li, L. Zhang, S. Liu, Z. Kang, Z. Liu, X. Lu, et al.; Single-atom-like b-n3 sites in ordered macroporous carbon for efficient oxygen reduction reaction. ACS Appl. Mater. Interfaces. 2021, 13, 53892-53903.

[135] Y. Hao, S. Wang, Y. Shao, Y. Wu, S. Miao; High-energy density Li-ion capacitor with layered SnS_2/reduced graphene oxide anode and bcn nanosheet cathode. Adv. Energy Mater. 2020, 10, 1902836.

[136] W. Lei, S. Qin, D. Liu, D. Portehault, Z. Liu, Y. Chen; Large scale boron carbon nitride nanosheets with enhanced lithium storage capabilities. Chem. Commun. 2013, 49, 352-354.

[137] R. Nandan, G.K. Goswami, K.K. Nanda; Direct synthesis of Pt-free catalyst on gas diffusion layer of fuel cell and usage of high boiling point fuels for efficient utilization of waste heat. Appl. Energy. 2017, 205, 1050-1058.

[138] Y. Zheng, Y. Jiao, L. Ge, M. Jaroniec, S.Z. Qiao; Two-step boron and nitrogen

doping in graphene for enhanced synergistic catalysis. Angew. Chem. Int. Ed. 2013, 52, 3110-3116.

[139] S. Wang, L. Zhang, Z. Xia, A. Roy, D.W. Chang, J.-B. Baek, L. Dai; BCN graphene as efficient metal-free electrocatalyst for the oxygen reduction reaction. Angew. Chem. Int. Ed. 2012, 51, 4209-4212.

[140] M. Chhetri, S. Maitra, H. Chakraborty, U.V. Waghmare, C.N.R. Rao; Superior performance of borocarbonitrides, BxCyNz, as stable, low-cost metal-free electrocatalysts for the hydrogen evolution reaction. Energy Environ. Sci. 2016, 9, 95-101.

[141] H.-W. Zhang, Y.-Y. Li, W.-Q. Huang, B.-X. Zhou, S.-F. Ma, Y.-X. Lu, A.-L. Pan, G.-F. Huang; Hollow BCN microrods with hierarchical multichannel structure as a multifunctional material: Synergistic effects of structural topology and composition. Carbon. 2019, 148, 231-240.

[142] D. Shi, B. Chang, Z. Ai, H. Jiang, F. Chen, Y. Shao, J. Shen, Y. Wu, X. Hao; Boron carbonitride with tunable B/N lewis acid/base sites for enhanced electrocatalytic overall water splitting. Nanoscale. 2021, 13, 2849-2854.

[143] C. Chen, D. Yan, Y. Wang, Y. Zhou, Y. Zou, Y. Li, S. Wang; B-N pairs enriched defective carbon nanosheets for ammonia synthesis with high efficiency. Small. 2019, 15, 1805029.

[144] Q. Geng, G. Huang, Y. Liu, Y. Li, L. Liu, X. Yang, Q. Wang, C. Zhang; Facile synthesis of B/N co-doped 2D porous carbon nanosheets derived from ammonium humate for supercapacitor electrodes. Electrochim. Acta. 2019, 298, 1-13.

[145] S. Wang, F. Ma, H. Jiang, Y. Shao, Y. Wu, X. Hao; Band gap-tunable porous borocarbonitride nanosheets for high energy-density supercapacitors. ACS Appl. Mater. Interfaces. 2018, 10, 19588-19597.

[146] M.-R. Liu, Q.-L. Hong, Q.-H. Li, Y. Du, H.-X. Zhang, S. Chen, T. Zhou, J. Zhang; Cobalt boron imidazolate framework derived cobalt nanoparticles encapsulated in B/N codoped nanocarbon as efficient bifunctional electrocatalysts for overall water splitting. Adv. Funct. Mater. 2018, 28, 1801136.

[147] Y. Qian, Z. Hu, X. Ge, S. Yang, Y. Peng, Z. Kang, Z. Liu, J.Y. Lee, D. Zhao; A metal-free ORR/OER bifunctional electrocatalyst derived from metal-organic frameworks for rechargeable zn-air batteries. Carbon. 2017, 111, 641-650.

[148] X. Chen, Y. Xie, Y. Shao, K. Shen, Y. Li; Facile synthesis of boron and nitrogen dual-doped hollow mesoporous carbons for efficient reduction of 4-nitrophenol. ACS Appl. Mater. Interfaces. 2021, 13, 42598-42604.

[149] C. Van Nguyen, S. Lee, Y.G. Chung, W.-H. Chiang, K.C.W. Wu; Synergistic effect of metal-organic framework-derived boron and nitrogen heteroatom-doped three-dimensional porous carbons for precious-metal-free catalytic reduction of nitroarenes. Appl. Catal., B. 2019, 257, 117888.

[150] Y. Li, H. Xu, H. Huang, L. Gao, Y. Zhao, T. Ma; Synthesis of Co–B in porous carbon using a metal–organic framework (MOF) precursor: A highly efficient catalyst for the oxygen evolution reaction. Electrochem. Commun. 2018, 86, 140-144.

[151] H. Tabassum, A. Mahmood, Q. Wang, W. Xia, Z. Liang, B. Qiu, R. zhao, R. Zou; Hierarchical cobalt hydroxide and B/N co-doped graphene nanohybrids derived from metal-organic frameworks for high energy density asymmetric supercapacitors. Sci. Rep. 2017, 7, 43084.

[152] H. Tabassum, W. Guo, W. Meng, A. Mahmood, R. Zhao, Q. Wang, R. Zou; Metal–organic frameworks derived cobalt phosphide architecture encapsulated into B/N co-doped graphene nanotubes for all ph value electrochemical hydrogen evolution. Adv. Energy Mater. 2017, 7, 1601671.

[153] H. Zhang, Z. Ma, J. Duan, H. Liu, G. Liu, T. Wang, K. Chang, M. Li, L. Shi, X. Meng, et al.; Active sites implanted carbon cages in core–shell architecture: Highly active and durable electrocatalyst for hydrogen evolution reaction. ACS Nano. 2016, 10, 684-694.

[154] X. Wei, N. Li, X. Zhang; Co/CoO/C@B three-phase composite derived from ZIF67 modified with $NaBH_4$ solution as the electrocatalyst for efficient oxygen evolution. Electrochim. Acta. 2018, 264, 36-45.

[155] M.A. Ahsan, T. He, K. Eid, A.M. Abdullah, M.F. Sanad, A. Aldalbahi, B. Alvarado-Tenorio, A. Du, A.R. Puente Santiago, J.C. Noveron; Controlling the interfacial charge polarization of MOF-derived 0D–2D vdw architectures as a unique strategy for bifunctional oxygen electrocatalysis. ACS Appl. Mater. Interfaces. 2022, 14, 3919-3929.

[156] Y. Wan, W. Zhang, X. Han, L. Zhou, H. Zhen, C. Wu, Q. Yu, G. Xiu; B,N-decorated carbocatalyst based on Fe-MOF/BN as an efficient peroxymonosulfate activator for bisphenol a degradation. J. Hazard. Mater. 2022, 430, 127832.

[157] B.Y. Guan, L. Yu, X.W. Lou; Formation of single-holed cobalt/N-doped carbon hollow particles with enhanced electrocatalytic activity toward oxygen reduction reaction in alkaline media. Advanced Science. 2017, 4, 1700247.

[158] S.L. Zhang, B.Y. Guan, X.W. Lou; Co–Fe alloy/N-doped carbon hollow spheres derived from dual metal–organic frameworks for enhanced electrocatalytic oxygen reduction. Small. 2019, 15, 1805324.

[159] L. Chai, L. Zhang, X. Wang, L. Xu, C. Han, T.-T. Li, Y. Hu, J. Qian, S. Huang; Bottom-up synthesis of MOF-derived hollow N-doped carbon materials for enhanced orr performance. Carbon. 2019, 146, 248-256.

[160] H. Xing, Y. Zhang, J. Hu, R. Krishna, L. Wang, L. Yang, X. Cui, S. Duttwyler; Rational design of microporous MOFs with anionic boron cluster functionality and cooperative dihydrogen binding sites for highly selective capture of acetylene. Angew. Chem. Int. Ed. 2020.

[161] L. Sun, Y. Yuan, F. Wang, Y. Zhao, W. Zhan, X. Han; Selective wet-chemical etching to create TiO_2@MOF frame heterostructure for efficient photocatalytic hydrogen evolution. Nano Energy. 2020, 74, 104909.

[162] X.-C. Xie, K.-J. Huang, X. Wu; Metal–organic framework derived hollow materials for electrochemical energy storage. J. Mater. Chem. A. 2018, 6, 6754-6771.

[163] J. Liu, D. Zhu, C. Guo, A. Vasileff, S.-Z. Qiao; Design strategies toward advanced

MOF-derived electrocatalysts for energy-conversion reactions. Adv. Energy Mater. 2017, 7, 1700518.

[164] C. Wang, J. Kim, J. Tang, M. Kim, H. Lim, V. Malgras, J. You, Q. Xu, J. Li, Y. Yamauchi; New strategies for novel MOF-derived carbon materials based on nanoarchitectures. Chem. 2020, 6, 19-40.

[165] K. Zhang, H. Hu, L. Shi, B. Jia, H. Huang, X. Han, X. Sun, T. Ma; Strategies for optimizing the photocatalytic water-splitting performance of metal–organic framework-based materials. Small Sci. 2021, 1, 2100060.

[166] K. Wang, C. Wu, F. Wang, G. Jiang; MOF-derived copx nanoparticles embedded in nitrogen-doped porous carbon polyhedrons for nanomolar sensing of p-nitrophenol. ACS Appl. Nano Mater. 2018, 1, 5843-5853.

[167] F. Pan, H. Zhang, K. Liu, D. Cullen, K. More, M. Wang, Z. Feng, G. Wang, G. Wu, Y. Li; Unveiling active sites of CO_2 reduction on nitrogen-coordinated and atomically dispersed iron and cobalt catalysts. ACS Catal. 2018, 8, 3116-3122.

[168] W. Xia, J. Zhu, W. Guo, L. An, D. Xia, R. Zou; Well-defined carbon polyhedrons prepared from nano metal–organic frameworks for oxygen reduction. J. Mater. Chem. A. 2014, 2, 11606-11613.

[169] Z. Zhu, H. Yin, Y. Wang, C.-H. Chuang, L. Xing, M. Dong, Y.-R. Lu, G. Casillas-Garcia, Y. Zheng, S. Chen, et al.; Coexisting single-atomic Fe and Ni sites on hierarchically ordered porous carbon as a highly efficient orr electrocatalyst. Adv. Mater. 2020, 32, 2004670.

[170] C. Tang, B.-Q. Li, Q. Zhang, L. Zhu, H.-F. Wang, J.-L. Shi, F. Wei; Cao-templated growth of hierarchical porous graphene for high-power lithium–sulfur battery applications. Adv. Funct. Mater. 2016, 26, 577-585.

[171] L. Tang, S. Zhang, Q. Wu, X. Wang, H. Wu, Z. Jiang; Heterobimetallic metal–organic framework nanocages as highly efficient catalysts for CO_2 conversion under mild conditions. J. Mater. Chem. A. 2018, 6, 2964-2973.

[172] C.L. Hobday, C.H. Woodall, M.J. Lennox, M. Frost, K. Kamenev, T. Düren, C.A. Morrison, S.A. Moggach; Understanding the adsorption process in ZIF-8 using high pressure crystallography and computational modelling. Nat. Commun. 2018, 9, 1429.

[173] J. Wang, Z. Huang, W. Liu, C. Chang, H. Tang, Z. Li, W. Chen, C. Jia, T. Yao, S. Wei, et al.; Design of N-coordinated dual-metal sites: A stable and active Pt-free catalyst for acidic oxygen reduction reaction. J. Am. Chem. Soc. 2017, 139, 17281-17284.

[174] Y.-H. Zhou, X. Cao, J. Ning, C. Ji, Y. Cheng, J. Gu; Pd-doped Cu nanoparticles confined by ZIF-67@ZIF-8 for efficient dehydrogenation of ammonia borane. Int. J. Hydrogen Energy. 2020, 45, 31440-31451.

[175] Z. Wang, B. Zhang, C. Ye, L. Chen; Recovery of Au(iii) from leach solutions using thiourea functionalized zeolitic imidazolate frameworks (Tu*ZIF-8). Hydrometallurgy. 2018, 180, 262-270.

[176] F. Chang, P. Su, U. Guharoy, R. Ye, Y. Ma, H. Zheng, Y. Jia, J. Liu; Edge-enriched N, S co-doped hierarchical porous carbon for oxygen reduction reaction. Chin. Chem. Lett. 2023, 34, 107462.

[177] J.V. Morabito, L.-Y. Chou, Z. Li, C.M. Manna, C.A. Petroff, R.J. Kyada, J.M. Palomba, J.A. Byers, C.-K. Tsung; Molecular encapsulation beyond the aperture size limit through dissociative linker exchange in metal–organic framework crystals. J. Am. Chem. Soc. 2014, 136, 12540-12543.

[178] O. Basu, S. Mukhopadhyay, A. De, A. Das, S.K. Das; Tuning the electrochemical and catalytic ORR performance of C60 by its encapsulation in ZIF-8: A solid-state analogue of dilute fullerene solution. Mater. Chem. Front. 2021, 5, 7654-7665.

[179] M. Gutiérrez, C. Martín, M. Van der Auweraer, J. Hofkens, J.-C. Tan; Electroluminescent guest@MOF nanoparticles for thin film optoelectronics and solid-state lighting. Adv. Opt. Mater. 2020, 8, 2000670.

[180] Y. Xia, X. Zhao, C. Xia, Z.-Y. Wu, P. Zhu, J.Y. Kim, X. Bai, G. Gao, Y. Hu, J. Zhong, et al.; Highly active and selective oxygen reduction to H_2O_2 on boron-doped carbon for high production rates. Nat. Commun. 2021, 12, 4225.

[181] J. Wang, H. Li, S. Liu, Y. Hu, J. Zhang, M. Xia, Y. Hou, J. Tse, J. Zhang, Y. Zhao; Turning on Zn 4s electrons in a N_2-Zn-B_2 configuration to stimulate remarkable orr performance. Angew. Chem. Int. Ed. 2021, 60, 181-185.

[182] X. Ma, J. Du, H. Sun, F. Ye, X. Wang, P. Xu, C. Hu, L. Zhang, D. Liu; Boron, nitrogen co-doped carbon with abundant mesopores for efficient CO_2 electroreduction. Appl. Catal., B. 2021, 298, 120543.

[183] B. Chang, L. Li, D. Shi, H. Jiang, Z. Ai, S. Wang, Y. Shao, J. Shen, Y. Wu, Y. Li, et al.; Metal-free boron carbonitride with tunable boron lewis acid sites for enhanced nitrogen electroreduction to ammonia. Appl. Catal., B. 2021, 283, 119622.

[184] M.A. Ahsan, T. He, K. Eid, A.M. Abdullah, M.L. Curry, A. Du, A.R. Puente Santiago, L. Echegoyen, J.C. Noveron; Tuning the intermolecular electron transfer of low-dimensional and metal-free BCN/C60 electrocatalysts via interfacial defects for efficient hydrogen and oxygen electrochemistry. J. Am. Chem. Soc. 2021, 143, 1203-1215.

[185] Q.-L. Zhu, W. Xia, T. Akita, R. Zou, Q. Xu; Metal-organic framework-derived honeycomb-like open porous nanostructures as precious-metal-free catalysts for highly efficient oxygen electroreduction. Adv. Mater. 2016, 28, 6391-6398.

[186] Q.-L. Zhu, W. Xia, L.-R. Zheng, R. Zou, Z. Liu, Q. Xu; Atomically dispersed Fe/N-doped hierarchical carbon architectures derived from a metal–organic framework composite for extremely efficient electrocatalysis. ACS Energy Lett. 2017, 2, 504-511.

[187] F.H. Stephens, V. Pons, R. Tom Baker; Ammonia–borane: The hydrogen source par excellence? Dalton Trans. 2007, 25, 2613-2626.

[188] A. Brockman, Y. Zheng, J. Gore; A study of catalytic hydrolysis of concentrated ammonia borane solutions. Int. J. Hydrogen Energy. 2010, 35, 7350-7356.

[189] U.B. Demirci; Ammonia borane, a material with exceptional properties for chemical hydrogen storage. Int. J. Hydrogen Energy. 2017, 42, 9978-10013.

[190] A. Harabor, P. Rotaru, R.I. Scorei, N.A. Harabor; Non-conventional hexagonal structure for boric acid. J. Therm. Anal. Calorim. 2014, 118, 1375-1384.

[191] C. Huang, M. Mutailipu, F. Zhang, K.J. Griffith, C. Hu, Z. Yang, J.M. Griffin, K.R.

Poeppelmeier, S. Pan; Expanding the chemistry of borates with functional $[BO_2]^-$ anions. Nat. Commun. 2021, 12, 2597.

[192] S. Kroeker, J.F. Stebbins; Three-coordinated boron-11 chemical shifts in borates. Inorg. Chem. 2001, 40, 6239-6246.

[193] S. Geng, F.U. Shah, P. Liu, O.N. Antzutkin, K. Oksman; Plasticizing and crosslinking effects of borate additives on the structure and properties of poly(vinyl acetate). RSC Adv. 2017, 7, 7483-7491.

[194] Z. Li, G. Zhu, G. Lu, S. Qiu, X. Yao; Ammonia borane confined by a metal−organic framework for chemical hydrogen storage: Enhancing kinetics and eliminating ammonia. J. Am. Chem. Soc. 2010, 132, 1490-1491.

[195] Z. Zhang, J. Sun, F. Wang, L. Dai; Efficient oxygen reduction reaction (ORR) catalysts based on single iron atoms dispersed on a hierarchically structured porous carbon framework. Angew. Chem. Int. Ed. 2018, 57, 9038-9043.

[196] P. Wei, X. Li, Z. He, X. Sun, Q. Liang, Z. Wang, C. Fang, Q. Li, H. Yang, J. Han, et al.; Porous N, B co-doped carbon nanotubes as efficient metal-free electrocatalysts for orr and zn-air batteries. Chem. Eng. J. 2021, 422, 130134.

[197] Q. Li, V.S.C. Kolluru, M.S. Rahn, E. Schwenker, S. Li, R.G. Hennig, P. Darancet, M.K.Y. Chan, M.C. Hersam; Synthesis of borophane polymorphs through hydrogenation of borophene. Science. 2021, 371, 1143-1148.

[198] D. Majchrzak, M. Grodzicki, K. Moszak, E. Zdanowicz, J. Serafińczuk, D. Pucicki, R. Kudrawiec, D. Hommel; Influence of pulsed Al deposition on quality of Al-rich Al(Ga)n structures grown by molecular beam epitaxy. Surfaces and Interfaces. 2021, 27, 101560.

[199] Y.J. Gong, H.L. Fei, X.L. Zou, W. Zhou, S.B. Yang, G.L. Ye, Z. Liu, Z.W. Peng, J. Lou, R. Vajtai, et al.; Boron- and nitrogen-substituted graphene nanoribbons as efficient catalysts for oxygen reduction reaction. Chem. Mater. 2015, 27, 1181-1186.

[200] H. Miao, S. Li, Z. Wang, S. Sun, M. Kuang, Z. Liu, J. Yuan; Enhancing the pyridinic N content of nitrogen-doped graphene and improving its catalytic activity for oxygen reduction reaction. Int. J. Hydrogen Energy. 2017, 42, 28298-28308.

[201] J. Wu, L. Ma, R.M. Yadav, Y. Yang, X. Zhang, R. Vajtai, J. Lou, P.M. Ajayan; Nitrogen-doped graphene with pyridinic dominance as a highly active and stable electrocatalyst for oxygen reduction. ACS Appl. Mater. Interfaces. 2015, 7, 14763-14769.

[202] T. Wang, Y. He, Y. Liu, F. Guo, X. Li, H. Chen, H. Li, Z. Lin; A ZIF-triggered rapid polymerization of dopamine renders Co/N-codoped cage-in-cage porous carbon for highly efficient oxygen reduction and evolution. Nano Energy. 2021, 79, 105487.

[203] J. Meng, C. Niu, L. Xu, J. Li, X. Liu, X. Wang, Y. Wu, X. Xu, W. Chen, Q. Li, et al.; General oriented formation of carbon nanotubes from metal–organic frameworks. J. Am. Chem. Soc. 2017, 139, 8212-8221.

[204] L. Li, P. Dai, X. Gu, Y. Wang, L. Yan, X. Zhao; High oxygen reduction activity on a metal–organic framework derived carbon combined with high degree of graphitization and pyridinic-N dopants. J. Mater. Chem. A. 2017, 5, 789-795.

[205] J. Li, H. Zhang, W. Samarakoon, W. Shan, D.A. Cullen, S. Karakalos, M. Chen, D. Gu, K.L. More, G. Wang, et al.; Thermally driven structure and performance evolution of atomically dispersed FeN_4 sites for oxygen reduction. Angewandte Chemie (International ed. in English). 2019, 58, 18971-18980.

[206] Q.-X. Chen, Y.-H. Liu, Z. He, J.-L. Wang, J.-W. Liu, H.-J. Jiang, W.-R. Huang, G.-Y. Gao, Z.-H. Hou, S.-H. Yu; Microchemical engineering in a 3D ordered channel enhances electrocatalysis. J. Am. Chem. Soc. 2021, 143, 12600-12608.

[207] Q. Zhang, M. Zhou, G. Ren, Y. Li, Y. Li, X. Du; Highly efficient electrosynthesis of hydrogen peroxide on a superhydrophobic three-phase interface by natural air diffusion. Nat. Commun. 2020, 11, 1731.

[208] E. Jung, H. Shin, W. Hooch Antink, Y.-E. Sung, T. Hyeon; Recent advances in electrochemical oxygen reduction to H_2O_2: Catalyst and cell design. ACS Energy Lett. 2020, 5, 1881-1892.

[209] P. Wang, T. Hayashi, Q.a. Meng, Q. Wang, H. Liu, K. Hashimoto, L. Jiang; Highly boosted oxygen reduction reaction activity by tuning the underwater wetting state of the superhydrophobic electrode. Small. 2017, 13, 1601250.

[210] L. Jing, Q. Tian, P. Su, H. Li, Y. Zheng, C. Tang, J. Liu; Mesoporous Co–O–C nanosheets for electrochemical production of hydrogen peroxide in acidic medium. J. Mater. Chem. A. 2022, 10, 4068-4075.

[211] L. Jing, C. Tang, Q. Tian, T. Liu, S. Ye, P. Su, Y. Zheng, J. Liu; Mesoscale diffusion enhancement of carbon-bowl-shaped nanoreactor toward high-performance electrochemical H_2O_2 production. ACS Appl. Mater. Interfaces. 2021, 13, 39763-39771.

[212] M. Sun, Q. Fu, L. Gao, Y. Zheng, Y. Li, M. Chen, X. Bao; Catalysis under shell: Improved co oxidation reaction confined in Pt@h-BN core–shell nanoreactors. Nano Research. 2017, 10, 1403-1412.

[213] H. Chen, K. Shen, Q. Mao, J. Chen, Y. Li; Nanoreactor of MOF-derived yolk–shell Co@C–N: Precisely controllable structure and enhanced catalytic activity. ACS Catal. 2018, 8, 1417-1426.

[214] Y. Boyjoo, H. Shi, E. Olsson, Q. Cai, Z.-S. Wu, J. Liu, G.Q. Lu; Molecular-level design of pyrrhotite electrocatalyst decorated hierarchical porous carbon spheres as nanoreactors for lithium–sulfur batteries. Adv. Energy Mater. 2020, 10, 2000651.

[215] W. Cheng, H. Zhang, D. Luan, X.W. Lou; Exposing unsaturated Cu_1-O_2 sites in nanoscale Cu-MOF for efficient electrocatalytic hydrogen evolution. Science Advances. 2021, 7, eabg2580.

[216] H. Su, S. Zhou, X. Zhang, H. Sun, H. Zhang, Y. Xiao, K. Yu, Z. Dong, X. Dai, X. Huang; Metal–organic frameworks-derived core–shell Fe_3O_4/Fe_3N@graphite carbon nanocomposites as excellent non-precious metal electrocatalyst for oxygen reduction. Dalton Trans. 2018, 47, 16567-16577.

[217] X. Wang, C. Han, H. Li, P. Su, N. Ta, Y. Ma, Z. Huang, J. Liu; Fabrication of monodispersed B, N co-doped hierarchical porous carbon nanocages through confined etching to boost electrocatalytic oxygen reduction. Nano Research. 2023, 16, 290-298.

[218] X. Zhao, P. Pachfule, S. Li, J.R.J. Simke, J. Schmidt, A. Thomas; Bifunctional

electrocatalysts for overall water splitting from an iron/nickel-based bimetallic metal–organic framework/dicyandiamide composite. Angew. Chem. Int. Ed. 2018, 57, 8921-8926.

[219] M. Yang, X. Shu, J. Zhang; A defect-rich N, P co-doped carbon foam as efficient electrocatalyst toward oxygen reduction reaction. ChemCatChem. 2020, 12, 4105-4111.

[220] X. Song, H. Zhang, Y. Yang, B. Zhang, M. Zuo, X. Cao, J. Sun, C. Lin, X. Li, Z. Jiang; Bifunctional nitrogen and cobalt codoped hollow carbon for electrochemical syngas production. Advanced Science. 2018, 5, 1800177.

[221] J. Tang, R.R. Salunkhe, J. Liu, N.L. Torad, M. Imura, S. Furukawa, Y. Yamauchi; Thermal conversion of core–shell metal–organic frameworks: A new method for selectively functionalized nanoporous hybrid carbon. J. Am. Chem. Soc. 2015, 137, 1572-1580.

[222] K. Wang, H. Chai, Y. Cao; Using anion-exchange to induce the formation of edge defects in conx to enhance orr activity. ChemCatChem. 2022, 14, e202200146.

[223] Q. Lai, J. Zheng, Z. Tang, D. Bi, J. Zhao, Y. Liang; Optimal configuration of n-doped carbon defects in 2D turbostratic carbon nanomesh for advanced oxygen reduction electrocatalysis. Angew. Chem. Int. Ed. 2020, 59, 11999-12006.

[224] M. Zhang, H. Tao, Y. Liu, C. Yan, S. Hong, J. Masa, A.W. Robertson, S. Liu, J. Qiu, Z. Sun; Ultrasound-assisted nitrogen and boron codoping of graphene oxide for efficient oxygen reduction reaction. ACS Sustainable Chemistry & Engineering. 2019, 7, 3434-3442.

[225] D.E. Goldsack, A.A. Franchetto; The viscosity of concentrated electrolyte solutions—iii. A mixture law. Electrochim. Acta. 1977, 22, 1287-1294.

[226] Z. Cao, P. Su, X. Wang, X. Liu, Y. Ma, C. Li, S. Ping Jiang, J. Liu; The structure–activity correlation of single-site Ni catalysts dispersed onto porous carbon spheres toward electrochemical CO_2 reduction. Fuel. 2022, 321, 124043.

[227] K. Zeng, J. Su, X. Cao, X. Zheng, X. Li, J.-H. Tian, C. Jin, R. Yang; B, n co-doped ordered mesoporous carbon with enhanced electrocatalytic activity for the oxygen reduction reaction. J. Alloys Compd. 2020, 824, 153908.

[228] X. Zhang, S. Yao, P. Chen, Y. Wang, D. Lyu, F. Yu, M. Qing, Z.Q. Tian, P.K. Shen; Revealing the dependence of active site configuration of N doped and N, S-co-doped carbon nanospheres on six-membered heterocyclic precursors for oxygen reduction reaction. J. Catal. 2020, 389, 677-689.

[229] T. Wang, X. Cao, L. Jiao; Progress in hydrogen production coupled with electrochemical oxidation of small molecules. Angew. Chem. Int. Ed. 2022, 61, e202213328.

[230] H.-Y. Wang, M.-L. Sun, J.-T. Ren, Z.-Y. Yuan; Circumventing challenges: Design of anodic electrocatalysts for hybrid water electrolysis systems. Adv. Energy Mater. 2023, 13, 2203568.

[231] Z. Li, Y. Yan, S.-M. Xu, H. Zhou, M. Xu, L. Ma, M. Shao, X. Kong, B. Wang, L. Zheng, et al.; Alcohols electrooxidation coupled with H_2 production at high current densities promoted by a cooperative catalyst. Nat. Commun. 2022, 13, 147.

[232] B. Chen, N.W. Ockwig, A.R. Millward, D.S. Contreras, O.M. Yaghi; High H_2 adsorption in a microporous metal–organic framework with open metal sites. Angew. Chem. Int. Ed. 2005, 44, 4745-4749.